UNIVERSITY OF
COPENHAGEN

Dynamics of Crystalline Paramagnets

Niels Andreas Bonde

Advisers: Prof. Jesper Bendix & Dr. Jacques Ollivier
Submitted to the PhD School of The Faculty of Science, University of Copenhagen on September 16th 2022.

Dynamics of Crystalline Paramagnets

Niels Andreas Bonde
Dept. of Chemistry
University of Copenhagen

This PhD thesis was submitted to the PhD School of the Faculty of Science, University of Copenhagen in accordance with the requirements for the candidacy for the degree of Doctor of Philosophy in Chemistry.

Here in the vault of heaven
Trying to titrate
I ended up in some dire straits
But that's okay

"Vault of heaven", Pixies[93]

Preface

This thesis is a presentation of selected elements of the work I have done during my PhD studies. In the period July 2018 - September 2022, I have been enrolled as a PhD student at the PhD School of the Faculty of Science at the University of Copenhagen (UCPH). My studies have been based on a four year collaboration between the Dept. of Chemistry at UCPH and Institut Laue-Langevin (ILL) in Grenoble, France, between which I have shared my time. My research was funded as well in collaboration, with the first year being paid by the Dept. of Chemistry and the final three years, plus a three months extension, by ILL. The collaboration also awarded my with two academic advisers, Prof. Jesper Bendix with UCPH and Dr. Jacques Ollivier with ILL.

My research has been focussed on the understanding of magnetic properties of molecules. This field of research has been ongoing for more than a hundred years and spans chemistry, physics, mathematics, biology, data science, and even philosophy. Many of them will be discussed throughout this thesis. I was brought up on chemistry, having done my bachelor's and master's studies at the Dept. of Chemistry, but I find my PhD studies to have been my first real foray into the many fields of science bordering chemistry, and I have very much enjoyed my stay there. It may even seem comical that I wrote this thesis for the candidacy for the title of Doctor of Philosophy in Chemistry, yet it does not contain a single chemical reaction! It is also my hope that this thesis will be of interest to people of more fields of research, not just chemistry. It is written in a way that I hope to be accessible to everyone with an understanding of basic chemistry and/or physics.

The thesis contains six chapters. The first is a general introduction to the field of molecular magnetism. It presents the most important aspects of the theory molecular magnetic materials and discusses the ways in which the properties of such a material can be measured and understood. The chapter also starts the discussion on the history of molecular magnetism, developing it through important historical achievements and my interpretation of the corresponding scientific Zeitgeist. The second chapter delves into the neutron sciences. During my studies, I have developed some expertise on the experimental technique of Inelastic Neutron Scattering (INS), particularly in regards to the study of molecular magnetic materials. Important aspects of the conceptualisation, theory, and execution of an INS experiment are presented and discussed, so that the reader may follow the experiments presented in later chapters. The following three chapters are each based on one of my published articles. I will highlight my contributions to those articles and present the important results in a broader context. The chapters do not follow chronologically the publications, but rather attempts to present the research in a coherent progression. It is not a prerequisite for understanding the contents of this thesis to read the articles, nor is it required to have read any published literature on the topic of molecular magnetism, but it would be wise to have done so. Chapters three to five are more of a discussion of key parts of the articles, and they can therefore be read in vacuo, but some of the perspectives may be lost. The final chapter is my attempt at predicting the future. Following the discussion in chapter one on the historical development of molecular magnetism, I present here my analysis of the current trends in molecular magnetism, and why I believe these trends are moving the field in a new direction. Tentatively and fully acknowledging my own insignificance, I shall attempt to place my research in this historical context.

Contents

Abstract

The study of the magnetic properties of molecules has been a long-standing topic within condensed matter physics and chemistry. The last three decades has seen a tremendous influx in the interest in single-molecule magnets because of their potential use in technological applications such as micro-electronics, data storage, and quantum computing. Controlling magnetic properties of molecules is exceedingly difficult, and applications are still in their infancy. Research therefore takes place on two fronts. One seeks to develop single-molecule magnets, and the other investigates model system, which may yield insights in to the fundamental chemistry and physics of single-molecule magnets. The work presented in this thesis takes the latter approach by investigating a series of model systems, for which the results are presented, and their significance in the context of molecular magnetism is discussed.

Chapter One is a general introduction to the field of molecular magnetism in two steps. The first is a conceptualisation of a Single-Molecule Magnet, their physical basis, their construction, the theories of their function, and how can they be studied. The second step is an analysis of the historical development of the field of molecular magnetism. The development of the field is segmented into ”waves”, and key discoveries and their influence is discussed.

Chapter two takes an in-depth look at the spectroscopic technique of Inelastic Neutron Scattering. Since the development of neutron scattering in the 1940’s, it has been used across chemistry, physics, biology, and engineering to study all forms of structures and dynamics. In particular, neutron scattering offers unique insights into all forms of magnetism. This chapter divulges the use of neutrons in studying the structures and dynamics of crystals of paramagnetic molecules. Finally, the use of computer simulations in modelling neutron experiments is discussed.

Chapter three discusses the effects of magnetic exchange through metallophilic bonds. A series of complexes of Co^{2+} and Ni^{2+} can be formed with metalloligands of the form $[M(SAc)_4]^{2-}$ (M = Pt^{2+} or Pd^{2+}, SAc^- = thioacetate). These complexes crystallise in either a monomeric or dimeric form, with the latter being formed due to a Pt^{2+}-Pt^{2+} or Pd^{2+}-Pd^{2+} metallophilic bond. This bond mediates an exchange interaction between the paramagnetic ions, which for the platinum-analogues can be anisotropic (for Co^{2+}) and strong (for Ni^{2+}), and for the palladium-analogues is weak. This is studied by inelastic neutron scattering, where an interference-effect in the momentum-transfer-dependence of the magnetic transitions are found, which provides an unambiguous parametrisation of the

crystal field and exchange interaction.

Chapter four investigates the ability of Pt^{2+} and Pd^{2+} in coordinating lanthanides. This is done through a comparative study of sandwich complexes of the form $(PPh_4)[Ln\{M(SAc)_4\}_2]$ ((PPh_4) = tetraphenylphosphonium, Ln = Tb^{3+}, Dy^{3+}, Ho^{3+}, and Er^{3+}, M = Pt^{2+} or Pd^{2+}, and SAc = thioacetate). These isostructural complexes present a crystal field, where in the axial components are dependent on the coordination strength of the filled d_{z^2} orbitals of Pt^{2+} or Pd^{2+}. Through a combined study by inelastic neutron scattering, DC- and torque-magnetometry, the crsytal field is determined, and the influence on the magnetic properties of the lanthanides are discussed.

Chapter five is a continuation of the investigation presented in the previous chapter. The low-energy electronic structure of the complex $(PPh_4)[Ho\{Pd(SAc)_4\}_2]$ (abbr. **HoPd**) is investigated using high-resolution inelastic neutron scattering. Inhomogeneous broadening of the magnetic transitions is deconvoluted into distributions of the spin-Hamiltonian parameters. The temperature-dependence of the inhomogeneous broadening suggests that the distributions in spin-Hamiltonian parameters is caused by the combined effects of static and dynamic distortions of the crystal lattice. This gives rise to an effective uncertainty in the energies of the Ho^{3+} electronic states. The implications of that uncertainty in the context of technological applications of molecular magnets are discussed.

Chapter six summarises the key results of the presented research. Particular attention is given to a discussion of the methodology of the investigation that led to the results. The chapter continues the discussion on the historical development of the field of molecular magnetism that was started in chapter one. It does so by looking at recent developments in the field and analysing their implications in an attempt to project future developments.

Resumé

Studiet af molekylers magnetiske egenskaber har længe været et forskningsområde indenfor fysik og kemi. De sidste tre årtier har set en opblomstring i interessen af enkeltmolkylemagneter, hvilket skyldes deres mulig anvendelse indenfor teknologi såsom mikroelektronik, dataopbevaring og kvantecomputere. At kontrollere de magnetiske egenskaber af molekyler er ekstremt svært, så deres anvendelser er stadig på fosterstadiet. Forskningen foregår derfor samtidigt på to fronter. Den ene forsøger at udvikle entelkmolekylemagneter, og den anden fokuserer på at undersøge modelsystemer, som kan give indblik i den grundlæggende kemi og fysik bag enkeltmolekylermagneter. Forskningen præsenteret i denne afhandling tager sidstnævnte tilgang ved at undersøge en serie modelsystemer, for hvilke resultaterne bliver præsenteret, og deres signifikans indenfor molekylær magnetisme bliver diskuteret.

Kapitel et er en generel introduktion til molekylær magnetisme i to trin. Det første trin er en konceptualisering af enkeltmolekylemagneter, deres grundlæggende fysik, deres konstruktion, teorierne om deres funktion, og hvordan kan de studeres. Det andet trin er en analyse af den historiske udvikling af forskningen i molekylære magneter. Udviklingen af forskningsområdet bliver segmenteret i "bølger", og de største opdagelser og deres indflydelse bliver diskuteret.

Kapitel to tager et dybdegående kig på den spektroskopiske teknik Uelastisk Neutron Spredning. Siden udviklingen af neutronspredningsteknikker i 1940'erne er de blevet brugt indenfor kemi, fysik, biologi, og ingeniørarbejde til at studere mange former for strukturer og dynamikker. Specielt giver neutronspredning unik indsigt i all former for magnetisme, og dette kapitel udlægger brugen af neutroner til at studere strukturer og dynamikker i krystalller af paramagnetiske molekyler. Til slut diskuteres brugen af computersimuleringer til modelleringen af neutroneksperimenter.

Kapitel tre diskuterer effekterne af magnetisk vekselvirkning via metallofile bindinger. En serie af komplekser af Co^{2+} og Ni^{2+} kan dannes ved brugen af metalloligander af typen $[M(SAc)_4]^{2-}$ ($M = Pt^{2+}$ eller Pd^{2+}, $SAc^- =$ thioacetat). Disse komplekser krystalliserer i enten en monomer eller dimer form, hvor sidstnævnte dannes pga. en Pt^{2+}-Pt^{2+} eller Pd^{2+}-Pd^{2+} metallofil binding. Denne binding giver anledning til en magnetisk vekselvirkning mellem de paramagnetiske ioner, hvilken for platinanalogerne kan være anisotrop (for Co^{2+}) og stærk (for Ni^{2+}), og for palladiumanalogerne er svag. Dette bliver studerert med uelastisk neutronspredning, hvor en interferenseffekt i momentoverførelsesafhængigheden af de magnetisk overgange giver en korrekt parametrisering af krystalfeltet og den magnetiske

vekselvirkning.

Kapitel fire undersøger evnerne af Pt^{2+} og Pd^{2+} til at koordinere lanthanider. Dette gøres gennem sammenligning af sandwichkomplekser af typen $(PPh_4)[Ln\{M(SAc)_4\}_2]$ ((PPh_4) = tetraphenylphosphonium, Ln = Tb^{3+}, Dy^{3+}, Ho^{3+}, og Er^{3+}, M = Pt^{2+} eller Pd^{2+}, og SAc = thioacetat). Disse isostrukturelle komplekser har et krystalfelt, hvor de aksiale komponenter er afhængige af koordinationsstyrken af de fyldte d_{z^2} orbitaler af Pt^{2+} eller Pd^{2+}. Via et kombineret studie med uelastisk neutronspredning, DC- og drejningsmomentmagnetometri. Bliver krystalfeltet bestemt, og dets indflydelse på de magnetiske egenskaber af lanthaniderne diskuteres.

Kapitel fem er en fortsættelse af forskningen præsenteret i forrige kapitel. Den lavenergetiske elektronstruktur af komplekset $(PPh_4)[Ho\{Pd(SAc)_4\}_2]$ (fork.. **HoPd**) undersøges ved hjælp af højopløst uelastisk neutronspredning. Uhomogen forbredning af de magnetiske overgange bliver afviklet i from af fordelinger i spin-Hamiltonoperatorparametrene. Temperaturafhængigheden af den uhomogene forbredning antyder at fordelingerne i spin-Hamiltonoperatorparametrene forårsages af både statisk og dynamisk forvrængning af krystalgitteret.

Kapitel seks opsummerer de afhandlingens vigtigske resultater. Der bliver fokuseret på metodologien der har ledt til resultaterne. Efterfølgende fortsætter diskussionen om den historiske udvikling af forskningen i molekylære magnettisme, som blev startet i kapitel et. Det gøres ved at undersøge de seneste udviklinger indenfor feltet og analysere deres indflydelse i et forsøg på at forudsige fremtidige udviklinger.

Acknowledgements

This thesis is not my work. It certainly does not feel like it. Instead, it feels like the concerted effort of many people. So many more than I can acknowledge on this page. Attempting to acknowledge them also seems futile because words are not capable of communicating my gratitude to all those who have been a part my life the last four years. Nevertheless, I shall here make an attempt to do justice to all those wonderful people.

I started at the university thinking I would study the chemistry of the brain, and I do not think I could have ended up much further from that. Somehow inorganic chemistry drew my attention, which in no small part was because of the phenomenal teachers in the inorganic group: Anders Hammershøj, Anders Døssing, Jesper Bendix, Høgni Weihe, and Stergios Pilligkos. I have had the great pleasure of considering them all as teachers and supervisors, and I extend my sincere gratitude to them. As my PhD drew me to Grenoble, I came to know the many phenomenal people of Institut Laue-Langevin, especially my supervisor Jacques Ollivier, who guided and helped me through many, many neutrons. My only regret is that Covid brought all of that to an abrupt end, but for everything Jacques did for me, I say *merci!*

There are so many more people I need to thank for having supported me through the years, so here is a quick summary: To Mathilde and Piskeriset, thank you for giving me a reason to live. To Mickey, I have very much enjoyed having you as my room mate. Thank you for not killing me. To Covid, thank you for also not killing me. To my friends at UCPH, ILL, and everywhere around the world, if it wasn't for you, I would never have gotten into this mess. Also, I would never have gotten out again, so thank you. To reviewer#2, thank you for the comments that just go on, and on, and on, and on, and on...To everyone I have met at ILL, UCPH, at conferences, courses, bars, in elevators, and at the middle of the night at reactors and synchrotrons, thank you for making science fun.

And thank you, kind reader, for wasting your time reading my thesis.

Niels Bonde

Niels Andreas Bonde

Publications

The following is a list of articles that I have been involved in the making of.

- **NAB-1** Bonde, N. A., Petersen, J. B., Sørensen, M. A., Nielsen, U. G., Fåk, B., Rols, S., Ollivier, J., Weihe, H., Bendix, J., & Perfetti, M. (2020). Importance of Axial Symmetry in Elucidating Lanthanide-Transition Metal Interactions. Inorganic Chemistry, 59(1), 235–243. `https://doi.org/10.1021/acs.inorgchem.9b02064`

- **NAB-2** Bonde, N. A., Appel, M., Ollivier, J., Weihe, H., & Bendix, J. (2022). Unequal sensitivities of energy levels in a high-symmetry Ho 3+ complex towards lattice distortions. Chemical Communications. `https://doi.org/10.1039/D2CC02068H`

- **NAB-3** Emil M. H. Larsen,Niels A. Bonde, Høgni Weihe, Jacques Ollivier, Mauro Perfetti, & Jesper Bendix. Experimental Assignment of Long-Range Magnetic Communication Through Pd & Pt Metallophilic Contacts

Experiments

The following is a list of the Inelastic Neutron Scattering experiments I have taken part in. They were all performed at Institut Laue-Langevin (ILL), Grenoble, France. Each experiment is branded with a Digital Object Identifier (DOI), and following the link will take the reader to a web page. Here information can be found on the experiment, participants, how to cite the data and how it has been cited, as well as possibilities for accessing the raw data.

- Niels Andreas Bonde; Mikkel Agerbæk Sørensen; Jesper Bendix; Jens Ole Christensen; Jacques Ollivier; Mauro Perfetti and Høgni Weihe. (2018). Quantifying antiferromagnetic exchange interactions mediated by metallophilic contacts. `https://doi.org/10.5291/ILL-DATA.4-06-7`

- Niels Andreas Bonde; Jacques Ollivier and Markus Appel. (2018). High resolution on the Ho SMM. `https://doi.org/10.5291/ILL-DATA.TEST-2872`

- Niels Andreas Bonde; Jacques Ollivier; Björn Fåk; Stéphane Rols and Jean-Marc Zanotti. (2018). High energy CEF bands on SMM. `https://doi.org/10.5291/ILL-DATA.TEST-2897`

- Niels Andreas Bonde; Mauro Perfetti; Jesper Bendix; Jacques Ollivier; Rouven Pfleger and Høgni Weihe. (2020). Correlation between phononic structure and magnetic properties in a new family of Ln(DOTA) complexes. `https://doi.org/10.5291/ILL-DATA.4-06-17`
- Niels Andreas Bonde; Bendix Jesper and Ollivier Jacques. (2020). Magnetic anisotropy in high-symmetry lanthanide complexes. `https://doi.org/10.5291/ILL-DATA.EASY-599`
- Niels Andreas Bonde; Rouven Pfleger; Jesper Bendix; Jacques Ollivier; Mauro Perfetti and Høgni Weihe. (2020). Investigation of Energy States and Magnetic Coupling on a Peroxide bridged Lanthanide dimer. Institut Laue-Langevin (ILL) `https://doi.org/10.5291/ILL-DATA.4-06-14`
- Niels Andreas Bonde; Jesper Bendix; Björn Fåk; Jacques Ollivier and Høgni Weihe. (2021). Combining strong Spin-Orbit and Exchange Coupling: The Enigmatic Magnetism of a W(IV) Dimer. `https://doi.org/10.5291/ILL-DATA.4-06-13`
- Niels Andreas Bonde; Jesper Bendix and Jacques Ollivier. (2021). Magnetic Dimensionality-Switching in Chains of High-Symmetry Lanthanide Single-Ion Magnets. `https://doi.org/10.5291/ILL-DATA.4-06-18`
- Niels Andreas Bonde, Høgni Weihe and Björn Fåk. (2021). Direct observation of spin-orbit coupling in a transition-metal ion complex.. `https://doi.org/10.5291/ILL-DATA.EASY-932`

Abbreviations

This is a list of abbreviations used throughout the articles listed above and in this thesis.

INS	Inelastic Neutron Scattering
$\vec{Q}, Q$	Momentum transfer; vector and magnitude of vector
$\vec{k}, k$	Neutron wave constant; vector and magnitude of vector
$\hbar\omega$	Energy transfer
$S(Q, \omega)$	Dynamic Structure Factor
$\vec{\mu}, \mu$	Magnetic moment; vector and magnitude.
$\vec{M}, M$	Magnetisation; vector and magnitude.
$\vec{H}, H$	Magnetic field; vector and magnitude.
χ	Magnetic susceptibility
$\vec{S}, \hat{S}, S$	Electron spin; vector, operator, and magnitude.
$\vec{L}, \hat{L}, L$	Orbital moment; vector, operator, and magnitude.
$\vec{J}, \hat{J}, J$	Coupled basis of spin and orbital moment; vector, operator, and magnitude.
j	Constant of the Heisenberg-Dirac-Van Vlec exchange interaction.
A	Hyperfine coupling constant.
CF	Crystal Field
LF	Ligand Field
Ln	Lanthanide
ESR/EPR	Electron Spin Resonance/Electron Paramagnetic Resonance
ILL	Institut Laue-Langevin
IN5	Cold neutron time-of-flight instrument at ILL.
IN4/PANTHER	Thermal neutron time-of-flight instrument at ILL.
IN16B BATS	Cold neutron back-scattering instrument at ILL.
Me	Methyl group CH_3
Et	Ethyl group C_2H_5
SAc^-	Thioacetate CH_3COS^-
TBA^-	Thiobenzoate $C_6H_5COS^-$
$NEt_4{}^+$	Tetraethylammonium $N(C_2H_5)_4{}^+$
$PPh_4{}^+$	Tetraphenylphosphonium $P(C_6H_5)_4{}^+$

Chapter 1

Introduction

The magnetic properties of molecules has been an ongoing topic of research for many years and spans many classical fields such as physics, chemistry, biology, mathematics, and data science.

Most research on the topic today focusses on the development of molecular magnets, which have properties that make it possible to use them in a technological setting. It might be difficult for the uninitiated to realize the use of a magnet as small as a molecule, because for most people, magnetism is only something that happens in the vicinity of a refrigerator. However, magnetism goes far beyond the standard bar magnet, that we use to hang children's art: From the several tonnes of rare-earth magnets used in each wind turbine[8] to the nanometer-scale magnets used in computer hard disks,[64] magnets are found everywhere in the modern world. While these magnets may have different chemical compositions, they are all founded on the same design approach, which revolves around the physical phenomenon called ferromagnetism. The approach is phenomenal at creating strong permanent magnets but has one drawback: The magnets only work when they are larger than a specific size, which is defined by the chemical composition. In simpler terms: If you cut a bar magnet in two, you get two bar magnets. Cut those in two, and you have four. Unfortunately, continuing this ad infinitum will not leave you with infinitely small bar magnets -just shards of non-magnetised bar material. To create a magnet smaller than this critical size, it is therefore required to take an entirely different approach, which would necessitate designing the magnet from the *bottom-up*. It would be a technological breakthrough if a magnet the size of a molecule ($\sim 1\,\text{nm}$) was invented, so a tremendous amount of research has been done towards that goal. Despite the fact that a magnet was recently made consisting of only a single atom[83], the commercially available nanometer-scale magnet is still a while off. Fortunately all of this research has yielded many interesting results, which have given rise to new avenues of science and technology. Of particular importance is the use of molecules in the storage and processing of information at the quantum level. Two decades ago it was theorized that molecules could be used as the quantum bits (abbr. Qubits) in a quantum computer[73], and it so happens that the criteria[38] for these molecules are very similar to those of a molecular magnet. The reason is that they both deal in 'information'. When magnetising a molecule or initiating a Qubit, information is being imparted to the system, and at a later stage, information -either the same or something else- may be extracted again. So what is critical in either case is that the molecule is capable of retaining information for an extended period of time. Unfortunately molecules are exceedingly poor at doing so. Molecules are fickle, unpredictable, and complicated entities. They are governed by the laws of the quantum world, and they do not care about our goals and aspirations for them. That is why -despite our best efforts- we are still novice at designing, operating, or controlling them. That is where fundamental research on the magnetic properties of molecules becomes important. The work presented in this thesis was not done for the deliberate purpose of developing a molecular magnet, but it has to be seen in the context of the development of molecular magnetism. That is why references will be found throughout this thesis to molecular magnetism and quantum computing (together they may colloquially be referred to as 'spintronics'), despite the fact that none of the molecules presented here would be agreeable candidates as molecular magnets or Qubits.

1.1 Principles of Molecular Magnetic Materials

It is an unfortunate aspect of the development of Single-Molecule Magnets (SMMs), that it is near-impossible to make measurements on *single* molecules. It can be done using delicate experimental techniques, but for the run-of-the-mill molecule aspiring to become the SMM of tomorrow's technology, it is not possible to go through the difficulty and cost of measuring on a single molecule. Instead measurements are done on ensembles of molecules, either single crystals, polycrystalline samples, or even amorphous or glass samples. The goal is then to translate the properties of the sample (found by measurements) to the properties of the particular molecule. For crystalline and polycrystalline samples, on which this thesis shall focus exclusively, it may be argued that every molecule in it is identical. If so, the properties of the sample perfectly reflect the properties of the single molecule. Unfortunately, when measurements on both the properties of the sample and the properties of the single molecule have been made, they often show a dramatic difference.[117, 50, 116] The conclusion must therefore be drawn, that the properties of the molecule can only be understood in the context of its environment. Because of this, it has now become a goal in and off itself to understand the magnetic properties of crystalline ensembles of molecules.

A note on terminology: Throughout literature, and indeed throughout this thesis, several seemingly similar terms may be thrown around. Generally, a molecule with magnetic properties may be called a Single-Molecule Magnet (abbr. SMM), but different names can be chosen depending on the context or to highlight a particular aspect of the molecule. For example, a lanthanide complex will usually contain only one paramagnetic ion (explained below) and may therefore be called a Single-Ion Magnet (abbr. SIM). Similarly there exists Single-Chain Magnets[1] (abbr. SCMs) where the properties stem from the infinite chain structure[21], and crystal dopants where the ”molecule” is a dopant or a defect in a crystal lattice and is named accordingly.[45] In some cases, ”super-paramagnet” may be used to highlight the fact that a paramagnet can retain its magnetisation for a long period of time. Throughout this thesis, the term ’molecule’ will generally be used instead of SMM,SIM etc., because so few of the molecules studied here behave as magnets.

Such an ensemble of molecules may be called a ’paramagnet’, because they align their magnetic moment parallel with an applied magnetic field. This causes an attraction between the two. This is opposed to diamagnetic materials, which are repelled by a magnetic field. The vast majority of matter is diamagnetic, but some elements in their pure form or ions thereof have a significant additional contribution of paramagnetism. What follows below is a rough introduction to the core principles of molecular magnetism:

What defines the magnetisation a molecule may achieve is its angular momentum and the interactions of that with its surroundings.[26] For molecular magnetic systems, it suffices to consider the angular momentum derived from 1) the intrinsic spin $\vec{s}$ of the electron, 2) the orbital angular momentum $\vec{l}$ of the electron, and the intrinsic spin $\vec{I}$ of the nucleus, around which the electron orbits. For a paramagnetic ion, any one or more of these phenomena (pictured in Fig. 1.1) may be present, and they may interact with one another, forming together a combined angular momentum:

---

[1] A chain may also be considered one-dimensional. Together with two-dimensional magnetic structures[65], they may be considered to fall under the field of low-dimensional magnetism. Three-dimensional magnetism would be considered a traditional magnet.

$$\vec{S} = \vec{s_1} + \vec{s_2} \tag{1.1}$$

$$\vec{L} = \vec{l_1} + \vec{l_2} \tag{1.2}$$

$$\vec{J} = \vec{S} + \vec{L} \tag{1.3}$$

$$\vec{F} = \vec{J} + \vec{I} \tag{1.4}$$

$$etc... \tag{1.5}$$

The combination of these sources of angular momentum may depending on the scenario be denoted $\vec{S}$, $\vec{L}$, $\vec{I}$, $\vec{J}$, or $\vec{F}$, but in any case the angular momentum will give rise to a magnetic moment. For example, the combination of electronic spin and orbital momentum is denoted $\vec{J}$ and has a magnetic moment equal to:

$$\vec{\mu_J} = -g\mu_B\vec{J} \tag{1.6}$$

Where g is the effective g-factor for the system, and $\mu_B = 9.27 \cdot 10^{-24} = J/T$ is the Bohr Magneton.

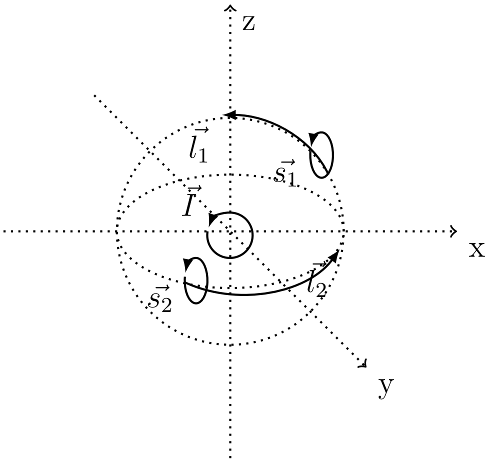

Figure 1.1: Angular momentum of an atom with nuclear spin $\vec{I}$ and two electrons of spin $\vec{s}$ and orbital angular momentum $\vec{l}$.

The strength of the interaction is in most cases given by a constant such that the Hamiltonian for the coupling of e.g. spin and orbital moment reads:

$$\hat{H_{SO}} = \lambda\vec{S} \cdot \vec{L} \tag{1.7}$$

The matter is made somewhat complicated by two observations: $\vec{J}$ may be enacted upon by other forces, and generally $\vec{J}$ can not be known exact. The latter is solved by considering $\vec{J}$ not as a vector but instead as a basis (set of functions) of total angular momentum J with a quantization of the projection of the vector on the (arbitrarily chosen) z-axis M_J. Throughout this thesis, the bra-ket notation $|J\ M_J\rangle$ will be used, which means the basis neatly follows a set of relations:

$$\langle J\ M_J'|\,\hat{J}^2\,|J\ M_J\rangle = \langle J\ M_J'|\,J(J+1)\,|J\ M_J\rangle = \delta\left(M_J' - M_J\right) J(J+1) \tag{1.8}$$

$$\langle J\ M_J'|\,\hat{J}_z\,|J\ M_J\rangle = \langle J\ M_J'|\,M_J\,|J\ M_J\rangle = \delta\left(M_J' - M_J\right) M_J \tag{1.9}$$

$$\begin{aligned}\langle J\ M_J'|\,\hat{J}_\pm\,|J\ M_J\rangle &= \langle J\ M_J'|\,\sqrt{J(J+1) - M_J\left(M_J \pm 1\right)}\,|J\ M_J \pm 1\rangle \\ &= \delta\left(M_J' - M_J \pm 1\right)\sqrt{J(J+1) - M_J\left(M_J \pm 1\right)}\end{aligned} \tag{1.10}$$

The Dirac delta function $\delta(...)$ here is used to identify orthonormal functions. This means the basis $|J\ M_J\rangle$ is defined by the eigen-operators $\hat{J}^2$ and $\vec{J}_z$, and the ladder operator (also known as step operators) $\hat{J}_\pm$ take the system from one value of M_J to a value one integer above or below. Employing this notation also makes it easier to describe the effect on the angular momentum by the interaction of the atom with its surroundings.

The effect of a magnetic field[2] $\vec{B}$ is given by the Zeeman interaction:

$$\hat{H}_Z = -g\mu_B \vec{B} \cdot \hat{J} \tag{1.11}$$

Where

$$\hat{J} = \begin{pmatrix} \hat{J}_x \\ \hat{J}_y \\ \hat{J}_z \end{pmatrix} = \begin{pmatrix} \frac{1}{2}\left(\hat{J}_+ + \hat{J}_-\right) \\ \frac{1}{2i}\left(\hat{J}_+ - \hat{J}_-\right) \\ \hat{J}_z \end{pmatrix} \tag{1.12}$$

is the operator that extracts the expectation value for the angular moment. It is also seen that the components of x and y are defined through the ladder operators, meaning they couple $|J\ M_J\rangle$ states that differ by $\Delta M_J = \pm 1$.

---

[2] A note on magnetic fields: Two closely related terms are used to describe magnetic fields. $\vec{H}$ is the magnetic field strength and has units of $\left[\frac{A}{m}\right]$ in SI and $[Oe]$ in cgs. $\vec{B}$ is the magnetic flux density and has units of $[T]$ in SI and $[G]$ in cgs. In a material, they are related by $\vec{H} = \frac{\vec{B}}{\mu_0} - \vec{M}$, where μ_0 is the vacuum permeability and $\vec{M}$ is the magnetisation. Both are used in literature on molecular magnetism and sometimes (erroneously) interchangeably.

Concerning the magnetic moment of an atom in a crystal lattice, the angular momentum may be enacted upon its surroundings. This interaction is generally referred to as the Crystal Field (CF) and is defined as an electrostatic interaction between the outer-shell electrons of the atom with the surrounding electric field.[20] The outer electric field is caused by the presence of electrons associated with the ligands that coordinate the central atom, and it generally suffices to consider only the contribution from the ligands closest to the central atom. This so-called inner coordination sphere produces an electric field that lifts the degeneracy of the orbital degrees of freedom $|L\ M_L\rangle$ of the total angular momentum. In doing so it causes the states of $|J\ M_J\rangle$ to mix and separate in energy. Since the electric field surrounds the atom, it can be thought of as a function on the surface of a sphere. As such it is possible to expand the electric field into a sum of spherical harmonics. This makes dealing with the electric field significantly easier, since the sum of spherical harmonics can be defined as a set of polynomia in the operators of eq. (1.8)-(1.10).[110, 97]

$$\hat{H}_{CF} = \sum_{k=2,4,6} \sum_{q=-k}^{k} B_k^q \hat{O}_k^q \tag{1.13}$$

Where B_k^q is a constant, and $\hat{O}_k^q$ is a polynomial in $\hat{J}^2$, $\hat{J}_z$, $\hat{J}_+$, and $\hat{J}_-$. For example

$$\hat{O}_2^0 = 3\hat{J}_z^{\ 2} - \hat{J}^2 \tag{1.14}$$

$$\hat{O}_4^0 = 35\hat{J}_z^{\ 4} - \left(30\hat{J}^2 - 25\right)\hat{J}_z^{\ 2} + \left(3\hat{J}^{2^2} - 6\hat{J}^2\right) \tag{1.15}$$

$$\hat{O}_4^4 = \frac{1}{2}\left(\hat{J}_+^{\ 4} + \hat{J}_-^{\ 4}\right) \tag{1.16}$$

to list a few. This formulation of the CF is known by Stevens Operators[110], and it is the most commonly used parametrisation, especially for lanthanides. Another known as the Wybourne parametrisation sees use as well because its values are more consistent across different lanthanides.[122] A third (and final) parametrisation is used most commonly for first-row transition elements. It is effectively equivalent to the Stevens parametrisation, but uses another notation with $D = 3B_2^0$ and $E = B_2^2$ and refers to these as 'axial' and 'orthorhombic', respectively.[3] All of these parametrisations will be used throughout this thesis, because the articles on which this thesis is based uses all of them. Sometimes it has been necessary to make conversions between the parametrisations to highlight a particular aspect, but at no point is it essential that any particular one is used. Only the orders $k = 2, 4, 6$ are shown here, and that is because of two important aspects of this parametrisation:

1) Only even order components are allowed, since odd components leave the Hamiltonian asymmetric, and 2) To describe the effect of an electric field on an orbital angular momentum l, only spherical harmonics up to order $k = 2l$ are needed. For f orbitals $l = 3$, meaning the CF description for lanthanides and actinides need only go to $k = 6$. The index q may in general take any integer value between $-k$ and k, but rarely are all of them necessary. This can be understood through the symmetry of the electric field, which will naturally take on the symmetry of the inner coordination sphere, i.e. the molecular symmetry. If for example the molecule has three-fold rotational symmetry, then the electric field will have three-fold rotational symmetry, and the crystal field parametrisation need only contain elements of $q = \pm 3, \pm 6$. The elements of $q = \pm 6$ appear for the same reason as discussed above in point number 2. Symmetry therefore reduces the total number of parameters needed to describe the CF. For example, D_{4d} symmetry only allows the components B_2^0, B_4^0, B_6^0. The challenge in modelling the CF is in determining the constants B_k^q, which define the strength of that particular component of the CF. Even for the highest symmetry complexes, for which only 4-6 parameters generally are necessary, it can be an exceedingly difficult task to determine the values of B_k^q. In some cases it may become necessary to limit the total number of parameters, either by removing those believed to be of lesser importance or by combining parameters of equal q, thereby forming an ”effective” parameter of that order.

To describe the magnetic properties of an atom with angular momentum J, it therefore becomes necessary to consider the Hamiltonian combining the effects of Zeeman interaction and a CF:

$$\left(\hat{H}_Z + \hat{H}_{CF}\right) |\psi\rangle = E\, |\psi\rangle \tag{1.17}$$

Where $|\psi\rangle$ is in general a linear combination of states of $|J\ M_J\rangle$. For a paramagnetic sample containing multiple, identical molecules, each having this set of $|\psi\rangle$ states, the magnetisation becomes a weighted average of the expectation value of the magnetic moment:

$$M = \sum_{i,f} P_i \langle\psi_f| - g\mu_B \hat{J}\, |\psi_i\rangle \tag{1.18}$$

where

$$P_i = \frac{e^{\frac{-E_i}{k_B T}}}{z} \tag{1.19}$$

$$z = \sum_i e^{\frac{-E_i}{k_B T}} \tag{1.20}$$

is the Boltzmann population factor for the i'th state.

In general, a paramagnet will be come magnetised in an external magnetic field H and gain a magnetisation M. An idealis paramagnet will gain a magnetisation which is proportional to the magnetic field H by a constant of proportionality χ, such that:

$$M = \chi H \tag{1.21}$$

For molecular magnetism it is common to refer to these quantities by various units. The magnetisation is usually given as the magnetic moment of each molecule in units of Bohr magnetons μ_B, and the susceptibility in CGS units of emu/mol. It is also common to present the data at a wide range of temperatures. An example of this is given in Fig. 1.2. In the general case, the susceptibility is simply:

$$\chi = \frac{\delta M}{\delta H} \tag{1.22}$$

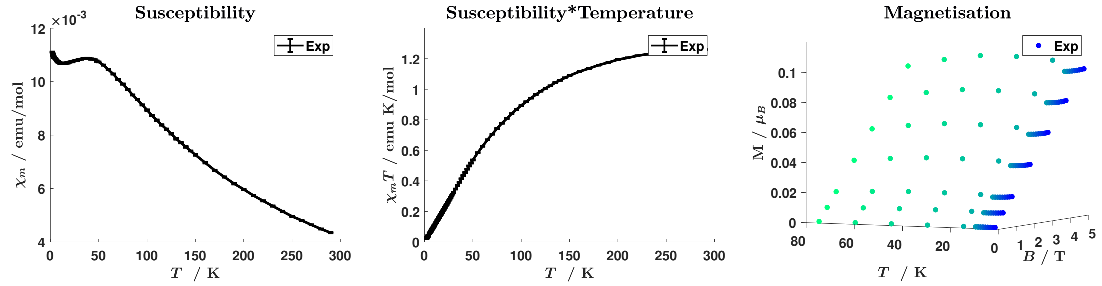

(a) (b) (c)

Figure 1.2: Example of the representation of magnetic data for the compound $K_4[W_2(\mu\text{-}O)Cl_{10}]$.

An important aspect of SMMs is their capability for retaining the magnetisation. As stated earlier, they are not necessarily very good at doing so, nevertheless the rate with which they become magnetised or demagnetised follows approximately first order kinetics.

It is agreeable to assume that the process of magnetisation after a field is applied and the process of demagnetisation after it is removed follow the same kinetics. In that case, the response of a super-paramagnet to a change in the field is given by:

$$M(t+dt) = M(t) + (\chi \cdot H(t+dt) - M(t)) \cdot \left(1 - e^{-k \cdot dt}\right) \tag{1.23}$$

Where k is the first order rate constant[3], which defines the rate with which the paramagnet becomes magnetised or demagnetised. This reduces to the well-known relations of first order kinetics, when a magnetic field is suddenly turned on or off:

$$\begin{aligned} Magnetisation :& M(dt) = H\chi \left(1 - e^{-k \cdot dt}\right) \\ Demagnetisation :& M(dt) = H_0 \chi e^{-k \cdot dt} \end{aligned} \tag{1.24}$$

This is illustrated in Fig. 1.3 first tile. It is however difficult experimentally to determine the rate constant by suddenly turning on or off the field and measuring the magnetisation. Instead, the response to a weak oscillating field is measured.

In Fig. 1.3 tiles two through four, the response of an ideal super-paramagnet to an oscillating magnetic field is shown. The field is given as:

$$H(t) = H_{DC} + H_{AC} sin\left(\omega t\right) \tag{1.25}$$

Where H_{DC} is a constant field on top of which an oscillating field of magnitude H_{AC} is added.[4] The angular frequency of the oscillation is given by $sin\left(\omega t\right)$. In the second tile, the rate of oscillation $\omega = \frac{1}{10}k$ is slow enough that the sample is able to reach its steady-state magnetisation. If the rates are comparable, as is the case in the third tile, the magnetisation appears to be lower and to lag behind by a phase-shift ϕ. If the rate of oscillation is high (fourth tile), the effect is exacerbated and the magnetisation appears to stagnate around its equilibrium. By varying the oscillating field and recording the amplitude and phase shift, it is possible to derive the rate constant. This is the function of an AC-magnetometer, and together with the DC-magnetometry data illustrated in Fig. 1.2, they make up the

---

[3] Not to be confused with $k = \left|\vec{k}\right|$, the magnitude of the neutron wave vector constant, which will be discussed later.

[4] DC and AC refer to the fact, that the fields are derived from an electromagnet, where a DC current produces a constant field and an AC current an oscillating field.

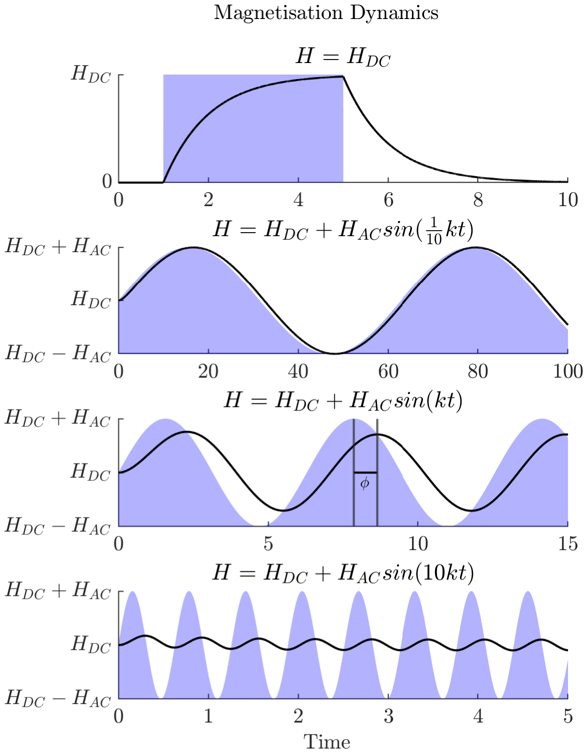

Figure 1.3: Illustration of the magnetisation dynamics for an ideal paramagnet with $k = 1$ and $\chi = 1$. Magnetic field is coloured in blue, and the magnetisation of the sample is given by the black line.

standard approach to measuring and modelling molecular magnets, and the techniques will be references throughout this thesis.

What determines the rate constant k for a given system is the ability of the molecule to interact with its surroundings. In a crystalline paramagnet, this interaction is called the Spin-Lattice Relaxation (SLR), because it is founded on the interaction with the spin-bearing molecule with the surrounding crystal lattice. A multitude of different effects determine the SLR of a given system, and many of them will be discussed throughout this thesis, but for now it is necessary to consider only the rudimentary aspects. A crystalline paramagnet will be comprised of large number of identical molecules, each one being associated with an angular momentum. The angular momenta add degrees of freedom to the crystal, which together with the vibrational degrees of freedom, are populated in such a way as to maximise entropy. In a magnetised crystal, all the angular momenta point the same way (opposite the magnetic field), meaning the entropy of the system is low. Releasing the magnetic field will see the angular momenta return to a disordered, high-entropy state. In doing so, energy has to be exchanged between the angular momenta and the lattice. The lattice carries energy in the form of lattice vibrations called phonons, and SLR is therefore determined in the largest part by the interaction of the phonons with the angular momenta. This is commonly called the spin-phonon coupling. There are many ways in which this interaction can occur, but in the end they all amount to the same thing, which is the determination of the first order rate constant k. The only experimental approach to determining the SLR processes relevant for a given system is by fitting the temperature-dependence (and possibly field-dependence) of the rate constant to a series of parameters:

$$k(T) = \overbrace{k_\tau}^{Tunnelling} + \overbrace{k_O e^{\frac{\Delta}{k_B T}}}^{Orbach} + \overbrace{k_D T}^{Direct} + \overbrace{k_R T^n}^{Raman} \tag{1.26}$$

The different named processes here will be discussed throughout the thesis when relevant.

1.2 The History of Molecular Magnetism

It was mentioned earlier that the current drive for the field of molecular magnetism is based on the potential technological applications. That has not always been the case, so I think it is worth wile spending some time looking at the historical development of the field. I consider the development of the field of molecular magnetism to have taken place in four waves. I use the term 'wave' instead of 'phase', 'period', or 'movement' to indicate that they are not entirely temporally distinct. The field has not moved from the first to the second and onwards in the same way a wave is not disconnected from its past, present or future. It developed out of its predecessors, it was well-defined for only a period, it then toppled over, and it finally crashed back into its successors. The distinction between waves is also not only temporal, it is also idealogical and methodological, as indicated in the changes to questions of 'why' and 'how' research has been conducted, and the following response of the scientific community.

In this chapter I wish to present the first three waves. These will be presented in a historical context, highlighting the most important results, and giving particular attention to the works that led to this thesis. The final wave will be presented in chapter 6 during my discussion of the future and perspectives of molecular magnetism.

1.2.1 Wave #0

I consider there to be an important distinction between the time before and after molecular magnetism became defined by a technological goal. As soon as it was realised that molecular magnets and the like could have technological uses, for example in data storage, the scientific community around molecular magnetism suddenly had a specific goal to achieve, and the race to be first had begun. The zeroth wave is everything that had happened up to this point. This wave encompasses an enormous body of work, where molecular magnetic materials have been studied because of a fundamental interest or to be used to model other systems such as alloys, ionic insulators, complexes, or bio-inorganic molecules. It is off course difficult to pinpoint a beginning, but 1929 might be a good choice. It was around this time that the then-called ”New Quantum Mechanics”[115] of atoms and molecules had been ”settled”, and two very notable contributions to the field of molecular magnetism are made: The works of J. H. Van Vleck[112, 114, 113] on electronic and magnetic susceptibilities, and the development of Crystal Field theory by Hans Bethe.[20] It has since then grown exponentially, and it still continues developing to this day. It is therefore difficult to pinpoint the most important contributions from this vast period, because they have had so far reaching importance, but for the work presented in this thesis, some do come to mind. There is no doubt that CF theory was developed by Bethe, but since then it has expanded significantly based on the works of Stevens[110, 97], Wybourne[122], and others.[26, 54] Following those contributions, it was Sievers[105] who laid the groundwork for the entire field of lanthanide SIMs developed much later. Simultaneously the theories of magnetic exchange were being developed by Anderson[9, 10], Goodenough[51] and Kanamori[71, 118]. These are now used throughout the field of magnetism for the design and understanding of magnetic interactions between ions.

1.2.2 Wave #1

The field of molecular magnetism was given a technological goal to achieve, when it was first shown that a molecule could have slow relaxation of magnetisation. This came with the discovery of an unassuming poly-nuclear cluster of manganese ions bound together by acetates (abbr. Mn_{12}).[100] With this came the idea, that permanent magnets as small as molecules could be made, and the field was changed forever. In the following years, many other examples of complexes with slow relaxation of magnetisation came about. What defines this wave, as being different to what came after, which will be discussed below, is the methodology of the research. In the largest part, the systems that were studied, and which fall within this wave, were found by serendipity. By a simple trial-and-error approach, many complexes were found to have the properties of a SMM. Many of them had drastically different designs and chemical make up, which later became defined as different 'topologies'. It would take more than a thesis to map out this divergent development, but certain complexes should be mentioned here, as they were key in the development of particular topologies. The unassuming cluster of manganese ions mentioned previously gave way for a large section of poly-nuclear complexes. These usually consisted of manganese(II/III/IV) ions, but chromium(III), and iron(III) were targeted as well.[80] This wave also saw the advent of single-ion magnetism based on lanthanides.[121] Particularly important is the Phthalocyanine[69] complex of terbium, which together with its isostructural dysprosium analogue, were the first lanthanide complexes showing slow relaxation of magnetisation.[67, 66]

1.2.3 Wave #2

The second wave started with the first formulations of theories for the understanding of, and the consequential development of, molecular magnetic materials. Following in the footsteps of Mn_{12}, a vast number of high-nuclearity complexes were investigated, which led to theories on the control of magnetic exchange and communication. These were naturally based on the theories presented earlier, but also sought to expand them for technological uses such as interacting with the magnetic moments of singular atoms.[70] The work presented in chapter 3 is an attempt at furthering the understanding of magnetic exchange by studying a peculiar case, in which the exchange is mediated by a rarely-studied bond type. Similarly, based on the experiences with lanthanides came the theories on CF-engineering, which aim to control both static and dynamic magnetic properties.[96] The principles behind this was developed by Sievers, and the most notable example of the successes stemming from this approach came with the development of "sandwich" complexes of Dysprosium. Of particular note is the series of cationic complexes using substituted cyclopentadienyl ligands.[52, 30, 61] The work presented in chapter 4 is an investigation of one important aspect of Ln-SIM design, which relates to the influence of axial ligands.

I bring up this point on the history of molecular magnetism, not because I wish to highlight the advances of one wave or the downfall of another, but simply to give context to the work I will be presenting in this thesis. I state above that the work presented in chapter 3 and 4 is based on work, that I consider to fall within wave #2, but that is only a half-truth. It is probably a truer statement that the systems, I have worked with, were developed as a result of wave #2, but my involvement with them could equally well be described within any wave; My research has all been founded on the fundamental interest in the function of molecular magnetism, which would place it firmly within wave #0. Equally, most of my result were -as is so often the case- found entirely by serendipity and are therefore at home in wave #1. All of this is to say that the field of molecular magnetism is vast. It is far greater and more complex than what I am capable of comprehending, and the myriad of niches and subfields within it makes it impossible to consider all aspects of it. Nevertheless, the work I will present spans multiple waves and will be of interest to a wide range of subfields, which is why I find it necessary to give my perspectives on many of them, despite the fact that I am by no means an expert on any.

Chapter 2

Neutron Scattering

The vast majority of work I have done during my PhD has revolved around neutrons. Neutron scattering is a versatile tool, that has been used within all forms of chemistry, physics, biology, medicine, and much more. It is used so widely, because neutrons are fundamentally inclined to interact with structures and dynamics at the scale of atoms and molecules, and neutrons can therefore be used to study atoms and molecules in ways no other technique can. The experimental technique known as Inelastic Neutron Scattering (abbr. INS) is phenomenal at measuring the structures and energy-transfer dynamics that are relevant for the magnetic properties of molecules. This includes both local excitations, such as those observed in paramagnetic ions, but also the dynamics of the crystalline lattice. As INS (and related techniques) will be discussed throughout this thesis, it is necessary first to divulge the inner workings of the neutron spectrometer. This chapter is therefore dedicated to the task of examining the fundamental aspects of the neutron scattering phenomenon, how it might be observed, and how it is utilized at neutron facilities and in neutron sciences. The final section is concerned with the possibility of simulating INS spectra from systems with localised magnetic moments and where and how that might be useful.

Knowing the history of the neutron is not a prerequisite for understanding neutron scattering, but it is helpful. Since the invention of neutron scattering in the mid 1940's, it is surprising how little has changed: Most of the techniques used today were developed back then and have not changed significantly, and most of the mathematical modelling of neutron scattering was written down -pen on paper- by the early neutron pioneers.[63] Table 2.1 gives an excerpt of important historical events from the neutron sciences, with a particular focus on the developments that are relevant for the work presented in this thesis.

1932	James Chadwick discovers the neutron.[28]
1945	The first measurements of neutron scattering by nuclei is performed.[39]
1939	The theory of magnetic scattering by paramagnetic salts is presented.[63]
1942	Chicago Pile-1, the first continuous nuclear reactor, lights up.[33]
1946	Wollan & Shull do the first neutron scattering experiments at the X-10 Graphite Reactor at Oak Ridge.[104]
1950's	Bert Brockhouse develops the neutron triple-axis spectrometer.[25]
1960	Cribier & Jacrot measure the Crystal Field of Er_2O_3 with INS[34]
1972	Institut Laue-Langevin is built.[1]
1977	Furrer & Güdel measure the singlet-triplet excitation of $Cu_2(OAc)_4(H_2O)_2$[44, 58]
1994	Brockhouse & Shull share the Nobel prize in physics for their contributions to the development of neutron sciences (Wollan died 1984).[85]

Table 2.1: Historical highlights from the development of neutron science.

It was within a few years of the discovery of the neutron that the idea of neutron scattering was brought forward. Soon thereafter, the mathematical models detailing neutron scattering was presented, and they are still in use today. Below is a short introduction to the concept of neutron scattering.

2.1 Principles of Neutron Scattering

The neutron has two fundamentally different ways of interacting with matter. 1) A nuclear interaction, in which the neutron interacts with the nucleus of the scattering atom, and 2) A magnetic interaction, in which the neutron interacts with a magnetic moment. If the magnetic moment is associated with an atom, the interaction may be considered local in the same way the interaction with a nucleus is local. This magnetic moment of the atom may arise from the spin of the electron, the orbital motion of the electron, the spin of the nucleus, or a combination thereof. It is of course not possible to control which of these two interaction processes will be in effect, and more often than not, it will be both. Luckily, it is exceedingly likely that, even though both processes occur, they can be treated separately.

This drastically simplifies things, and allows for the separation of the mathematical models that describe the two processes. Cases will of course occur, in which it is necessary to deal with both processes at the same time, but these will be considered when necessary.

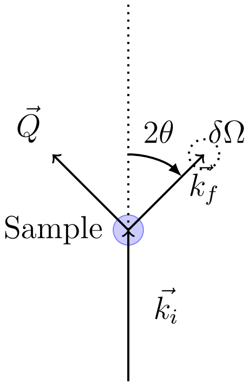

Figure 2.1: Illustration of neutron scattering. $\vec{k_i}$ and $\vec{k_f}$ are the wave vectors for the incoming and outgoing neutron, respectively. $\delta\Omega$ is the small solid angle the neutron is scattered into. The angle between the initial and final neutron is stated as 2θ. The momentum transfer between the sample and the neutron is $\vec{Q} = \vec{k_i} - \vec{k_f}$.

The neutron may appear as both a particle and a wave.[120] It is defined by a wave constant $\vec{k}$ and frequency ω, such that the wave function of the neutron is:

$$\psi = e^{i\left(\vec{k}\cdot\vec{r}-\omega t\right)} \tag{2.1}$$

The scattering of neutrons from condensed matter can therefore be understood as both the interaction of singular particles with matter or by the scattering of waves. In either case, at the core of the description of neutron scattering is the definition of the scattering cross section $\frac{\delta^2\sigma}{\delta\Omega\delta\omega_f}$. It describes how frequent a neutron is scattered from a sample in a direction $\vec{k_f}$ into a small solid angle Ω with final energy $\hbar\omega_f$, and it can simply be understood as "what is observed in an experiment".

$$\frac{\delta^2\sigma}{\delta\Omega\delta\omega_f} = \left(\frac{m_e}{2\pi\hbar^2}\right)^2 \frac{k_f}{k_i} \sum P_{\Psi_i} \left|\langle\Psi_f|\,\hat{V}\,|\Psi_i\rangle\right|^2 \tag{2.2}$$

The fundamental principle of neutron scattering is that the observed scattering is a result of a change in the sample. The experiment simply measures the change in the momentum and kinetic energy of the neutron, and since these parameters are governed by the laws of conservation, the sample must have compensated by en equal and opposite quantity. This is given by the expression $\left|\langle\Psi_f|\,\hat{V}\,|\Psi_i\rangle\right|^2$, in which Ψ describes the system (neutron and sample), and $\hat{V}$ the interaction between these giving rise to a change from the initial to final state. The energy transferred between the neutron and the sample is given as ΔE= $\hbar(\omega_i - \omega_f)$. Similarly, the momentum transferred is given as $\hbar\vec{Q}$, or often simply $Q = \left|\vec{Q}\right|$, which is just the magnitude of the momentum transfer.

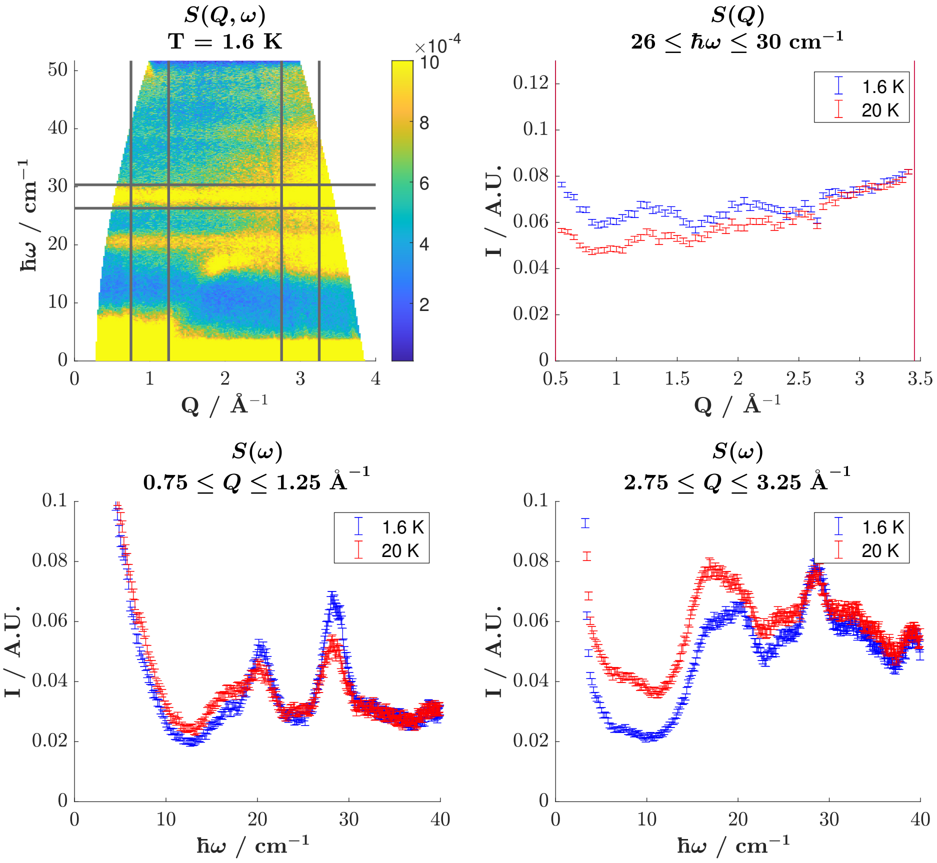

Figure 2.2: INS of a Ni^{2+} dimer (see chapter 3) taken with $\lambda = 3\,$Å at T=1.6 K. Data is represented in four plots: Top left) Colour plot $S(Q,\omega)$. Black lines illustrate the integrated ranges in Q and $\hbar\omega$ presented in $S(Q)$ and $S(\omega)$ plots. The spectra are discussed in the text.

The cross section is closely related to the dynamic structure factor $S(Q,\omega)$ of the sample, which is simply the model description of the scattering done by that sample. The two are so close in definition that they are often used interchangeably. As previously stated, the scattering by a sample can be derived from different interactions, and if so it is possible to decompose the observed scattering $\frac{\delta^2\sigma}{\delta\Omega\delta\omega_f}$ into contributions from *different* $S(Q,\omega)$ components. What will generally be considered in this thesis is the dynamic structure factor of the magnetic scattering by paramagnetic salts, but it is by no means the only scattering observed. The data presented here will naturally also contain elastic Bragg scattering, incoherent scattering, phonon scattering, and many sources of spurious scattering, but they will not be decomposed to individual $S(Q,\omega)$ components, as theey are not of direct interst.

The Neutron Cheat Sheet

Wave equation	$\Psi = e^{i\left(\vec{k}\cdot\vec{r}-\omega t\right)}$
Wave vector	$\vec{k},\, k = \left\|\vec{k}\right\| = \frac{2\pi}{\lambda}$
Momentum	$\vec{p} = \hbar\vec{k}$
Momentum transfer	$\vec{Q} = \vec{k}_i - \vec{k}_f, Q = \left\|\vec{Q}\right\|$
If $k_i = k_f$ then	$Q = \frac{4\pi sin\theta}{\lambda}$
Energy	$E = \frac{1}{2}mv^2 = \frac{h^2}{2m\lambda^2} = \frac{\hbar^2k^2}{2m} = k_BT$
Approx	$E\,[\text{meV}] \approx 5.2 \cdot (v\,[km/s])^2 \approx \frac{82}{\left(\lambda[\text{Å}]\right)^2}$
	$\approx 2.1 \cdot \left(k\left[\text{Å}^{-1}\right]\right)^2 \approx 86 \cdot T\,[mK]$
Energy Transfer	$\hbar\omega = \frac{\hbar^2}{2m}\left(k_i^2 - k_f^2\right)$
Conversions	$1\,meV = 8.07\,\text{cm}^{-1} = 242\,GHz = 11.6\,K$

Fig. 2.2 illustrates different ways of representing INS. The colour plot $S(Q,\omega)$ show the intensity of neutrons scattered with a particular momentum transfer and energy loss, i.e. Stokes scattering. There a many distinct "features" in this spectrum, and much of the difficulty in analysing INS is to distinguish and identify them. To help in doing so, it is common to represent integrated "cuts" in $S(Q,\omega)$ as either $S(Q)$ or $S(\omega)$. In these integrated spectra, it is easier to see the relative intensity as a function of Q or ω, and how it might change as a function of e.g. temperature. Particularly important is the $S(\omega)$ plots, of which there are two shown here. They are each obtained at different intervals of Q, indicated by the black lines in Fig. 2.2 top left. They show how different types of dynamics have different $Q-$dependences. For the work presented in this thesis, it is particularly relevant to distinguish scattering by the magnetic moment of isolated spins and phonon scattering. In general, the Q-dependence of magnetic scattering will follow the magnetic form factor (explained later) of the paramagnetic ion, which monotonically decreases with increasing Q. The intensity of phonon scattering - at least the type we observe here - will generally follow a Q^2 dependence. To distinguish magnetic INS from phonon INS it is thus best to

focus on the low-Q region, where magnetic INS will be the most intense and phonon INS the least. The issue is exacerbated when looking at the Q-dependence of magnetic transitions. In this spectrum there are two, each being identified by a band of intensity at a value of energy-transfer $\hbar\omega = 20$ and $28\,\mathrm{cm}^{-1}$. The Q-dependence of the most intense is shown in the second tile. It is clearly neither monotonic nor decreasing. Instead it is increasing in an oscillatory manner. The reason for the oscillations are explained in chapter 3, and the increase is caused by overlapping phonon scattering.

2.2 Inelastic Magnetic Scattering

We shall now turn our attention to what is probably the most important aspect of neutron scattering for this thesis: The process of inelastic scattering of neutrons by the magnetic moment of atoms and molecules. As stated previously, there are three different ”sources” of magnetic moments in an atom: The nuclear spin, the electron spin, and the orbital moment of the electron. All three can give rise to magnetic scattering, each in their own unique way. There exists also a mathematical model describing the neutron scattering from each of these sources of magnetic moments, and they may often be treated individually. We can make certain generalisations, which will make it clearer, when and where each of these models may be used, and how they might be combined when necessary.

The spin of the electron can quite easily give rise to INS. The reason is that transitions in the $|S\ M_S\rangle$ basis are in the range of $10^0 - 10^2$ cm^{-1}, which is perfectly suited for measuring with INS. When concerned with only the scattering from localised spins, the observed INS may be understood within the so-called spin-only scattering model.

2.2.1 The Spin-Only Approximation

A large part of the INS discussed in this thesis can be understood within the spin-only approximation. It describes, as the name suggests, the scattering of neutrons from localised magnetic moments derived from electronic spins. Beginning at the end, the INS observed from a single paramagnetic ion is given by eq. (2.3):

$$\frac{\delta^2\sigma}{\delta\Omega\delta\omega_f} = \left(-\frac{1}{2}\gamma r_0\right)^2 \frac{1}{Q^2}\frac{k_f}{k_i}\sum_{M_S'}\sum_{M_S} P_{M_S}\left|\left\langle S\ M_S' \middle| gF(Q)e^{i\vec{R}\cdot\vec{Q}}\left[\hat{S}\times\vec{Q}\right]\times\vec{Q} \middle| S\ M_S\right\rangle\right|^2 \tag{2.3}$$

It details how the INS can be understood as the sum of all possible magnetic transitions in the sample. These are described as $|S\ M_S'\rangle \leftarrow |S\ M_S\rangle$, whereby the sample changes state from $|S\ M_S\rangle$ to $|S\ M_S'\rangle$. In doing so, both energy and momentum may be exchanged with the neutron, which is what is observed. As the neutron is a spin-1/2 particle it can therefore be found in either of two states, and in the scattering process, the spin state of the neutron may change. Because of the law of conservation of angular momentum, the spin of the sample must as well change, such that the total angular momentum is conserved. This is the foundation of all INS on paramagnetic ions, as transitions in the $|S\ M_S\rangle$ basis necessarily change the projection of angular momentum. It is by the action of the $\hat{S}$ operator, that transitions in the $|S\ M_S\rangle$ basis may occur:

$$\hat{S} = \begin{pmatrix} \hat{S}_x \\ \hat{S}_y \\ \hat{S}_z \end{pmatrix} = \begin{pmatrix} \frac{1}{2}\left(\hat{S}_+ + \hat{S}_-\right) \\ \frac{1}{2i}\left(\hat{S}_+ - \hat{S}_-\right) \\ \hat{S}_z \end{pmatrix} \tag{2.4}$$

Transition probabilities are related to the operators $\hat{S}_+,\ \hat{S}_-,\ \&\ \hat{S}_z$, which gives rise to the selection rule $\Delta_{M_S} = M_S' - M_S = 0, \pm 1$. It means that transitions can only occur, if the initial and final state have a projection of angular momentum that is equal or differs by an value of 1. This distinguishes the transitions as either being spin-flip ($\Delta_{M_S} = \pm 1$) or non-spin-flip $\Delta_{M_S} = 0$, and is often considered a variable (like momentum- or energy transfer) in the INS experiment. Due to instrumental limitations, however, the change in the spin of the neutron is rarely measured, and eq. (2.3) must be understood as the sum of all scattered neutrons. None of the experiments discussed in this thesis are capable of making the distinction between spin-flip and non-spin-flip neutrons, and 2.3 reflects that.

The double vector cross product $\left[\hat{S} \times \vec{Q}\right] \times \vec{Q}$ is important in dictating the geometry of scattering. It shows that it is only the component of $\hat{S}$ *perpendicular* to $\vec{Q}$ that gives rise to INS. In other words, it is possible to orient the molecule in the spectrometer in such a way that no scattering occurs. When considering powder-averaged INS (see section 2.3), this term augments the Q-dependence of many transitions.

Similarly, the term $e^{i\vec{R}\cdot\vec{Q}}$ is capable of augmenting the transition probabilities and Q-dependence of INS. For single ions, its position may be chosen as the center of reference, and $\vec{R} = 0$ makes the whole argument equal to 1. The influence of the expression is relevant only for coupled systems, where more than one ion is present, and their exchange interaction with one another means that they cannot be treated individually. Here, the expression will be $\neq 1$ for at least one ion. It expresses neatly the interference between scattered waves of neutrons. For localised clusters of paramagnetic ions, this term functions to modulate the Q-dependence of INS transitions, which may be used as a fingerprint of the particular system. An example of this will be discussed more in detail in chapter 3.

$F(Q)$ is the spherically averaged form factor. The form factor of paramagnetic ions is simply the Fourier transform of the magnetisation density. This is generally not spherically symmetric, since the ion is anisotropic. However, sphericity is often an agreeable assumption for two reasons: First, it is cumbersome to calculate the anisotropic form factor, because it is dependent on the particular orbital the electron is in, which might not be known. Secondly, it is not necessarily possible to observe the anisotropic form factor, because it is often only relevant at high Q. The INS of paramagnetic ions is generally measured at low Q, because here the intensity of magnetic scattering is high and phonon scattering is low. Fig. 2.3 illustrates this by showing the anisotropic form factor of a single electron in a d_{z^2} orbital. It shows that the anisotropy is highly dependent on the value of Q: the black outer line is given by $F(Q = 0) = 1$ meaning the intensity of scattering is large, since it is proportional to F^2. It is however nearly perfectly isotropic, in the sense that is scatters equally in all directions. At larger values of Q, where the anisotropy becomes relevant, the intensity is drastically reduced. It is also not generally possible to go to arbitrarily high Q, as INS spectrometers (and the physics governing them!) are limited.

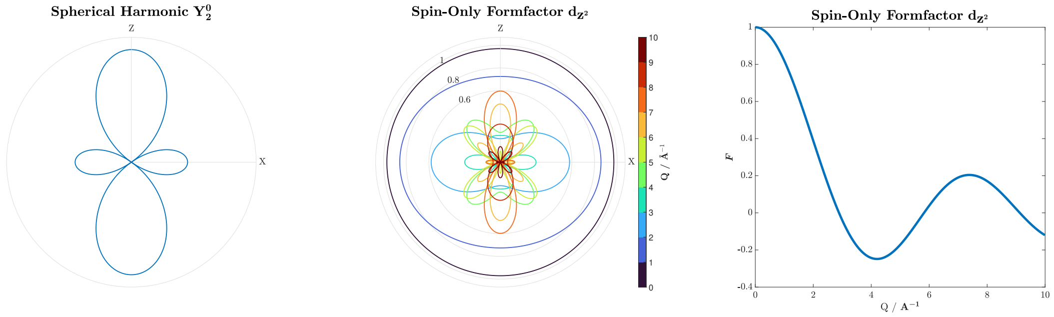

(a)

(b)

(c)

Figure 2.3: **(a)** Polar plot of the Y_2^0 spherical harmonic function, which defines the angular dependence of the d_{z^2} orbital. **(b)** Polar plot of the anisotropic spin-only form factor for an electron in the d_{z^2} orbital calculated following Boothroyd.[23] The color illustrates the different values of Q at which the form factor is evaluated. The value of the form factor is given as the radius from the center. **c** the spherically averaged form factor.

The complexity of calculating a form factor for anything more complicated than a single electron in a d_{z^2} orbital makes doing so only appropriate as an exercise in quantum mechanics.

In nearly all cases, and definitely for the work presented here, it is sufficient to use a simplified spherically averaged form factor, which can be found tabulated for nearly all paramagnetic ions.

2.2.2 Other sources of magnetic scattering

The orbital magnetic moment can give rise to INS, but often the magnetic transitions associated with the orbital moment is much higher in energy than what is observable with ”normal” INS spectrometers. An INS transition associated with the orbital magnetic moment stems from a transition in the $|L\ M_L\rangle$ basis, which is generally split by a ligand field in the range $10^2 - 10^4$ cm^{-1}. In comparison, the upper limit of the energy range for normal INS spectrometers is $10^2 - 10^3$ cm^{-1}. Localised transitions in the orbital moment is therefore rarely observed. If they are observable, the INS follows an expression identical to the spin-only scattering:

$$\frac{\delta^2\sigma}{\delta\Omega\delta\omega_f} = \left(-\frac{1}{2}\gamma r_0\right)^2 \frac{1}{Q^2}\frac{k_f}{k_i}\sum_{M_L'}\sum_{M_L} P_{M_L}\left|\left\langle L\ M_L'\left|g_L F_L(Q) e^{i\vec{R}\cdot\vec{Q}}\left[\hat{L}\times\vec{Q}\right]\times\vec{Q}\right| L\ M_L\right\rangle\right|^2 \tag{2.5}$$

The only difference in the calculation of orbital-only scattering relative to spin-only scattering is that $g_L = 1$ and the orbital form factor $F_L(Q)$ is computed differently.

The magnetic moment of the nucleus is very weak compared to the magnetic moment of the electron, as illustrated by the ratio of the Bohr magneton to the nuclear magneton:

$$\frac{\mu_B}{\mu_N} = \frac{9,274\cdot 10^{-24}\ \text{J T}^{-1}}{5,058\cdot 10^{-27}\ \text{J T}^{-1}} = 1834 \tag{2.6}$$

As such, it is quite rare to observe the influence of the nuclear magnetic moment with INS. It is still possible to do so, and the information that can be gained is comparable to NMR, but the analysis of the experiment is very different to spin-only scattering. The interaction is given by:

$$\frac{\delta^2\sigma}{\delta\Omega\delta\omega_f} = \frac{k_f}{k_i}\sum_{M_I'}\sum_{M_I} P_{M_I}\cdot\langle I\ M_I'|\,\frac{1}{2I+1}\left((I+1)\,b^+ + Ib^-\right)+\frac{1}{2I+1}\left(b^+ - b^-\right)\hat{I}\,|I\ M_I\rangle \tag{2.7}$$

It is clearly quite a different expression to the electronic scattering (spin and/or orbital). It contains the $\hat{I}$ operator, similar to $\hat{S}$ or $\hat{L}$, and is therefore capable of enacting changes in the $|I\ M_I\rangle$ basis. Beyond that however, not much similarity can be found. The expression contains the parameters b^+ and b^-, which are isotope-specific scattering lengths, but the most notable aspect of this expression is the lack of terms giving directionality in the scattering. The expression for the electronic scattering contains both the magnetic form factor $F(Q)$ and the momentum transfer $\vec{Q}$, but the nuclear component is isotropic. The mathematical implementation of this notion is rather convoluted, but the physical interpretation is simple: The radial extent of magnetic moment from the nucleus is much smaller than the wavelength of the neutron. As such, a ”nuclear magnetic form factor” is well approximated by a constant, since:

$$F_N = \int \rho_M(\vec{r})e^{-i\vec{Q}\cdot\vec{r}}dr \approx \int \delta(\vec{r})e^{-i\vec{Q}\cdot\vec{r}}dr = 1 \tag{2.8}$$

Where ρ_M is the magnetisation density and $\delta(r)$ is the Dirac delta function. For the same reason, the neutron would also be incapable of observing any shape to the magnetisation density stemming from a nuclear quadrupole moment. It shows that INS from magnetic nuclei is independent of momentum transfer, in stark contrast to INS from electronic magnetic moments.

The nuclear spin, the orbital moment, and the electronic spin may of course interact with one another, thereby making the modelling more complicated. Particularly important is the interaction between orbital moment and electronic spin, i.e. the spin-orbit coupling. The concept of spin-orbit coupling is discussed elsewhere, but for this chapter it is necessary to consider how the scattering from such systems can be described. If the spin-orbit coupling is sufficiently strong, such as would be the case for e.g. lanthanide ions, it is amenable to do away with the $|S\ M_S\rangle$ and $|L\ M_L\rangle$ bases and instead describe all INS transitions in a combined $|J\ M_J\rangle$ basis. In this case, the model for describing magnetic transitions takes on a form identical to the spin-only model. The only changes necessary are the implementation of the Landé g-factor and the formulation of an effective form factor. In other words, the models presented in section 2.2.1 are perfectly suited to describe INS from systems such as lanthanides. In the unfortunate situation where energies associated with the $|S\ M_S\rangle$ basis, the $|L\ M_L\rangle$ basis, and their spin-orbit coupling are of comparable magnitudes, the only way to describe the INS is by doing the full treatment. This includes first setting up and diagonalizing the full product basis, and then calculating all transition probabilities associated with the spin and the orbital parts. This is cumbersome, and rarely does it lead to something useful. It is therefore best left considered only when necessary, which for this thesis it is not.

2.3 Simulations of INS

INS data is often incomprehensible. The sheer volume of data and the complexity of it makes the analysis of INS complicated. For those working with INS, there are generally only two ”tools” available: Comparison and simulation.

Comparison is simple: Two (somehow) related samples will produce similar INS spectra, and their difference will be apparent. When working with lanthanides, to give an example, it is often necessary to do experiments on two or more lanthanides. Since the samples will largely be isostructural (due to the similar chemical properties of the lanthanides), the samples will yield near-identical phonon scattering but widely different magnetic scattering. By comparing two such samples, it is made significantly easier to distinguish the different sources of scattering.

Simulations are a fairly recent invention. Since the development of neutron sciences in the mid thirties, scientists have been modelling neutron scattering on analytical solutions to Hamiltonians and interaction potentials. Since then, Moore’s Law[2] and computational software like LAPACK[72] have given scientists seemingly infinite computer power at no cost. This makes it possible to analyse neutron experiments in a completely different way, simulation. Today, every aspect of neutron scattering involves simulation; from the design of the instrument to the publication of a set of data points with a simulated line going through them.

The simulation of INS on paramagnetic ions is naturally no different. Most modern publications on the topic includes simulations corroborating the observed spectra, and there are even free simulation packages available. Despite this, I decided that for the work I would be doing during my PhD studies, I should write my own program capable of delivering simulations of INS from the type of systems, I would be working on. It turned out to be a much more involved process, than I had imagined, but also much more fruitful.

This section is dedicated to detailing the challenges of simulating INS, and how it can be overcome computationally. In principle, simulating INS from paramagnetic systems simply involves plugging numbers into eq. (2.3). In practice, there are many different ways of doing just that. As there is (often) no analytical solution to eq. (2.3), approximations have to be made, and it is left to the programmer to judge them. Similarly, simulating an INS spectrum necessarily includes simulating particular aspects of the spectrometer, namely resolution. As there is no clear-cut way of doing so, it is -again- left to the programmer to portray the details of the spectrometer. The program I wrote came to be called ’Banana’ (Code appended in

SI), and Fig. 2.3 shows a simplified schematic of how it works.

The spin system is the description of what is being measured. For easy-of-use and compatibility-reasons, the spin system is defined in the MATLAB package EasySpin.[111] Banana is capable of simulating INS from localised spins, and not extended or itinerant systems. The spin system is the smallest unit, which is repeated throughout the crystal. It might be a single paramagnetic ion in a molecule or it might be multiple, but it is necessary that it is finite. It includes the spin of the paramagnetic ion(s), and all parts of the spin-Hamiltonian. Furthermore, the element, oxidation state, and position of every ion is appended.

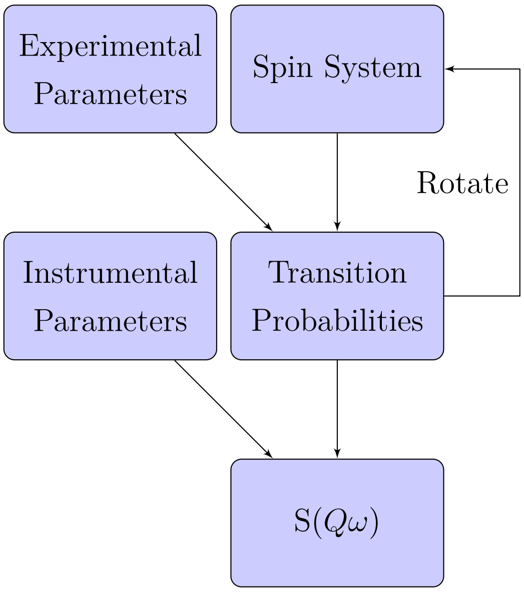

Figure 2.4: Flowchart of the program Banana

Experimental parameters includes magnetic form factors and nuclear scattering lengths. There are many resources available for tabulated formulations of the form factors, and these have been implemented in Banana. They are automatically fetched based on the element and oxidation state given in the spin system. Similarly, the nuclear scattering lengths, which are necessary for systems including hyper-fine interactions, are also tabulated and automatically fetched.

The spin system and experimental parameters together define the transition probabilities, i.e. the likelihood of a neutron causing a magnetic transition in the spin system and later being observed at a particular point in energy- and momentum-transfer space.

$$\propto \left\langle S\ M_S' \middle| gF(Q)e^{i\vec{R}\cdot\vec{Q}}\left[\hat{S}\times\vec{Q}\right]\times\vec{Q} \middle| S\ M_S \right\rangle \tag{2.9}$$

Most experiments are performed on powder samples, so the simulated INS has to be powder averaged, which is done by calculating the transition probabilities of multiple orientations of the spin system. This means rotating both the set of ions in the system and the spin that defines them. Rotating a molecule is straightforward and is easily calculated through a matrix representation of Euler rotations. The rotation of the position of all ions in the system is expressed in the same frame of reference, since the term $e^{i\vec{Q}\cdot\vec{R}}$ defines Q in the laboratory frame. This term defines the interference of scattered waves of neutrons from each ion in the system and is therefore only sensitive to the relative position of each ion. The position $\vec{R}$ of each ion is defined in the laboratory frame and rotated around a center of gravity. Rotating the spin can principally be done the same way but is more easily calculated through a rotation operator:

$$\hat{R} = e^{-i\theta\vec{r}\cdot\hat{S}} \tag{2.10}$$

The operator is defined as the matrix exponential of the product of the spin operator (defined in eq. (2.4)) with a unit-length vector $\vec{r}$, around which a rotation of θ is performed. When representing the basis as vectors, this operator can be expressed as a matrix, which makes the computation simple. Its action on the basis is to rotate the system, but expressing it in the original basis, thereby keeping the frame of reference constant.

The 'Instrumental Parameters' is a complicated set of descriptors of the instrument that is being simulated. Every INS spectrometer will be optimised to span a particular part of energy- and momentum space, and in doing so compromises are made. In particular, the resolution of the spectrometer is important to consider, both in analysing the data and in the simulation. Generally, the resolution of a spectrometer is understood as the width of the elastic peak. For time-of-flight INS spectrometers, if the energy-transfer is large, a correction has to be made for the energy-dependence of the resolution. This simply stems from the fact, that the higher energy a neutron has the faster it is moving, and it is more difficult for the detector to pinpoint the time of arrival. Since peaks in INS generally is assumed to be Gaussian, the peaks are defined as

$$I(\hbar\omega) = \frac{A}{\sigma\sqrt{2\pi}} e^{\frac{-(\hbar(\omega-\omega_0))^2}{2\sigma^2}} \tag{2.11}$$

with A being the height of the peak, $\hbar\omega_0$ the center, and σ being the peak width as a function of energy transfer. The instrumental parameters together with the transition probabilities gives the simulated INS spectra. The spectra are calculated as the intensity as a function of energy-transfer and the three dimensions of $\vec{Q}$. This is sometimes referred to as 4-dimensional INS and is most useful for single-crystal experiments, as the powder-averaging makes the three dimensions of $\vec{Q}$ equivalent. The simulation is therefore averaged across $\vec{Q}$ and plotted as $S(Q, \omega)$.

The only caveat to simulating INS is related to *absolute* values of scattering. Simulating the magnetic scattering of paramagnetic ions in absolute units is straightforward: The output of Banana multiplied by the neutron flux and the sample amount can be understood in absolute units. The problem is that it is exceedingly difficult to correlate the observed INS to the flux and the sample amount, and it is very rarely done. This allows for a free parameter to be added, which scales the simulation to the experimental data. For the same reason, it is very difficult to compare two samples, no matter how alike they are. To do so, the spectra are usually normalised to the elastic peak, which ought to be very similar between similar samples. This means that the intensity of magnetic peaks in different samples are difficult to compare, but if a sample exhibits multiple magnetic transitions, their relative intensity must match.

Chapter 3

For the Love of Heavy Metals

The first project I was involved with during my PhD happens to be the one, I published the last (NAB-3). This chapter is based on that article, but it will not be a stepwise walk through it. Instead I will choose to highlight the parts I find the most interesting and give more attention (than what can be done in an article) to what led to this research.

3.1 Background

It is always difficult to pin point the beginning of a story, but to my mind, it started in 1963 with an article by Ralph G. Pearson.[87] In this article he formulates the first theory for a particular effect, which chemists had known about for a very long time, but which had never been put in to words. His theory was based on a set of principles, which we know now as the concept of Hard/Soft Acids/Bases (HSAB), and their use in understanding and predicting chemical reactions is ubiquitous.[11] Considering simple principles that atoms and molecules can be considered either "Hard" or "Soft", and "Acid" or "Base", and that acids and bases react preferentially with one another if they are of the same "kin", make it possible to predict the outcome of a vast array of reactions. Especially within inorganic coordination chemistry, the HSAB principles are gospel, because they are one of a very limited number of ways of predicting the outcome of a reaction.

The next key development of this story happened about fifty years later in Boston. Here Prof. Linda Doerrer is working on the development of hetero-bimetallic complexes of the type seen in Fig. 3.1. These complexes are formed by linking two metal ions, one hard one soft, by a bi-dentate ligand that has one hard "tooth" and one soft. There are plenty of example of such ligands having both hard and soft points of coordination, e.g. thiocyanate and anions of mercaptopyridines, but thiocarboxylates are particularly interesting. The reason is that there is a very short distance (≈ 2.6 Å) between the hard and soft points of coordination, meaning thiocarboxylates are adapt at bringing metal ions of different kin close together. This is the case for the complex seen in Fig. 3.1, where the soft Pt^{2+} ion

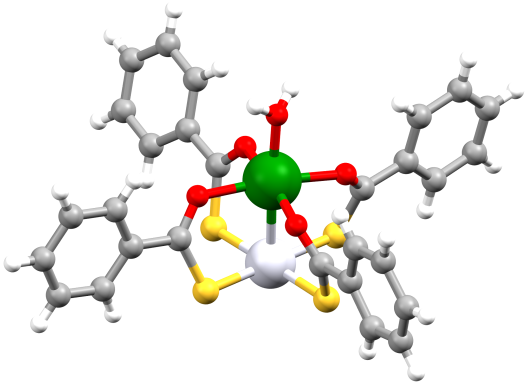

Figure 3.1: Crystal structure of [$FePt(TBA)_4$] (TBA=thiobenzoate).[36] A water molecule acts as a ”capping ligand” forming the octahedral coordination environment of the Fe^{2+}.

coordinates the soft sulphur, and the hard(er) Fe^{2+} coordinates the hard oxygen. This brings the two metal ions into close proximity of one another. In fact the distance between them ($\approx$ 2.6 Å) is comparable to distance commonly seen between a complex metal ion and its first coordination sphere. It is therefore very reasonable to assume that the metal ions act as ligands toward one another. The Doerrer group has produced a vast array of complexes by using different hard metal ions, by changing the ligand backbone, by implementing various capping ligands, and -critically- by changing the conditions for the crystallisation.[36, 12, 14, 60, 13, 84, 18, 19, 106] The immensity of this body of work, and its importance, cannot be overstated. It forms one of the most important (and to my mind the most coherent) study of structure-property relations in inorganic coordination chemistry. As such it has gained significant attention, and particularly important for the field of molecular magnetism has been the investigations on the complexes of paramagnetic ions. This was also my entry, and in the following I wish to go through a project that took four years and which eventually led to my article *Experimental Assignment of Long-Range Magnetic Communication Through Pd & Pt Metallophillic Contacts.* (NAB-3).

3.2 Initial Considerations

What spurred this whole project was a peculiar phenomenon that was found for complexes of the form [$L^1MPt(SAc)_4L^2$] where M=Ni^{2+} or Co^{2+} and L^1 and L^2 are capping ligands. It was commonly found for the complexes studied by the Doerrer group that the capping ligands

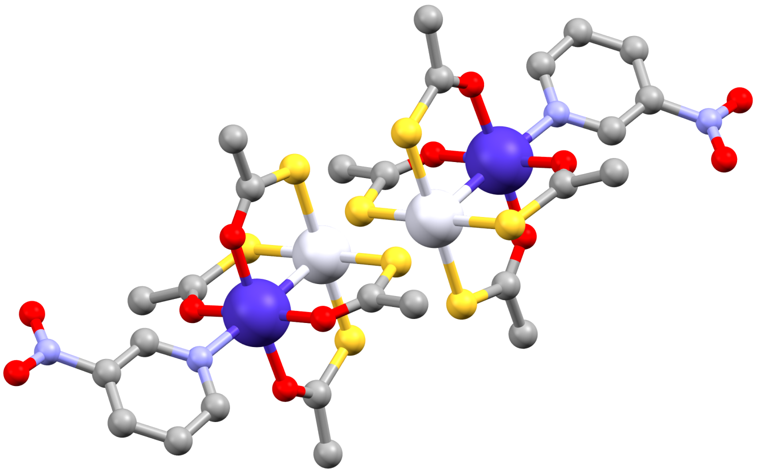

Figure 3.2: Crystal structure of **$\{\mathrm{CoPt}\}_2$** highlighting the packing from the Pt^{2+}-Pt^{2+} metallophilic bond. Hydrogen omitted for clarity.[12]

could be either solvent molecules or certain strongly-coordinating ligands. Of the ligands that were studied, pyridine (Py) and m-nitropyridine (Py-NO_2) produced very different crystal structures, despite their chemical similarity. With pyridine, the complexes would crystallise with it as the two capping ligands producing structures of the form $[\mathrm{MPt(SAc)_4Py_2}]$ (abbr. **{CoPt}** and **{NiPt}**). With m-nitropyridine, only one would coordinate the paramagnetic ion, leaving the Pt^{2+} bare. In the crystalline phase, these molecules lie end-to-end in such a way as to produce a (nearly) linear connection between neighbouring Pt^{2+} ions. This is illustrated in Fig. 3.2. This can be considered a *dimeric* structure of the form $[\mathrm{MPt(SAc)_4Py{-}NO_2}]_2$ (abbr. **$\{\mathrm{CoPt}\}_2$** and **$\{\mathrm{NiPt}\}_2$**).

This is interesting because it illustrates an important aspect of Pt^{2+}: The platinum group metals have a propensity to interact with elements from within that group. This phenomenon is commonly referred to as ”metallophilicity”, and it is related to the HSAB principle by the fact that all of the elements of the group are very soft.[7, 124] The issue of the analogy is that the metal-metal interaction, as found in **$\{\mathrm{CoPt}\}_2$** and **$\{\mathrm{NiPt}\}_2$**, is formed between identical molecules, making it impossible to distinguish one as being the acid and the other as the base. Nevertheless, the Pt^{2+}-Pt^{2+} interaction here is so strong that it is able to out-compete the coordination of Py-NO_2, atleast in the solid state. What makes these systems interesting from the point of view of molecular magnetism is the fact, that the two paramagnetic Co^{2+} or Ni^{2+} ions in the dimer structures interact with one another through a phenomenon called magnetic exchange. This effect describes the interaction between two spins $\vec{S_1}$ and $\vec{S_2}$ and is determined by the parameter J. The effect cause the spins to align either parallel (ferromagnetic $J \leq 0$) or anti-parallel (anti-ferromagnetic $J \geq 0$), and the strength of the interaction is given by the value of J.

$$\hat{H}_{Ex} = j\hat{S}_1 \cdot \hat{S}_2 \tag{3.1}$$

This is of course a well-known effect, but what makes the exchange interaction of **$\{$CoPt$\}_2$** and **$\{$NiPt$\}_2$** unique is two things: The exchange occurs across a metallophilic Pt^{2+}-Pt^{2+} bond, which is very rare and poorly understood, and the exchange is much stronger than what would be thought possible for ions separated by the ≈ 8.5 Å found here. This merited some more attention, and of course that involved neutrons!

3.3 Going Up?

The strong (anti-ferromagnetic) exchange interaction in **$\{$CoPt$\}_2$** and **$\{$NiPt$\}_2$** was found by the Doerrer group based on their analysis of SQUID magnetometry data. In most cases that is the right and proper way of extracting information on the magnetic properties of complexes, but here there were a few too many parameters, which inevitably leads to poor determination of them. For example for the dimers, the parameters needed are an axial and orthorhombic CF parameter D and E, an isotropic exchange interaction j, and a combination of terms to account for diamagnetism[15] and temperature-independent paramagnetism. That is already many parameters to find by normal magnetometry, and on top of that complexity is the issue of the crystal packing. In the dimer structures, the distance between paramagnetic ions is ≈ 8.5 Å through the Pt^{2+}-Pt^{2+} bond, but a direct through-space distance between paramagnetic ions of different dimers could be as little as 7 Å. It could therefore technically not be known based solely on magnetometry data, whether the exchange found in dimers resulted from an interaction across the metallophilic bond or through space. Fortunately, INS is extremely good at measuring both dynamics and structures of molecular systems. The principles of INS from paramagnetic ions was discussed in chapter 2, but particular effects relevant for INS of paramagnetic dimers need highlighting. For two paramagnetic ions of spins $\vec{S_1}$ and $\vec{S_2}$ coupled by a magnetic exchange of eq. (3.2), the total spin is $\vec{S}_{Tot} = \vec{S_1} + \vec{S_2}$, and it is useful to call this by the bra-ket notation as $\left|\begin{smallmatrix} S_1 & M_{S_1} \\ S_2 & M_{S_2}\end{smallmatrix} \; S_{Tot} \; M_{S_{Tot}}\right\rangle$. The INS from such a system is given by:

$$
\begin{aligned}
\frac{\delta^2\sigma}{\delta\Omega\delta\omega_f} \propto \frac{1}{Q^2}\frac{k_f}{k_i} \sum_{M'_{S_{Tot}}} \sum_{M_{S_{Tot}}} P_{M_{S_{Tot}}} \\
\cdot \left| \left\langle \begin{matrix} S_1 & M'_{S_1} \\ S_2 & M'_{S_2} \end{matrix} \; S_{Tot} \; M'_{S_{Tot}} \right| g_1 F_1(Q) e^{i\vec{R}_1\cdot\vec{Q}} \left[\hat{S}_1 \times \vec{Q}\right] \times \vec{Q} \right. \\
\left. + g_2 F_2(Q) e^{i\vec{R}_2\cdot\vec{Q}} \left[\hat{S}_2 \times \vec{Q}\right] \times \vec{Q} \left| \begin{matrix} S_1 & M_{S_1} \\ S_2 & M_{S_2} \end{matrix} \; S_{Tot} \; M_{S_{Tot}} \right\rangle \right|^2
\end{aligned}
\tag{3.2}
$$

This equation is a modification of the spin-only scattering function eq. (2.3) discussed in chapter 2, but expanded to illustrate each and every component. The equation may seem somewhat daunting, but it really is very simple and follows the same logic as any case of magnetic INS from paramagnetic systems. The first part $\frac{1}{Q^2}\frac{k_f}{k_i}$ is just a matter of normalisation, and the rest is simply a sum of all possible transitions in the $|S_{Tot} \; M_{S_{Tot}}\rangle$ basis, each transition being weighted by the Boltzmann population factor for the initial state $P_{M_{S_{Tot}}}$. What causes the transition are matrix elements of the operator, which is a sum of two terms, each one operating on the spin of $\vec{S_1}$ or $\vec{S_2}$ through the action of $\hat{S}_1$ and $\hat{S}_2$. g_n and $F_n(Q)$ is the g-factor and form factor for each ion, which in this case is the same for the two ions, but $e^{i\vec{R}_n\cdot\vec{Q}}$ will of course be different.

An interesting phenomenon occurs with the scattering of dimers. This was illustrated By Alfred Furrer and Hans Güdel, who in the 1970's studied the magnetic INS from molecular paramagnetic clusters. This was a completely new thing at the time, and much of the theory and understanding of INS from such systems was developed then.[42, 44, 43, 59] They were studying simple molecular dimers like copper acetate[58] [$Cu_2(OAc)_2(OH_2)_2$] and 'acid rhodo chromium chloride'[57] [$(NH_3)_5Cr(\mu\text{-}OH)Cr(NH_3)_5]Cl_5 \cdot H_2O$. They found that the momentum-transfer-dependence of the magnetic transitions does not follow the form factor of the ions. Rather the intensity decays with increasing Q, as is to be expected for magnetic transitions, but does so in an oscillatory manner. This is illustrated in Fig. 3.3 for a magnetic transition in a chromium dimer, where the Q-dependence appears as the product of the square of the form factor $F^2(Q)$ and an expression $1 - \frac{sin(QR)}{QR}$, where R is the distance between the chromium ions. This latter expression modulates the Q-dependence as a function of the distance between the two ions, and therefore offers a unique experimental determination of the distance between coupled ions.

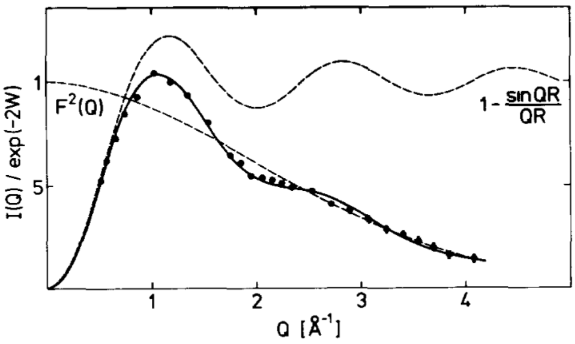

Figure 3.3: Q-dependence of the singlet-triplet excitation at 15.4 cm^{-1} of acid rhodo chromium chloride. Reproduced with permission from Furrer & Güdel [43].

In the cases studied by Furrer and Güdel, there were no issues of identifying the coupled ions, but in **{CoPt}$_2$** and **{NiPt}$_2$** there was uncertainty in which ions were coupling. Observing this oscillation in the INS of those complexes would give us an opportunity to unequivocally determine the coupling scheme, and we did observe it! Sort of. Fig. 3.4 (c) & (d) show the Q-dependence of the main transitions (explained below) of **{CoPt}$_2$** and **{NiPt}$_2$**, and in both cases there is an oscillation. It is however not as clear as the example seen in Fig. 3.3, and that is the result of two effects. 1) The intensity does not fall off with increasing Q, which it should because of the dependence on the form factor. Instead it stays somewhat constant, and that is because of a large contribution to the intensity from incoherent phonon scattering. 2) The oscillations do not follow the expression $1 - \frac{sin(QR)}{QR}$ developed by Furrer and Güdel, instead they seem to be different for **{CoPt}$_2$** and **{NiPt}$_2$** and also different for each transition in that system. This is because the expression $1 - \frac{sin(QR)}{QR}$ only holds for the coupling of isotropic ions, or atleast for the case of an exchange interaction much stronger than the crystal field. In those cases, transitions are pure singlet-triplet ($|S = 1\rangle \leftarrow |S = 0\rangle$) or similar, and the Q-dependence will follow the simple expression, which makes it possible to directly calculate the distance between the ions. For **{CoPt}$_2$** and **{NiPt}$_2$**, the exchange interaction and the CF are of comparable magnitude, making each magnetic transition a complicated amalgamation of both single-ion and dimer transitions. Those do not follow any simple expression for the Q-dependence, and the only way to analyse them is by fully simulating the spectra. The simulations are shown in Fig. 3.4 as solid lines, and there is clearly agreement in energy, intensity, and Q-dependence of all the observed transitions. Based on this there can be no doubt that the coupling is between two ions separated by 8.5 Å, exactly the distance across the Pt^{2+}-Pt^{2+} metallophilic bond.

We measured INS at IN5 on the samples **{CoPt}**, **{NiPt}**, **{CoPt}$_2$**, and **{NiPt}$_2$**. Out primary interest was naturally the dimers, but the monomers were studied as well in an attempt to identify the CF and the exchange interaction separately. For both **{CoPt}** and

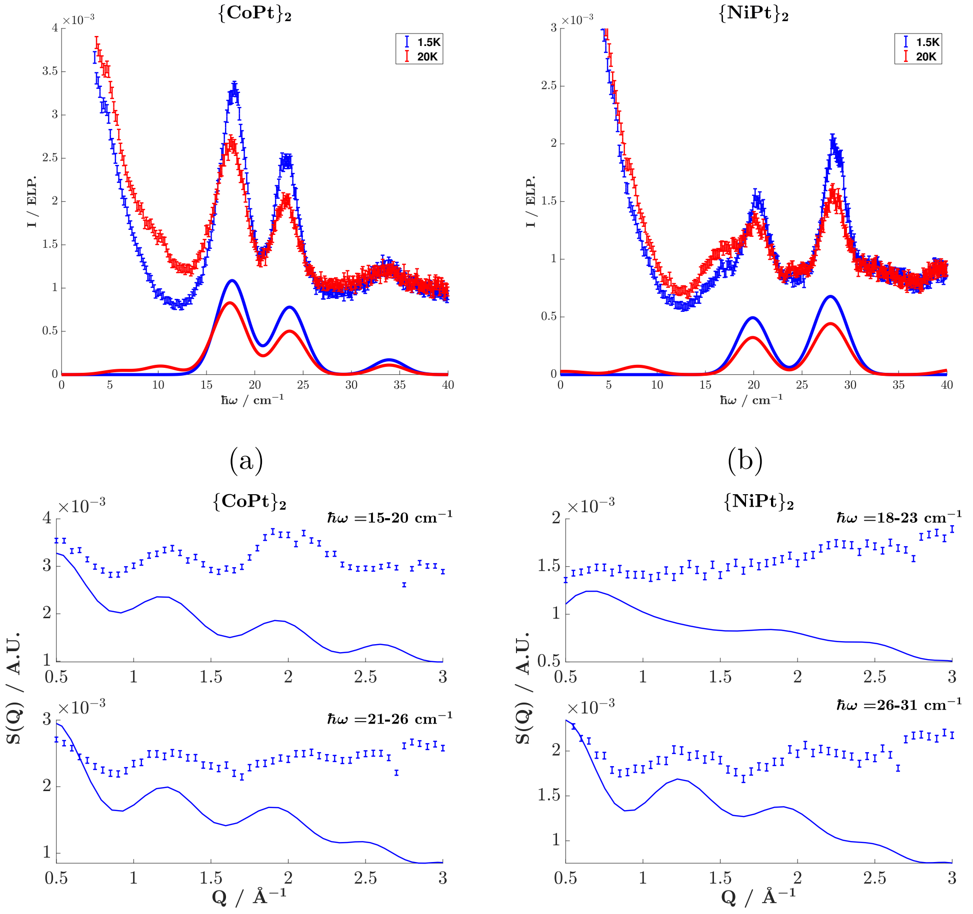

(a) (b)

(c) (d)

Figure 3.4: INS spectra of (a) **{CoPt}**$_{\mathbf{2}}$, (b) **{NiPt}**$_{\mathbf{2}}$ in the range $0.75 \leq Q \leq 1.25$ Å The Q-dependence of the two main transitions of **{CoPt}**$_{\mathbf{2}}$ (c) and **{NiPt}**$_{\mathbf{2}}$ (f) show the interference effect resulting from the coupling of two ions.

{NiPt}, one magnetic transition was observed at 130 cm^{-1} and 12 cm^{-1}, respectively, (see NAB-3 Fig. 3) which exactly gives the axial CF parameter. Our findings for the monomers correlated well with what the Doerrer group had found. The dimers however tell quite a different story. In both cases, we observed magnetic transitions (see Fig. 3.4), which was nice, but it was not without significant difficulty that I came to realise the cause of these transitions.

{CoPt}$_{\mathbf{2}}$ is at the same time simple and complicated. What we found for **{CoPt}** was a very large positive axial CF $D = 65$ cm^{-1}, and the same holds true for **{CoPt}**$_{\mathbf{2}}$, as would be expected considering the minor change in coordination. This leaves a $|\pm1/2\rangle$ ground state for each Co^{2+} ion well-separated from the $|\pm 3/2\rangle$. The exchange interaction between these two ions can therefore be seen as the coupling of two spin-1/2 ions, producing a singlet ground state and a triplet first excited state. This is illustrated in Fig. 3.5. Much to our surprise, we observed three magnetic transitions in $\mathbf{\{CoPt\}_2}$, which we now know can only arise as the result of an anisotropic exchange interaction. It takes a form similar to (3.2), but with the implementation of a diagonal tensor, also in units of cm^{-1}:

$$\hat{H}_{ex} = \hat{S}_{Co_1} \begin{pmatrix} 10 & & \\ & 7 & \\ & & 13 \end{pmatrix} \hat{S}_{Co_2} \tag{3.3}$$

This came as a surprise because none of the previous studies on this compound by the Doerrer group or the in-depth ab initio calculations by another group[98] had ever suggested there to be any anisotropy to the exchange. It might even now seem trivial that there would be some anisotropy to the exchange, but up until this experiment, the analysis done by the Doerrer group and the analysis by my colleagues and I both suggested there to be an isotropic exchange but a large orthorhombic CF, which was also corroborated by the ab initio calculations. This was simply a misinterpretation of the magnetometry data, because no orthorhombic field is present.

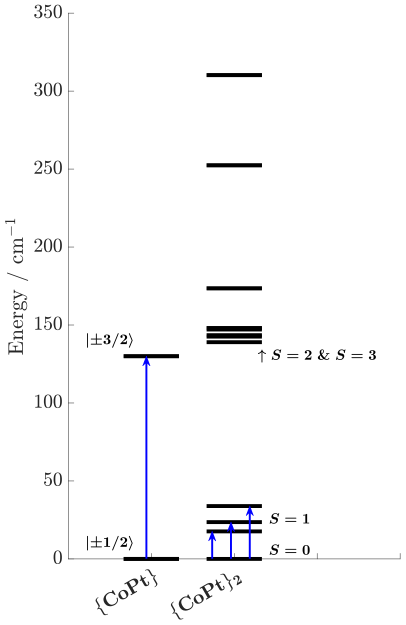

Figure 3.5: Energy level diagram of **{CoPt}** and $\mathbf{\{CoPt\}_2}$. Blue arrows indicate observed (cold) magnetic transitions.

$\mathbf{\{NiPt\}_2}$ had as well some surprises up its sleeve. The first is the strength of the exchange interaction, which had been determined by the Doerrer group to be $J = 25.2\,\mathrm{cm}^{-1}$ and we determined to be $J = 24.5\,\mathrm{cm}^{-1}$. This is a surprisingly large number considering the distance of $\approx 8.5\,\text{Å}$ between the two ions. It has previously been suggested that there is a upper limit to the exchange interaction for electronic insulators, which is determined by the distance.[32] This example not only breaks through the roof of that limit, but it does so based on a coupling across a very rare and poorly understood Pt^{2+}-Pt^{2+} metallophilic bond! A second point of interest comes from a change in the CF. For **{NiPt}$_2$** the axial CF is reduced by one third compared to **{NiPt}**. This may very well simply be due to the change in coordination strength from the nitrogroup ($pK_b = 8.7$ for pyridine and 11.3 for nitropyridine[62]), but I find it tempting to consider the Pt^{2+}. If the metallophilic bond is based on molecular orbitals formed between the filled d_{z^2} orbitals (with the addition of 6s and 6p orbitals), that might pull electron density away from the Ni^{2+} ion, thereby reducing the contribution to the CF from the Pt^{2+}. It might even be possible to prove that by either (or a combination of) ^{195}Pt-NMR or high-resolution X-ray crystallography.

3.4 Further Considerations

One of the reasons why it took four years to get this project published was a very simple questions that someone, I forget who, had asked: "If it works for platinum, what about palladium?" It is a very simple questions that, had we not asked it, every reviewer would have. What no one had guessed was just how difficult a question it would be to answer! It turns out there is a drastic difference between platinum and palladium, both in their effects on the magnetic properties of these complexes, but also in the chemistry of making them. It was only because of his stupendous perseverance, that my friend and colleague Emil M. H. Larsen was able to synthesise the palladium-analogues of these compounds. I will not spend any time here discussing the chemistry of the palladium-analogues, but simply the magnetic properties. [1] We were not able to do INS on the palladium-analogues, so the results discussed below cannot be stated with the same accuracy as for the platinum-analogues, but there are definitely points of comparison worth discussing.

The first point is that we found no difference in the CFs (see NAB-3 table 2) for either paramagnetic ion in the palladium-analogues vs. the platinum-analogues. This irks me greatly because it discredits my previously discussed "tempting hypothesis" on the importance of the platinum (or palladium) in the CF of the paramagnetic ions. It also goes against a previous publication on the topic: In an article by Bonde et. al.[22] it is shown that there is significant difference in the coordination strength of Pt^{2+} and Pd^{2+} in these exact ligands towards lanthanides.[2]

The second point of interest comes from something that *is* different between the two

---

[1] For those interested in his tale of woe, there are some details to be found in the supporting information of NAB-3.

[2] This article is NAB-1 and it will be discussed in detail in the next chapter.

systems: Despite their near-identical crystal structures, the exchange interaction in the palladium-analogues is lower than in the platinum-analogues by one order of magnitude! This does fortunately follow some logic: The exchange is mediated by the overlap of orbitals, which have a larger radial extent in Pt^{2+} than in Pd^{2+}.

This brings about an interesting point, which also relates to my tempting hypothesis. Nearly every application of SMMs would require placing it on a surface and interacting with through various means.[38] These complexes would be prime candidates for deposition on surfaces of soft or 'metallophilically inclined' elements, as the Pt^{2+}/Pd^{2+} ion and the four coordinating sulphurs would bind strongly to such a surface.[50, 106] An interaction could then occur between the paramagnetic ion and surface or bulk substrate, for example if the substrate contains paramagnetic ions as well. Alternatively, if the tempting hypothesis is correct, then it ought to be the case that the CF of the paramagnetic ion is determined (in some part) by the degree to which the Pt^{2+}/Pd^{2+} d_{z^2} orbital is hybridized with the electronic bands of the substrate. If the population of those bands could be controlled by external forces, such as would be the case for semiconductor materials, the delocalisation of the electrons in the Pt^{2+}/Pd^{2+} d_{z^2} orbital might shift accordingly. In other words, it would be possible to have external control the CF of the paramagnetic ion.

Chapter 4

The Question of Coordination

One of the most fundamental aspects of chemistry is the ”bond”. The simple attraction between two or more atoms gives rise to the seemingly infinite complexity of the world around us. What I find the most interesting, is that the more you study the bond, the more difficult it becomes to define. It may be that a simple electrostatic interaction is enough to describe the formation of the ionic bond of simple salts; It may be that a two-electron molecular orbital is enough to describe the bonds of organic compounds; Tt may be that dipolar interactions explain the properties of water; And it may be that metallophilic interactions explain the dimerisation of some heterobimetallic lantern complexes. However for metal ions in complexes, the situation is more complicated. Somehow the idea of a simple bond is no longer enough; Somehow the attraction between a metal ion and a ligand can not be described the simple bonds previously mentioned, but rather a complex amalgamation of them. This makes it exceedingly complicated to give a clear picture of the bonding of complexes, and most often we are left with just fragments, each one representing part of the bond. By studying each fragment *individually* it is fortunately possible to piece together the picture - or atleast some semblance of it.

This chapter is dedicated to a study I was involved in, in which we try to understand a particularly complicated bond. This bond is formed (arguably!) between a Ln(III) ion and a Pt(II) or Pd(II) ion.

4.1 Background

In many ways the background for this study has already been presented in chapter 3. The reason is that the study presented in this chapter, as well as the previous, stem from the works of the group of Linda Doerrer. However before we get to the connection with the Doerrer group, it is necessary to consider some of the principal design criteria for SMMs.

When it comes to the design of Lanthanide Single-Ion Magnets (abbr. Ln-SIMs), there are quite a few theories on the optimisation of their properties. Some theories have even been reasonably successful. It is now generally accepted, that to create an efficient Ln-SIM, it should obey the following design criteria:

1. **Finity:** The most important aspect of molecular magnetism is that the ”spin system” is finite. The spin system can technically be anything, electronic spin, orbital moment, nuclear spin, it can stem from one or more sources, but it has to be finite. This is probably the most difficult part of the design of a Ln-SIM to achieve. The reason is twofold: 1) In a crystal lattice, the magnetic communication between neighbouring Ln ions may be significant, and the spin system is therefore not localised to the ”single” SIM. This can in part be overcome by increasing the distance between neighbouring Ln ions, either by having bulky ligands or by dilution of the magnetic Ln ion into an isostructural diamagnetic compound.[75] 2) Nearly every atom in a crystal will carry a nuclear spin, which can interact with the Ln ion: ^{1}H (100% abundance $I = 1/2$), ^{13}C (1% abundance $I = 1/2$), and ^{14}N (100% abundance $I = 1$). This phenomenon is called the ”spin bath”[94], and the only solution is to use isotopically enriched, nuclear spin-free ligands.[16]

2. **Symmetry:**The crystal field of lanthanides act as an electrostatic interaction with the outer-shell 4f electrons.[20] This lifts the degeneracy of the f-orbitals and causes a zero-field splitting within the free ion terms. Since lanthanides have a ground term which is well-isolated from the first excited term[89], it is amenable to describe the action of the CF solely on the ground term.[110, 97] A lifting of the degeneracy is necessary to produce useful static magnetic properties[96] and to reduce the effect of magnetic relaxation.[86] However, a CF of low symmetry is capable of mixing states of the $|J\ M_J\rangle$ basis, thereby allowing for for quantum tunnelling to become an important mechanism of magnetic relaxation.[17] The first experimental proof of this was found by a former colleague M. A. Sørensen.[107] High symmetry is therefore a must.

3. **Rigidity:** The theory of spin-lattice relaxation describes the processes of magnetic relaxation of a spin through interaction with its surroundings. The theory is long,[103] complicated,[77] and under constant development.[56] It is therefore not easy to summarise it, but it appears that there is one, principal design philosophy, which has been successful at limiting the spin-lattice relaxation: Rigidity and weight of ligands. Both of these effects will cause the ligands to move less as a result of phonons or local vibrations. That produces a smaller change in the CF, and therefore a smaller coupling

between it and the vibration.[1]

Since the Doerrer metalloligand $[Pt(SAc)_4]^{2-}$ has a well-defined structure with a high symmetry and is quite rigid, it was a prime candidate for a Ln-SIM. The only issue with it, is that the bite angle - the capacity of the oxygen to wrap around the metal ion - is limited, and it cannot encapsulate a Ln ion, like it can a 3d metal ion. Two ligands must then be used, creating a sandwich-type structure. This could even be seen as a positive, considering the enormous success of sandwich-type Ln-SIMs like the complexes of phthalocyanine[67, 66, 82, 69], cyclopentadiene[52, 61, 24], and poly-oxometallates.[6, 46, 101] With a tripositive Ln ion and two dinegative ligands, a cationic counter ion is necessary, which gives another synthetic degree of freedom. As it turns out, this counter ion was central in defining the properties of these compounds.

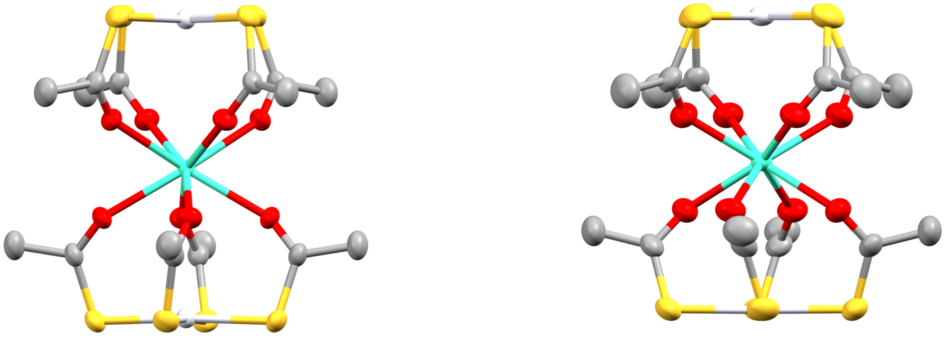

(a) $NEt_4^+[Gd\{Pt(SAc)_4\}_2]$ (b) $PPh_4^+[Gd\{Pt(SAc)_4\}_2]$

Figure 4.1: Comparison of Gd(III)-analogues with two different counter ions.[108]

The compounds that came from this idea were developed, in the largest part, by M. A. Sørensen. They have the general formula $A[Ln\{M(SAc)_4\}_2]$ where A is either NEt_4^+ or PPh_4^+, Ln=lanthanide(III), and M=Pt(II) or Pd(II).[108] Examples of the Gd(III) analogues are seen in Fig. 4.1. Their structures can be summarised as follows: 1) The coordinating oxygen form a prism around the Ln ion described by two angles: θ gives the angle from the molecular z-axis to the Ln-O bond, and ϕ is the angle of rotation between the upper and lower planes of oxygen. 2) There is a near-linear trend in the structural parameters going

---

[1] An example of this will be discussed in chapter 5.

across the f-elements. 3) Due to packing effects, the counter ion changes the coordination environment, particularly ϕ, making the complexes with a NEt_4^+ counter ion C_4 symmetric and those with PPh_4^+ near-perfect D_{4d} symmetric. 4) There is no structural change going from Pt(II) to Pd(II).[108, 22] Their striking likeness is their greatest feature. It makes it possible to compare the effects of minor changes to the structure. Through the works of M. A. Sørensen, M. Perfetti, and U. B. Hansen came a phenomenally detailed description of the Pt(II)-analogues of the lanthanides terbium, dysprosium, holmium, and erbium.[107, 92, 91] This includes the determination of the four important CF parameters B_2^0, B_4^0, B_6^0, and B_4^4. The natural follow-up questions that arose from this work was "What is the role of platinum?". If these metalloligands are capable of engaging in a metallophilic bond strong enough to out-compete the coordination of m-nitropyridine, which was found for the complexes of Co(II) and Ni(II) presented in chapter 3, then surely that must be capable of influencing the CF. The most direct way of probing that interaction would be by analysing the Pd(II)-analogues, since any difference between the two sets would be attributable to the difference of Pt(II) and Pd(II). Since the metallophilic bond of the dimer complexes discussed in the previous chapter was much stronger for the Pt^{2+}-analogues than the Pd^{2+}-analogues, resulting from the larger radial extent of the d_{z^2} orbital, then Pt^{2+} should be a stronger ligand towards the lanthanide. This turned out to be a truth with modifications.

4.2 INS: A How-To Guide

Since the Pt(II)-analogues had been extensively studied using a combination of SQUID-magnetometry, torque-magnetometry[2], and INS, the same would be the case for the Pd(II)-analogues. Before my involvement in this process, there had been rather comprehensive magnetometry measurements done, which meant I was largely focussed on the analysis of the INS. Data was recorded at IN5 on the compounds $PPh_4^+[Tb\{Pd(SAc)_4\}_2]$ (**TbPd**), $PPh_4^+[Dy\{Pd(SAc)_4\}_2]$ (**DyPd**), $PPh_4^+[Ho\{Pd(SAc)_4\}_2]$ (**HoPd**), and $PPh_4^+[Er\{Pd(SAc)_4\}_2]$ (**ErPd**). There are a three reasons, why these three lanthanides were chosen: 1) There is a great advantage in measuring INS on several different lanthanides of the same structure, since all of the non-magnetic scattering, phonons, vibrations, Bragg scattering, incoherent scattering etc., will be near identical. Since non-magnetic INS makes up for such large portion of the total observed INS, it can be difficult to pin point the magnetic scattering of

---

[2] Torque-magnetometry is an experimental technique that measures the torque between a magnetic field and the magnetic moment of a single crystal.[90]

interest. Measuring multiple lanthanides makes it possible to compare the spectra, which highlights the differences attributed to the magnetic scattering. 2) The intensity of magnetic INS transitions is proportional to the square of the g-factor (see eq. (2.3)). Since the Landé g-factor for the lanthanides is only larger than one for the later half, there is significant difference in intensity between eg. Sm^{3+} $g_J = 2/7$ and Tb^{3+} $g_J = 3/2$.[3] 3) It is generally perceived that these lanthanides make for the best SMM candidates, since they offer the "best" combination of large total angular momentum and large g-factors, resulting in the possibility of largest magnetic moment. It was very deliberately chosen that we would only investigate the complexes of $\mathrm{PPh_4}^+$ and not those of $\mathrm{NEt_4}^+$. This was inspired by one of the conclusions that came from the works on the Pt^{2+}-analogues: There is a drastic difference in the B_4^4 parameter as a function of ϕ,[17] which is dictated by the counter ion, and that influences the rate of tunnelling.[107] In the complexes of $\mathrm{PPh_4}^+$, both the B_4^4 parameter and the rate of tunnelling is smaller, so in an attempt to optimise the dynamic magnetic properties, they were the natural choice. It should also be noted, that the B_4^4 parameter appears only because the complexes are not perfect $\mathrm{D_{4d}}$. The B_6^4 parameter should be included as well, but there was never found any evidence of its importance, as any influence it might have could equally well be explained by the B_4^4.

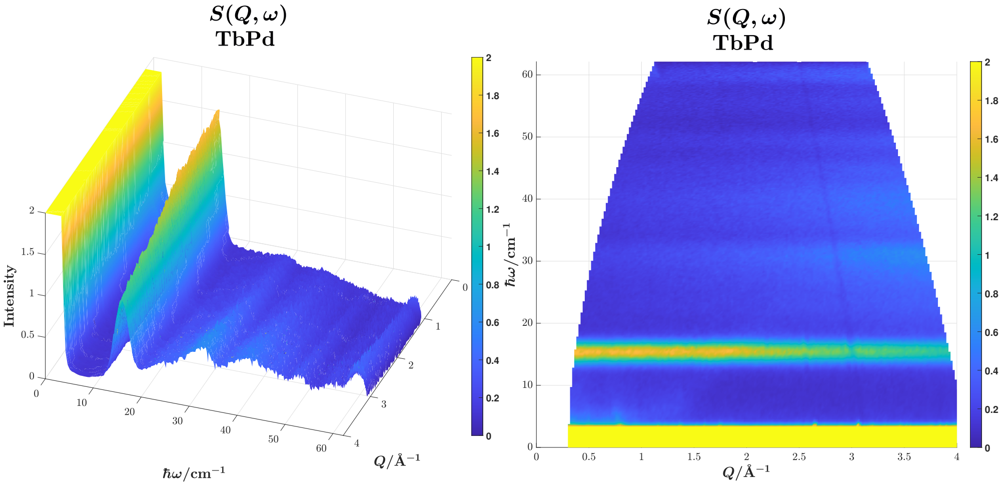

(a)

(b)

Figure 4.2: $S(Q,\omega)$ of **TbPd** at 1.6 K in **(a)** perspective and **(b)** regular top view.

Fig. 4.2 shows the $S(Q,\omega)$ of **TbPd** measured with incident neutron wavelength of $\lambda = 2.8$Å. Only the neutron energy-loss side (Stokes scattering) is shown, since the neutron

---

[3] Please note that the Landé g-factor may be denoted in literature as either g_J or g_L.

energy-gain side has nearly no intensity at 1.6 K. If only life was as easy, as it is to interpret this spectrum, I think everyone would be a lot happier. What is observed here is a prime example of a magnetic excitation. At $\approx 15\,\mathrm{cm}^{-1}$ a signal of large intensity is observed, which decays with increasing momentum transfer. This dependence is shown in more detail in Fig. 4.3. At the lowest temperature (1.6 K), the intensity of the excitation clearly follows the form factor of Tb^{3+} identifying this as a local excitation. As the temperature increases, the total intensity decreases. Since the intensity of local magnetic transitions follow directly the Boltzmann population of the CF state, from which the transition originates, the transition must stem from the ground state. It must also be noted, that the Q-dependence at higher temperatures no longer follow the form factor, but rather seems to "flatten out". This is not because of a any fundamental change to the excitation, but instead comes from an increase in the background. The primary source of background scattering is incoherent phonon scattering, which tends to increase with temperature and has a characteristic Q-dependence of $I \propto Q^2$. Adding this to a monotonically decreasing form factor, and the resultant excitation - even one as intense as this - may not be easy to identify as magnetic.[4]

It may not seem at first, that a single excitation could be very useful information, since there could be as many as 78 magnetic excitations in the CF states of Tb^{3+} ($^7F_6$). The value of observing just a single excitation stems from the fact, that **TbPd** has near-perfect D_{4d} symmetry. For this high a symmetry, only four CF parameters are necessary, and the energy of all 78 excitations are defined entirely by these four parameters. A single INS excitation can provide a phenomenally important insight, if (and only if) the system being investigated has high symmetry or for another reason has a simple parametrisation. Consider as an example a Tb^{3+} complex with no symmetry. It would require 27 CF parameters, and the determination of those necessitates 27 unique observables. If those had to be found by INS, it would require observing excitations between all 13 unique CF states, and correlating the intensity of each transition to their exact composition, which will be linear combination of different $|J\ M_J\rangle$. That is an insurmountable task. Fortunately that is not needed for **TbPd**, as the process of developing a CF parametrisation for such a system can follow a simple routine:

1. From the susceptibility measurements (see NAB-1 Fig. S21), it is evident that **TbPd**

---

[4] When seeking difficult-to-observe magnetic excitations, it is common to prepare a deuterated sample, which drastically decreases the background. This is due to the difference in the incoherent cross sections of ^{1}H ($\sigma_{inc} = 25\,barn$) and ^{2}H ($\sigma_{inc} = 4.0\,barn$). This would also have been massively helpful in this scenario, but the process of deuteration for such compounds is extremely time-consuming and prohibitively expensive.

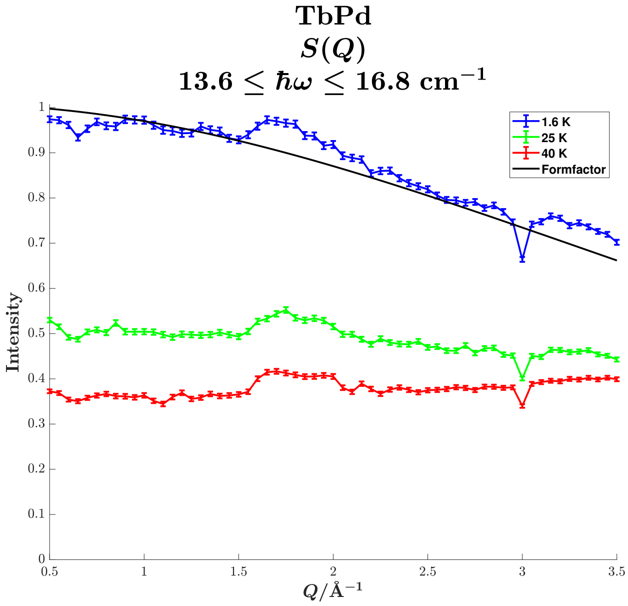

Figure 4.3: Q-dependence of the observed magnetic excitation in the **TbPd** and the theoretical form factor of Tb^{3+}.

has a non-magnetic ground state $|0\rangle$.

2. From the temperature-dependence of the INS peak, it is probable that it originates from the ground state. A state then has to be found at an energy of $\approx 15\,\text{cm}^{-1}$. The only state(s) to which an excitation from $|0\rangle$ can occur is $|\pm1\rangle$.

3. Having locked in the energy and identity of the ground and first excited states, it becomes much easier to find the next states by fitting magnetometry data, either DC-magnetometry (see NAB-1 Fig. S21-S22.) or torque magnetometry (see NAB-1 Fig. 2). Doing so placed a clustering of $|\pm2\rangle$ and $|\pm6\rangle$, which will be mixed together by the off-diagonal B_4^4 parameter, in the range 50-80 cm^{-1}. The INS excitation from the first excited state $|\pm1\rangle$ to these states (see table 4.1) should be allowed, which led me to look more closely at the INS spectra in the appropriate energy interval. Lo and behold, at 40 and 45 cm^{-1}, two hot INS transitions are visible (see Fig. 4.4). These are only visible at very low momentum-transfer, which is why I had originally failed to spot them.

This is an example of how the analysis of INS generally follows an iterative (neural) fitting routine.

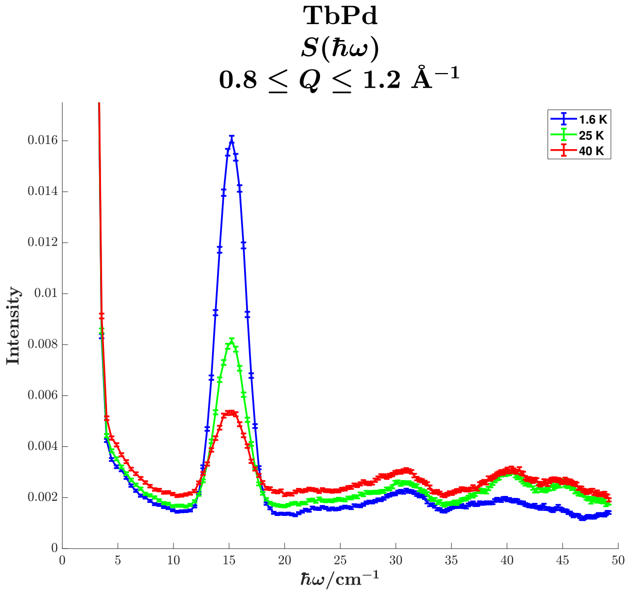

Figure 4.4: Integrated spectra of **TbPd** with incident neutron wavelength $\lambda = 2.8$Å. Spectra normalized to the elastic peak at 1.6 K.

4. The process has to go back and forth between fitting magnetometry data, simulating spectra, re-analysing INS or looking at it in another way. I found great help and inspiration in working together with my colleague at the time M. Perfetti, who is an expert on torque magneometry. By ping-ponging our ideas (and CF parametrisations!), we were able to converge on a model.

E / cm^{-1}	E (exp) / cm^{-1}	Composition
0	0	$\|0\rangle$
16.6	15.4	$\|\pm1\rangle$
53.6	55.7	$0.266\,\|+6\rangle + 0.655\,\|+2\rangle + 0.266\,\|-6\rangle + 0.655\,\|-2\rangle$
60.8	61.6	$0.690\,\|+6\rangle + 0.155\,\|+2\rangle - 0.690\,\|-6\rangle - 0.155\,\|-2\rangle$
62.8	61.6	$0.655\,\|+6\rangle - 0.266\,\|+2\rangle + 0.655\,\|-6\rangle - 0.266\,\|-2\rangle$
75.7		$0.155\,\|+6\rangle - 0.690\,\|+2\rangle - 0.155\,\|-6\rangle + 0.690\,\|-2\rangle$

Table 4.1: Lowest energy levels of **TbPd** with energy calculated from fitted CF parameters and experimental energies from INS.

Unfortunately not all of the compounds in the **LnPd** series was as easy to model as **TbPd**. **ErPd** (see NAB-1 Fig. S16-S17) only had one INS peak, and the model was based almost exclusively on fitted magnetometry data. Fig. 4.5 shows selected INS spectra for **HoPd** and **DyPd** and illustrate the importance of comparisons between lanthanides to identify magnetic scattering. When looking at the $S(Q,\omega)$ plots, there are no magnetic excitations popping out, like in the case of **TbPd**. What is most clear is the equivalence of the phononic background: The two spectra were measured with the same incident neutron wavelength $\lambda = 2.2$Å, which makes it easier to see the near-identical phonon scattering.

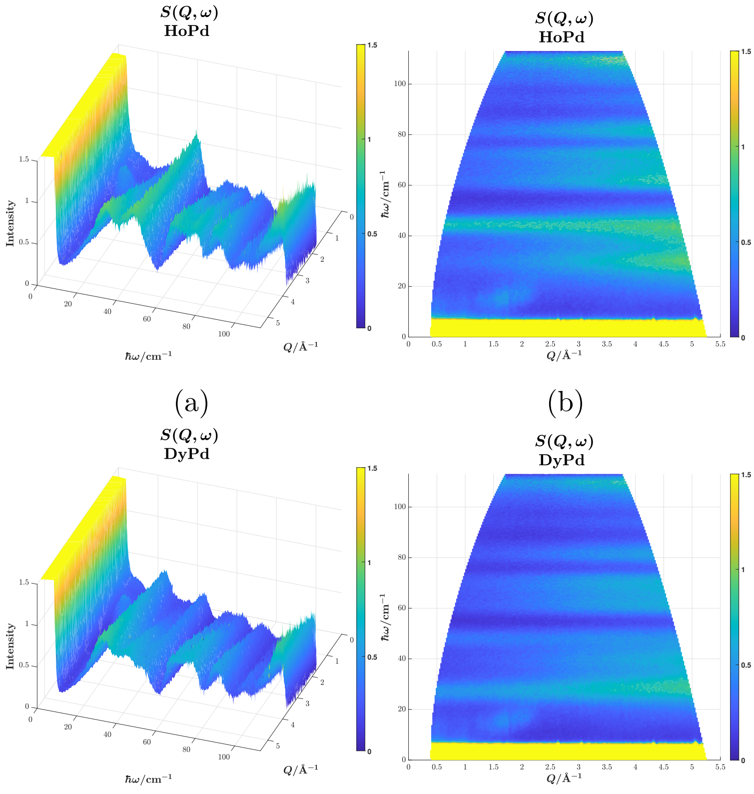

(a) (b)

(c) (d)

Figure 4.5: $S(Q,\omega)$ of **(a)**,**(b) HoPd** and **(c)**,**(d) DyPd** at 1.6 K

The presence of magnetic scattering only becomes apparent when looking at the various ”cuts” that can be made through the data. In Fig. 4.6 a slice of the low momentum-transfer region for **HoPd** and **DyPd** is shown. Here it suddenly becomes much clearer that the spectra are littered with magnetic scattering - it was just being obfuscated by the phonon scattering. Quite often, in fact, a magnetic peak will be ”on top” of a phonon, as is the case here for both: **HoPd** has a clear magnetic peak at $\approx 45\,\mathrm{cm}^{-1}$ and **DyPd** at $\approx 25\,\mathrm{cm}^{-1}$, both of which sit on top of a plethora of phonons.

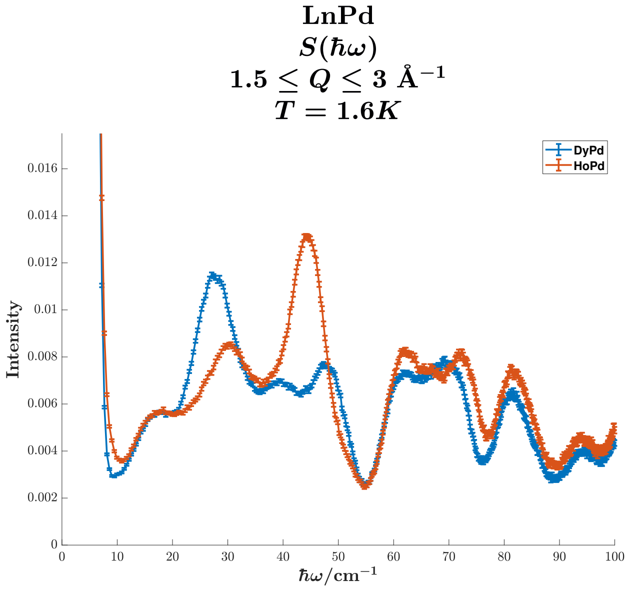

Figure 4.6: Comparison of **DyPd** and **HoPd** at 1.6 K. The spectra are normalized to the elastic peak.

4.3 Some Assembly Required

The process of analysing INS on isostructural lanthanide complexes is quite simple. It just takes a very long time. In the case of **LnPd**, it was a tremendous help that the isostructural **LnPt** series had already been under intense scrutiny. I had at the outset a CF parametrisation for **LnPt**, which was in the same ballpark as what was found for **LnPd**. It is very similar to other projects, I have worked on, where ab initio calculations gave a starting point for a parametrisation, which is then refined using INS or related techniques.

Fig. 4.7 shows the fruits of my labour: The full energy level diagram for the **LnPd** series (atleast the ones we measured) with simplified compositions. The black arrows indicate the observed INS transitions, and it is evident that there is can be a great difference in the number of transitions observed for each lanthanide - despite the fact that they have a near-identical CF. It would of course be possible to raise the temperature to a point where all (or atleast more) states are populated, and more transitions could be observed. This unfortunately also increases the phonon background, likely to a point where it would be impossible to observe the magnetic INS. For a lanthanide complex, where it is necessary to observe multiple magnetic transitions to deduce the CF, it becomes a requirement to fully

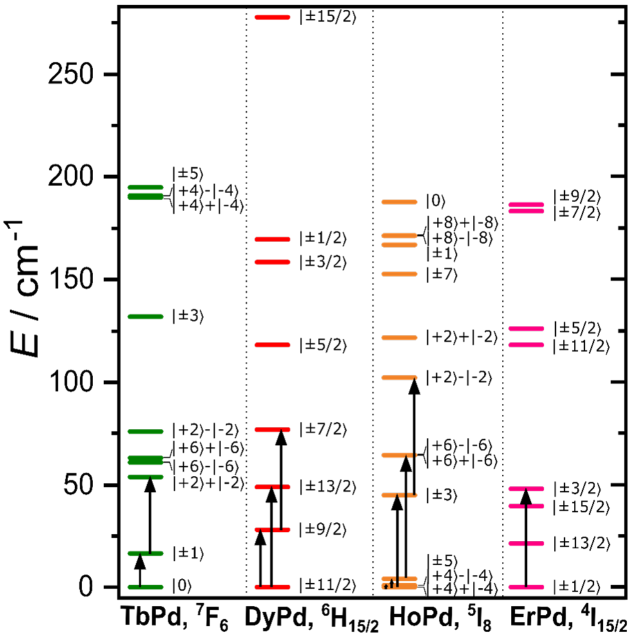

Figure 4.7: Energy level diagram of **TbPd**, **DyPd**, **HoPd**, and **ErPd** based on best fit parameters. Black arrows indicate observed magnetic INS transitions. Reproduced from NAB-1

deuterate the sample. [5]

Returning to the original question, which spurred this entire investigation: What is the nature of the bond between the Ln^{3+} and Pt^{2+} or Pd^{2+}? In having gone through the (extensive) CF analysis of the **LnPt** and **LnPd** series, it is possible to get an idea (read: inkling) of the nature of the bond by comparing the relative coordination strength towards the Ln^{3+}. In so doing, two observations can be made: 1) The B_4^4 parameter was unchanged between **LnPd** and **LnPt**. This came as no surprise, since this parameter is related to the off-axis coordination environment. This is defined entirely by the position of the oxygen sitting at the eight corners of the square anti-prism, and these are completely indifferent to the exchange of Pt^{2+} to Pd^{2+}. This means no change in the off-axis coordination strength and thus no change in B_4^4. 2) The axial CF parameters B_2^0,B_4^0, and B_6^0 in **LnPd** were compressed (see NAB-2 table S3) relative to **LnPt** by ≈ 20%. This as well followed our original assumption that the lower radial extent of the Pd^{2+} ion would make it less perturbing toward the Ln^{3+}, thus decreasing the axial CF. What came as a surprise was the way this decrease manifests itself in each of the axial CF parameters. It is by no means a straight-

---

[5] See Fig. A.1 for an example of INS for comparable Ln compounds, which have been deuterated.

forward reduction, but is instead dependent on both the lanthanide and the parameter (see NAB-2 Fig. S19). Clearly the coordination strength is not defined simply by a point-charge electrostatic interaction, but rather a lanthanide electron-configuration-specific interaction. This suggests (atleast in my opinion) that the complexation of Ln^{3+} and Pt^{2+}/Pd^{2+} is based on a cooperative sharing of electron density, i.e. a bond!

4.3.1 Questions and Concerns on Relaxation

Despite the fact that the nature of the bond was to my mind the most interesting aspect of the comparison of **LnPd** and **LnPt**, it was actually not the reason, why they were studied. As mentioned previously, one of the key design elements of Ln-SIMs is *symmetry*, and an important aspect of that is the axiality of the complex. It follows from the works of Sievers[105] and Rhinehart & Long[96] that it is possible to stabilise states of large $|M_J\rangle$, which is considered a good thing, by either a) having high coordination strength ligands at the axial positions and weak around the equatorial plane, or b) having weak coordination strength ligands at the axial position and strong around the equatorial plane, with the optimal scenario being determined by the choice of lanthanide. Particularly important for the development of Ln-SIMs has been the designs of Dy^{3+} ions in strong axial fields, so we are presented here with a unique opportunity to study the effects of isolated changes in the axial field. As I recall, before we made the exact comparison, we all expected that **DyPt** would perform better as a SMM than **DyPd** because of the stronger axial coordination of Pt^{2+} compared to Pd^{2+}, which is why it was so surprising to observe the opposite! Fig. 4.8 shows the spin-lattice relaxation lifetime T_1 of **DyPd** and **DyPt**. The experimental points are fitted to a sum of a thermally activated Orbach[86] relaxation process and a temperature-independent quantum tunnelling of magnetisation according to the equation:

$$T_1 = \left(k_\tau + k_O e^{\frac{-\Delta}{k_B T}}\right)^{-1} \tag{4.1}$$

The two are indeed very comparable, as would be expected considering their near-identical structures, but they do differ in one important aspect: The tunnelling rate of magnetisation is slower in **DyPd** than in **DyPt** by ≈20%. At least so we think, but we do of course not have data for **DyPd** to as low a temperature as for **DyPt**. Nevertheless, I pose a theory as to why this is the case, and it all has to do with the composition of the ground state. In both **DyPd** and **DyPt**, the ground state is composed primarily of $|\pm 11/2\rangle$, but it is contaminated with $|\pm 3/2\rangle$ due to the B_4^4 parameter. "Turning up" the axial CF parameters from those in **DyPd** to **DyPt** (see NAB-1 Fig. S35-S37) increases the overall spread of the CF states, but inadvertently causes a reduction in the energy difference between the ground state and the fourth excited state, which is comprised primarily of $|\pm 3/2\rangle$. This gives a relative increase in the importance of the B_4^4 parameter, causing the ground state to be admixed to a greater extent with $|\pm 3/2\rangle$. That increase in the impurity of the ground state is giving rise to a greater influence by quantum tunnelling of magnetisation.

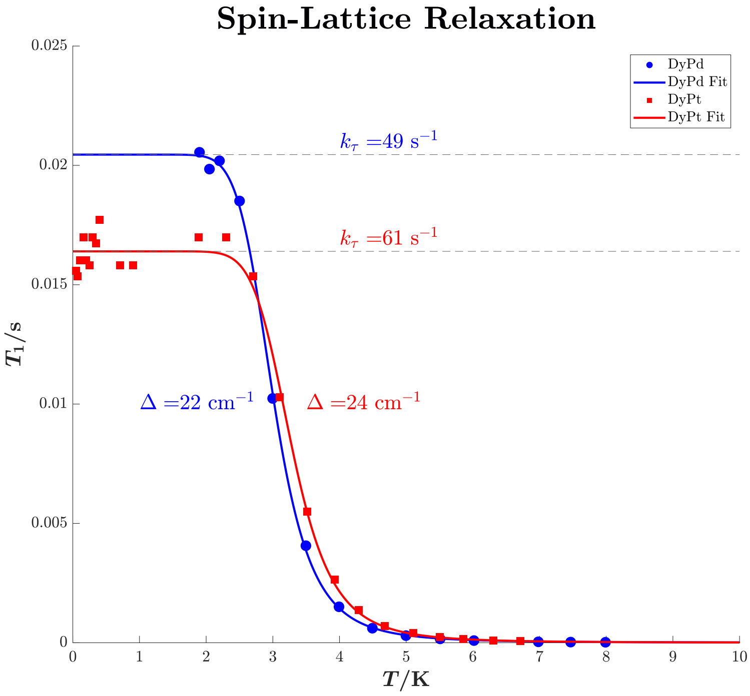

Figure 4.8: Comparison of spin-lattice relaxation lifetimes for **DyPd** and **DyPt**. The reported T_1 is equivalent to the inverse of the first order rate constant discussed in chapter 1. k_τ is the tunnelling rate constant. Data taken from NAB-1 and [107].

The astute reader may have noticed that the values for the SLR processes reported here are slightly different to those reported in NAB-1 and by M. A. Sørensen[107]. For example, literature value of k_τ for **DyPd** is reported as $52\,\mathrm{s}^{-1}$ and $63\,\mathrm{s}^{-1}$ for **DyPt**, whereas here they are 49 and $61\,\mathrm{s}^{-1}$, respectively. This is an example of one of the many ways in which problems with fitting AC magnetometry data can manifest itself. Here, the data sets are fitted using the exact same routine and conditions, which will not originally have been the case, and is the reason why there is a difference. It is a part of a greater set of issues, which AC magnetometry suffers from, particularly over-parametrisation and the lack of means to analyse the uncertainty. Both of these amount to the same thing, which is that it is exceedingly difficult to draw conclusions based on fitted parameters. Luckily there seems to be changes happening to the way magnetometry data is analysed; I will highlight the works D. Reta and N. F. Chilton, who have developed routines for modelling the uncertainties in AC magnetometry.[95] Their results suggest that uncertainties in fitted SLR parameters can very easily be on the same order of magnitude as the parameter. I will add that equally pervasive is the over-parametrisation of DC-magnetometry data. For **DyPd** and **DyPt** it appears that the SLR follows a combination of tunnelling and Orbach relaxation, which together form what is probably the simplest model used throughout literature. Even so, fitting three parameters to each of these data sets is probably over-parametrisation, especially when taken in conjunction with the lack of uncertainties on the data points. All of this is combined is a (rather long-winded) way of saying that any conclusions I draw based on this analysis must be taken with a grain of salt the size of Mount Everest.

Chapter 5

Phonons and the SMM Identity Crisis

5.1 Background

During the investigation of the **LnPd** series of compounds at IN5, a peculiar result was obtained for **HoPd**. It had previously been shown, that the lowest energy states of **HoPd** were $|\pm 4\rangle$. It was also recognized that these states would be split by the off-diagonal CF element B_4^4 into

$$\begin{aligned} |\Psi_1\rangle &= \frac{1}{\sqrt{2}}\left(|{+4}\rangle - |{-4}\rangle\right), E \propto \left(B_4^4\right)^2 \\ |\Psi_0\rangle &= \frac{1}{\sqrt{2}}\left(|{+4}\rangle + |{-4}\rangle\right), E = 0 \end{aligned} \tag{5.1}$$

Since the splitting between these states is directly related to B_4^4, if the energy gap between the split states could be measured, the CF parameter could be identified exactly. As was discussed previously, for the entire series of **LnPd** we found no evidence of the influence of the B_6^4 parameter. Or rather, any influence of it would be indistinguishable from the influence of B_4^4. As such, throughout the works on the **LnPd** or **LnPt** series, the reported values of B_4^4 must be taken as an "effective" parameter, encompassing both contributions. We sought to measure the very lowest energy INS of **HoPd** hoping that we would observe a magnetic transition, thus giving the value of B_4^4. Much to our surprise, we did not observe one - we observed three! In Fig. 5.1 at an energy of approximately 1cm^{-1}, where we were expecting to observe the magnetic transition based on our previous modelling of the B_4^4 parameter, a multiplet of (seemingly) three transitions were observed.

It is impossible for the CF of **HoPd** to be split in such a way, that three transitions so close in energy would be observable by INS. The only possible explanation for the 'extra' transitions was a hyperfine interaction with the Ho nucleus. Holmium is one of the rare examples of elements with only one naturally occurring isotope, ^{165}Ho, which has a nuclear spin of $I = 7/2$. The spin-orbit angular momentum J of Ho^{3+} and its nuclear spin I may interact with each other, following

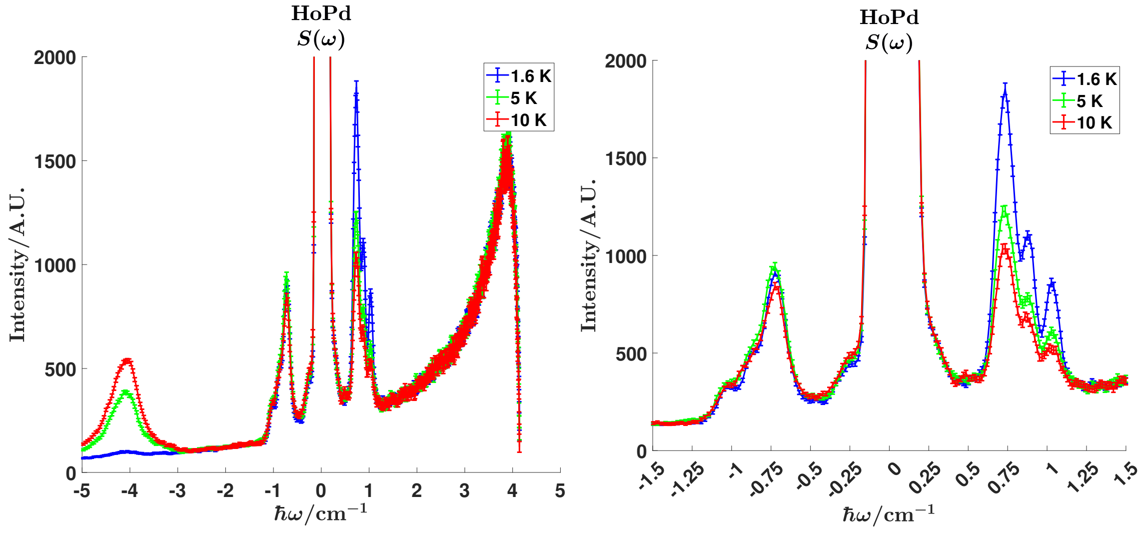

(a) (b)

Figure 5.1: INS spectra of **HoPd** measured at IN5 with λ =10 Å.

$$\hat{H}_{HF} = A\hat{J} \cdot \hat{I} \tag{5.2}$$

where A couples the spin-orbit angular momentum J and the nuclear spin I.

Without even taking into account the hyper fine interaction, it is possible from these spectra to determine the sought-after B_4^4, and in essence we had accomplished what we had hoped to do. However as is so often the case with INS, when you "zoom in" on the dynamics of a sample, new and interesting phenomena appear, and we were now left with the mystery of the hyper fine interaction. The interaction of this nuclear spin with the electronic states of Ho^{3+} splits each state $|\Psi_0\rangle$ and $|\Psi_1\rangle$ into four Kramers states, each being defined by a nuclear component $|M_I\rangle$ =$|\pm1/2\rangle$,$|\pm3/2\rangle$,$|\pm5/2\rangle$, and $|\pm7/2\rangle$. What is observed in this spectrum is in fact not three magnetic transitions, but four. These are illustrated in Fig. 5.2.

Within the fields of molecular magnetism and spintronics, there is significant interest in hyperfine interactions of the paramagnetic ion. It is important here to distinguish between two different cases: 1) The interaction of the electronic states with the nuclear spin of the central ion, 2) The influence of the vast number of nuclear spins present throughout the crystal lattice. The latter is generally referred to as a 'spin bath' model[94], and examples of its importance to the coherence properties of localised spins are plentiful[35, 81]. It is however beyond the context of this discussion, and the focus will therefore be placed on the

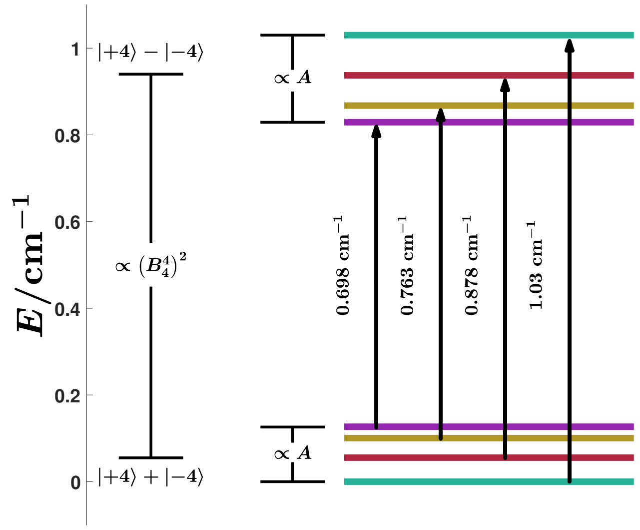

Figure 5.2: Lowest energy levels of **HoPd**. Each Kramers doublet is coloured according to the spin of the nuclear component with $|M_I\rangle = |\pm 7/2\rangle$ (jade), $|\pm 5/2\rangle$ (ruby), $|\pm 3/2\rangle$ (amber), and $|\pm 1/2\rangle$ (amethyst). Adapted from NAB-2.

prior case.

While it is true that for lanthanide paramagnets, the static magnetic properties are defined by the electronic state, the dynamic magnetic properties are highly dependent on a nuclear contribution. This was first proven for Ho^{3+} ions ($^5I_8$, $I = 7/2$) doped in a LiYF_4 Scheelite, where the magnetic hysteresis at milikelvin temperatures showed four ”steps”, consistent with the splitting of the ground state into four nuclear Kramers states.[49] Similarly, the Tb^{3+}-phthalocyanine complex $[\mathrm{TbPc}_2]^-$ ($^7F_6$, $I = 3/2$) has been shown to exhibit tunnelling between nuclear states both in the crystalline phase[66] and in molecules deposited on a surface.[82] It may seem that a hyperfine interaction is a negative in the context of controlling molecular spins, since it can enable processes of magnetic relaxation, but it also gives rise to a new form of qubit topology.[1] In this topology, the quantum information is encoded in the combined states of electronic and nuclear spin. The vanadyl ion of V^{4+} ($S = 1/2$, $I = 7/2$) has been a long-standing candidate as a qubit, because its well-isolated

---

[1] ”Topology” in this context refers to the many different groups of molecular magnetic materials under investigation for use in spintronics. Examples include single lanthanide ions[121] , 3d metal clusters[31], single-chain magnets[21], single-molecule toroics[74], and crystal dopants.[45].

$S = 1/2$ ground state couples to the $I = 7/2$ nuclear spin.[123] It was also shown for a Ho^{3+} polyoxometallate complex[46] **HoW10** that these combined electronic and nuclear states are particularly robust against certain sources of decoherence.[101] This complex will be discussed in greater detail in section 5.2.

All of this interest in hyperfine interactions led to more neutrons. I had the opportunity to use the high-resolution backscattering instrument IN16B BATS, which is phenomenal at observing dynamics in this energy range. Fig. 5.3 illustrates this by comparing the spectra from IN5 and IN16B BATS measured on **HoPd** at T = 1.6 K.

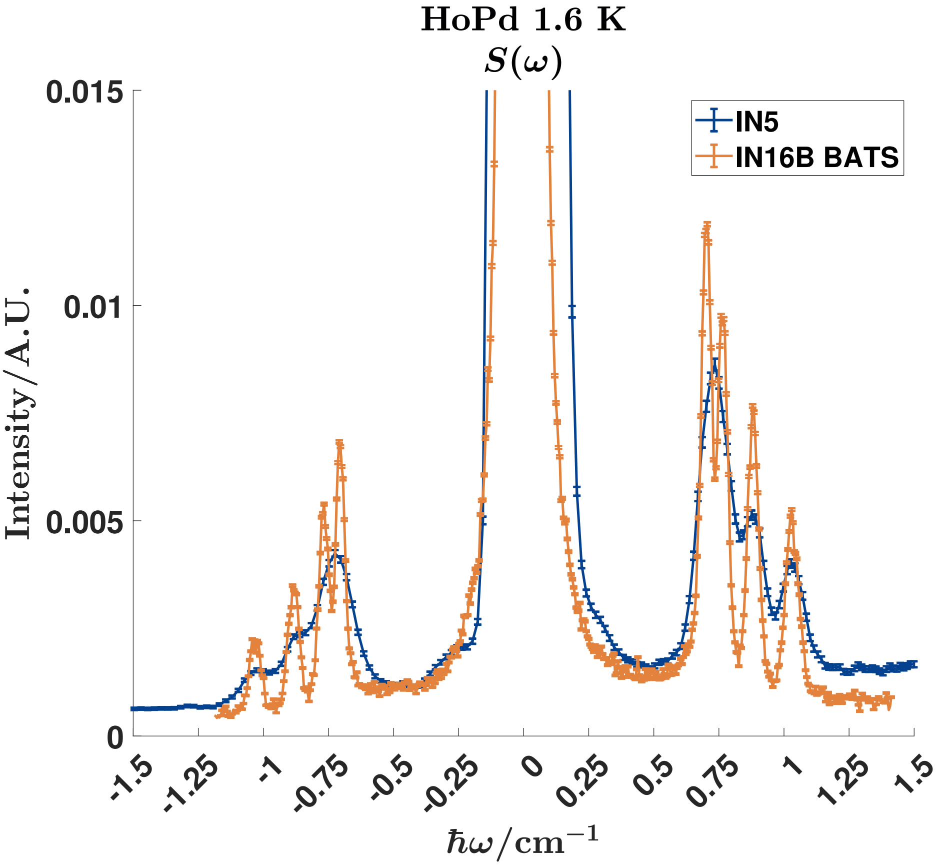

Figure 5.3: INS spectra of **HoPd** comparing the two instruments IN5 and IN16B BATS. Spectra are normalized to the integral of the elastic peak.

It is interesting to compare the spectra observed at IN5 and at IN16B BATS. Since the two spectra were measured using the very same sample in the very same sample holder, any observable difference in the spectra stems from the difference in resolution of the two instruments. In fact, this sample was used as an internal standard at ILL, and the spectra it produced were used to compare the two instruments. The same sample was actually also measured at IN4 (now called PANTHER) and a similar comparison with IN5 could be made. All-in-all, **HoPd** is probably one of the samples that has had most beam time at ILL, and it is definitely among the most well-studied molecular paramagnets. It is certainly the most irradiated. It is clearly seen in Fig. 5.3, that the resolution at IN16B is significantly better than at IN5. The reason for this was discussed in chapter 2, but it is now apparent how important resolution is. At IN16B, four easily distinguishable peaks are visible, whereas at IN5 the two lowest in energy overlap to such an extent that they cannot be separated.

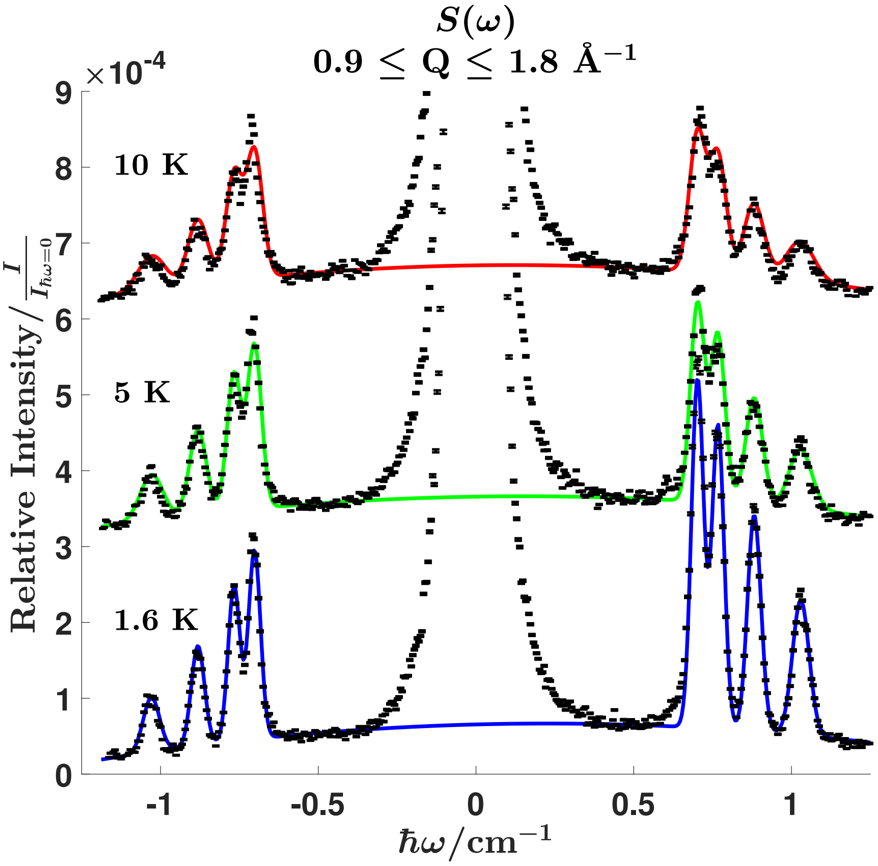

Figure 5.4: INS spectra of **HoPd** at T = 1.6, 5, and 10 K. Data (errorbars) taken at IN16B. Solid lines represent simulated spectra. Reproduced from NAB-2

The results of the experiment are shown in Fig. 5.4. It might seem strange, considering the phenomenal increase in resolution, that this result was rather disappointing. In Fig. 5.2 the lowest energy states of **HoPd** are shown, and the four black arrows correspond to the four observed INS transitions. In fact, a total of 16 INS transitions between the eight

Kramers states are possible. It is amenable to distinguish these transitions into two categories: *ESR-active* transitions and *NMR-active* transitions. The four observed transitions highlighted with black arrows in 5.6 (center panel) are ESR-active, meaning that the transition probability between the two states is derived from a non-zero matrix element in the electronic component of their wave functions. The 12 ”missing” INS transitions are NMR-active, which mean they derive their transition probability from a non-zero matrix element between the nuclear components of their wave functions.

Despite our inability to discern these NMR-active transitions in the spectra, they do still occur. The reason they are not easy to see is twofold: 1) In general, NMR-active transitions, as was discussed in subsection 2.2.2, are two to three orders of magnitude less intense than ESR-active transitions, and 2) the (much more intense) ESR-active transitions here are subject to inhomogeneous broadening. At the time of writing this thesis, I am still not aware of any examples of INS spectra, wherein pure NMR-active and ESR-active transitions are both discernible and distinguishable.[2] This was part of the reason, why we wanted to do this experiment. It turned out, that the issue of intensity was dwarfed by inhomogeneous broadening. This will be the topic of the next section.

As a response to the numerous times I have been asked why the inhomogeneous broadening observed in **HoPd** can not simply be explained with a Debye-Waller factor, it is worth taking a brief aside for this discussion. To initialize that avenue of thought, let us consider the Debye-Waller factor, where it comes from, and how it is used. It finds its home in crystallography, because of its common use when looking at Bragg scattering. It does not matter whether that is based on the scattering of neutrons, x-rays, electrons or anything else. It commonly takes the form expressed in eq. (5.1), where $\vec{u}$ is a vector describing the displacement of the atom and $\langle ... \rangle$ indicates averaging.

$$DWF = e^{\left(-\left\langle \left(\vec{Q}\cdot\vec{u}\right)^2 \right\rangle\right)} \tag{5.3}$$

Its effect on the observed scattering is equivalent to the effect of atomic form factors (see section 2.2.1), ie. to decrease the intensity with increasing Q. It is not capable of causing the broadening effect, which does not decrease the total intensity, only relocate it.

---

[2] There are of course plenty of publications of pure NMR-active transitions studied with INS. One recent example, also from IN16B, show how nuclear spins of Nd^{3+} respond to the magnetic ordering in $NdMnO_3$.[29]

5.2 Inhomogeneous Broadening

Inhomogeneous broadening, in essence, is the observation of a peak, where the shape is broader than what the instrumental resolution allows. In trying to understand why **HoPd** suffers from inhomogeneous broadening, we inadvertently came to ask a very simple question, one that is nevertheless rarely considered: What is the uncertainty of an energy level?

It might seem a strange question to ask, because how can an uncertainty in the energy be an intrinsic property of the energy level and not an issue of the measurement? Furthermore, since the absolute energy of the level can never be measured, how can the uncertainty be given as an absolute? Even furthermore, if the absolute energy is not given, but rather the relative energy of one level to another, how can the ground state, which has zero energy by definition, have a non-zero uncertainty?

The tentative answer to these seemingly paradoxical questions is actually rather simple: The study of single-molecule magnets does not involve the study of *singular* molecules -It involves the study of ensembles of molecules. The uncertainty in the energy level is not an intrinsic property of a single molecule, but rather a property of the sample. The uncertainty stems from the fact that no two molecules in the sample are exactly alike. The reason why no two molecules are exactly the same is twofold: 1) Static distortions of the crystal lattice mean that each molecule are not necessarily found in exactly the same environment. These static effects are caused by crystal mosaicity, surfaces and cracks, and lattice defects. 2) Dynamic distortions are caused by the fluctuating magnetic and electrostatic fields the molecule is subjected to. The fluctuating magnetic field may result from the random and ever-changing spins surrounding the molecule (the spin-bath), and the electrostatic field may change due to the motion of the surrounding atoms. In a crystal, atoms are moving constantly as a result of both localised vibrations within the molecule and extended (lattice) vibrations. The latter is generally referred to as 'phonons', but within the context of this discussion, where it is impossible to experimentally distinguish the effect of local and extended vibrations, 'phonon' shall cover any movement of atoms.

The questions to ask instead are: How might we measure the differences between molecules in a given sample, and how are those differences attributed to the chemistry of the sample? There is unfortunately no single way to answer those questions for every case, because how the difference between molecules is measured, and the range to which they are different, is highly dependent on *what* is different. In the case of **HoPd**, what is different is the electrostatic forces acting on the Ho^{3+} ion, which manifests itself as inhomogeneous broadening of

INS. The same type and level of discussion could equally well be applied to any other physical property which may be different for all of the molecules in the sample, like rotational tunnelling of the methyl groups or the ^{33}S NMR shift. No matter what is being studied, the point is the same: Even in a perfect crystal, there may be differences between ”crystallographically identical” molecules, which could have profound influences on the physical properties of the crystal. Again in the case of **HoPd**, we happened to be able to measure and model a particular effect giving rise to the differences between molecules. This effect has important implications within the fields of molecular magnetism and spintronics, and **HoPd** thus became an interesting case study despite the fact that it is a non-functioning SMM and would be a terrible candidate for a spintronic device.

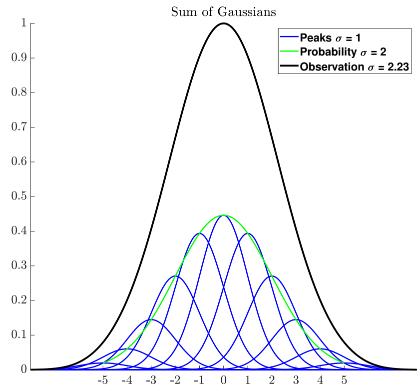

Figure 5.5: Illustration of how a sum of Gaussians may approximate a single, larger Gaussian.

The following is a deconvolution of the inhomogeneous broadening observed for **HoPd**. It may not be easy to see, but every INS transition in Fig. 5.4 has a unique height, width and temperature-dependence, and importantly, they are all broader than the elastic peak in the middle. Since the resolution is given (primarily) by the width of the elastic peak, the INS peaks being broader than that indicate that they are not the result of a single and unique process of physical transformation of the sample. Instead the peaks result from the compilation of multiple processes, each of which are closely related but nevertheless distinct.

The inelastic scattering of a neutron by a localised magnetic transition, like a spin transitions in a paramagnet, happens independently of all other neutrons and spins. This implies that the observed INS from a crystalline paramagnet can be understood as the sum of neutrons scattered by many molecules, all of which undergo the same physical transformation. If however the molecules in the sample are not identical, the physical transformation they undergo may be different and therefore the neutrons may be scattered differently. For **HoPd**, the difference between the molecules is so small, that the scattered neutrons do not split into multiple, distinguishable peaks, but instead overlap to such a degree that they it appears as a single, broad peak. It is fortunately still possible to gain insights simply by doing the appropriate error propagation.

Before going into details with the origin and deconvolution of the inhomogeneous broad-

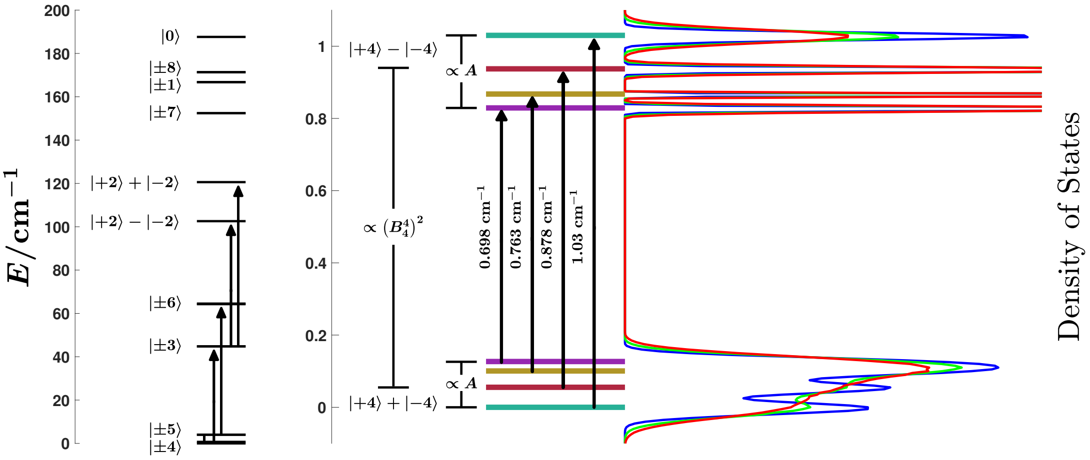

Figure 5.6: Energy levels of **HoPd** with black arrows indicating observed INS transitions. Left panel: The full CF-splitting of energy levels, each one indicated by its primary $|J\ M_J\rangle$ component(s). Center panel: Splitting of the lowest energy levels. Each Kramers doublet is coloured according to the spin of the nuclear component with $|M_I\rangle = |\pm7/2\rangle$ (jade), $|\pm5/2\rangle$ (ruby), $|\pm3/2\rangle$ (amber), and $|\pm1/2\rangle$ (amethyst). Right panel: Temperature dependent uncertainty of the corresponding energy level. Reproduced from NAB-2.

ening, I will skip to the conclusion of the entire investigation and highlight the key findings that came from it. I do this primarily to assure the reader that -contrary to popular belief- interesting things can indeed come from doing error propagation, but also to bring to their attention Fig. 5.6, which I consider to be my magnum opus of scientific communication. It illustrates, I believe very succinctly and successfully, both *how* we were able to observe the inhomogeneous broadening and *why* it is so important. On the left is an energy level diagram of the full CF-split ground term of Ho^{3+} in **HoPd**. The energy levels are all identified by the primary components of $|J\ M_J\rangle$ that make up that state, and the black arrows indicate the observed INS transitions. This ties NAB-2 together with its predecessors, naturally NAB-1 but also the works of M. A. Sørensen, M. Perfetti, and U. B. Hansen, who laid the groundwork for this study.[108, 107, 92] The center panel is equivalent to Fig. 5.2 and illustrates the low-energy states, and how they are defined by the two parameters B_4^4 and A. The right panel is where things get interesting. It shows how each state is defined by a distribution in energy, which results from the fact that no two molecules in the sample are exactly alike. The surprising result is how each state is unique in its response to this inequivalence.

Going back to the INS experiment of **HoPd**, we observed four broad INS transitions. The energy of that transition (and its position in the spectrum) is defined by the splitting between two energy levels. The splitting results from two parameters: The CF parameter B_4^4 and the hyperfine interaction A. It is technically true that all the CF parameters (and all other spin-Hamiltonian parameters) have influence on the splitting between these states, however the effect of those is so small that they can be ignored. If that is the case then any inhomogeneous broadening must result from inconsistencies in these two parameters between different molecules. It is possible to model this inconsistency, and thus the inhomogeneous broadening, by describing B_4^4 and A by Gaussian distributions:

$$\begin{aligned} G_{B_4^4} &= \frac{1}{\sigma_{B_4^4}\sqrt{2\pi}} exp\left(\frac{-\left(B_4^4 - \mu_{B_4^4}\right)^2}{2\sigma_{B_4^4}^2}\right) \\ G_A &= \frac{1}{\sigma_A\sqrt{2\pi}} exp\left(\frac{-\left(A - \mu_A\right)^2}{2\sigma_A^2}\right) \end{aligned} \tag{5.4}$$

This implies that these two parameters are not described by exact values, but rather a probability ($G_{B_4^4}$ and G_A) of finding a molecule with a particular parameter value. The most probable value is given by $\mu_{B_4^4}$ and μ_A, and the width of the parameter distribution is given by $\sigma_{B_4^4}$ and σ_A. Modelling the inhomogeneous broadening is then a problem of finding these parameter distributions.

The cause for the parameter distributions is a matter of some debate, as there can be many influences that give rise to such a distribution. In my article *Unequal sensitivities of energy levels in a high-symmetry Ho^{3+} complex towards lattice distortions* (NAB-2), on which this chapter is based, we argue that the leading cause of parameter broadening observed in **HoPd** is phonons. This argument is based on the observation that the INS peak width increases with temperature. This observation indicates that whatever is causing the parameter distributions is limited by the thermal energy of the sample, such as would be the case for phonons. It also makes sense that phonons are the leading cause, since they cause vibrations in the ligands surrounding the Ho^{3+} ion. The vibration produces a varying electrostatic field, which can manifest itself as a distribution in the CF parameters. It is probable that other sources of lattice distortions play a role; crystal mosaicity, cracks, surface effects etc. are all capable of causing differences in the CF. It might therefore be prudent to distinguish static and dynamic distortions, distinguishing them by whether they appear to have a temperature dependence. The spectra of **HoPd** were taken at the lowest temperature of 1.6 K. We can consider 1.6 K a low temperature, but it is still infinitely higher than 0 K. It is unfortunately also impossible to measure a spectrum at 0 K, so we can never truly disregard either static or dynamic effects.

It is not practical to calculate $\sigma_{B_4^4}$ and σ_A by analytical means (see section 2.3), so they are instead found by an iterative fitting routine.

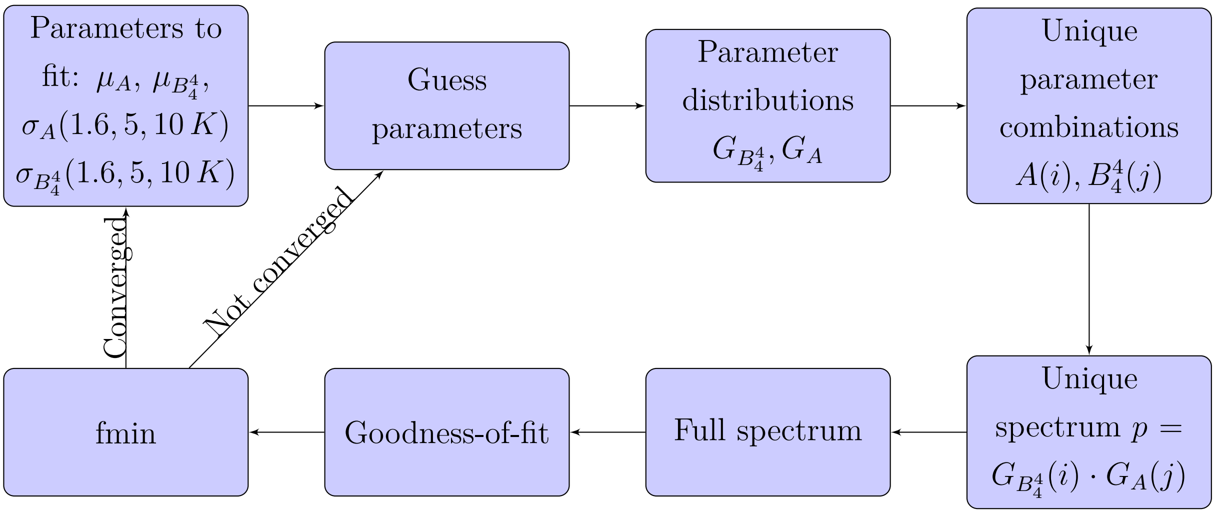

Figure 5.7: Flowchart for the fitting routine for parameter distributions.

The fitting routine is based on my INS simulation program Banana (see section 2.3) and the fminsearch routine implemented in Matlab. The flowchart in Fig. 5.2 illustrates the process, but in essence there are only two steps to the routine.

- The first step involves simulating the INS spectrum for the parameters to be tested. This requires approximating $G_{B_4^4}$ and G_A by n points each. For each combination of $A(i)$, $B_4^4(j)$, a spectrum is simulated having a weight of $p = G_{B_4^4}(i) \cdot G_A(j)$. The n^2 spectra are summed and scaled ex post facto to the experimental data.
- The goodness-of-fit is evaluated as $gof = \sum (I_{obs} - I_{sim})^2$ and passed to the fitting routine fmin. Since the above step is a black box, fmin tests multiple small changes (function calls) to the fitting parameters before proceeding to next iteration. Because of the computational heft of the first step, and the simplicity of fmin, convergence is slow.

Simulating INS of **HoPd** is done in much the same way as the previously discussed complexes. The only amendment involves the transitions related to the nuclear spin:

$$\begin{aligned} \frac{\delta^2\sigma}{\delta\Omega\delta\omega_f} &= \frac{k_f}{k_i}\frac{1}{Q^2}\sum_{m'_F}\sum_{m_F} P_{m_F}\cdot\Bigg|\Bigg\langle \begin{matrix} J\ M_J \\ I\ M_I\end{matrix}\ F\ M'_F\Bigg| -\frac{1}{2}\gamma r_0 g_J F_{\mathrm{Ho}^{3+}}(Q)\left[\hat{J}\times\vec{Q}\right]\times\vec{Q} \\ &+ \left(\frac{1}{2I+1}\left((I+1)\,b^+ + Ib^-\right) + \frac{1}{2I+1}\left(b^+ - b^-\right)\hat{I}\right)\Bigg|\begin{matrix}J\ M_J\\ I\ M_I\end{matrix}\ F\ M_F\Bigg\rangle\Bigg|^2 \end{aligned} \tag{5.5}$$

Here $\vec{F} = \vec{J} + \vec{I}$ is the combined basis of spin-orbital angular momentum $\vec{J}$ and nuclear spin $\vec{I}$. INS transitions are now defined by two terms. The first defines the interaction of the neutron with the magnetic moment from the electrons, and its expression is equivalent to the spin-only scattering discussed in subsection 2.2.1. The second defines the interaction of the neutron with the nucleus, and importantly includes the nuclear spin operator $\hat{I}$, making the expression capable of enacting transitions in the $|I\ M_I\rangle$ basis. The constants b^+ and b^- are known as nuclear scattering lengths and are observable quantities, which have been measured and tabulated. For Ho they happen to be $b^+ = 6.9\,\mathrm{fm}$ $b^- = 10.3\,\mathrm{fm}$.

Following the fitting procedure, the parameters were found to be: $\mu_A = 829.7$ MHz and $\mu_{B_4^4} = 3.623{\cdot}10^{-3}$ cm^{-1} and the temperature dependent $\sigma_A(1.6, 5, 10\,K)$ and $\sigma_{B_4^4}(1.6, 5, 10\,K)$ are given in table 5.1.

Temperature (K)	σ_A (MHz)	σ_A/μ_A (%)	$\sigma_{B_4^4}$ (cm^{-1})	$\sigma_{B_4^4}/\mu_{B_4^4}$ (%)
1.6	31.49	3.80	3.762e-5	1.04
5	47.99	5.78	4.859e-5	1.34
10	59.34	7.15	5.949e-5	1.64

Table 5.1: Fitted parameters for the distribution of the Crystal Field. Adapted from NAB-2.

To the best of my knowledge, this is the first time the effects of lattice distortions on the CF have been found from inhomogeneous broadening in INS. Previous studies of the effect have been based on inhomogeneous broadening observed in ESR. INS and ESR are very closely related, and often experiments compliment each other. For example, IN16B is switchable between two modes, one with a maximum energy transfer of $0.5\,\mathrm{cm}^{-1}$ and one with $1.3\,\mathrm{cm}^{-1}$, which closely resembles X-band ($10\,\mathrm{GHz} = 0.33\,\mathrm{cm}^{-1}$) and Q-band (35 GHz $= 1.2\,\mathrm{cm}^{-1}$). When the scientific interest is on the energy of spin transitions, as would be the case when studying paramagnets, the information that can be gained from ESR and INS is essentially identical.

It also comes as no surprise that ESR has been used to study inhomogeneous broadening. ESR is easier, faster, and cheaper than INS. It is also much more available, since dedicated

ESR facilities are only required when very high magnetic fields are necessary. In the case of inhomogeneous broadening, however, ESR comes with some significant drawbacks compared to INS. ESR is a fantastic tool to study inhomogeneous broadening, but it is also very susceptible to certain sources of inhomogeneous broadening, which is not the case for INS.

INS	ESR
Spin-flip/Non-spin-flip	Parallel mode/Perpendicular mode
Field optional	Field necessary
Gram-scale	Milligram-scale
Single crystal/powder	Single crystal/powder/solution/glass
Continuous measurements only	Pulsed measurements available

Table 5.2: Simple comparison of INS and ESR.

Comparing INS and ESR, it is clear that ESR in many ways is more complicated. It involves changing magnetic fields, standing waves, and usually requires alignment of a single crystal. These aspects all have the possibility of introducing inhomogeneous broadening: Inhomogeneity in the magnetic field or standing wave means that there can be difference in the resonance condition. Placement and alignment of the crystal can shift the resonance condition and give rise to more peaks, and crystal mosaicity (or other faults) can cause broadening. These difficulties are neglected in an INS experiment, simply because it normally takes place in zero field with unpolarised neutrons and with a polycrystalline sample.

More important than these technical difficulties is the influence of lifetimes. In spectroscopy, for the peak width to be narrow the lifetime of the excited state has to be longer than the characteristic time scale of the excitation. If the lifetime is short, the uncertainty in the life time is concomitantly small, and hence the uncertainty in the energy is large, giving rise to broad peaks.

The characteristic time scale of the ESR experiment is $10^{-9}\,s$, since the frequency is in GHz. The characteristic time scale for the interaction of neutron with a localised spin is quite a lot shorter, since the time the neutron spends in the vicinity of the spin is low:

$$t = \frac{d}{v} \approx \frac{10^{-9}\,m}{10^{3}\,m/s} = 10^{-12}\,s \tag{5.6}$$

This back-of-the-envelope calculation assumes that the range of interaction is similar to the distance between neighbouring spins (approximately $10\,\text{Å}$) and a neutron velocity of $1\,km/s$, which corresponds to a wavelength of $4\,\text{Å}$. The characteristic time scale of the INS experiment is thus three orders of magnitude shorter than in ESR. That means that the peak width coming from short life times is minimised.

The results of this study in and of them selves are not incredibly interesting. The distribution in CF parameters is only relevant, if it can be correlated to something, which is difficult to do, when there is only "one" data point. That is why in my paper, there is a large section dedicated to comparing **HoPd** with its (only?) close relative, $Na_9[Ho(W_5O_{18})_2]\cdot nH_2O$. This complex (abbr. **HoW**$_{10}$) forms one of a series of isostructural compounds of Ln = Tb, Dy, Ho, Er, Tm, and Yb.[5, 4] and was studied by Stephen Hill & Eugenio Coronado[46, 101] using ESR.

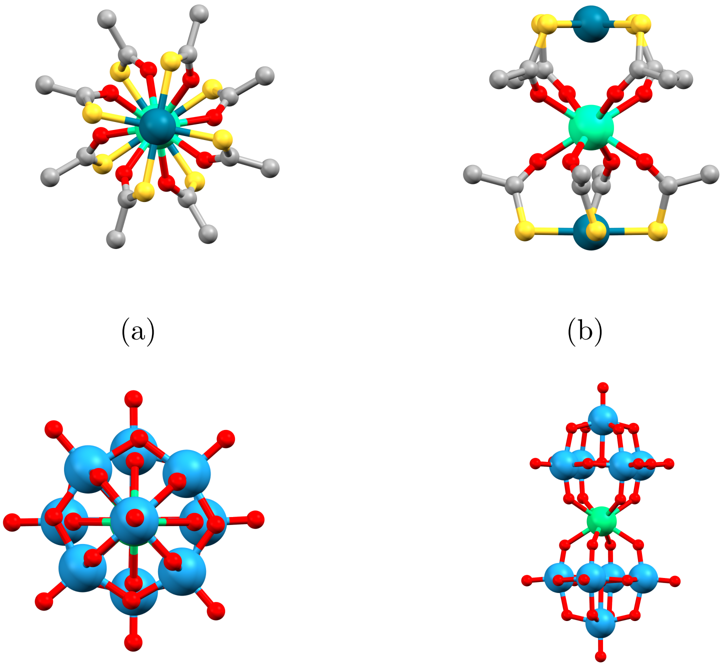

(a) (b)

(c) (d)

Figure 5.8: Structural comparison of **HoPd** (top)[108] and **HoW**$_{10}$ (bottom).[6] Counter ions and hydrogen omitted for clarity.

The structural similarities are striking. Both **HoPd** and **HoW**$_{10}$ are encapsulated by a (reasonably) square anti-prism and capped axially by either Pd^{2+} ions (**HoPd**) or O^{2-} ions (**HoW**$_{10}$). This also manifests in strikingly similar CFs - as would be expected. **HoW**$_{10}$ also has a ground state $|\pm4\rangle$ split by a B_4^4. The only notable difference is the fact that upper and lower planes of O atoms in **HoW**$_{10}$ are no co-planar, as they are in **HoPd**. That of course means that the local structure of $\mathbf{HoW}_{10}$ has by definition no symmetry, and as well it crystallises in $P\overline{1}$, but it can reasonably be approximated by its ideal D_4d symmetry. In fact, the low symmetry of $\mathbf{HoW}_{10}$ was necessary for the ESR experiments to work. They were performed with X-band perpendicular excitation, which is incapable of causing a transition between *pure* states of $|\pm 4\rangle$. All of the intensity they observe results from the admixture of other values of $|M_J\rangle$ into the ground state, which is caused by the low symmetry CF.

The point of comparing **HoPd** and $\mathbf{HoW}_{10}$ stems from the fact, that Hill & Coronado also determined the distribution in B_4^4. Because the two compounds are near-identical, any difference in $\sigma_{b_4^4}$ between them must stem from a difference in the susceptibility of the CF towards distortions. If a distribution in a CF parameter is caused by phonons distorting the CF, it is expected that the less prone the ligands are to vibrations, the less the distribution in the parameter is. So how can we know, how much the ligands are vibrating as a result of phonons? Technically, we can not know, because calculating (or even understanding) phonons in systems as complex as these is effectively impossible. We can only really make approximations. Consider for example the diatomic harmonic oscillator; The range of movement of one particle is inversely proportional to its mass, meaning that the heavier the atom, the less it moves. The ligands in $\mathbf{HoW}_{10}$ are significantly heavier than the ligands in **HoPd** and should - based on this simple reasoning - vibrate comparatively less. That is why $\sigma_{B_4^4}$ in $\mathbf{HoW}_{10}$ should be smaller than in **HoPd**, which is (fortunately) exactly what is observed. At 5 K, $\sigma_{B_4^4}/\mu_{B_4^4}$ (the ratio of the distribution to its mean value) is 1.34 % for **HoPd** and 0.67 % for $\mathbf{HoW}_{10}$.

	HoPd	HoW
θ	59.1°	57.4 – 59.3°
ϕ	44.3°	42.7 – 47.1°
γ	0°	1.11°

Table 5.3: Summary of important structural parameters of **HoPd** and $\mathbf{HoW}_{10}$. θ is the angle between the molecular z-axis and the O atom. The upper and lower planes of O atoms are defined by an angle of rotation ϕ and an angle of co-planarity γ.

Unfortunately, 5 K is the only temperature for which there is enough data to make the comparison. The true test for the hypothesis that heavier ligands mean smaller distribution in CF parameters would require much more complex testing; it would necessarily involve the temperature-dependence over a much larger range, and preferably look at the distribution in *all* CF parameters. The difficulty there lies in the fact, that the axial CF parameters for lanthanides cause splittings in the order of $10^2 - 10^3\,\mathrm{cm}^{-1}$. If the test would be based on inhomogeneous broadening in transitions between such highly split states, the resolution would have to be exorbitant - way out of the range of INS. In many ways it would appropriate to reconsider which element should be chosen for the experiment. It would be best to have an element which is both monoisotopic, to make it possible to model the HF interaction, and with an electron configuration that allows for reasonably many electronic states at energies that can be measured precisely. These requirements reduce the list of possibilities to V, Mn, and Co. The only one of these elements, for which there is precedent of the type of experiments and calculations necessary to perform the analysis is vanadium, as there is already a large body of work devoted to the vanadyl ion VO^{2+}.

The energy levels can also be attributed an uncertainty, if the covariance of σ_A and $\sigma_{B_4^4}$ is assumed to be zero:

$$\sigma_E = \sqrt{\left|\frac{\delta E}{\delta A}\right|^2 \sigma_A^2 + \left|\frac{\delta E}{\delta B_4^4}\right|^2 \sigma_{B_4^4}^2} \tag{5.7}$$

This provides an uncertainty (see supporting information B for tabulated values) of each level, which is expressed in Fig. 5.2. It gives the same information as Fig. 5.6 right panel, only for the full CF split ground term. It is clear that every state is perturbed differently by the distributions in a parameter. For example, the two states at ≈100 and 120 cm^{-1} is the linear and anti-linear combination of $|\pm 2\rangle$. They are very susceptible to changes in the B_4^4 parameter and are therefore the most broadened.

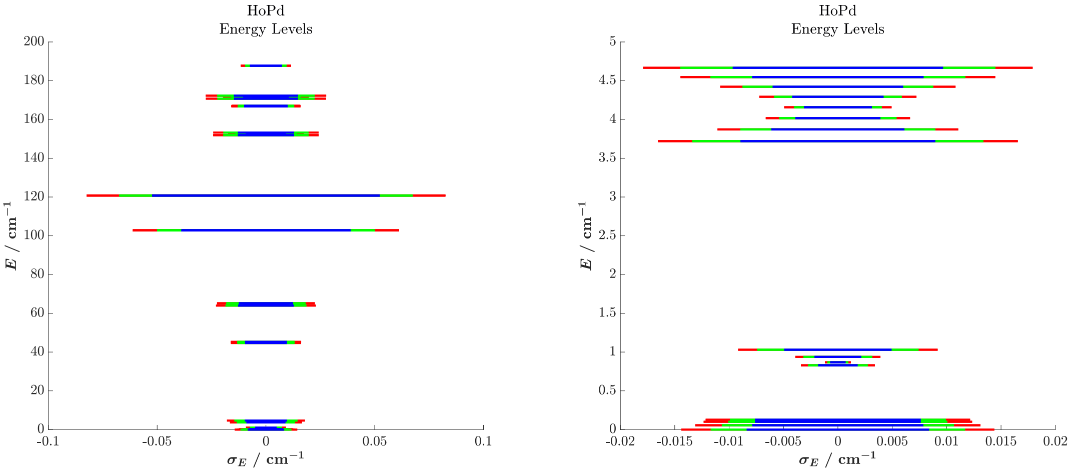

(a) (b)

Figure 5.9: (a) Energy Level diagram for **HoPd** with the width of the line representing the uncertainty in the energy. (b) zoom of (a) showing the lowest energy states.

The ground Kramers state has an uncertainty of $\sigma_E = 0.017\,\mathrm{cm}^{-1}$ at 1.6 K. In the context of lanthanides, where energies of the CF are in the order of $10^2 - 10^3\,\mathrm{cm}^{-1}$ and electronic terms $10^3 - 10^5\,\mathrm{cm}^{-1}$, a number in the order of $10^{-2}\,\mathrm{cm}^{-1}$ might seem insignificant. I will however pose that the number is very significant, given the right context. It so happens that $0.017\,\mathrm{cm}^{-1}$ is approximately equal to 500 MHz, which is a number most will recognize as a common NMR frequency. Seen in that context, 500 MHz is by no means a small number - at 500 MHz ± 5 kHz (± 10 ppm) enormously precise measurements of energies between states can be made, which can then be correlated to the structure of the molecule. To put it bluntly, the uncertainty of a single energy level in **HoPd** is greater than the entire energy range of the NMR spectrometer.[3]

It is interesting to consider the implications of such an uncertainty in the energy levels. Most of the potential applications of SMMs revolve around reading and writing information to the molecule through changing its state. That process inevitably involves a transferral of energy from one system to another, and as such there will be an uncertainty in that energy resulting from the uncertainty in the energy levels. That uncertainty can be calculated for each possible transition in the SMM. It will be dependent on the CF and the phonon modes that cause fluctuations in the CF. It is therefore possible to consider the robustness (i.e. unchangingness) of a transition towards distortions of the CF. A similar idea is presented by Hill & Coronado for **HoW$_{10}$** in the concept of 'atomic clock transitions'.[119, 101, 48] These are just transitions in the SMM that are robust towards stray magnetic fields, but the same could be applied to any part of the spin-Hamiltonian. It could even be possible to define a figure of merit for the robustness of a transition $f \leftarrow i$:

$$FOM(f \leftarrow i) = \sum_p \frac{\delta \Delta E_{f \leftarrow i}}{\delta \hat{H}_p} \tag{5.8}$$

This simply states that the robustness is given as a change in the difference in energy between states $|i\rangle$ and $|f\rangle$ as a function of a change in a spin-Hamiltonian parameter $\hat{H}_p$. This could be applied for any spin-Hamiltonian parameter, and should arguably be applied for all! This also makes it clear to see the connection with spin-phonon coupling, as the fundamental expression[76] governing that is simply:

$$\hat{H}_{sph} = \sum_{\alpha\vec{q}} \left(\frac{\delta \hat{H}}{\delta Q_{\alpha\vec{q}}} \right) \hat{Q}_{\alpha\vec{q}} \tag{5.9}$$

---

[3] 500 MHz is the Larmor frequency of ^{1}H at 11.7 T.

This simply states that the spin-phonon coupling is the sum of changes to the spin-Hamiltonian as a function of the phonon modes $Q_{\alpha\vec{q}}$ times the distortion caused by that mode,$\hat{Q}_{\alpha\vec{q}}$. There is no real way of measuring the spin-phonon coupling for each mode, and they are usually calculated by means of ab initio (this will be discussed in chapter 6), but it is possible to give *a measure* of the spin-phonon coupling. The distribution parameters σ_A and $\sigma_{B_4^4}$ are just that, as they are a weighted average of the spin-phonon couplings. As such the distribution parameters can act as a benchmark for the calculation of spin-phonon couplings.

Chapter 6

Conclusions and Perspectives

This chapter is dedicated to my perspectives on the field of molecular magnetism; where it is going, what challenges need to be overcome, and how this thesis fits into that development. To start off the discussion, I will summarise what I consider to be the most important aspects of the work, I have done the last four years.

6.1 What's in a number?

It has become a firm-held belief -and a motto- of mine that numbers are meaningless and results are irrelevant. The only thing that matters is methodology and reasoning: How did a result come about and why was it sought out. Everything I have worked with in the last years have been to advance the understanding of molecular magnets. This is the case despite the fact that every system I have worked with have been entirely non-functioning as ”molecular magnets”. They have all been model systems with no inherent value other than what they teach us about *how* to understand ”real” SMMs. As such there is no value in the results, only in the methodologies and ideas that have been developed. As an example of this, consider the work presented in chapter 3. There is no value in knowing that the exchange interaction between Ni^{2+} ions in $\mathbf{\{NiPt\}_2}$ is $24.5\,\mathrm{cm}^{-1}$, as it does not aid our understanding of magnetic exchange beyond what is already known. The value is instead found in the development of methods for the measurement and modelling of magnetic exchange. The use of analysing interference effects in the momentum-transfer-dependence of magnetic transitions, and the aid of simple computer simulations towards that goal, might be useful for future studies, where the exact nature of an exchange need to be known. The same goes for the works on the **LnPd** series: The value is not found in the slight difference in tunnelling rates of magnetisation in **DyPd** and **DyPt**, nor in the distribution in spin-Hamiltonian parameters for **HoPd**. The value is found in the development of methods for the exact determination of CFs through the combination (and detailed analysis) of multiple experimental techniques.

6.2 Wave #3

As promised in chapter 1, I will now present my perspectives on wave #3, which I consider to be on the rise. I will argue that over the last decade or so, it has become apparent that molecular magnetism is far more complex than what any one person can comprehend. I consider the rules and criteria that have been declared for the coherent design of SMMs and the like to be tantamount to hubris. They are certainly not capable of capturing the unfathomable complexity of the problem. I also do not believe that it is possible to exchange them for better rules, because any proposition would stem from the same mind, limited fundamentally by its inability to comprehend the quantum world. This is not a swan song, because I do not believe the story ends here. I do however believe that it is changing, and that it needs to do so lest it stagnate.

My belief is based on two things: My perception of today's Zeitgeist and recent works by selected researchers, who I consider to be the most brilliant in field. I reckon it is probably impossible to know what today's Zeitgeist is, so my analysis of it must be read with scepticism or even downright repudiation. However I do believe that there is evidence to suggest that changes are happening in the field of molecular magnetism as a result of a stagnation in the development of SMMs. As discussed in chapter 1, what defines Wave #2 has been the development of theories for the coherent design and optimisation of SMMs: CF engineering for the promotion of easy-axis magnetisation[105, 96] and quenching of the Orbach[86] relaxation pathway[17, 37]; Design principles for the reduction of tunnelling from the interaction with electronic[99] or nuclear spins[123, 16]; CF optimisation for robustness towards stray magnetic fields[101]; Structural requirements[109, 68] for the physical implementation[38] of molecules in spintronic devices[73]; And much more. The field has undoubtedly seen fantastic technological advances founded on these theories: Magnetic hysteresis at liquid Nitrogen temperatures[61], reading and writing information to a single atom[83], development of molecular logic gates[41], and much more. It however seems now that we have run head-first into the wall of spin-lattice relaxation.[88] It was believed that CF engineering would raise the barrier for Orbach relaxation and therefore increase the temperature at which SMMs would "work", but cases are now being explored with SMMs having Orbach barriers greater than 1100 K yet do not show any signs of magnetic memory even at 2 K.[47] It appears that the culprit is Raman relaxation[102], which unlike Orbach relaxation does not lend itself easily to optimisation through chemical design.[27] The Raman process has been known for many years, and it is commonly implemented in the analysis of SMMs by fitting magnetic relaxation. A common poor correlation between observation and theory has been a long-standing debate,[56] and a recent model suggest that what we have hitherto believed to be the Raman process has in fact been a sum of many, unknown processes.[55] Understanding the Raman process has proven itself to be a Herculean task, because it is founded on the (incredibly complex) topic of spin-phonon coupling.[76] This form of intra-molecular *communication*[78] result from the interaction of the electronic states of the SMM with the local[40], anharmonic[79], and harmonic phonons.[30] The complexity of that interaction cannot be overstated, and that is why every modern attempt at doing so is based on the most advanced levels of computation. Recent advances show that the combination of high-level ab initio calculations and extended molecular-dynamics (MD) simulations delivers models of magnetic relaxation in molecular systems in fantastic agreement with observations.[76, 24] This type of investigation has so far only been possible for simple molecular systems, and even in these cases the combination of ab initio and MD produces models of such great complexity that it becomes necessary to implement machine learning algorithms to understand them![77]

This may seem to be just another chapter in the long-winded (and in my opinion stupid) argument that computational chemists are putting ”real” chemists out of a job, but I do not think that is the case. I think computational chemistry is changing the way, we have to think about chemistry and how to approach it. In particular when it comes to molecular magnetism and solid state physics, the computational approach is adding something truly unique: It is not about simply calculating a number, as has been the case for much of the ab inito of yesterday, but is instead seeking out regions of physics that cannot be explored by any known experimental technique. The computational approach is changing the *process* by which information and knowledge may be acquired, and that is why it deserves to be coined by its own wave, and why I think the future will be found in silico.

6.3 Final thoughts

Where does that leave us? If the future will be found in a computer chip, will all of the work I, my colleagues, or indeed anyone in the field have done be for nothing? I hope not, and I have reason(s) to believe that will not be the case. The first is simply that computational chemistry is still very much in its infancy, and the only way of teaching it how to walk is by experimentalists holding its hand. As it matures, though, we need to seek to bridge the gap between computational and experimental chemistry, and that will require an enormous effort on behalf of all those involved. I especially think we need to take a very critical look at the way in which molecular magnets are analysed today, and try to develop new methods and theories for their analysis. I dare not dream that the methods and ideas, I have worked on during my thesis, will be a part of that development, but if it were the case that my efforts have been a contribution, my only hope is that they will be so, because they inspired someone to change the process by which they acquire knowledge.

Change the process
Change the outcome

Mick Gordon[53]

Bibliography

[1] *A Bit of History*. URL: `https://www.ill.eu/about-the-ill/documentation/a-bit-of-history` (visited on 09/04/2022).

[2] *A Dictionary of Physics*. 6th ed. Oxford University Press, 2009. URL: `http://www.oxfordreference.com/view/10.1093/acref/9780199233991.001.0001/acref-9780199233991`.

[3] A. Abragam and B. Bleaney. *Electron Paramagnetic Resonance of Transition Ions*. General Publishings Company, Ltd., 1986.

[4] Murad A Aldamen et al. "Mononuclear Lanthanide Single Molecule Magnets Based on the Polyoxometalates [Ln(W5O18)2]9- and [Ln(beta2-SiW11O39)2]13- (LnIII = Tb, Dy, Ho, Er, Tm, and Yb)". In: *Inorganic Chemistry* 48.8 (2009), pp. 3467–3479.

[5] Murad A. ALDamen et al. "Mononuclear Lanthanide Single-Molecule Magnets Based on Polyoxometalates". In: 339.Journal of the American Chemical Society (2008), pp. 8874–8875.

[6] Murad A. AlDamen et al. "Mononuclear lanthanide single molecule magnets based on the polyoxometalates [Ln(W5O18)2]9- and [Ln(β2-SiW11O39)2]13- (LnIII) Tb, Dy, Ho, Er, Tm, and Yb)". In: *Inorganic Chemistry* 48.8 (2009), pp. 3467–3479.

[7] Alessandro Aliprandi et al. "Recent advances in phosphorescent Pt (II) complexes featuring metallophilic interactions: Properties and applications". In: *Chemistry Letters* 44.9 (2015), pp. 1152–1169.

[8] P. Alves Dias et al. *The role of rare earth elements in wind energy and electric mobility.* 2020, p. 43.

[9] P W Anderson. "Antiferromagnetism. Theory of Suyerexchange". In: *Physical Review* 79.2 (1950), pp. 350–356.

[10] Philip W. Anderson. "Theory of Magnetic Exchange Interactions:Exchange in Insulators and Semiconductors". In: *Solid State Physics - Advances in Research and Applications* 14.C (1963), pp. 99–214.

[11] Paul W. Ayers. “The physical basis of the hard/soft acid/base principle”. In: *Faraday Discussions* 135 (2007), pp. 161–190.

[12] Frederick G. Baddour et al. “Heterobimetallic lantern complexes that couple antiferromagnetically through noncovalent Pt-Pt interactions”. In: *Inorganic Chemistry* 52.9 (2013), pp. 4926–4933.

[13] Frederick G. Baddour et al. “Pt-Mg, Pt-Ca, and Pt-Zn Lantern Complexes and Metal-Only Donor-Acceptor Interactions”. In: *Inorganic Chemistry* 56.1 (2017), pp. 452–469.

[14] Frederick G. Baddour et al. “Pt $\cdots$ Pt vs Pt $\cdots$ S contacts between Pt-containing heterobimetallic lantern complexes”. In: *Inorganic Chemistry* 52.23 (2013), pp. 13562–13575.

[15] Gordon A. Bain and John F. Berry. “Diamagnetic corrections and Pascal’s constants”. In: *Journal of Chemical Education* 85.4 (2008), pp. 532–536.

[16] Gopalakrishnan Balasubramanian et al. “Ultralong spin coherence time in isotopically engineered diamond”. In: *Nature Materials* 8.5 (2009), pp. 383–387.

[17] José J. Baldoví et al. “Rational design of single-ion magnets and spin qubits based on mononuclear lanthanoid complexes”. In: *Inorganic Chemistry* 51.22 (2012), pp. 12565–12574.

[18] Stephanie A. Beach and Linda H. Doerrer. “Heterobimetallic Lantern Complexes and Their Novel Structural and Magnetic Properties”. In: *Accounts of Chemical Research* 51.5 (2018), pp. 1063–1072.

[19] Stephanie A. Beach, Arnold L. Rheingold, and Linda H. Doerrer. “Comparison of O,S- vs N,S-donor ligands in PtNi heterobimetallic lantern complexes”. In: *Polyhedron* 208.May (2021), p. 115403.

[20] H. Bethe. “Termaufspaltung in Kristallen”. In: *Annalen der Physik* 395.2 (1929), pp. 133–208.

[21] Lapo Bogani et al. “Single chain magnets: Where to from here?” In: *Journal of Materials Chemistry* 18.40 (2008), pp. 4750–4758.

[22] Niels A. Bonde et al. “Importance of Axial Symmetry in Elucidating Lanthanide-Transition Metal Interactions”. In: *Inorganic Chemistry* 59.1 (2020), pp. 235–243.

[23] Andrew T. Boothroyd. *Principles of Neutron Scattering from Condensed Matter.* Oxford University PressOxford, July 2020.

[24] Matteo Briganti et al. “A Complete Ab Initio View of Orbach and Raman Spin–Lattice Relaxation in a Dysprosium Coordination Compound”. In: *Journal of the American Chemical Society* 143.34 (Sept. 2021), pp. 13633–13645.

[25] Brockhouse. *Research w ith inelastic Neutron Scattering at the NRU Reactor*. Tech. rep. 1964.

[26] Carl J. Ballhausen. *Introduction to ligand field theory*. McGraw-Hill Book Co., Inc, 1965.

[27] Alejandro Castro-Alvarez et al. “High performance single-molecule magnets, Orbach or Raman relaxation suppression?” In: *Inorganic Chemistry Frontiers* 7.13 (2020), pp. 2478–2486.

[28] J. Chadwick. “The Existence of a Neutron”. In: *Proceedings of the Royal Society* 136.830 (1932), pp. 692–708.

[29] Tapan Chatterji et al. “ Direct evidence for the Nd magnetic ordering in NdMnO 3 from the hyperfine field splitting of Nd nuclear levels ”. In: *Journal of Physics: Condensed Matter* 21.12 (2009), p. 126003.

[30] A. Chiesa et al. “Understanding magnetic relaxation in single-ion magnets with high blocking temperature”. In: *Physical Review B* 101.17 (2020), pp. 1–9.

[31] George Christou et al. “Single-Molecule Magnets”. In: *MRS Bulletin* 25.11 (Nov. 2000), pp. 66–71.

[32] R. E. Coffman and G. R. Buettner. “A limit function for long-range ferromagnetic and antiferromagnetic superexchange”. In: *The Journal of Physical Chemistry* 83.18 (1979), pp. 2387–2392.

[33] U.S. Atomic Energy Commission. *The First Reactor*. Oak Ridge, Tennessee, U.S: U.S. Atomic Energy Commission, Division of Technical Information, 1967.

[34] D. Cribier and B. Jacrot. “Neutron Scattering and the Crystalline Stark Effect in Rare Earth Oxides”. In: *Comptes Rendus* 250 (1960).

[35] Łukasz Cywiński, Wayne M. Witzel, and S. Das Sarma. “Electron spin dephasing due to hyperfine interactions with a nuclear spin bath”. In: *Physical Review Letters* 102.5 (2009), pp. 1–4. arXiv: `0809.0003`.

[36] Eric W. Dahl et al. “Antiferromagnetic coupling across a tetrametallic unit through noncovalent interactions”. In: *Chemical Science* 3.2 (2012), pp. 602–609.

[37] Atanu Dey, Pankaj Kalita, and Vadapalli Chandrasekhar. “Lanthanide(III)-Based Single-Ion Magnets”. In: *ACS Omega* 3.8 (2018), pp. 9462–9475.

[38] David P. DiVincenzo. “The physical implementation of quantum computation”. In: *Fortschritte der Physik* 48.9-11 (2000), pp. 771–783. arXiv: `0002077 [quant-ph]`.

[39] J. R. Dunning et al. “Interaction of Neutrons with Matter”. In: *Physical Review* 48.3 (1935), pp. 265–280.

[40] Luis Escalera-Moreno et al. “Spin states, vibrations and spin relaxation in molecular nanomagnets and spin qubits: A critical perspective”. In: *Chemical Science* 9.13 (2018), pp. 3265–3275.

[41] Jesús Ferrando-Soria et al. “A modular design of molecular qubits to implement universal quantum gates”. In: *Nature Communications* 7 (2016).

[42] A. Furrer and H. U. Gudel. “Molecular electronic excitations in a Cr3+ dimer observed by neutron inelastic scattering”. In: *Journal of Physics C: Solid State Physics* 10.8 (1977).

[43] Albert Furrer and Hans U. Güdel. “Neutron inelastic scattering from isolated clusters of magnetic ions”. In: *Journal of Magnetism and Magnetic Materials* 14.2-3 (1979), pp. 256–264.

[44] Alfred Furrer. “Neutron Inelastic Scattering from Isolated CLusters of Magnetic Ions”. PhD thesis. Eidg. Technische Hochschule Zürich, 1978.

[45] Adam Gali. “Theory of the neutral nitrogen-vacancy center in diamond and its application to the realization of a qubit”. In: *Physical Review B - Condensed Matter and Materials Physics* 79.23 (2009), pp. 1–6.

[46] Sanhita Ghosh et al. “Multi-frequency EPR studies of a mononuclear holmium single-molecule magnet based on the polyoxometalate [HoIII(W5O 18)2]9-”. In: *Dalton Transactions* 41.44 (2012), pp. 13697–13704.

[47] Marcus J. Giansiracusa et al. “A large barrier single-molecule magnet without magnetic memory”. In: *Dalton Transactions* 48.29 (2019), pp. 10795–10798.

[48] Silvia Giménez-Santamarina et al. “Exploiting clock transitions for the chemical design of resilient molecular spin qubits”. In: *Chemical Science* 11.39 (2020), pp. 10718–10728.

[49] R. Giraud et al. “Nuclear spin driven quantum relaxation in LiY0.998Ho0.002F4”. In: *Physical Review Letters* 87.5 (2001), pp. 57203–1–57203–4. arXiv: `0102231 [cond-mat]`.

[50] Jordi Gómez-Segura, Jaume Veciana, and Daniel Ruiz-Molina. “Advances on the nanostructuration of magnetic molecules on surfaces: The case of single-molecule magnets (SMM)”. In: *Chemical Communications* 36 (2007), pp. 3699–3707.

[51] John B. Goodenough. “Theory of the role of covalence in the perovskite-type manganites [La,M(II)]MnO3”. In: *Physical Review* 100.2 (1955), pp. 564–573.

[52] Conrad A.P. Goodwin et al. “Molecular magnetic hysteresis at 60 kelvin in dysprosocenium”. In: *Nature* 548.7668 (2017), pp. 439–442.

[53] Mick Gordon. “DOOM: Behind the Music”. In: *Game Developer Conference*. 2017. URL: `https://www.youtube.com/watch?v=U4FNBMZsqrY`.

[54] J. S. Griffith. *The Theory of Transition-Metal Ions*. Cambridge University Press, 1964.

[55] Lei Gu and Ruqian Wu. “Origin of the anomalously low Raman exponents in single molecule magnets”. In: *Physical Review B* 103.1 (Jan. 2021), p. 014401.

[56] Lei Gu and Ruqian Wu. “Origins of Slow Magnetic Relaxation in Single-Molecule Magnets”. In: *Physical Review Letters* 125.11 (Sept. 2020), p. 117203.

[57] H. U. Güdel and A. Furrer. “Neutron inelastic scattering study of exchange teractions in a chromium(III) dimer: µ-hydroxo- bis[pentaamminechromium- (III)] chloride monohydrate”. In: *Molecular Physics* 33.5 (1977), pp. 1335–1344.

[58] Hans U. Güdel, Anton Stiebler, and Alfred Furrer. “Direct Observation of Singlet-Triplet Separation in Dimeric Copper(II) Acetate by Neutron Inelastic Scattering Spectroscopy”. In: *Inorganic Chemistry* 18.4 (1979), pp. 1021–1023.

[59] Hans Ulrich Güdel, A. Furrer, and J. K. Kjems. “Neutron scattering in dimers”. In: *Journal of Magnetism and Magnetic Materials* 54-57.PART 3 (1986), pp. 1453–1458.

[60] Jesse L. Guillet et al. “Thiocyanate-Ligated Heterobimetallic PtM Lantern Complexes Including a Ferromagnetically Coupled 1D Coordination Polymer”. In: *Inorganic Chemistry* 55.16 (2016), pp. 8099–8109.

[61] Fu Sheng Guo et al. “Magnetic hysteresis up to 80 kelvin in a dysprosium metallocene single-molecule magnet”. In: *Science* 362.6421 (2018), pp. 1400–1403.

[62] Alaattin Güven. “Acidity study on 3-substituted pyridines”. In: *International Journal of Molecular Sciences* 6.11 (2005), pp. 257–275.

[63] O. Halpern and M. H. Johnson. “On the magnetic scattering of neutrons”. In: *Physical Review* 55.10 (1939), pp. 898–923.

[64] *Hard Drives Methods And Materials*. 2022. URL: `https://volga.eng.yale.edu/teaching-resources/hard-drives/methods-and-materials` (visited on 08/09/2022).

[65] Bevin Huang et al. “Emergent phenomena and proximity effects in two-dimensional magnets and heterostructures”. In: *Nature Materials* 19.12 (2020), pp. 1276–1289.

[66] Naoto Ishikawa, Miki Sugita, and Wolfgang Wernsdorfer. “Quantum tunneling of magnetization in lanthanide single-molecule magnets: Bis(phthalocyaninato)terbium and bis(phthalocyaninato)dysprosium anions”. In: *Angewandte Chemie - International Edition* 44.19 (2005), pp. 2931–2935.

[67] Naoto Ishikawa et al. “Lanthanide double-decker complexes functioning as magnets at the single-molecular level”. In: *Journal of the American Chemical Society* 125.29 (2003), pp. 8694–8695.

[68] Mark Jenkins et al. “Coupling single-molecule magnets to quantum circuits”. In: *New Journal of Physics* 15 (2013). arXiv: `1306.4276`.

[69] Jianzhuang Jiang, ed. *Functional Phthalocyanine Molecular Materials*. Vol. 135. Structure and Bonding December. Berlin, Heidelberg: Springer Berlin Heidelberg, 2010.

[70] Uwe Kaiser, Alexander Schwarz, and Roland Wiesendanger. “Magnetic exchange force microscopy with atomic resolution”. In: *Nature* 446.7135 (2007), pp. 522–525.

[71] Junjiro Kanamori. “Superexchange interaction and symmetry properties of electron orbitals”. In: *Journal of Physics and Chemistry of Solids* 10.2-3 (1959), pp. 87–98.

[72] *LAPACK - Linear Algebra PACKage*. URL: `http://www.netlib.org/lapack/index.html` (visited on 07/14/2022).

[73] M. N. Leuenberger and D. Loss. “Quantum computing in molecular magnets”. In: *Nature* 410.6830 (2001), pp. 789–793.

[74] Xiao Lei Li and Jinkui Tang. “Recent developments in single-molecule toroics”. In: *Dalton Transactions* 48.41 (2019), pp. 15358–15370.

[75] Leonel Llanos and Daniel Aravena. “Relaxation time enhancement by magnetic dilution in single-molecule magnets: An ab initio study”. In: *Journal of Magnetism and Magnetic Materials* 489.April (2019), p. 165456.

[76] Alessandro Lunghi and Stefano Sanvito. “How do phonons relax molecular spins?” In: *Science Advances* 5.9 (2019), pp. 1–8.

[77] Alessandro Lunghi and Stefano Sanvito. “The Limit of Spin Lifetime in Solid-State Electronic Spins”. In: *The Journal of Physical Chemistry Letters* 11.15 (Aug. 2020), pp. 6273–6278.

[78] Alessandro Lunghi et al. “Intra-molecular origin of the spin-phonon coupling in slow-relaxing molecular magnets”. In: *Chemical Science* 8.9 (2017), pp. 6051–6059.

[79] Alessandro Lunghi et al. “The role of anharmonic phonons in under-barrier spin relaxation of single molecule magnets”. In: *Nature Communications* 8 (2017), pp. 1–7.

[80] Diamantoula Maniaki, Evangelos Pilichos, and Spyros P. Perlepes. “Coordination clusters of 3d-metals that behave as Single-Molecule Magnets (SMMs): Synthetic routes and strategies”. In: *Frontiers in Chemistry* 6.SEP (2018).

[81] N. Mizuochi et al. “Coherence of single spins coupled to a nuclear spin bath of varying density”. In: *Physical Review B - Condensed Matter and Materials Physics* 80.4 (2009), pp. 5–8. arXiv: `0811.4731`.

[82] Stefan Müllegger et al. “Radio frequency scanning tunneling spectroscopy for single-molecule spin resonance”. In: *Physical Review Letters* 113.3 (2014), pp. 1–5.

[83] Fabian D. Natterer et al. “Reading and writing single-atom magnets”. In: *Nature* 543.7644 (2017), pp. 226–228. arXiv: `1607.03977`.

[84] Arunpatcha Nimthong-Roldán et al. “Quasi-1D chains of dinickel lantern complexes and their magnetic properties”. In: *Dalton Transactions* 46.17 (2017), pp. 5546–5557.

[85] NobelPrize.org. *The Nobel Prize in Physics 1994*. 2022. URL: `https://www.nobelprize.org/prizes/physics/1994/summary/` (visited on 09/04/2022).

[86] R Orbach. “On the theory of spin-lattice relaxation in paramagnetic salts”. In: *Proceedings of the Physical Society* 77.4 (1961), pp. 821–826.

[87] Ralph G. Pearson. “Hard and Soft Acids and Bases”. In: *Journal of the American Chemical Society* 85.22 (Nov. 1963), pp. 3533–3539.

[88] Kasper S. Pedersen et al. “Design of Single-Molecule Magnets: Insufficiency of the Anisotropy Barrier as the Sole Criterion”. In: *Inorganic Chemistry* 54.15 (2015), pp. 7600–7606.

[89] P. S. Peijzel et al. “A complete 4f energy level diagram for all trivalent lanthanide ions”. In: *Journal of Solid State Chemistry* 178.2 SPEC. ISS. (2005), pp. 448–453.

[90] Mauro Perfetti. “Cantilever torque magnetometry on coordination compounds: from theory to experiments”. In: *Coordination Chemistry Reviews* 348 (2017), pp. 171–186.

[91] Mauro Perfetti and Jesper Bendix. “The Multiple Faces, and Phases, of Magnetic Anisotropy”. In: *Inorganic Chemistry* 58.18 (Sept. 2019), pp. 11875–11882.

[92] Mauro Perfetti et al. “Magnetic Anisotropy Switch: Easy Axis to Easy Plane Conversion and Vice Versa”. In: *Advanced Functional Materials* 28.32 (2018), pp. 1–8.

[93] Pixies, Charles Thompson, and Tom Dalgety. *Vault of Heaven.* 2022.

[94] N. V. Prokof’ev and P. C.E. Stamp. “Theory of the spin bath”. In: *Reports on Progress in Physics* 63.4 (2000), pp. 669–726. arXiv: `0001080 [cond-mat]`.

[95] Daniel Reta and Nicholas F. Chilton. “Uncertainty estimates for magnetic relaxation times and magnetic relaxation parameters”. In: *Physical Chemistry Chemical Physics* 21.42 (2019), pp. 23567–23575.

[96] Jeffrey D. Rinehart and Jeffrey R. Long. “Exploiting single-ion anisotropy in the design of f-element single-molecule magnets”. In: *Chemical Science* 2.11 (2011), pp. 2078–2085.

[97] C. Rudowicz and C. Y. Chung. “The generalization of the extended Stevens operators to higher ranks and spins, and a systematic review of the tables of the tensor operators and their matrix elements”. In: *Journal of Physics Condensed Matter* 16.32 (2004), pp. 5825–5847.

[98] Zoraida Sandoval-Olivares, Eduardo Solis-Céspedes, and Dayán Páez-Hernández. “Antiferromagnetic Coupling Supported by Metallophilic Interactions: Theoretical View”. In: *Inorganic Chemistry* 61.3 (2022), pp. 1401–1417.

[99] R. Sessoli. “Quantum tunnelling of the magnetisation in molecular nanomagnets”. In: *Europhysics News* 34.2 (2003), pp. 41–45.

[100] R. Sessoli et al. “Magnetic bistability in a metal-ion cluster”. In: *Nature* 365.6442 (Sept. 1993), pp. 141–143.

[101] Muhandis Shiddiq et al. "Enhancing coherence in molecular spin qubits via atomic clock transitions". In: *Nature* 531.7594 (Mar. 2016), pp. 348–351.

[102] K. N. Shrivastava. "Raman Relaxation Times in Electronic Systems". In: *Physica Status Solidi (b)* 51.1 (May 1972), pp. 377–387.

[103] K. N. Shrivastava. "Theory of Spin–Lattice Relaxation". In: *physica status solidi (b)* 117.2 (June 1983), pp. 437–458.

[104] C G Shull. "Physics With Early Neutrons". In: *Conference on Neutron Scattering*. Gatlinburg, Tennessee, 1976.

[105] J. Sievers. "Asphericity of 4 f-shells in their Hund's rule ground states". In: *Zeitschrift für Physik B Condensed Matter* 45.4 (1982), pp. 289–296.

[106] Hannah Skipper et al. "Hard-soft chemistry design principles for predictive assembly of single molecule-metal junctions". In: *J. Am. Chem. Soc* 143.40 (2021), pp. 16439–16447.

[107] Mikkel A. Sørensen et al. "Chemical tunnel-splitting-engineering in a dysprosium-based molecular nanomagnet". In: *Nature Communications* 9.1 (Dec. 2018), p. 1292.

[108] Mikkel A. Sørensen et al. "Imposing high-symmetry and tuneable geometry on lanthanide centres with chelating Pt and Pd metalloligands". In: *Chemical Science* 8.5 (2017), pp. 3566–3575.

[109] Philip C.E. Stamp and Alejandro Gaita-Ariño. "Spin-based quantum computers made by chemistry: Hows and whys". In: *Journal of Materials Chemistry* 19.12 (2009), pp. 1718–1730. arXiv: `0807.1986`.

[110] K. W.H. Stevens. "Matrix elements and operator equivalents connected with the magnetic properties of rare earth ions". In: *Proceedings of the Physical Society. Section A* 65.3 (1952), pp. 209–215.

[111] Stefan Stoll and Arthur Schweiger. "EasySpin, a comprehensive software package for spectral simulation and analysis in EPR". In: *Journal of Magnetic Resonance* 178.1 (2006), pp. 42–55.

[112] J. H. Van Vleck. "On dielectric constants and magnetic susceptibilities in the new quantum mechanics Part I. A general proof of the Langevin-Debye formula". In: *Physical Review* 29.5 (1927), pp. 727–744.

[113] J. H. Van Vleck. “On Dielectric Constants and Magnetic Susceptibilities in the New Quantum Mechanics Part III—Application to Dia- and Paramagnetism”. In: *Physical Review* 31.4 (Apr. 1928), pp. 587–613.

[114] J. H. Van Vleck. “On dielectric constants and magnetic susceptibilities in the new quantum mechanics. Part II - Application to dielectric constants”. In: *Physical Review* 30.1 (1927), pp. 31–54.

[115] J. H. Van Vleck. “The New Quantum Mechanics”. In: *Chemical Reviews* (1929), pp. 467–507.

[116] Lucia Vitali et al. “Electronic structure of surface-supported bis(phthalocyaninato) terbium(lll) single molecular magnets”. In: *Nano Letters* 8.10 (2008), pp. 3364–3368.

[117] S. Voss et al. “Electronic structure of Mn12 derivatives on the clean and functionalized Au surface”. In: *Physical Review B - Condensed Matter and Materials Physics* 75.4 (2007), pp. 1–7.

[118] Høgni Weihe and Hans U. Güdel. “Quantitative Interpretation of the Goodenough - Kanamori Rules: A Critical Analysis”. In: *Inorganic Chemistry* 36.17 (July 1997), pp. 3632–3639.

[119] Gary Wolfowicz et al. “Atomic clock transitions in silicon-based spin qubits”. In: *Nature Nanotechnology* 8.8 (2013), pp. 561–564. arXiv: `1301.6567`.

[120] E. O. Wollan and C. G. Shull. “Neutrons as Waves and Particles”. In: *Physics Today* 3.7 (1950), pp. 20–25.

[121] Daniel N. Woodruff, Richard E P Winpenny, and Richard A. Layfield. “Lanthanide Single-Molecule Magnets”. In: *Chemical Reviews* 113.7 (July 2013), pp. 5110–5148.

[122] Brian G. Wybourne. *Spectroscopic Properties of Rare Earths.* John Wiley, 1965.

[123] Chung Jui Yu et al. “Long Coherence Times in Nuclear Spin-Free Vanadyl Qubits”. In: *Journal of the American Chemical Society* 138.44 (2016), pp. 14678–14685.

[124] Qingshu Zheng et al. “The Energetic Significance of Metallophilic Interactions”. In: *Angewandte Chemie* 131.36 (2019), pp. 12747–12753.

Appendix A

Figures

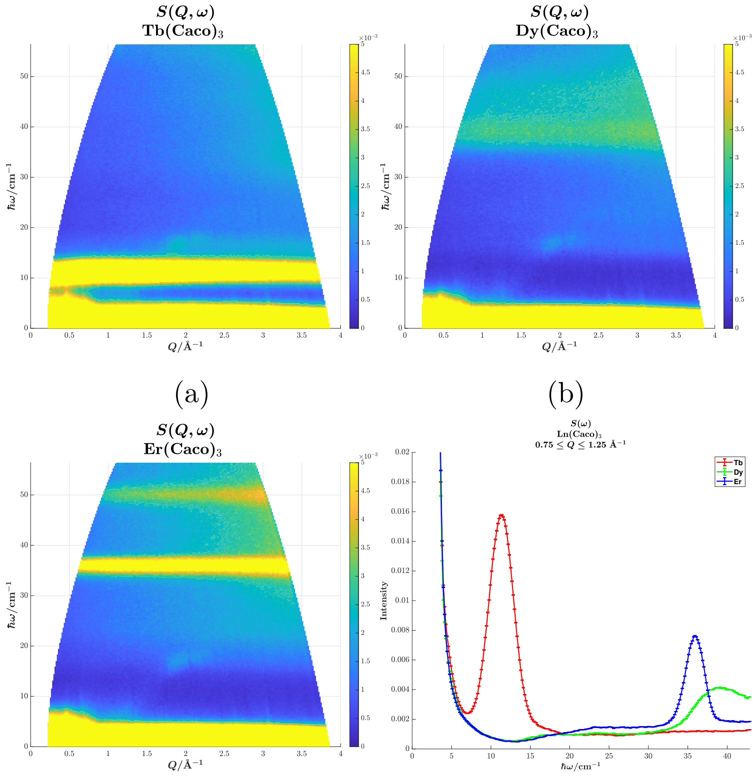

(a) (b)

(c) (d)

Figure A.1: $S(Q, \omega)$ of $[\mathrm{Ln(As(CH_3)_2O_2)_3}] \cdot 8\,\mathrm{D_2O}$ at $\lambda = 3\,\text{Å}$ and 1.6 K with **(a)** Tb^{3+},**(b)** Dy^{3+} and **(c)** Er^{3+}. **(d)** Integrated spectra.

This figure illustrate the importance of deuteration in INS experiments. Even at only $\approx$ 50% deuteration, the spectra have significantly lowered phonon background as compared to the spectra of comparable compounds like **LnPd** (see chapter 4), that were not deuterated. The peaks in **(d)** are all magnetic, and only the flat bottom is incoherent background.

Appendix B

Tables

HoPd Eigenstates, values and uncertainties.

$\lvert m_J\rangle$	$\lvert m_I\rangle$	E/cm^{-1}	$\sigma_E/10^{-2}\,\mathrm{cm}^{-1}$		
			$1.6\,K$	$5\,K$	$10\,K$
$0.7057\lvert +4\rangle$ $+0.7057\lvert -4\rangle$ $-0.0611\lvert 0\rangle$	$\lvert \pm 7/2\rangle$	0	1.676	2.338	2.878
	$\lvert \pm 5/2\rangle$	0.05543	1.573	2.135	2.622
	$\lvert \pm 3/2\rangle$	0.1006	1.523	2.013	2.469
	$\lvert \pm 1/2\rangle$	0.1268	1.523	1.985	2.432
$0.7071\lvert +4\rangle$-$0.7071\lvert -4\rangle$	$\lvert \pm 1/2\rangle$	0.8290	0.3627	0.5498	0.680
	$\lvert \pm 3/2\rangle$	0.8675	0.1413	0.1936	0.2380
	$\lvert \pm 5/2\rangle$	0.9372	0.4298	0.6338	0.7826
	$\lvert \pm 7/2\rangle$	1.030	0.9865	1.484	1.834
$-0.9990\lvert -5\rangle$ $+0.04300\lvert -1\rangle$	$\lvert \pm 7/2\rangle$	3.720	1.790	2.677	3.308
	$\lvert \pm 5/2\rangle$	3.872	1.224	1.793	2.213
	$\lvert \pm 3/2\rangle$	4.017	0.7824	1.079	1.327
	$\lvert \pm 1/2\rangle$	4.158	0.6247	0.8067	0.9874
$-0.9990\lvert +5\rangle$ $+0.04300\lvert +1\rangle$	$\lvert \pm 1/2\rangle$	4.292	0.8397	1.174	1.445
	$\lvert \pm 3/2\rangle$	4.422	1.199	1.753	2.164
	$\lvert \pm 5/2\rangle$	4.547	1.575	2.343	2.894
	$\lvert \pm 7/2\rangle$	4.666	1.934	2.897	3.581
$-0.9968\lvert -3\rangle$ $+0.0723\lvert +1\rangle$ $+0.0330\lvert -7\rangle$ $+0.01230\lvert +5\rangle$	$\lvert \pm 7/2\rangle$	44.67	1.915	2.625	3.226
	$\lvert \pm 5/2\rangle$	44.75	1.750	2.343	2.876
	$\lvert \pm 3/2\rangle$	44.83	1.632	2.137	2.619
	$\lvert \pm 1/2\rangle$	44.92	1.571	2.029	2.483
$0.9968\lvert +3\rangle$-$0.0723\lvert -1\rangle$ -$0.0330\lvert +7\rangle$-$0.01230\lvert -5\rangle$	$\lvert \pm 1/2\rangle$	45.00	1.574	2.032	2.487
	$\lvert \pm 3/2\rangle$	45.08	1.638	2.146	2.630

	$\|\pm5/2\rangle$	45.16	1.758	2.355	2.890
	$\|\pm7/2\rangle$	45.25	1.922	2.634	3.238
$0.7001\|-6\rangle$-$0.7001\|+6\rangle$ $+0.0993\|+2\rangle$-$0.0993\|-2\rangle$	$\|\pm7/2\rangle$	63.99	2.558	3.719	4.589
	$\|\pm5/2\rangle$	64.15	2.075	2.932	3.611
	$\|\pm3/2\rangle$	64.30	1.724	2.320	2.848
	$\|\pm1/2\rangle$	64.43	1.670	2.156	2.639
$0.7039\|-6\rangle$ $+0.7039\|+6\rangle$ -$0.0675\|+2\rangle$-$0.0675\|-2\rangle$	$\|\pm1/2\rangle$	64.73	1.048	1.358	1.663
	$\|\pm3/2\rangle$	64.85	1.453	1.993	2.451
	$\|\pm5/2\rangle$	65.01	1.950	2.789	3.438
	$\|\pm7/2\rangle$	65.16	2.490	3.643	4.497
$0.7001\|-2\rangle$-$0.7001\|+2\rangle$ $+0.0993\|-6\rangle$-$0.0993\|+6\rangle$	$\|\pm7/2\rangle$	102.8	7.763	10.00	12.24
	$\|\pm5/2\rangle$	102.8	7.764	10.00	12.24
	$\|\pm3/2\rangle$	102.8	7.764	10.00	12.24
	$\|\pm1/2\rangle$	102.8	7.764	10.00	12.24
$0.7039\|-2\rangle$ $+0.7039\|+2\rangle$ $+0.0675\|-6\rangle$ $+0.0675\|+6\rangle$	$\|\pm1/2\rangle$	120.8	10.46	13.48	16.49
	$\|\pm3/2\rangle$	120.8	10.46	13.48	16.49
	$\|\pm5/2\rangle$	120.8	10.46	13.48	16.49
	$\|\pm7/2\rangle$	120.8	10.46	13.48	16.49
$0.9993\|-7\rangle$ $+0.0319\|-3\rangle$ -$0.0206\|+1\rangle$	$\|\pm7/2\rangle$	151.9	2.580	3.921	4.850
	$\|\pm5/2\rangle$	152.1	1.855	2.816	3.483
	$\|\pm3/2\rangle$	152.3	1.133	1.714	2.120
	$\|\pm1/2\rangle$	152.5	0.4409	0.6451	0.7963
$0.9993\|+7\rangle$ $+0.0319\|+3\rangle$ -$0.0206\|-1\rangle$	$\|\pm1/2\rangle$	152.7	0.4211	0.6139	0.7576
	$\|\pm3/2\rangle$	152.9	1.113	1.684	2.082
	$\|\pm5/2\rangle$	153.1	1.841	2.794	3.456
	$\|\pm7/2\rangle$	153.3	2.575	3.912	4.839
$0.9962\|-1\rangle$ $+0.0734\|+3\rangle$ $+0.0422\|-5\rangle$ $+0.0182\|+7\rangle$	$\|\pm7/2\rangle$	166.8	2.004	2.602	3.186
	$\|\pm5/2\rangle$	166.9	1.987	2.573	3.151
	$\|\pm3/2\rangle$	166.9	1.976	2.554	3.126
	$\|\pm1/2\rangle$	166.9	1.962	2.528	3.094
$0.9962\|+1\rangle$ $+0.0734\|-3\rangle$ $+0.0422\|+5\rangle$ $+0.0182\|-7\rangle$	$\|\pm1/2\rangle$	166.9	1.959	2.524	3.089
	$\|\pm3/2\rangle$	167.0	1.962	2.530	3.097
	$\|\pm5/2\rangle$	167.0	1.972	2.549	3.121

	$\lvert\pm 7/2\rangle$	167.0	1.992	2.584	3.164
-0.7070$\lvert+8\rangle$-0.7070$\lvert-8\rangle$	$\lvert\pm 7/2\rangle$	170.7	2.936	4.465	5.524
	$\lvert\pm 5/2\rangle$	171.0	2.088	3.176	3.929
	$\lvert\pm 3/2\rangle$	171.2	1.244	1.891	2.340
	$\lvert\pm 1/2\rangle$	171.4	0.4026	0.6115	0.7564
0.7071$\lvert+8\rangle$-0.7071$\lvert-8\rangle$	$\lvert\pm 1/2\rangle$	171.6	0.4412	0.6703	0.8291
	$\lvert\pm 3/2\rangle$	171.8	1.277	1.943	2.403
	$\lvert\pm 5/2\rangle$	172.1	2.112	3.213	3.974
	$\lvert\pm 7/2\rangle$	172.3	2.945	4.479	5.540
0.9981$\lvert 0\rangle$ +0.0433$\lvert+4\rangle$ +0.0433$\lvert-4\rangle$	$\lvert\pm 7/2\rangle$	187.8	1.456	1.876	2.296
	$\lvert\pm 5/2\rangle$	187.8	1.459	1.881	2.302
	$\lvert\pm 3/2\rangle$	187.8	1.462	1.887	2.310
	$\lvert\pm 1/2\rangle$	187.8	1.464	1.891	2.314

Table B.1: Table of eigenvalues, energies and the calculated uncertainties on the energy. Component of the spin-orbit basis $|m_J\rangle$ and nuclear spin $|m_I\rangle$ given separately.

Appendix C

Computer code

```
%% Project Banana 33 function

function [ElistSorted,rdQlength,rdResult,Erange,gauss]=
   Banana33Fun(Sys,temperature,wavelength,QNodes,E,sigmaFun)

%% Setup Simulation Parameters
Exp.Field=[0,0,1e-16];
%% Solve Hamiltonian
rdSys=Sys; % Sets up a simplified spin system rdSys to pass to
   sham
nuclei=0;
if myIsField(rdSys,'A')
    hyperFine=true;
    Nucs=strsplit(Sys.Nucs,',');
    nuclei=0; % Variable for number of nuclei to which there is
       hyperfine coupling
    for i = 1:length(Nucs)
        Nucs{i}=strcat(Nucs{i}(isletter(Nucs{i})),Nucs{i}(~
           isletter(Nucs{i}))); % renames isotopelement to
           elementisotope
        if min(isletter(Nucs{i})) == 0 %% Returns true if not all
            characters of string are letters
        nuclei=nuclei+1;
        end
    end
else
```

```
    hyperFine=false;
    Nucs=strsplit(rdSys.Nucs,','); % split string into each nuclei
    rdSys=rmfield(rdSys,'Nucs'); % When no hyperfine, do not pass Nucs to sham
    for i = 1:length(Nucs)
        Nucs{i}=Nucs{i}(isletter(Nucs{i})); % Removes isotope from nucs
    end
end
spins=length(rdSys.S);
ham=sham(rdSys,Exp.Field);
[v,energy]=eig(ham);
[energies,energiesIndex]=sort((diag(energy)-min(diag(energy)))/(clight*1e-4));
v=v(:,energiesIndex');
nStates=size(v,1);

%% Calculate Boltzmann Population
P=exp(-energies./(0.69503476*temperature));
P=(P./sum(P,1));

%% Make list of allowed transitions
Ei=81.81/(wavelength^2)*8.07; %Incident neutron energy in cm-1
if isempty(E)
    E = [-inf,Ei*0.99]; % multiplying by 0.99 to not have transition energy near Ei for rounding error
elseif max(E,[],'all') > 0.99*Ei
    E(find(E>0.99*Ei))=0.99*Ei;
end
energydifference=energies-energies'; % Rows are final energy states and columns initial
logicalGrid=zeros(size(energydifference));
for i=1:size(E,1)
```

```
    logicalGrid=logicalGrid+ (energydifference < max(E(i,:))).*(
       abs(energydifference) > sigmaFun(0)/10).*(energydifference
        > min(E(i,:)));
end
logicalGrid=logicalGrid.*(repmat(max(P,[],2),1,size(P,1))>1e-9)';
    % Removes transitions from states with P<1e-9
%logicalGrid=ones(size(logicalGrid)); % Use if all transitions
   necessary.
%Note imaginary transitions
[final,initial]=find(logicalGrid);
nTransitions=length(final);
energiesList=energies(final)-energies(initial);

%% Calculate Rotations
molPos=Sys.Pos';
molPos=molPos-sum(molPos,2)/size(molPos,2); %center of gravity
load('dodecahedronRotations.mat')
nRotations=size(rotations,3);
    for r = 1:nRotations
        Positions(:,:,:,:,r)=permute(rotations(:,:,r)*molPos
           ,[3,4,1,2]);
        axang(r,:)=rotm2axang(rotations(:,:,r)); % Store all
           rotation axis and angles
    end

%% Calculate electron spin matrix elements
electronMatrixElements=complex(zeros([size(v),3,spins]));
for s=1:spins
    Sx=sop(rdSys,strcat('x',num2str(s)),'sparse');
    Sy=sop(rdSys,strcat('y',num2str(s)),'sparse');
    Sz=sop(rdSys,strcat('z',num2str(s)),'sparse');
    for r=1:nRotations
        Rv=expm(-1i*(axang(r,1)*Sx+axang(r,2)*Sy+axang(r,3)*Sz)*
           axang(r,4))*v;
```

```
        electronMatrixElements(:,:,1,s,r) = Rv'*Sx*Rv;
        electronMatrixElements(:,:,2,s,r) = Rv'*Sy*Rv;
        electronMatrixElements(:,:,3,s,r) = Rv'*Sz*Rv;
    end
end
electronMatrixElements=electronMatrixElements.*2.6954e-15; % 1/2
   gamma r_0

%% Calculate nuclear spin matrix elements
if myIsField(rdSys,'A')
    load('ScatteringLengths.mat');
nuclearMatrixElements=complex(zeros([size(v),3,nuclei]));
for s=(spins+1):(spins+nuclei)
%      elementIsotope=strcat(rdNucs{s-spins}(isletter(rdNucs(s-
   spins))),rdNucs{s-spins}(~isletter(rdNucs(s-spins))));
    elementIsotope=Nucs{s-spins};
    if ~myIsField(ScatteringLengths,elementIsotope)
    elseif isnan(ScatteringLengths.(elementIsotope).A) || isnan(
       ScatteringLengths.(elementIsotope).B)
           error('Nuclear Scattering Length Parameters Not Known'
              )
    end
    Sx=sop(rdSys,strcat('x',num2str(s)),'sparse');
    Sy=sop(rdSys,strcat('y',num2str(s)),'sparse');
    Sz=sop(rdSys,strcat('z',num2str(s)),'sparse');
    for r=1:nRotations
        Rv=expm(-1i*(axang(r,1)*Sx+axang(r,2)*Sy+axang(r,3)*Sz)*
           axang(r,4))*v;
        nuclearMatrixElements(:,:,1,s-spins,r) = Rv'*Sx*
           ScatteringLengths.(elementIsotope).B*1e-15*Rv+Rv'*Rv*
           ScatteringLengths.(elementIsotope).A*1e-15;
        nuclearMatrixElements(:,:,2,s-spins,r) = Rv'*Sy*
           ScatteringLengths.(elementIsotope).B*1e-15*Rv+Rv'*Rv*
           ScatteringLengths.(elementIsotope).A*1e-15;
```

```
        nuclearMatrixElements(:,:,3,s-spins,r) = Rv'*Sz*
           ScatteringLengths.(elementIsotope).B*1e-15*Rv+Rv'*Rv*
           ScatteringLengths.(elementIsotope).A*1e-15;
    end
end
else
    nuclearMatrixElements=0;
end

%% Find Form Factors
load('MagneticFormFactors.mat')
for n=1:spins
    element=Nucs{n}(isletter(Nucs{n}));
    f(:,:,:,n)=MagneticFormFactors.(element).(strcat('Ox',string(
       Sys.Ox(n))))';
end

%% Engage!
ki=permute([0,0,1]*2*pi/wavelength,[1,3,2]);
vSpace=permute(getHEALPixNodes(QNodes),[1,3,2]);
g=permute(Sys.g,[1,3,4,2]);
sqrMod=zeros(12*QNodes^2,nTransitions);
Qlength=zeros(12*QNodes^2,nTransitions);

if hyperFine
    if  spins~=1
        %'Hyperfine and spins'
        for i=1:nTransitions
            S=electronMatrixElements(final(i),initial(i),:,:,:);
            I=nuclearMatrixElements(final(i),initial(i),:,:,:);
            kf=sqrt(ki(3)^2-energiesList(i)/16.721);
            tmpQ=ki-kf*vSpace;
            tmpQlength=sqrt(sum(tmpQ.^2,3));
            tmpq=tmpQ./tmpQlength;
```

```
                trippleCrossProduct=S-sum(S.*tmpq,3).*tmpq;
                F(:,1,1,:)=f(1,:).*exp(-f(2,:).*(tmpQlength/(4*pi))
                   .^2)+f(3,:).*exp(-f(4,:).*(tmpQlength/(4*pi)).^2)+
                   f(5,:).*exp(-f(6,:).*(tmpQlength/(4*pi)).^2+f(7,:)
                   );
                positionFactors=exp(1i*sum(Positions.*tmpQ,3)); %Dot
                   product of position and Q
                ionSum=-sum(F.*positionFactors(:,:,:,1:spins).*
                   trippleCrossProduct.*g,2)+sum(I.*positionFactors
                   (:,:,:,(spins+1):(spins+nuclei)),4);
                Qlength(:,i)=tmpQlength;
                sqrMod(:,i)=sum(sum(sum(conj(ionSum).*ionSum,3),4)*kf
                   /ki(3),5);
            end
        else
            %'Hyperfine and spin'
            positionFactors=1;
            for i=1:nTransitions
                S=electronMatrixElements(final(i),initial(i),:,:,:);
                I=nuclearMatrixElements(final(i),initial(i),:,:,:);
                kf=sqrt(ki(3)^2-energiesList(i)/16.721);
                tmpQ=ki-kf*vSpace;
                tmpQlength=sqrt(sum(tmpQ.^2,3));
                tmpq=tmpQ./tmpQlength;
                trippleCrossProduct=S-sum(S.*tmpq,3).*tmpq;
                F(:,1,1,:)=f(1,:).*exp(-f(2,:).*(tmpQlength/(4*pi))
                   .^2)+f(3,:).*exp(-f(4,:).*(tmpQlength/(4*pi)).^2)+
                   f(5,:).*exp(-f(6,:).*(tmpQlength/(4*pi)).^2+f(7,:)
                   );

                ionSum=-F.*trippleCrossProduct.*g+I;
                Qlength(:,i)=tmpQlength;
                sqrMod(:,i)=sum(sum(conj(ionSum).*ionSum,3)*kf/ki(3)
                   ,5);
```

```
        end
    end
else
    if  (spins+nuclei)~=1
        %'spins'
        for i=1:nTransitions
            S=electronMatrixElements(final(i),initial(i),:,:,:);
            kf=sqrt(ki(3)^2-energiesList(i)/16.721);
            tmpQ=ki-kf*vSpace;
            tmpQlength=sqrt(sum(tmpQ.^2,3));
            tmpq=tmpQ./tmpQlength;
            trippleCrossProduct=S-sum(S.*tmpq,3).*tmpq;
            F(:,1,1,:)=f(1,:).*exp(-f(2,:).*(tmpQlength/(4*pi))
               .^2)+f(3,:).*exp(-f(4,:).*(tmpQlength/(4*pi)).^2)+
               f(5,:).*exp(-f(6,:).*(tmpQlength/(4*pi)).^2+f(7,:)
               );
            positionFactors=exp(1i*sum(Positions.*tmpQ,3)); %Dot
               product of position and Q
            ionSum=-sum(F.*positionFactors.*trippleCrossProduct.*
               g,4);
            Qlength(:,i)=tmpQlength;
            sqrMod(:,i)=sum(sum(sum(conj(ionSum).*ionSum,3),4)*kf
               /ki(3),5);

        end
    else
        %'spin'
        positionFactors=1;
       for i=1:nTransitions
            S=electronMatrixElements(final(i),initial(i),:,:,:);
            kf=sqrt(ki(3)^2-energiesList(i)/16.721);
            tmpQ=ki-kf*vSpace;
            tmpQlength=sqrt(sum(tmpQ.^2,3));
            tmpq=tmpQ./tmpQlength;
```

```
            trippleCrossProduct=S-sum(S.*tmpq,3).*tmpq;
            F(:,1,1,:)=f(1,:).*exp(-f(2,:).*(tmpQlength/(4*pi))
               .^2)+f(3,:).*exp(-f(4,:).*(tmpQlength/(4*pi)).^2)+
               f(5,:).*exp(-f(6,:).*(tmpQlength/(4*pi)).^2+f(7,:)
               );
            ionSum=-F.*trippleCrossProduct.*g;
            Qlength(:,i)=tmpQlength;
            sqrMod(:,i)=sum(sum(conj(ionSum).*ionSum,3)*kf/ki(3)
               ,5);

       end
    end
end

%% Add together all transitions
Result=sqrMod*avogadro.*permute(P(initial,:),[3,1,2]);

%% Reduce data to Length of Q and sort
Qlog=abs(vSpace(:,1,3)-vSpace(:,1,3)')<1e-9;
[V,D]=eig(double(Qlog));
QavgOperator=sparse((V(:,diag(D)>1e-9).^2)');
[rdQlength,sortIdx1]=sort(QavgOperator*Qlength);
for t=1:length(temperature)
    rdResult(:,:,t)=QavgOperator*Result(:,:,t);
end
rdResult=rdResult(sortIdx1(:,1),:,:);
eMat=energiesList'.*ones(size(rdResult,1),size(rdResult,2));
[ElistSorted,sortIdx2]=sort(energiesList);
eMat=eMat(:,sortIdx2');
rdQlength=rdQlength(:,sortIdx2');
rdResult=rdResult(:,sortIdx2',:);

%% Calculate gaussian peak shapes and plot
Erange=min(energiesList)-10*sigmaFun(0):sigmaFun(0)/100:max(
```

```
   energiesList)+10*sigmaFun(0);
gauss=zeros(1,length(Erange),length(temperature));
for i = 1:nTransitions
    gauss=gauss+mean(rdResult(:,i,:),1).*gaussmf(Erange, [
       sigmaFun(ElistSorted(i)) ElistSorted(i)]);
end

end %% End function
```

Appendix D

Publications

NAB-1

Importance of Axial Symmetry in Elucidating Lanthanide-Transition Metal Interactions.

Bonde, N. A., Petersen, J. B., Sørensen, M. A., Nielsen, U. G., Fåk, B., Rols, S., Ollivier, J., Weihe, H., Bendix, J., & Perfetti, M.

Inorganic Chemistry 2020, 59(1), 235–243.

`https://doi.org/10.1021/acs.inorgchem.9b02064`

Inorganic Chemistry
Article
Cite This: *Inorg. Chem.* 2020, 59, 235−243
pubs.acs.org/IC

Importance of Axial Symmetry in Elucidating Lanthanide−Transition Metal Interactions

Niels A. Bonde,[†,‖] Jonatan B. Petersen,[†,§] Mikkel A. Sørensen,[†] Ulla G. Nielsen,[‡] Björn Fåk,[‖] Stéphane Rols,[‖] Jacques Ollivier,[‖] Høgni Weihe,[†] Jesper Bendix,[*,†] and Mauro Perfetti[*,†]

[†]Department of Chemistry, University of Copenhagen, Universitetsparken 5, DK-2100 Copenhagen, Denmark
[‖]Institut Laue-Langevin, 71 avenue des Martyrs, CS 20156, 38042 Grenoble Cedex 9, France
[‡]Department of Physics, Chemistry and Pharmacy, University of Southern Denmark, Campusvej 55, 5230 Odense M, Denmark

Supporting Information

ABSTRACT: In this paper, we experimentally study and model the electron donating character of an axial diamagnetic Pd^{2+} ion in four metalloligated lanthanide complexes of formula $[PPh_4][Ln\{Pd(SAc)_4\}_2]$ (SAc^- = thioacetate, Ln = Tb, Dy, Ho, and Er). A global model encompassing inelastic neutron scattering, torque magnetometry, and dc magnetometry allows to precisely determine the energy level structure of the complexes. Solid state nuclear magnetic resonance reveals a less donating character of Pd^{2+} compared to the previously reported isostructural Pt^{2+}-based complexes. Consequently, all complexes invariably show a lower crystal field strength compared to their Pt^{2+}-analogues. The dynamic properties show an enhanced single molecule magnet behavior due to the suppression of quantum tunneling, in agreement with our model.

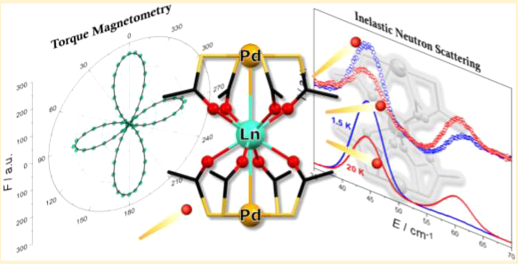

INTRODUCTION

Lanthanides are elements of primary importance in many fields of science due to their unique properties. Their applications are many, from magnetic resonance imaging contrast agents[1] to enzyme cofactors[2] and anticounterfeiting agents[3] and as constituent units in bulk[4] and molecular magnets.[5]

The property that defines the magnetic behavior of lanthanide complexes is the magnetic anisotropy. Over the past decade, the scientific community debated how molecular geometry affects the magnetic properties.[6−10] The consensus is that a plausible strategy for generating high magnetization reversal barriers[11−13] and suppressing quantum tunneling effects[14] is targeting (pseudo)-axial geometries. Among the "special" positions where a ligand can be placed, the principal axis of a linear symmetry is certainly one of the most intriguing to study. Indeed, in a purely electrostatic framework, an axial ligand influences only the diagonal crystal field (CF) parameters.

However, imposing high symmetry on lanthanide complexes is often synthetically challenging. A successful strategy to overcome this problem has been to use structure-directing ligands. For example, (pseudo)-D_{5h} geometry was obtained using 5-fold symmetric polyoxometallates,[15,16] C_3 symmetry using tripodal polydentate amines,[17,18] and pseudo-D_{4d} symmetry using transition metal-based tetradentate metalloligands.[19]

An experimentally satisfactory insight on electronic structures of both high-[14,20] and low-symmetry[21] lanthanide complexes can only be obtained merging spectroscopic and magnetometric techniques.

A chemical degree of freedom that is usually poorly exploited, is the nature of the ligands belonging to the coordination sphere of the lanthanide. This is due to the hard character of the Ln^{3+} ions, which tend to coordinate hard donors such as oxygen and nitrogen. However, a careful ligand tailoring can force the lanthanide to be coordinated, or at least close, to other atoms. Recently, great attention has been devoted in the study of the interaction between lanthanide ions and diamagnetic transition metals, particularly Pt^{2+} and Pd^{2+}. Paddlewheel metalloligands have been employed to synthesize mononuclear[19] and polynuclear[22−25] lanthanide complexes exhibiting the Ln−Pd or Ln−Pt interaction.

In two previous reports,[14,20] we successfully unraveled the electronic structure of the $[PPh_4][Ln\{Pt(SAc)_4\}_2]$ (SAc^- = thioacetate, Ln = Tb, Dy, Ho, and Er) complexes combining inelastic neutron scattering (INS) and single-crystal cantilever torque magnetometry (CTM).

In this work, we present a detailed crystal field analysis of four new tetragonal lanthanide paddlewheel complexes of formula $[PPh_4][Ln\{Pd(SAc)_4\}_2]$ (SAc^- = thioacetate, Ln = Tb, Dy, Ho and Er), in which two diamagnetic Pd^{2+} ions are placed on the principal anisotropy axis (the 4-fold molecular and crystallographic axis). The influence of the transition metal

Received: July 10, 2019
Published: December 11, 2019

DOI: 10.1021/acs.inorgchem.9b02064

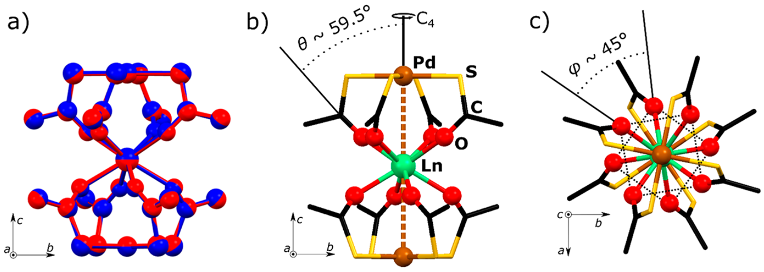

Figure 1. (a) Structural overlays of room temperature crystal structures of **ErPd** (red) and **ErPt** (blue). (b and c) Molecular structure of **ErPd** viewed along the *a* crystallographic axis and the *c* crystallographic axis, respectively. Color code: Pd, brown; Er, green; O, red; S, yellow; C, black. Hydrogen atoms and the PPh_4^+ counterion were omitted for clarity.

on the electronic structure of the lanthanide ions and on their static and dynamic magnetic properties is discussed and compared with the previously studied platinum analogues.

■ EXPERIMENTAL SECTION

Synthesis. The synthesis of the complexes in the form of small square-shaped crystals was performed following a previously published procedure for the Gd-analogue.[19]

Inelastic Neutron Scattering. The INS data were recorded at Institut Laue-Langevin, Grenoble, France, using the direct geometry cold and thermal neutron time-of-flight instruments IN5 and IN4. Samples of approximately 1 g were wrapped in aluminum foil and placed in cylindrical aluminum canisters. Using a standard ILL Orange Cryostat, the compounds were measured at selected temperatures and wavelengths in the range 1.5−200 K and 1.45−6 Å. Detector efficiency was corrected for by normalizing the spectra to a standard vanadium sample, and the IN4 data set was corrected for absorption, but otherwise the data are presented as obtained. Data reduction, binning, and plotting were performed using LAMP (large array manipulation program)[26] for the IN5 data set and in Mantid[27] for the IN4 data set.[28−30]

Cantilever Torque Magnetometry. The torque data were obtained at the LaMM (Laboratory of Molecular Magnetism) at the University of Florence using an experimental setup described elsewhere.[31] The single crystals were indexed on an Xcalibur3 single crystal diffractometer equipped with a Sapphire 3 CCD detector and a Mo source (Kα, $\lambda = 0.71$ Å). The indexed crystals were fixed on the upper plate of a rotating capacitor with grease. The variation of the capacitor's capacitance was recorded and converted into a molar torque signal by scaling it for the crystal's mass. The experimental data were simulated and fitted using a home-written program in FORTRAN 90.

Nuclear Magnetic Resonance. Solid state $^{89}Y\{^1H\}$ cross-polarization (CP) magic-angle spinning (MAS) NMR spectra were recorded on powdered samples (~150 mg) at room temperature using an Agilent INOVA 600 MHz NMR spectrometer (14.1 T) equipped with a 5 mm double resonance MAS NMR probe tuned to ^1H (599.58 MHz) and ^{89}Y (29.38 MHz) using 2 kHz spinning speed, a ramped CP sequence with a contact time of 20 ms, and a relaxation delay of 30 s. $Y(NO_3)_3 \cdot 6H_2O$ was used for setup of the CP conditions and as a secondary shift reference ($\delta(^{89}Y) = -53.2$ ppm).[32]

Shielding constants were calculated by DFT using the NMR module of the ADF 2016 program package.[33,34] The coordinates from the crystal structure of $PPh_4[Y\{Pt(SAc)_4\}_2]$ were used, excluding the PPh_4^+ ion and replacing the Pt^{2+} ion with the Pd^{2+} ion.[19] This approximation is very reasonable because the complexes are strictly isostructural (see main text). Calculations were done with the PBE and BP86 functionals and a basis set consisting of QZ4P (Y, Pt and Pd), DZP (S, O and C), and SZ (H) with the scalar-relativistic ZORA Hamiltonian.[35−39] Chemical shifts were referenced against $Y(H_2O)_8^{3+}$ ($\delta(^{89}Y) \equiv 0$ ppm), calculated with the same method on an optimized geometry in ORCA 4.0.0 with PBE0/ma-def2-TZVP and C-PCM ($\varepsilon = 80.4$).[40−44]

SQUID Magnetometry. The dc magnetic measurements were obtained using a Quantum Design MPMS SQUID magnetometer. The ac measurements were obtained in a Quantum Design PPMS equipped with AC susceptibility probe (working in the range 10 Hz-10 kHz) and a Quantum Design MPMS SQUID magnetometer (0.1 Hz to 1 kHz). The sample was in the form of a pressed powder pellet (ca. 20 mg) wrapped in Teflon. The dc data were simulated using the Easy Spin "curry" function.[45] The ac data were fitted using a home-written program in MATLAB based on the Cole−Cole function.[46]

Crystal Field Model. In lanthanide-based molecular materials, the magnetic properties at room temperature and below are largely determined by the splitting of the ground *J* multiplet due to the presence of the ligands around the metal ion. This splitting is usually reproduced using a Hamiltonian containing two terms: a crystal field term that describes the effect of the ligands and a Zeeman term that models the interaction with a magnetic field. The crystal field part of the Hamiltonian depends on the symmetry of the complex and may contain up to 27 parameters for C_1 symmetry.[47,48] However, high symmetry can drastically reduce this number. For symmetries close to D_{4d}, only seven CF parameters do not vanish.[19] If the deviation from perfect D_{4d} symmetry is sufficiently small, the minimum number of parameters necessary to reproduce experimental data can often be further reduced to three[49,50] or four.[14,20] In this report we have used the latter approach, in order to have a direct comparison between with the previously reported Pt-based analogues.[14,20]

The employed Hamiltonian was:

$$\hat{\mathcal{H}} = \sum_{k=2,4,6} b_k^0 \hat{O}_k^0 + b_4^4 \hat{O}_4^4 + \mu_B g_J \boldsymbol{B} \cdot \hat{\boldsymbol{J}} \tag{1}$$

where b_k^q are the Stevens' CF parameters that multiply the appropriate $\hat{O}_k^q$ Stevens' CF operator, μ_B is the Bohr magneton, g_J is the Landé *g*-factor, $\boldsymbol{B}$ is the magnetic field, and $\hat{\boldsymbol{J}}$ is the total angular momentum operator. The first term in eq 1 accounts for the axial crystal field, the second term for the (small) transverse component of the crystal field produced by the deviations from almost perfect D_{4d} symmetry, and the last term is the Zeeman interaction with a magnetic field. In the paper we have reported the parameters expressed in Wybourne's notation (B_k^q) to ease the comparison between different lanthanide complexes, while the fitted Stevens' parameters and the conversion between the two notations are reported in the Supporting Information.

■ RESULTS AND DISCUSSION

The sandwich-type complexes studied in this paper contain a tripositive single lanthanide ion (or Y^{3+}) encapsulated by two identical Pd-based complexes. For the sake of simplicity, we will refer to the complexes with the name of the central lanthanide followed by the axial metal in bold (i.e., **LnM**). The complexes crystallize in the tetragonal *P*4/*n* space group and are strictly isostructural with the previously reported Gd-

DOI: 10.1021/acs.inorgchem.9b02064
Inorg. Chem. 2020, 59, 235−243

analogue and with their **LnPt** counterparts,[19] as shown in Figure 1a for **ErPd**. The Y-based complexes (see NMR discussion) are also isostructural. The molecular structure is reported in parts b and c of Figure 1. The average Ln−O distance is 2.329, 2.352, 2.343, and 2.329 Å in **TbPd**, **DyPd**, **HoPd**, and **ErPd**, respectively. The Ln−Pd distance is 3.642, 3.649, 3.646, and 3.640 Å in **TbPd**, **DyPd**, **HoPd**, and **ErPd**, respectively. The distances between the Ln center and the two Pd atoms are slightly different, with the Ln ion being placed 0.02−0.03 Å away from the geometric center. The twist angle between the two squares formed by the oxygen atoms (φ) is very close to 45° in all compounds (maximum deviation: −0.6° in **HoPd**), while the oxygen atoms are averagely tilted by $\theta = 59.5°$ from the *c* crystallographic axis (with a maximum deviation of ca. 0.1°).

We have reported a significant change in the electronic structure of the **GdPd** complex when the Pd atoms were replaced by Pt atoms. The overall splitting of the ground $J = {}^{7}/_{2}$ multiplet increased by a factor of 2.5 going from Pd to Pt (0.46 vs 1.13 cm^{-1} for **GdPd** vs **GdPt**). In the case of the Gd complexes, we were able to investigate the effect using X-band EPR.[19] Yamashita et al. investigated dimeric compounds with similar ligands, exhibiting shorter Ln−Pd (Ln = Gd) and Ln−Pt (Ln = Gd, Tb, Ho, Er) distances compared to our complexes. They have experimentally investigated their compounds using UV−vis and XANES spectroscopy, invariably obtaining a shift in the Pt L_3-edge that suggested a coordination geometry of Pt^{2+} approaching square pyramidal.[22−25] Moreover, using DFT calculations on the La-substituted structure, they have corroborated that an interaction between the coordinated lanthanide and Pd or Pt is present, and that the higher radial extension of the $5d_{z^2}$ orbital of Pt compared to the $4d_{z^2}$ orbital of Pd enhances the polarization of the transition metal ion.[25] However, to the best of our knowledge, the only CF investigation performed so far on a complex containing the Ln−Pd interaction was done on **GdPd**.[19] Gd^{3+} is has a half-filled ($4f^7$) configuration, which yields typical CF splittings orders of magnitude smaller compared to the other paramagnetic lanthanide complexes. Thus, considerations about the CF splitting of this ion cannot be trivially extended to the other members of an isostructural series. We were thus curious to detect and quantify the effect of the axial metal on the crystal field splitting of the more anisotropic lanthanides.

We decided to use torque magnetometry, which provides an excellent picture of the magnetic anisotropy of lanthanides with large magnetic moments.[31] Torque magnetometry measurements have been performed on single crystals of the four studied compounds at selected temperatures (T = 2−300 K) and fields (B = 0.5−12 T). The magnetic field was parallel to the *ab* crystallographic plane at the beginning of the rotation and parallel to the *c* axis at $\theta = 90°$. The in-plane rotation was not performed since the anisotropy in this plane was expected to be orders of magnitude weaker,[20] as verified *a posteriori* (see below). A sketch of the experimental setup and other experimental details are reported in Figure S1 and Table S1. Data and fits are reported in Figures S2−S5.

In Figure 2a, we show the torque measurements obtained at T = 2 K and B = 1 T for all the samples. The magnitude of the magnetic anisotropy (proportional to the highest value of the torque signal)[31] follows the order: **DyPd** > **ErPd** > **TbPd** > **HoPd**. The tetragonal symmetry of the systems allows to describe the anisotropy at certain experimental conditions (T and B) simply looking at the shape of the torque signal.[20,31] Considering our experimental setup, and neglecting the small in-plane anisotropy, a positive torque between 0 and 90° implies easy axis magnetic anisotropy (**DyPd**, **HoPd**) while an opposite phase reflects easy plane anisotropy (**TbPd**, **ErPd**). The steep slope of the **DyPd** curve near zero and its smooth slope at $\theta = 90°$ can be readily explained due to the low temperature and high field regime, as previously reported.[31] A similar explanation can describe the curves of **TbPd** and **ErPd**.[20] On the contrary, the plateau of the **HoPd** curve at around 90° is the signature that the compound will exhibit a magnetic anisotropy switch.[20,51] A comparison with the previously published **LnPt** analogues reveals that the torque response at low temperature of all the derivatives has similar shape and slightly smaller magnitude, except for **HoPd**, which has a significantly smaller anisotropy compared to **HoPt**.[14,20] This suggests a similar composition of the ground state, but an overall decrease of the energy of the first excited state compared to the **LnPt**, which is expected to be more pronounced in **HoPd**.

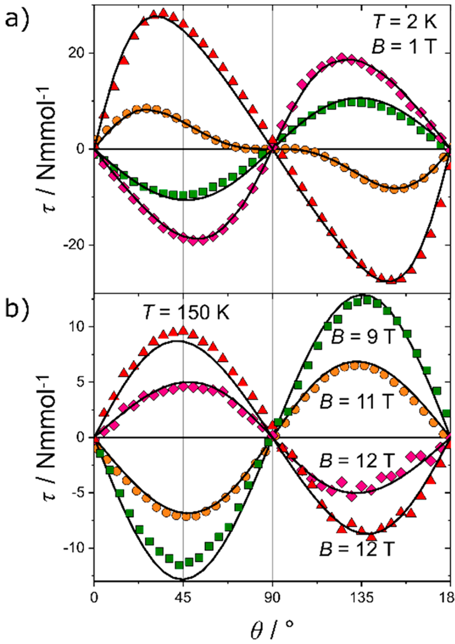

Figure 2. Torque signal recorded at (a) T = 2 K, B = 1 T and (b) T = 150 K, various fields. Color code: **TbPd**, green squares; **DyPd**, red triangles; **HoPd**, orange circles; **ErPd**, pink diamonds. The black lines are the best fit (see text).

Data obtained at a higher temperature (and field) are reported in Figure 2b. The torque curves of **HoPd** and **ErPd** change sign compared to the low temperature, similar to their **LnPt** analogues. **HoPd** (**ErPd**) is easy axis (easy plane) in Figure 2a but it becomes easy plane (easy axis) in Figure 2b. Conversely, **TbPd** and **DyPd** do not change magnetic anisotropy. Their **LnPt** analogues exhibit a similar behavior, but the **DyPt** derivative was predicted to change magnetic anisotropy at around T = 120 K, which is not the case for **DyPd**.[51] The magnitude of the signal in **TbPd** and **ErPd** is, again, slightly smaller than for their Pt analogues (particularly **TbPd**), while for **HoPd** it is very similar. For **DyPt**, we do not

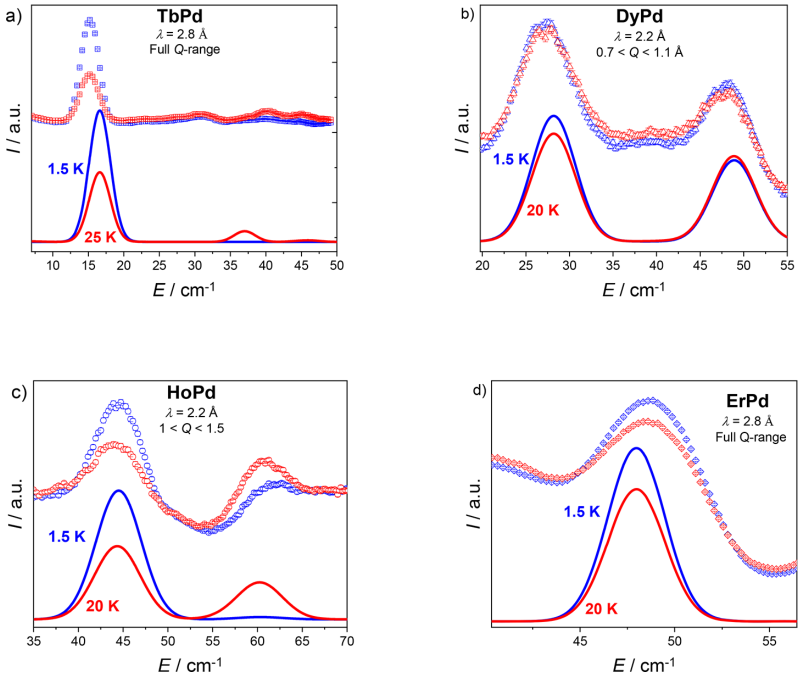

Figure 3. INS spectra of (a) **TbPd**, (b) **DyPd**, (c) **HoPd**, and (d) **ErPd** at low (1.5 K, blue) and high (20 or 25 K, red) temperature. The incident neutron wavelength and Q-integration range is indicated in each panel. The symbols represent experimental points while the solid lines are the simulations. Uncertainties are always smaller than the symbols.

have data at sufficiently high temperature for a direct comparison.

The overall picture that emerged from the torque data is that the axial transition metal ion has indeed an influence on the crystal field splitting of the lanthanide ion. Based solely on torque data, a decrease of the CF strength is expected in the **LnPd** derivatives compared to their **LnPt** analogues (very marked for **TbPd** and less so for **HoPd**). However, a more valuable quantitative information can be gained if the CTM data are flanked by spectroscopic measurements.[20,52]

Inelastic neutron scattering has in several instances been used to gain insight on the electronic structure of lanthanide-based complexes.[14,20,53−57] The INS study of heavy lanthanides can, despite the challenge posed by large cross section for neutron absorption, provide an accurate mapping of both the magnetic excitations and the lattice phonons of the host crystal. An up-to-date list of references on INS studies can be found in a recent review.[58] Due to the prevalence and intensity of phonons in the investigated energy and wave-vector transfer regime, it becomes particularly useful to investigate isostructural series, because the phononic excitations tend to be nearly the same, whereas the magnetic excitations typically vary widely along the series.

In Figure 3, we report the main INS excitations that we have identified in the present systems. The **TbPd** spectrum in Figure 3a exhibits a cold peak at 15.4 cm^{-1}. The $S(Q,\omega)$ plots are reported in Figure S6. Moreover, two very weak hot magnetic excitations can be identified at 40.3 and at 45.0 cm^{-1} from Figure S7. The **DyPd** spectrum (Figure 3b) presents a cold excitation at 27.4 cm^{-1} and another excitation of magnetic origin at 47.6 cm^{-1}. The nature of this last excitation (hot or cold) is uncertain based solely on the experimental data, since it is superimposed with two phonons, as testified by the $S(Q,\omega)$ plots in Figure S8 and the spectrum in Figure S9. Our global model, however, identifies it as a cold and a hot transition almost coincident in energy (see below). The **HoPd** data set is certainly the richest in information. The spectrum reported in Figure 3c was obtained using an incident wavelength λ_i = 2.2 Å ($S(Q,\omega)$ plot in Figure S10) and reveals two excitations, a cold transition at 44.4 cm^{-1} and hot transition at 61.3 cm^{-1}, the latter of which is comprised of two contributions. This is evidenced by the intensity as a function of temperature (Figure S11), in which a rapid increase followed by a near constant intensity is only reproduced by two hot transitions. A separate experiment at λ_i = 6 Å (Figure S12−S13) reveals two additional cold transitions, at 0.847 and 4.2 cm^{-1}. The high-energy transfer regime of **HoPd**, obtained at IN4 (Figure S14−S15), shows a single cold magnetic excitation at around 45 cm^{-1}, consistent with the global model.[59] The two very intense peaks are identified as phonons based on the peak position, which moves to lower energy with increasing temperature. Finally, the **ErPd** spectrum exhibits a single, cold transition at 48.4 cm^{-1}, see also $S(Q,\omega)$ plot in Figure S16 and integrated spectrum in Figure S17.

In a previous article, we have demonstrated the importance of combining spectroscopic and magnetometric data to obtain a correct parametrization of lanthanide-based systems.[20] In this paper we have also used a combined INS + CTM fit, from which we extracted the CF parameters reported in Table 1 in Wybourne's notation,[60] to allow for a straightforward comparison. The estimation of the errors and the parameter values expressed in Stevens' notation are reported in the Supporting Information. As expected for isostructural compounds, the parameters have the same sign and similar

Table 1. CF Parameters in Wybourne's Notation Converted from the Stevens' Parameters b_k^q Extracted from the Combined CTM and INS Fit (Table S2)

	TbPd	DyPd	HoPd	ErPd
B_2^0/cm^{-1}	−154	−65	−192	−162
B_4^0/cm^{-1}	−967	−1068	−980	−804
B_6^0/cm^{-1}	+300	+288	+335	+383
B_4^4/cm^{-1}	−94[a]	−113[a]	−115	−115[a]

[a] Fixed parameter (see main text).

magnitude across the series (Figure S18). The magnitude of the B_4^4 parameter, which accounts for the imperfections of the idealized D_{4d} symmetry, was fitted for the Ho derivative for which we experimentally measured the tunnel splitting (INS peak at 0.847 cm^{-1} in Figure S13). The output of the fit (B_4^4 = −115 cm^{-1}) is identical to that previously reported for **HoPt**.[20] The conserved value is not surprising, since the perturbation to the crystal field produced by replacing Pt for Pd is purely axial. Consequently, the value of B_4^4 for **TbPd**, **DyPd** and **ErPd** was fixed to the value determined for their **LnPt** analogues. The small value of B_4^4 also justifies not investigating the in-plane rotation with torque magnetometry, since, with this magnitude of B_4^4, the expected torque signal in the plane is orders of magnitude weaker than the one from plane to axis.[20]

In Figure S19, we report a graphical comparison between the **LnPd** parameters determined in this work and the previously reported **LnPt** parameters.[14,20] Interestingly, the replacement of the axial metal does not seem to have the same influence on all the diagonal parameters. On one hand, absolute values of B_2^0 and B_6^0 in **LnPd** are consistently smaller compared to the **LnPt** analogues (notice that since $B_2^0 < 0$, the **LnPd** parameters are less negative than the **LnPt** ones). On the other hand, the relative magnitude of B_4^0 between **LnPd** and **LnPt** derivatives does not exhibit any clear trend.

A more quantitative information regarding the influence of the CF parameters on the splitting can be obtained by calculating the CF strength[61] of the **LnPd** and **LnPt**[14,20] complexes, that we have reported in Table S3. A particularly relevant parameter in such symmetric compounds is the total CF strength S_{tot} (obtained as the average between the second, fourth and sixth rank CF strength) because it measures the magnitude of the CF splitting. The ratio S_{tot}(**LnPd**)/S_{tot}(**LnPt**) corresponds to 0.80, 0.75, 0.95, and 0.86 for Ln = Tb, Dy, Ho, and Er, respectively. Thus, the crystal field is indeed reduced for the Pd derivatives, with the most and least reduced being **DyPd** and **HoPd**, respectively. This result agrees with the qualitative analysis of the CTM measurements.

In Figure 4, we report the energy level diagram obtained for **LnPd** and the main composition of each level (detailed information about the composition is reported in the Tables S4−S7). With these assignments, the experimentally detected INS transitions fulfill the selection rule $\Delta m_J = 0, \pm 1$. The maximum deviation between the fitted and the experimental energies is 2.1 cm^{-1}, for the hot transition of **TbPd**. A comparison with the previously reported **LnPt** complexes reveals a similar main composition of the ground state for all the compounds. Interestingly, the identity of the first and the second excited Kramers' doublet is reversed in **DyPt** and **DyPd**. **DyPd** has a main composition of the energy levels which closely resembles the one of the previously reported $[NEt_4][Dy\{Pt(SAc)_4\}_2]$ complex. The anionic part of this last salt is chemically identical to **DyPt**, but exhibits lower

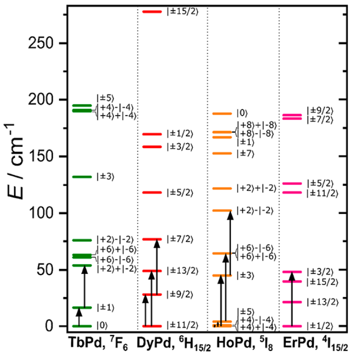

Figure 4. Energy level splitting and main composition of the ground multiplets obtained from the combined fit of CTM and INS data. Black arrows represent the experimentally observed INS transitions.

symmetry (C_4), due to a twist angle of φ = 24.11° between the two oxygen squares (refer to Figure 1c).[14]

According to our model, Pt acts as a more donating "ligand" toward the lanthanide. In order to verify this, we used nuclear magnetic resonance (NMR) with the diamagnetic Y^{3+} ion as a probe to monitor the influence of the axial transition metal. We thus synthesized **YPd** and **YPt** (see Figure S20 for the powder diffractograms). However, to overcome the poor solubility of the complexes, the low sensitivity, and long measurement times typical of ^{89}Y-NMR, we decided to use cross-polarization magic angle spinning (CP-MAS) solid-state NMR. The shift in NMR signals can indeed be directly linked to the strength of the interaction.[62]

In Figure 5 we report the experimental solid-state CP-MAS spectra of **YPd** and **YPt**, both showing a single peak at 100.5 and 114.5 ppm, respectively. The upfield shift of 14 ppm observed when going from the Pd to the Pt derivative indicates a smaller electron donation from the axial metal to Y^{3+} in the **YPd** complex compared to the **YPt** analogue, as predicted by the elucidated crystal field model.

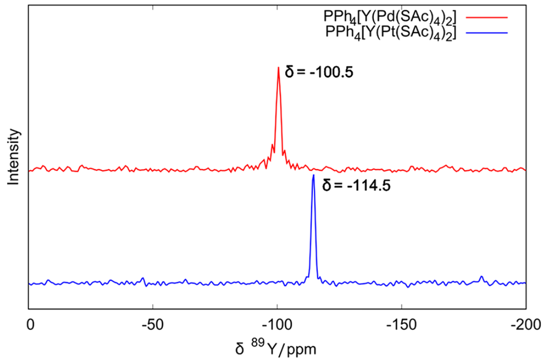

Figure 5. Experimental CP-MAS NMR spectra of **YPd** (red) and **YPt** (blue).

The experimental result is corroborated by DFT calculations on the chemical shifts (Table S8 gives the atomic coordinates used in the calculation). The chemical shifts of **YPd** and **YPt** are calculated to be in the ranges 95−98 and 115−118 ppm, respectively, depending on whether the correction for the response of the exchange correlation potential to the magnetic field (f_{XC}) was applied or not (see Table S9 for a detailed report).[63]

We can conclude that the filled d_{z^2} orbital of the transition metal acts similar to a ligand, donating electron density to the trivalent lanthanide. This effect is more pronounced in Pt than in Pd due to the larger spatial extension of the $5d_{z^2}$ orbital compared to the $4d_{z^2}$ orbital. Our conclusion agrees with a recently reported localized orbital bonding simulation performed on a La−Pd and La−Pt complexes with similar ligands.[22,25]

The set of CF parameters that we extracted allowed the excellent simulation of the static magnetic properties (χT and magnetization curves, Figures S21 and S22). For all the complexes, the χT curves approach the Curie constant at around 100 K, testifying to the relatively small splitting of the ground multiplet compared to the thermal energy at room temperature. The magnetization curves are not particularly rich in information, except for **TbPd**, where the almost linear behavior of M vs B suggests a poorly magnetic ground state (according to our model, the ground state is nonmagnetic, and the first excited state is a $|\pm 1\rangle$ doublet).

The model allows us to simulate the magnetic anisotropy phase diagram[64] for all the investigated compounds. **TbPd** is relatively uninteresting (easy plane anisotropy in the investigated T and B range). **DyPd** shows an easy cone region at low temperature and high fields (Figure S23), conversely to **DyPt**, that was predicted to change the anisotropy (easy axis to easy plane) at ca. 120 K.[14] **HoPd** and **ErPd** show a phase diagram qualitatively similar to the their Pt analogues[20] (Figures S24 and S25).

The dynamic magnetic properties of the compounds were investigated using ac susceptometry. As expected from their Pt analogues, only **DyPd** and **ErPd** showed a nonzero imaginary component of the magnetic susceptibility. It is interesting to notice that **TbPd** and **HoPd** (as well as their Pt analogues) do not exhibit slow relaxation of the magnetization in the investigated frequency range, while two distinct relaxation pathways were recently detected in low-symmetry dimeric complexes containing the Tb−Pt[24] and the Ho−Pt[25] interaction. In order to exclude that the magnetization dynamics were influenced by intermolecular interactions, we have performed a dilution experiment on **HoPd** and **TbPd** by synthetizing the $\mathbf{Ho_{0.1}Y_{0.9}Pd}$ and $\mathbf{Tb_{0.1}Y_{0.9}Pd}$ derivatives. As reported in Figure S26, neither of them showed an out of phase signal. This testifies that magnetic interactions on these systems do not quench the magnetic relaxation, and further corroborates our model of the electronic structure.

The slow relaxation of **ErPd** is very convoluted. A field scan at the lowest temperature (T = 1.8 K) reveals no slow relaxation in zero field and two active relaxation pathways when a field is applied (Figure S27). A similar behavior was observed by us[20] in **ErPt** and by others[25] in a dimer containing the Er−Pt bond. The relaxation time associated with each process was extracted using a sum of two Cole−Cole functions[65] and is reported in Figure S28. We then measured the in-phase and out-of-phase magnetic susceptibility at B = 0.5 T (slow process active) and B = 0.06 T (fast process active). The slow relaxation pathway (Figure S29) rapidly becomes less favorable when the temperature is increased, and it exhibits a constant relaxation time (τ_{tun} = 0.3 s), indicating a quantum tunneling regime. The fast process (Figure S30) has instead a well-defined temperature dependence that was fitted using a combination of direct and Raman processes (Figure S31).

In contrast to **ErPd**, the relaxation of **DyPd** follows the well-understood combination of quantum tunneling and Orbach processes. In zero applied dc field, **DyPd** shows a peak at around 10 Hz that rapidly moves toward lower frequencies when a dc field is applied (Figure S32). We thus performed temperature-dependent measurements in a broad frequency range ($\nu = 10^{-1}$−10^4 Hz) at zero field and in an optimum field of 0.1 T. The extracted relaxation times (T_1) for the zero-field scan (real and imaginary component of the susceptibility in Figure S33) are plotted as red symbols in Figure 6. As often seen in Dy(III) complexes,[66] the data could be fitted with a combination of thermally activated Orbach process and quantum tunneling using the formula:

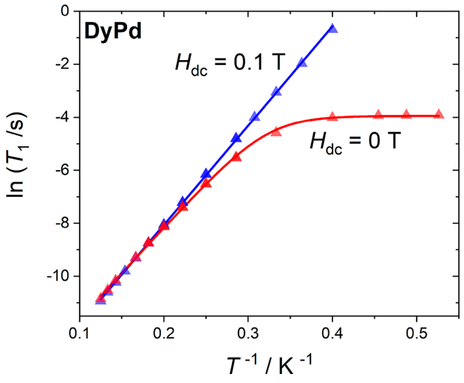

Figure 6. Longitudinal relaxation time extracted from the fit of the ac susceptibility in zero applied field (red triangles) and 0.1 T applied field (blue triangles). The lines are the best fit; see text.

$$T_1^{-1} = \tau_{\text{tun}}^{-1} + \tau_0^{-1} e^{-\Delta/k_B T} \tag{2}$$

In eq 2, τ_{tun} is tunneling time, τ_0 is the pre-exponential factor and Δ is the effective barrier for the thermally activated process. The transition between a tunneling regime and a thermally activated one is clearly marked by a decrease in the relaxation time distribution parameter (α) by one order of magnitude (α = 0.360 at T = 1.9 K vs α = 0.025 at T = 8 K, see Figure S34). The parameters obtained from the fitting are τ_{tun} = 1.93(5) 10^{-2} s, τ_0 = 2.9(2) 10^{-7} s, and Δ = 23.8(1) cm^{-1}. We notice a remarkably good match between the relaxation barrier and the energy of the first excited doublet determined using INS (27.4 cm^{-1}), as previously observed for **DyPt**.[14]

Interestingly, the tunneling relaxation rate that we obtain from the fit ($\tau_{\text{tun}}^{-1} \sim 52$ s^{-1}) is smaller than the one extracted from **DyPt** (63 s^{-1}), that is, the tunneling is suppressed in **DyPd** compared to **DyPt**.[14] This can be explained plotting the energy level scheme obtained varying linearly the CF parameters obtained for **DyPd** into the ones reported for **DyPt**[14] (Figure S35). As already pointed out, the overall effect of the ligand field is an increase of the CF strength for **DyPt** compared to **DyPd**; however, there is a concomitant clustering of all the levels except the highest one ($|\pm 15/2\rangle$). This creates a 4-fold decrease in mixing between the $|\pm 11/2\rangle$ ground state and the excited $|\pm 3/2\rangle$ doublet in **DyPd** (0.3%) compared to **DyPt** (1.2%). In other words, the ground state is less pure in **DyPt** than in **DyPd** (see Figure S36). In Figure S37 we fixed

$B_4{}^4$ to the value obtained for both compounds and two of the three diagonal parameters to an average value between **DyPd** and **DyPt**, while varying the last CF parameter. In this way, we can identify the CF parameter majorly responsible for this state ordering. The $B_2{}^0$ parameter shows the largest relative difference and, as it turns out, has the largest impact on the energies of the states involved in determining the purity of the ground state. Although the $B_6{}^0$ parameter also varies greatly, its influence on the ground state is less significant due to the concomitant mixing of the $|\pm 3/2\rangle$ and $|\pm 5/2\rangle$.

When a static dc field is applied, the tunneling path of the slow relaxation gets disfavored (blue triangles in Figure 6) and the data can be fitted using a single Orbach process (see Figure S38). Moreover, the α values decrease significantly at low temperature compared to the zero-field case (Figure S33). We obtain a similar barrier ($\Delta = 26(1)$ cm^{-1}) and pre-exponential factor ($\tau_0 = 1.76(5) \times 10^{-7}$ s) compared to the zero-field data, thus adding credibility to our model.

■ CONCLUSIONS

We have demonstrated that the series of perfectly tetragonal lanthanide complexes can be extended to cover the heavy lanthanide derivatives as well as Y^{3+} with square-planar coordinated Pd^{2+} as structure-directing element. Notably, the tuning is done on the symmetry axis and hence addresses directly the special nature of the axial position in the crystal field models. By a multitechnique approach encompassing torque-magnetometry, powder-averaged magnetometry, and INS spectroscopy, detailed and consistent modeling of the electronic structure for the Tb-, Dy-, Ho-, and Er-based systems could be obtained. In comparison with the previously studied Pt^{2+} complexes, the total ligand field strength was found to be reduced in the palladium systems by 5−20%, despite identical positions of the oxygen donors for the pairs of Pd and Pt derivatives. Interestingly, the ligand field compression, when going from Pt to Pd, is present in all derivatives, irrespectively to the nature of the electron density of the lanthanide. This clearly defines that the axially positioned anchor in the metalloligands acts as donor for the lanthanide ions implying that the filled d_{z^2} orbital of the transition metal can be seen as an effective ligand, donating electron density to the trivalent lanthanide. This effect is more pronounced in Pt than in Pd, as previously reported in other complexes exhibiting the Ln−Pt and Ln−Pd interactions,[22−25] as expected from the larger spatial extension of the $5d_{z^2}$ orbital compared to the $4d_{z^2}$ orbital. These findings are further supported by the direct observation of a pronounced difference of nuclear shielding in the solid state ^{89}Y-NMR spectra of the Pd and Pt derivatives.

The decreased axial ligand field component in the palladium systems would naïvely suggest poorer single molecule magnet properties as compared to the platinum analogues. However, since the smaller overall ligand field in the palladium derivatives leads to less clustering of levels close to the intermediate m_J ground state and a concomitant enhanced purity of the ground doublet, quantum tunneling is suppressed relative to the platinum derivative, and longer relaxation times are measured at temperatures lower than 2.5 K.

■ ASSOCIATED CONTENT

Supporting Information

The Supporting Information is available free of charge at https://pubs.acs.org/doi/10.1021/acs.inorgchem.9b02064.

Torque experimental setup, torque measurements and fits, inelastic neutron scattering measurements and fits, crystal field parameters in Stevens' notation and associated errors, crystal field strength, energy and composition of the eigenfunctions, magnetic anisotropy phase diagrams, powder diffractograms, chemical shifts calculations, static and dynamic magnetic properties, and associated fits (PDF)

Accession Codes

CCDC 1939733−1939736 contain the supplementary crystallographic data for this paper. These data can be obtained free of charge via www.ccdc.cam.ac.uk/data_request/cif, or by emailing data_request@ccdc.cam.ac.uk, or by contacting The Cambridge Crystallographic Data Centre, 12 Union Road, Cambridge CB2 1EZ, UK; fax: +44 1223 336033.

■ AUTHOR INFORMATION

Corresponding Authors

*(M.P.) E-mail: mauro.perfetti@chem.ku.dk.
*(J.B.) E-mail: bendix@kiku.dk.

ORCID

Ulla G. Nielsen: 0000-0002-2336-3061
Jesper Bendix: 0000-0003-1255-2868
Mauro Perfetti: 0000-0001-5649-0449

Present Address

§School of Chemistry, University of Manchester, Oxford Road, M13 9PL, Manchester, U.K.

Author Contributions

The manuscript was written by M.P., N.A.B., J.B.P., and J.B., with feedback from all the authors. All authors have given approval to the final version of the manuscript.

Notes

The authors declare no competing financial interest.

■ ACKNOWLEDGMENTS

Prof. R. Sessoli is acknowledged for allowing access to the torque magnetometer. Prof. L. Sorace and Prof. R. Sessoli are kindly acknowledged for scientific discussion. The 600 MHz NMR instrument was funded by the Villum Foundation via The Villum Center for Bioanalytical Services. The Danish Agency for Science, Technology and Innovation, through DANSCATT, and the Independent Research Fund Denmark Project 8021-00410B are also acknowledged for funding.

■ REFERENCES

(1) Bottrill, M.; Kwok, L.; Long, N. J. Lanthanides in magnetic resonance imaging. *Chem. Soc. Rev.* **2006**, *35*, 557−571.

(2) Chistoserdova, L. New pieces to the lanthanide puzzle. *Mol. Microbiol.* **2019**, *111* (5), 1127−1131.

(3) Bünzli, J. C. G. Rising stars in science and technology: luminescent lanthanide materials. *Eur. J. Inorg. Chem.* **2017**, *2017* (44), 5058−5063.

(4) Kilbourn, B. T. Metallurgical applications of yttrium and the lanthanides. *JOM* **1988**, *40* (5), 22−25.

(5) McAdams, S. G.; Ariciu, A.-M.; Kostopoulos, A. K.; Walsh, J. P.; Tuna, F. Molecular single-ion magnets based on lanthanides and actinides: Design considerations and new advances in the context of quantum technologies. *Coord. Chem. Rev.* **2017**, *346*, 216−239.

(6) Rinehart, J. D.; Long, J. R. Exploiting single-ion anisotropy in the design of f-element single-molecule magnets. *Chem. Sci.* **2011**, *2* (11), 2078−2085.

(7) Chilton, N. F. Design criteria for high-temperature single-molecule magnets. *Inorg. Chem.* **2015**, *54* (5), 2097−2099.

(8) Briganti, M.; Garcia, G. F.; Jung, J.; Sessoli, R.; Le Guennic, B.; Totti, F. Covalency and magnetic anisotropy in Lanthanide Single Molecule Magnets: the DyDOTA Archetype. *Chem. Sci.* **2019**, *10*, 7233.

(9) Boulon, M. E.; Cucinotta, G.; Luzon, J.; Degl'Innocenti, C.; Perfetti, M.; Bernot, K.; Calvez, G.; Caneschi, A.; Sessoli, R. Magnetic Anisotropy and Spin-Parity Effect Along the Series of Lanthanide Complexes with DOTA. *Angew. Chem.* **2013**, *125* (1), 368−372.

(10) Cucinotta, G.; Perfetti, M.; Luzon, J.; Etienne, M.; Car, P. E.; Caneschi, A.; Calvez, G.; Bernot, K.; Sessoli, R. Magnetic Anisotropy in a Dysprosium/DOTA Single-Molecule Magnet: Beyond Simple Magneto-Structural Correlations. *Angew. Chem., Int. Ed.* **2012**, *51* (7), 1606−1610.

(11) Ding, Y. S.; Chilton, N. F.; Winpenny, R. E.; Zheng, Y. Z. On Approaching the Limit of Molecular Magnetic Anisotropy: A Near-Perfect Pentagonal Bipyramidal Dysprosium (III) Single-Molecule Magnet. *Angew. Chem.* **2016**, *128* (52), 16305−16308.

(12) Gregson, M.; Chilton, N. F.; Ariciu, A.-M.; Tuna, F.; Crowe, I. F.; Lewis, W.; Blake, A. J.; Collison, D.; McInnes, E. J.; Winpenny, R. E.; et al. A monometallic lanthanide bis (methanediide) single molecule magnet with a large energy barrier and complex spin relaxation behaviour. *Chem. Sci.* **2016**, *7* (1), 155−165.

(13) Chen, Y.-C.; Liu, J.-L.; Ungur, L.; Liu, J.; Li, Q.-W.; Wang, L.-F.; Ni, Z.-P.; Chibotaru, L. F.; Chen, X.-M.; Tong, M.-L. Symmetry-supported magnetic blocking at 20 K in pentagonal bipyramidal Dy (III) single-ion magnets. *J. Am. Chem. Soc.* **2016**, *138* (8), 2829−2837.

(14) Sørensen, M. A.; Hansen, U. B.; Perfetti, M.; Pedersen, K. S.; Bartolomé, E.; Simeoni, G. G.; Mutka, H.; Rols, S.; Jeong, M.; Zivkovic, I.; Retuerto, M.; Arauzo, A.; Bartolomé, J.; Piligkos, S.; Weihe, H.; Doerrer, L. H.; van Slageren, J.; Rønnow, H. M.; Lefmann, K.; Bendix, J. Chemical tunnel-splitting-engineering in a dysprosium-based molecular nanomagnet. *Nat. Commun.* **2018**, *9* (1), 1292.

(15) Li, J.; Yuan, C.; Yang, L.; Kong, M.; Zhang, J.; Ge, J.-Y.; Zhang, Y.-Q.; Song, Y. Magnetic Anisotropy along a Series of Lanthanide Polyoxometalates with Pentagonal Bipyramidal Symmetry. *Inorg. Chem.* **2017**, *56* (14), 7835−7841.

(16) Cardona-Serra, S.; Clemente-Juan, J.; Coronado, E.; Gaita-Ariño, A.; Camón, A.; Evangelisti, M.; Luis, F.; Martínez-Pérez, M.; Sesé, J. Lanthanoid Single-Ion Magnets Based on Polyoxometalates with a 5-fold Symmetry: The Series [LnP5W30O110] 12−(Ln3+= Tb, Dy, Ho, Er, Tm, and Yb). *J. Am. Chem. Soc.* **2012**, *134* (36), 14982−14990.

(17) Kanesato, M.; Yokoyama, T. Synthesis and structural characterization of Ln (III) complexes (Ln= Eu, Gd, Tb, Er, Tm, Lu) of tripodal tris [2-(salicylideneamino) ethyl] amine. *Chem. Lett.* **1999**, *28* (2), 137−138.

(18) Kanesato, M.; Yokoyama, T.; Itabashi, O.; Suzuki, T. M.; Shiro, M. Synthesis and Structural Characterization of Praseodymium (III) and Neodymium (III) Complexes of Tripodal Tris (2-(salicylideneamino) ethyl) amine. *Bull. Chem. Soc. Jpn.* **1996**, *69* (5), 1297−1302.

(19) Sørensen, M. A.; Weihe, H.; Vinum, M. G.; Mortensen, J. S.; Doerrer, L. H.; Bendix, J. Imposing high-symmetry and tuneable geometry on lanthanide centres with chelating Pt and Pd metalloligands. *Chem. Sci.* **2017**, *8* (5), 3566−3575.

(20) Perfetti, M.; Sørensen, M. A.; Hansen, U. B.; Bamberger, H.; Lenz, S.; Hallmen, P. P.; Fennell, T.; Simeoni, G. G.; Arauzo, A.; Bartolomé, J.; Bartolomé, E.; Lefmann, K.; Weihe, H.; van Slageren, J.; Bendix, J. Magnetic Anisotropy Switch: Easy Axis to Easy Plane Conversion and Vice Versa. *Adv. Funct. Mater.* **2018**, *28* (32), 1801846.

(21) Perfetti, M.; Gysler, M.; Rechkemmer-Patalen, Y.; Zhang, P.; Taştan, H.; Fischer, F.; Netz, J.; Frey, W.; Zimmermann, L. W.; Schleid, T.; et al. Determination of the electronic structure of a dinuclear dysprosium single molecule magnet without symmetry idealization. *Chem. Sci.* **2019**, *10* (7), 2101−2110.

(22) Izuogu, D. C.; Yoshida, T.; Zhang, H.; Cosquer, G.; Katoh, K.; Ogata, S.; Hasegawa, M.; Nojiri, H.; Damjanović, M.; Wernsdorfer, W.; Uruga, T.; Ina, T.; Breedlove, B. K.; Yamashita, M. Slow Magnetic Relaxation in a Palladium−Gadolinium Complex Induced by Electron Density Donation from the Palladium Ion. *Chem. - Eur. J.* **2018**, *24* (37), 9285−9294.

(23) Yoshida, T.; Cosquer, G.; Izuogu, D. C.; Ohtsu, H.; Kawano, M.; Lan, Y.; Wernsdorfer, W.; Nojiri, H.; Breedlove, B. K.; Yamashita, M. Field-Induced Slow Magnetic Relaxation of GdIII Complex with a Pt− Gd Heterometallic Bond. *Chem. - Eur. J.* **2017**, *23* (19), 4551−4556.

(24) Yoshida, T.; Izuogu, D. C.; Iwasawa, D.; Ogata, S.; Hasegawa, M.; Breedlove, B. K.; Cosquer, G.; Wernsdorfer, W.; Yamashita, M. Multiple Magnetic Relaxation Pathways and Dual-Emission Modulated by a Heterometallic Tb-Pt Bonding Environment. *Chem. - Eur. J.* **2017**, *23* (44), 10527−10531.

(25) Yoshida, T.; Izuogu, D. C.; Zhang, H.-T.; Cosquer, G.; Abe, H.; Wernsdorfer, W.; Breedlove, B. K.; Yamashita, M. Ln−Pt electron polarization effects on the magnetic relaxation of heterometallic Ho− and Er−Pt complexes. *Dalton Trans.* **2019**, *48* (21), 7144−7149.

(26) Richard, D.; Ferrand, M.; Kearley, G. Analysis and visualisation of neutron-scattering data. *J. Neutron Res.* **1996**, *4* (1−4), 33−39.

(27) Arnold, O.; Bilheux, J.-C.; Borreguero, J.; Buts, A.; Campbell, S. I.; Chapon, L.; Doucet, M.; Draper, N.; Ferraz Leal, R.; Gigg, M.; et al. Mantid—Data analysis and visualization package for neutron scattering and μ SR experiments. *Nucl. Instrum. Methods Phys. Res., Sect. A* **2014**, *764*, 156−166.

(28) Sørensen, M. A.; Bendix, J.; Bonde, N. A.; Christensen, J. O.; Ollivier, J.; Perfetti, M.; Weihe, H. Quantifying antiferromagnetic exchange interactions mediated by metallophilic contacts; Institut Laue-Langevin (ILL): Grenoble: 2018, DOI: 10.5291/ILL-DATA.4-06-7.

(29) Bendix, J.; Bonde, N. A.; Perfetti, M.; Ollivier, J. High Resolution on the Ho SMM; Institut Laue-Langevin (ILL): Grenoble, 2018; DOI: 10.5291/ILL-DATA.TEST-2872.

(30) Bonde, N. A.; Fåk, B.; Ollivier, J.; Rols, S.; Zenotti, J. M. High energy CEF bands on SMM; Institut Laue-Langevin (ILL): Grenoble, 2018; DOI: 10.5291/ILL-DATA.TEST-2897.

(31) Perfetti, M. Cantilever torque magnetometry on coordination compounds: from theory to experiments. *Coord. Chem. Rev.* **2017**, *348*, 171−186.

(32) Merwin, L.; Sebald, A. The first 89Y CP-MAS spectra. *J. Magn. Reson.* **1990**, *88* (1), 167−171.

(33) Te Velde, G. t.; Bickelhaupt, F. M.; Baerends, E. J.; Fonseca Guerra, C.; van Gisbergen, S. J.; Snijders, J. G.; Ziegler, T. Chemistry with ADF. *J. Comput. Chem.* **2001**, *22* (9), 931−967.

(34) Schreckenbach, G.; Ziegler, T. Calculation of NMR shielding tensors using gauge-including atomic orbitals and modern density functional theory. *J. Phys. Chem.* **1995**, *99* (2), 606−611.

(35) Perdew, J. P.; Ernzerhof, M.; Burke, K. Rationale for mixing exact exchange with density functional approximations. *J. Chem. Phys.* **1996**, *105* (22), 9982−9985.

(36) Becke, A. D. Density-functional exchange-energy approximation with correct asymptotic behavior. *Phys. Rev. A: At., Mol., Opt. Phys.* **1988**, *38* (6), 3098.

(37) Perdew, J. P. Density-functional approximation for the correlation energy of the inhomogeneous electron gas. *Phys. Rev. B: Condens. Matter Mater. Phys.* **1986**, *33* (12), 8822.

(38) van Lenthe, E.; Baerends, E.-J.; Snijders, J. G. Relativistic total energy using regular approximations. *J. Chem. Phys.* **1994**, *101* (11), 9783−9792.

(39) Van Lenthe, E.; Baerends, E. J. Optimized Slater-type basis sets for the elements 1−118. *J. Comput. Chem.* **2003**, *24* (9), 1142−1156.

(40) Neese, F. The ORCA program system. *Reviews: Computational Molecular Science* **2012**, *2* (1), 73−78.

(41) Adamo, C.; Barone, V. Toward reliable density functional methods without adjustable parameters: The PBE0 model. *J. Chem. Phys.* **1999**, *110* (13), 6158−6170.

(42) Weigend, F.; Ahlrichs, R. Balanced basis sets of split valence, triple zeta valence and quadruple zeta valence quality for H to Rn: Design and assessment of accuracy. *Phys. Chem. Chem. Phys.* **2005**, *7* (18), 3297−3305.

(43) Zheng, J.; Xu, X.; Truhlar, D. G. Minimally augmented Karlsruhe basis sets. *Theor. Chem. Acc.* **2011**, *128* (3), 295−305.

(44) Barone, V.; Cossi, M. Quantum calculation of molecular energies and energy gradients in solution by a conductor solvent model. *J. Phys. Chem. A* **1998**, *102* (11), 1995−2001.

(45) Stoll, S.; Schweiger, A. EasySpin, a comprehensive software package for spectral simulation and analysis in EPR. *J. Magn. Reson.* **2006**, *178* (1), 42−55.

(46) Cole, K. S.; Cole, R. H. Dispersion and absorption in dielectrics I. Alternating current characteristics. *J. Chem. Phys.* **1941**, *9* (4), 341−351.

(47) Rudowicz, C.; Karbowiak, M. Disentangling intricate web of interrelated notions at the interface between the physical (crystal field) Hamiltonians and the effective (spin) Hamiltonians. *Coord. Chem. Rev.* **2015**, *287*, 28−63.

(48) Stevens, K. W. H. Matrix Elements and Operator Equivalents Connected with the Magnetic Properties of Rare Earth Ions. *Proc. Phys. Soc., London, Sect. A* **1952**, *65* (3), 209.

(49) AlDamen, M. A.; Cardona-Serra, S.; Clemente-Juan, J. M.; Coronado, E.; Gaita-Arino, A.; Marti-Gastaldo, C.; Luis, F.; Montero, O. Mononuclear Lanthanide Single Molecule Magnets Based on the Polyoxometalates [Ln(W5O18)(2)](9-) and [Ln(beta(2)-SiW11O39)(2)](13-) (Ln(III) = Tb, Dy, Ho, Er, Tm, and Yb). *Inorg. Chem.* **2009**, *48* (8), 3467−3479.

(50) Ishikawa, N.; Sugita, M.; Okubo, T.; Tanaka, N.; Iino, T.; Kaizu, Y. Determination of Ligand-Field Parameters and F-Electronic Structures of Double-Decker Bis(Phthalocyaninato)Lanthanide Complexes. *Inorg. Chem.* **2003**, *42* (7), 2440−2446.

(51) Perfetti, M.; Bendix, J. Descriptors of magnetic anisotropy revisited. *Chem. Commun.* **2018**, *54* (86), 12163−12166.

(52) Perfetti, M.; Lucaccini, E.; Sorace, L.; Costes, J. P.; Sessoli, R. Determination of Magnetic Anisotropy in the LnTRENSAL Complexes (Ln= Tb, Dy, Er) by Torque Magnetometry. *Inorg. Chem.* **2015**, *54* (7), 3090−3092.

(53) Pedersen, K. S.; Ungur, L.; Sigrist, M.; Sundt, A.; Schau-Magnussen, M.; Vieru, V.; Mutka, H.; Rols, S.; Weihe, H.; Waldmann, O.; et al. Modifying the properties of 4f single-ion magnets by peripheral ligand functionalisation. *Chem. Sci.* **2014**, *5* (4), 1650−1660.

(54) Marx, R.; Moro, F.; Dörfel, M.; Ungur, L.; Waters, M.; Jiang, S.-D.; Orlita, M.; Taylor, J.; Frey, W.; Chibotaru, L.; et al. Spectroscopic determination of crystal field splittings in lanthanide double deckers. *Chem. Sci.* **2014**, *5* (8), 3287−3293.

(55) Vonci, M.; Giansiracusa, M. J.; Van den Heuvel, W.; Gable, R. W.; Moubaraki, B.; Murray, K. S.; Yu, D.; Mole, R. A.; Soncini, A.; Boskovic, C. Magnetic Excitations in Polyoxotungstate-Supported Lanthanoid Single-Molecule Magnets: An Inelastic Neutron Scattering and ab Initio Study. *Inorg. Chem.* **2017**, *56* (1), 378−394.

(56) Giansiracusa, M. J.; Moreno-Pineda, E.; Hussain, R.; Marx, R.; Martínez Prada, M.; Neugebauer, P.; Al-Badran, S.; Collison, D.; Tuna, F.; van Slageren, J.; Chilton, N. F.; et al. Measurement of magnetic exchange in asymmetric lanthanide dimetallics: towards a transferable theoretical framework. *J. Am. Chem. Soc.* **2018**, *140* (7), 2504−2513.

(57) Giansiracusa, M. J.; Vonci, M.; Van den Heuvel, W.; Gable, R. W.; Moubaraki, B.; Murray, K. S.; Yu, D.; Mole, R. A.; Soncini, A.; Boskovic, C. Carbonate-Bridged Lanthanoid Triangles: Single-Molecule Magnet Behavior, Inelastic Neutron Scattering, and Ab Initio Studies. *Inorg. Chem.* **2016**, *55* (11), 5201−5214.

(58) Dunstan, M.; Mole, R.; Boskovic, C. Inelastic Neutron Scattering of Lanthanoid Complexes and Single-Molecule Magnets. *Eur. J. Inorg. Chem.* **2019**, *2019* (8), 1090−1105.

(59) It would be tempting to assign the two excitations at ca. 120 cm-1 and 180 cm-1 to cold magnetic excitations, however the levels composition predicted by the model and the Q dependence of the S(Q,E) plot do not support that assignment.

(60) Wybourne, B. G. *Spectroscopic properties of rare earths*; Interscience Publishers: New York, 1965.

(61) Flanagan, B. M.; Bernhardt, P. V.; Krausz, E. R.; Lüthi, S. R.; Riley, M. J. A Ligand-Field Analysis of the trensal (H3trensal= 2, 2', 2"-Tris (salicylideneimino) triethylamine) Ligand. An Application of the Angular Overlap Model to Lanthanides. *Inorg. Chem.* **2002**, *41* (20), 5024−5033.

(62) Baddour, F. G.; Hyre, A. S.; Guillet, J. L.; Pascual, D.; Lopez-de-Luzuriaga, J. M.; Alam, T. M.; Bacon, J. W.; Doerrer, L. H. Pt−Mg, Pt−Ca, and Pt−Zn Lantern Complexes and Metal-Only Donor−Acceptor Interactions. *Inorg. Chem.* **2017**, *56* (1), 452−469.

(63) Autschbach, J. The role of the exchange-correlation response kernel and scaling corrections in relativistic density functional nuclear magnetic shielding calculations with the zeroth-order regular approximation. *Mol. Phys.* **2013**, *111* (16−17), 2544−2554.

(64) Perfetti, M.; Bendix, J. The Multiple Faces, and Phases of Magnetic Anisotropy. *Inorg. Chem.* **2019**, *58*, 11875.

(65) Car, P. E.; Perfetti, M.; Mannini, M.; Favre, A.; Caneschi, A.; Sessoli, R. Giant field dependence of the low temperature relaxation of the magnetization in a dysprosium(III)-DOTA complex. *Chem. Commun.* **2011**, *47* (13), 3751−3753.

(66) Cosquer, G.; Pointillart, F.; Golhen, S.; Cador, O.; Ouahab, L. Slow magnetic relaxation in condensed versus dispersed dysprosium (III) mononuclear complexes. *Chem. - Eur. J.* **2013**, *19* (24), 7895−7903.

Supporting Information

Importance of axial symmetry in elucidating lanthanide-transition metal interactions.

Niels A. Bonde,[†][‖] *Jonatan B. Petersen,* [†][§] *Mikkel A. Sørensen,* [†] *Ulla G. Nielsen,* [‡] *Björn Fåk,* [‖] *Stéphane Rols,* [‖] *Jacques Ollivier,* [‖] *Høgni Weihe,* [†] *Jesper Bendix,* [†]* *and Mauro Perfetti*[†]*

[†] Department of Chemistry, University of Copenhagen, Universitetsparken 5, DK-2100 Copenhagen, Denmark.

[‖] Institut Laue-Langevin, 71 avenue des Martyrs, CS 20156, 38042 Grenoble Cedex 9, France

[‡] Department of Physics, Chemistry and Pharmacy, University of Southern Denmark, Campusvej 55, 5230 Odense M, Denmark

Contents

1. Cantilever torque magnetometry

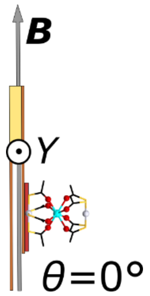

Figure S1. Experimental setup at the beginning (θ = 0°) of each counterclockwise rotation along the **Y** axis.

When an anisotropic single crystal is fixed on top of the upper flexible plate of a capacitor, the resultant magnetic torque can elastically deflect the plate producing a difference in capacitance that can be easily detected using sensitive capacitance bridges. The basic feature of the technique is thus to profit from the magnetic torque ($\boldsymbol{\tau} = \mathbf{M} \times \mathbf{B}$) acting on an anisotropic sample inserted inside a homogenous magnetic field. More details about the technique can be found elsewhere.[1]

Table S1. Mass of the measured crystals, scaling factor used for the CTM data (due to the uncertainty on the measured mass) and director cosines of the rotation axis (**Y**) and of the magnetic field (**B**) in the *abc* crystallographic reference frame at θ = 0°.

	Mass [µg]	**Scaling factor**	**Y**			**B**		
			a	*b*	*c*	*a*	*b*	*c*
TbPd	82	0.98	-0.707	0.707	0	-0.707	-0.707	0
DyPd	51	1.00	-0.707	0.707	0	-0.707	-0.707	0
HoPd	105	0.99	-0.707	0.707	0	-0.707	-0.707	0
ErPd	75	1.03	-0.707	0.707	0	-0.707	-0.707	0

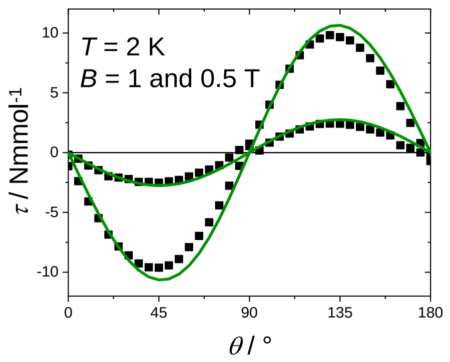
T = 2 K
B = 1 and 0.5 T
τ / Nmmol-1
10
5
0
-5
-10
0
45
90
135
180
θ / °

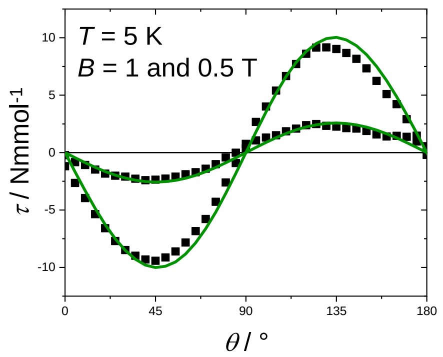
T = 5 K
B = 1 and 0.5 T
τ / Nmmol-1
10
5
0
-5
-10
0
45
90
135
180
θ / °

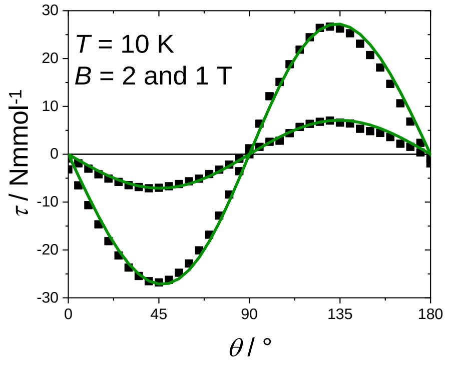
T = 10 K
B = 2 and 1 T
τ / Nmmol-1
30
20
10
0
-10
-20
-30
0
45
90
135
180
θ / °

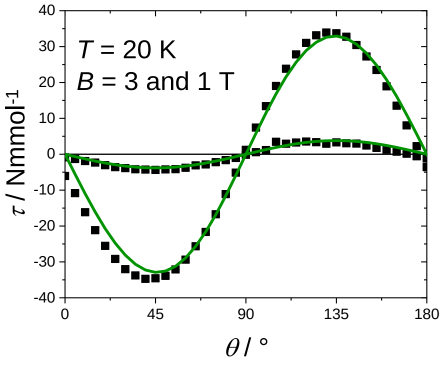
T = 20 K
B = 3 and 1 T
τ / Nmmol-1
40
30
20
10
0
-10
-20
-30
-40
0
45
90
135
180
θ / °

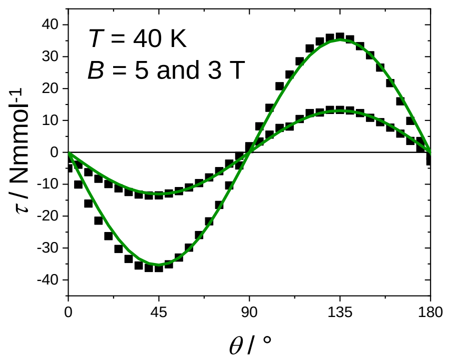
T = 40 K
B = 5 and 3 T
τ / Nmmol-1
40
30
20
10
0
-10
-20
-30
-40
0
45
90
135
180
θ / °

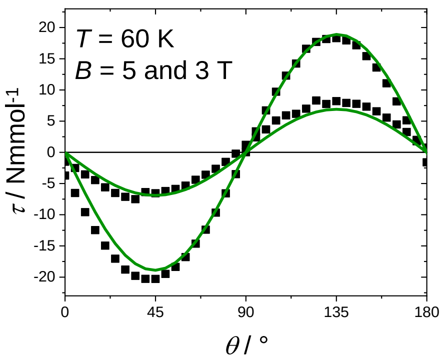
T = 60 K
B = 5 and 3 T
τ / Nmmol-1
20
15
10
5
0
-5
-10
-15
-20
0
45
90
135
180
θ / °

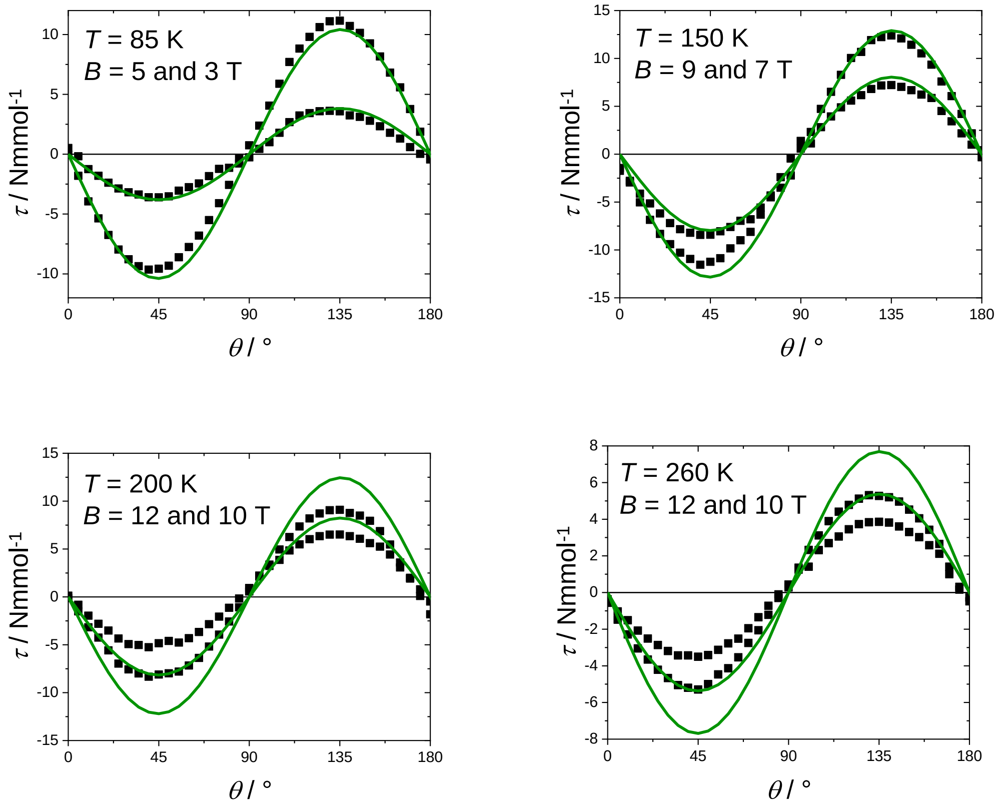

Figure S2. Torque signal recorded on a **TbPd** single crystal in the temperature interval 2-260 K. Black squares are the experimental points while the green lines are the best fit (see text). In each graph the highest field corresponds to the most intense torque signal.

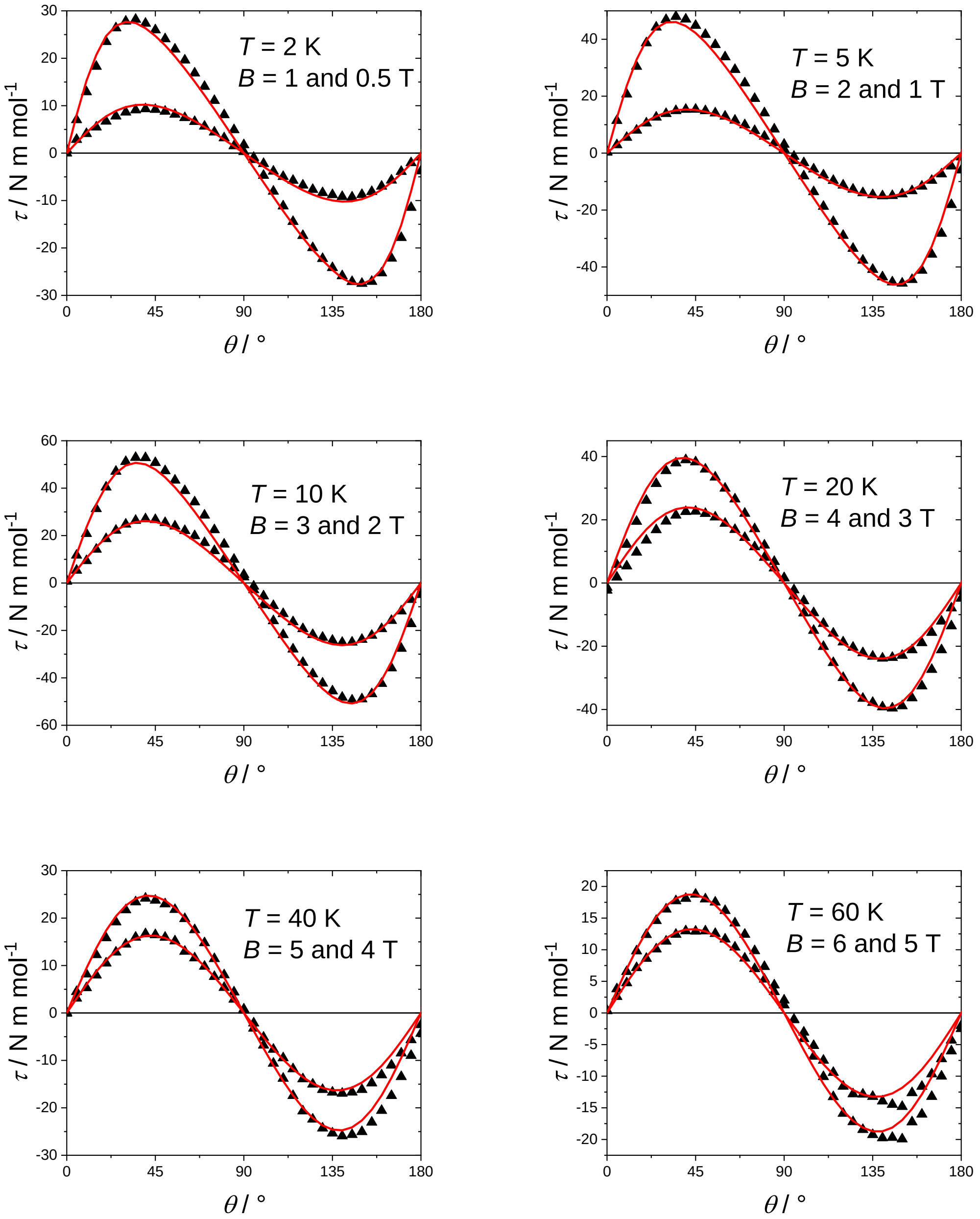
T = 2 K
B = 1 and 0.5 T
T = 5 K
B = 2 and 1 T
T = 10 K
B = 3 and 2 T
T = 20 K
B = 4 and 3 T
T = 40 K
B = 5 and 4 T
T = 60 K
B = 6 and 5 T
τ / N m mol-1
θ / °
0
45
90
135
180
30
20
10
0
-10
-20
-30
40
-40
60
-60
15
5
-5
-15

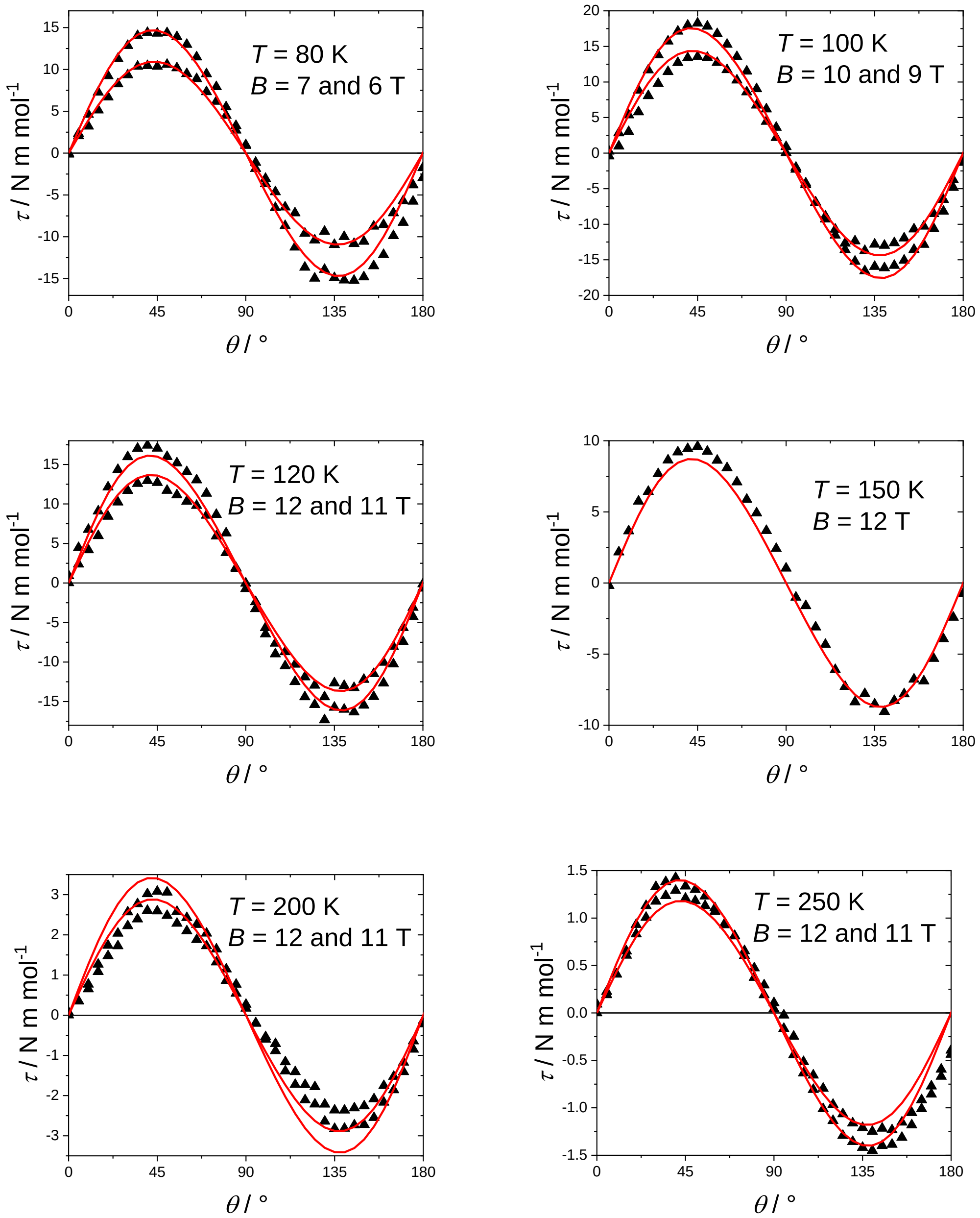

Figure S3. Torque signal recorded on a **DyPd** single crystal in the temperature interval 2-250 K. Black triangles are the experimental points while the red lines are the best fit (see text). In each graph the highest field corresponds to the most intense torque signal.

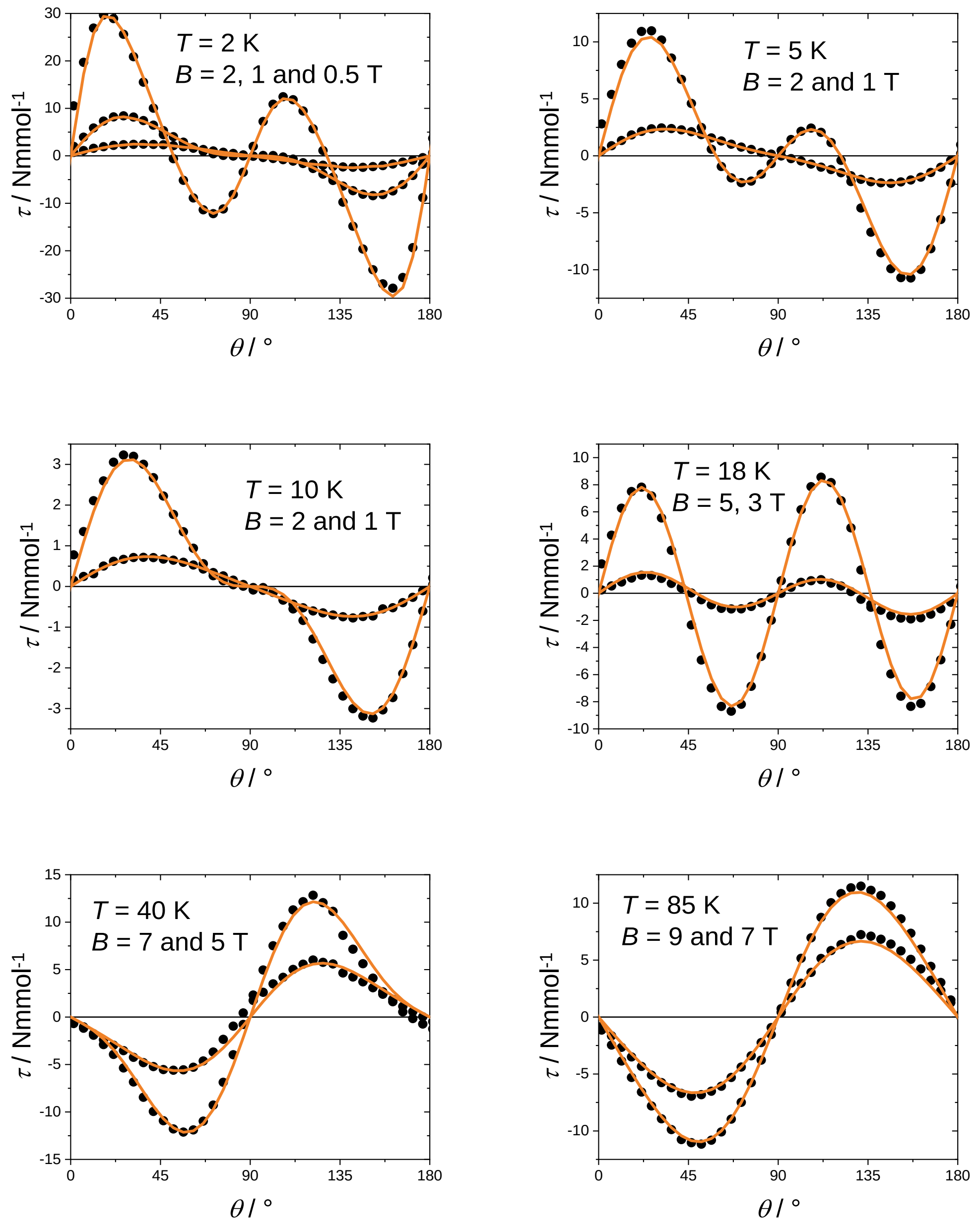
T = 2 K
B = 2, 1 and 0.5 T
T = 5 K
B = 2 and 1 T
T = 10 K
B = 2 and 1 T
T = 18 K
B = 5, 3 T
T = 40 K
B = 7 and 5 T
T = 85 K
B = 9 and 7 T
τ / Nmmol-1
θ / °
0
45
90
135
180
30
20
10
0
-10
-20
-30
5
-5
3
2
1
-1
-2
-3
8
6
4
-4
-6
-8
15
-15

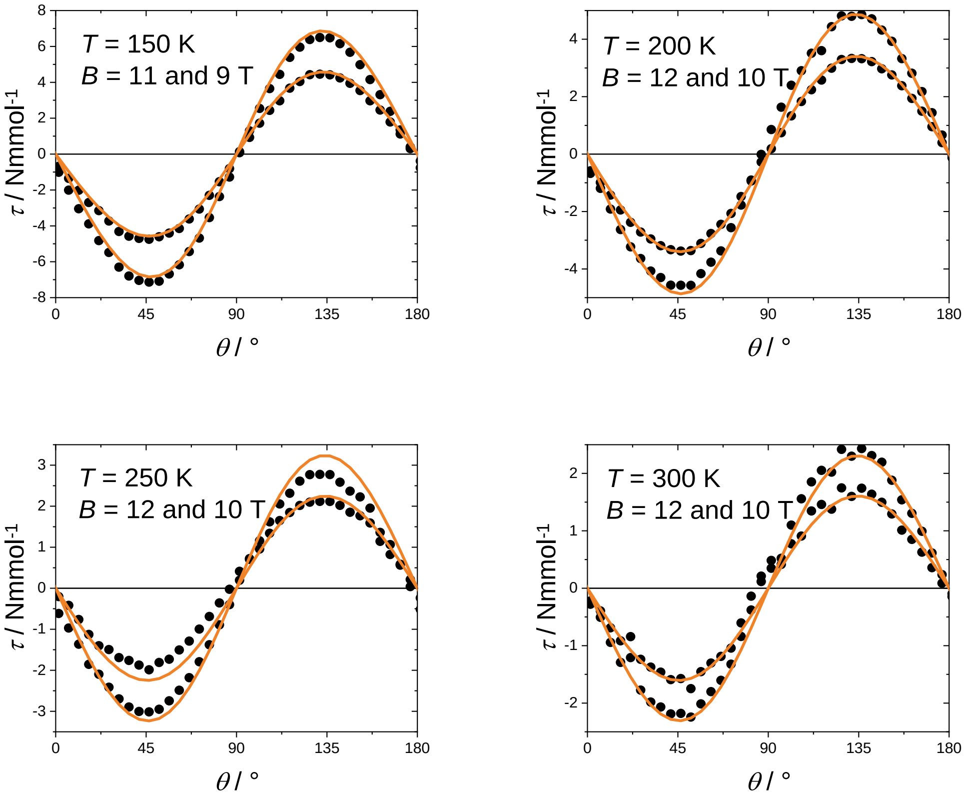

Figure S4. Torque signal recorded on a **HoPd** single crystal in the temperature interval 2-300 K. Black circles are the experimental points while the orange lines are the best fit (see text). In each graph the highest field corresponds to the most intense torque signal.

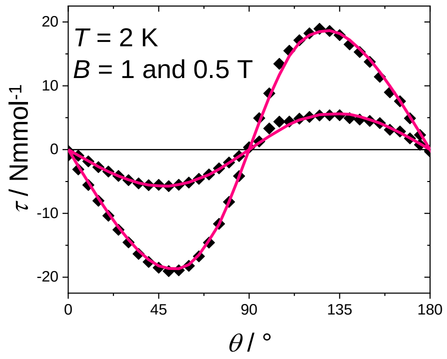
T = 2 K
B = 1 and 0.5 T
τ / Nmmol-1
θ / °
20
10
0
-10
-20
0
45
90
135
180

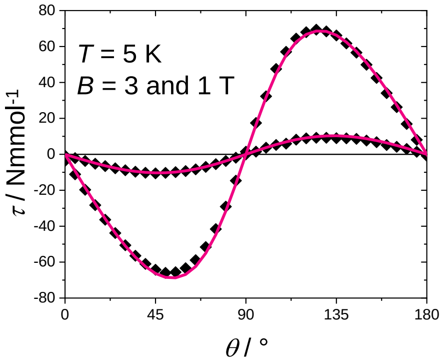
T = 5 K
B = 3 and 1 T
τ / Nmmol-1
θ / °
80
60
40
20
0
-20
-40
-60
-80
0
45
90
135
180

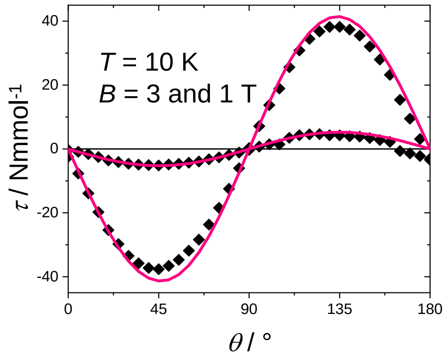
T = 10 K
B = 3 and 1 T
τ / Nmmol-1
θ / °
40
20
0
-20
-40
0
45
90
135
180

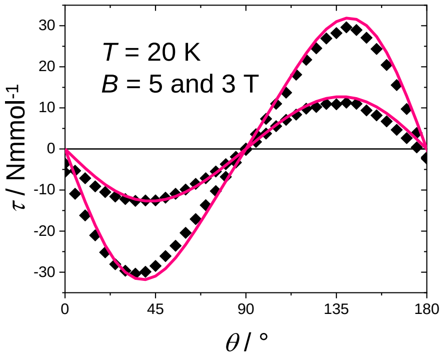
T = 20 K
B = 5 and 3 T
τ / Nmmol-1
θ / °
30
20
10
0
-10
-20
-30
0
45
90
135
180

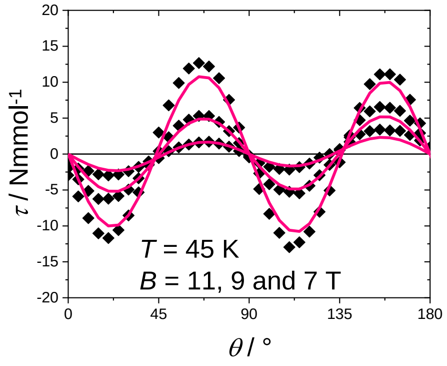
T = 45 K
B = 11, 9 and 7 T
τ / Nmmol-1
θ / °
20
15
10
5
0
-5
-10
-15
-20
0
45
90
135
180

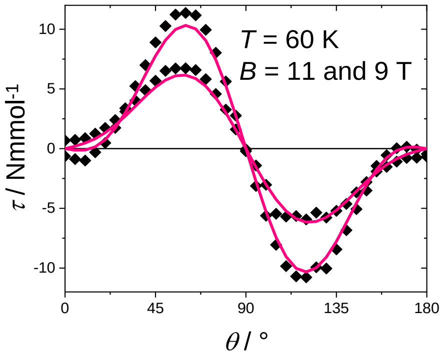
T = 60 K
B = 11 and 9 T
τ / Nmmol-1
θ / °
10
5
0
-5
-10
0
45
90
135
180

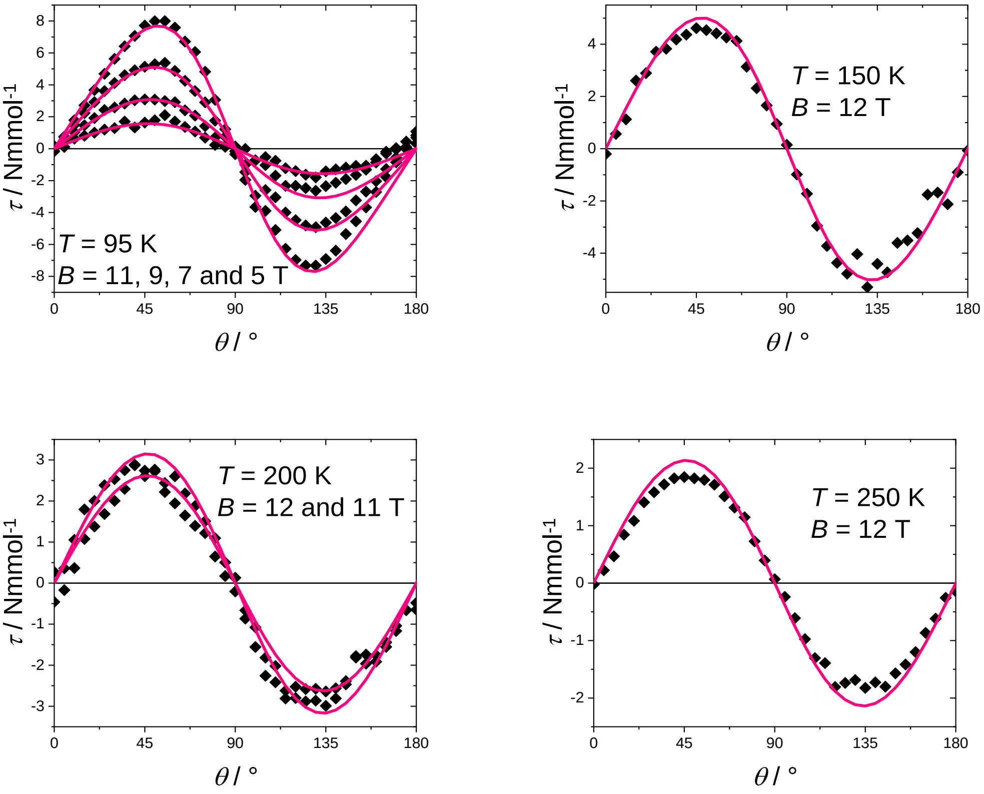

Figure S5. Torque signal recorded on an **ErPd** single crystal in the temperature interval 2-250 K. Black diamonds are the experimental points while the pink lines are the best fit (see text). In each graph the highest field corresponds to the most intense torque signal.

2. Inelastic Neutron Scattering

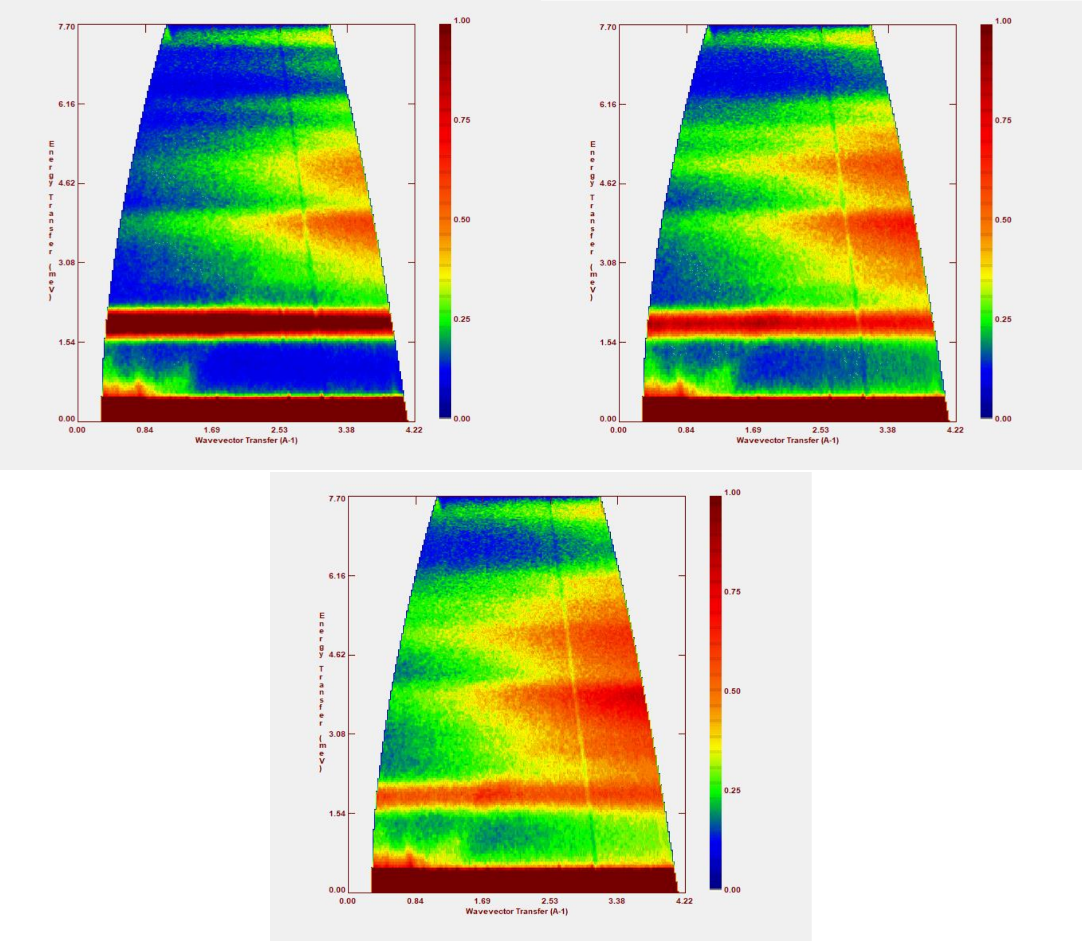

Figure S6. Stokes-regime $S(Q,\omega)$ of **TbPd** measured with incident neutron wavelength $\lambda_i =$ 2.8 Å at T = 1.5 K (top left), 25 K (top right), and 40 K (bottom). Energy conversion: 1 meV = 8.065 cm^{-1}.

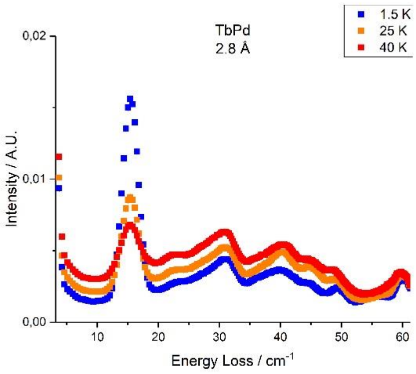

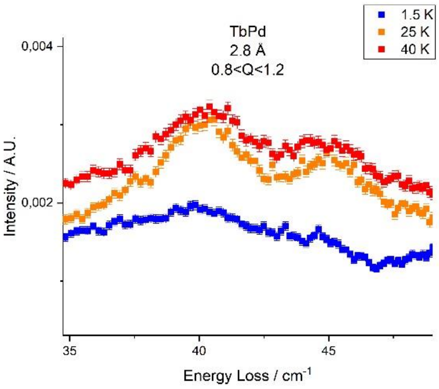

Figure S7. INS spectrum of **TbPd** measured at incident neutron wavelength $\lambda_i = 2.8$ Å at T = 1.5 K, 25 K, and 40 K (uncertainty smaller than point size). Spectrum integrated over the entire available Q-range (left), and a zoom of the spectrum integrated in the range $0.8 \leq Q \leq 1.2$ Å^{-1} (right).

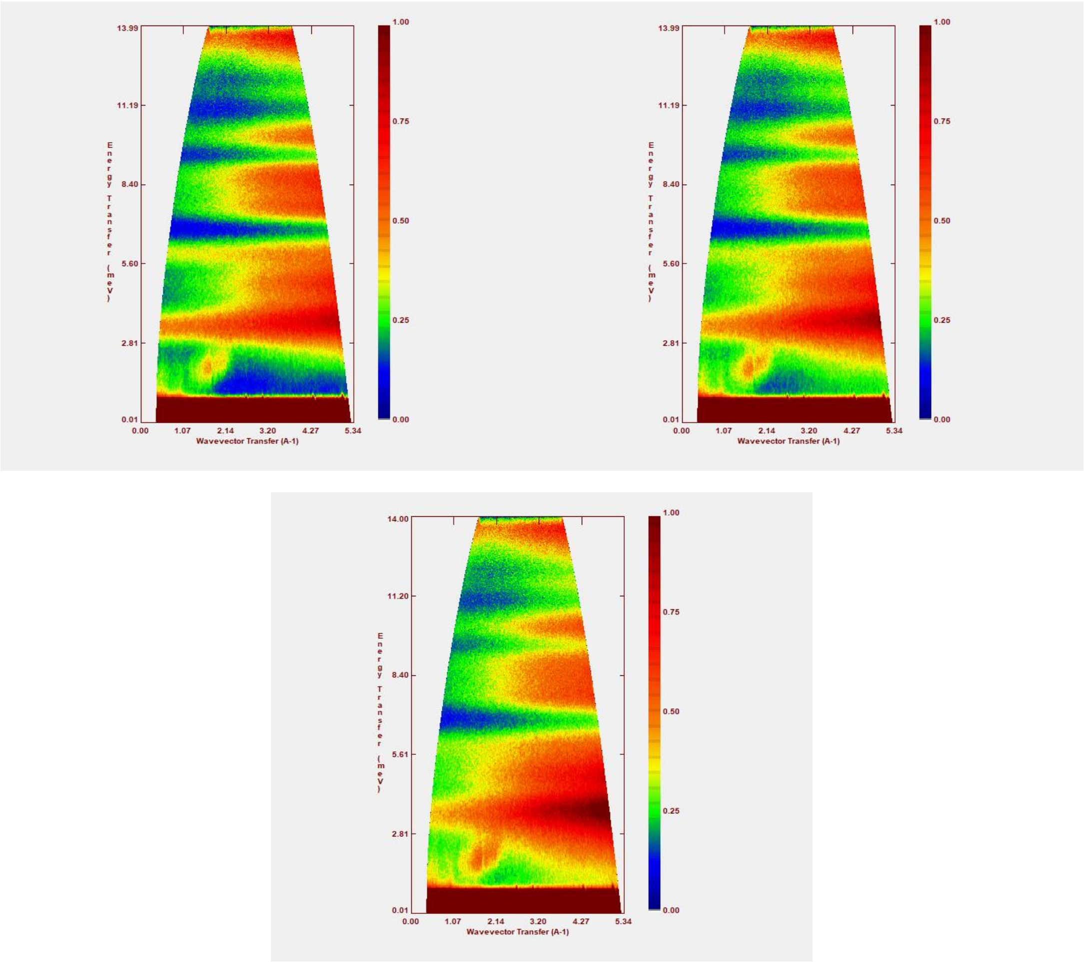

Figure S8. Stokes-regime $S(Q,\omega)$ of **DyPd** measured with incident neutron wavelength λ_i = 2.2 Å at T = 1.5 K (top left), 20 K (top right), and 35 K (bottom). Energy conversion: 1 meV = 8.065 cm^{-1}.

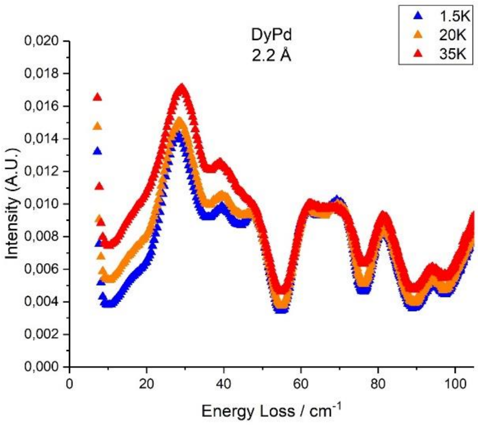

Figure S9. INS spectra of **DyPd** measured at incident neutron wavelength $\lambda_i = 2.2$ Å at T = 1.5, 20 and 35 K (uncertainty smaller than point size). Spectrum integrated over the entire available Q-range.

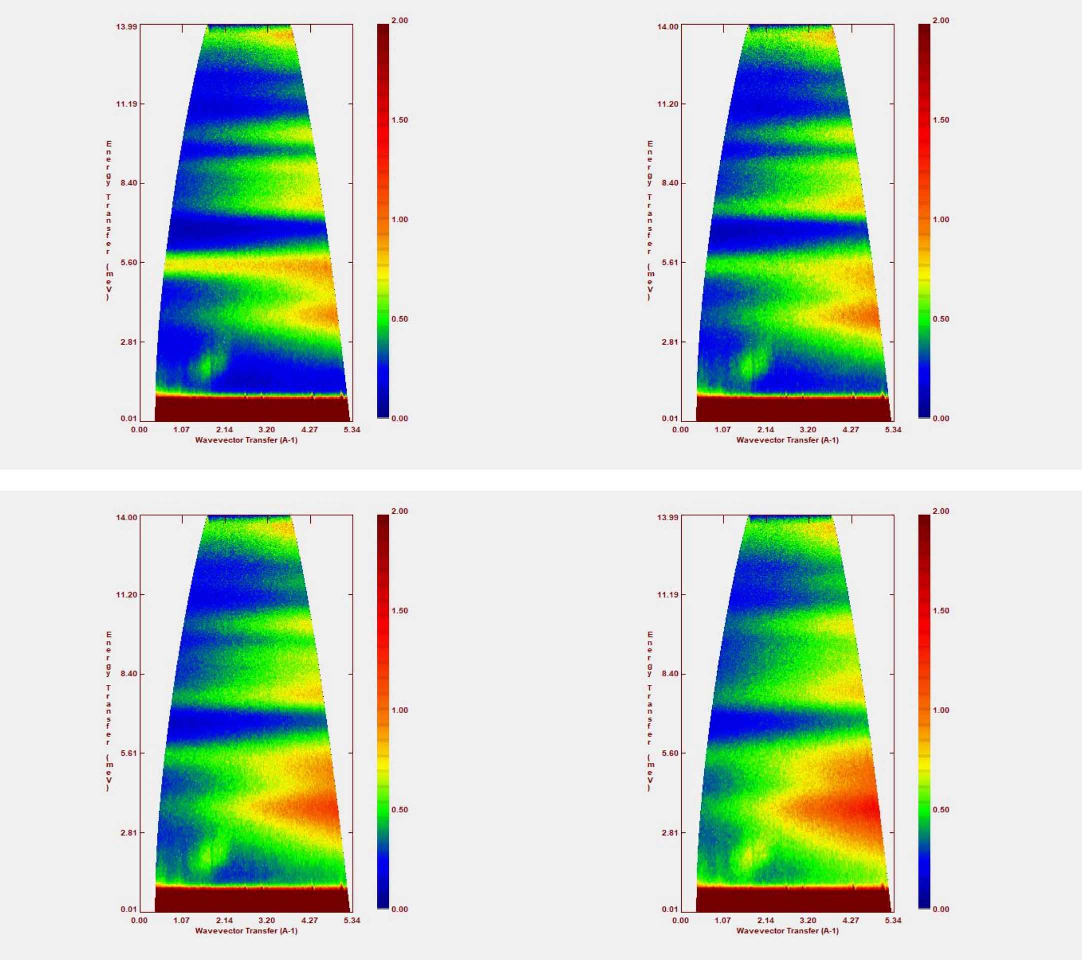

Figure S10. Stokes-regime $S(Q,\omega)$ of **HoPd** measured with incident neutron wavelength λ_i = 2.2 Å at T = 1.5 K (top left), 20 K (top right), and 35 K (bottom left), and 50 K (bottom right). Energy conversion: 1 meV = 8.065 cm^{-1}.

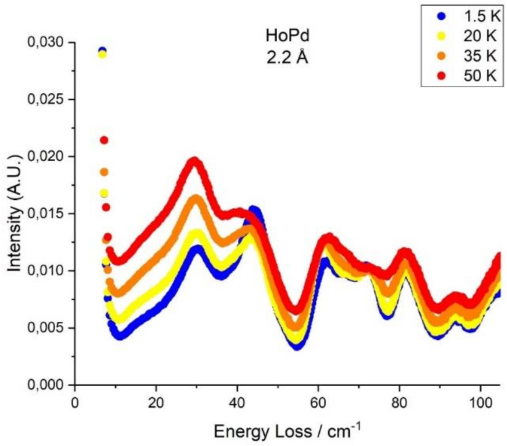

Figure S11. INS spectra of **HoPd** measured at incident neutron wavelength $\lambda_i = 2.2$ Å at T = 1.5, 20, 35, and 50 K (uncertainty smaller than point size). Spectrum integrated over the entire available Q-range.

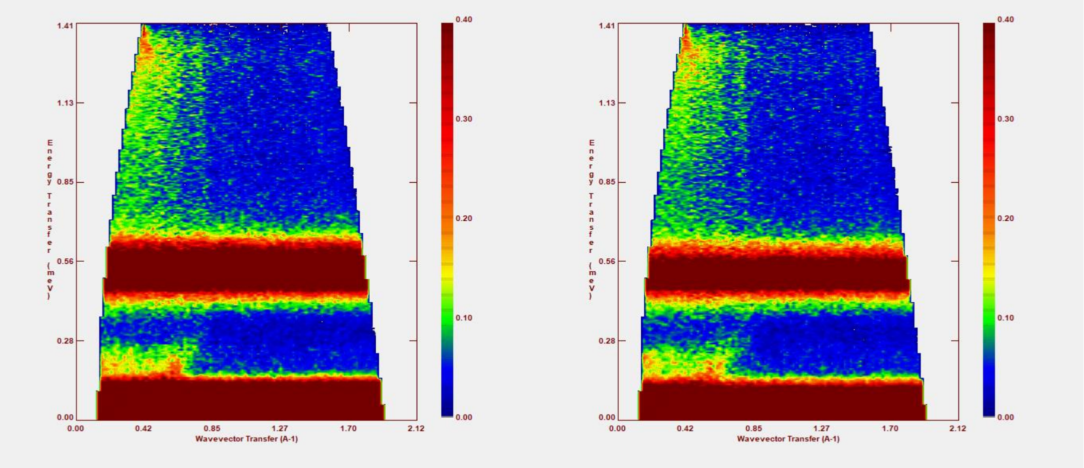

Figure S12. Stokes-regime $S(Q,\omega)$ of **HoPd** measured with incident neutron wavelength λ_i = 6 Å at T = 1.5 and 10 K. Energy conversion: 1 meV = 8.065 cm^{-1}.

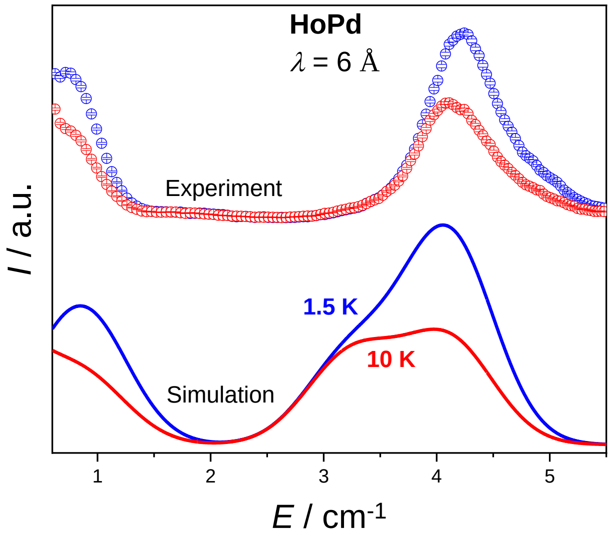

Figure S13. INS spectra of **HoPd** measured at incident neutron wavelength $\lambda_i = 6$ Å at $T = 1.5$ K and 10 K. Spectrum integrated over the entire available Q-range.

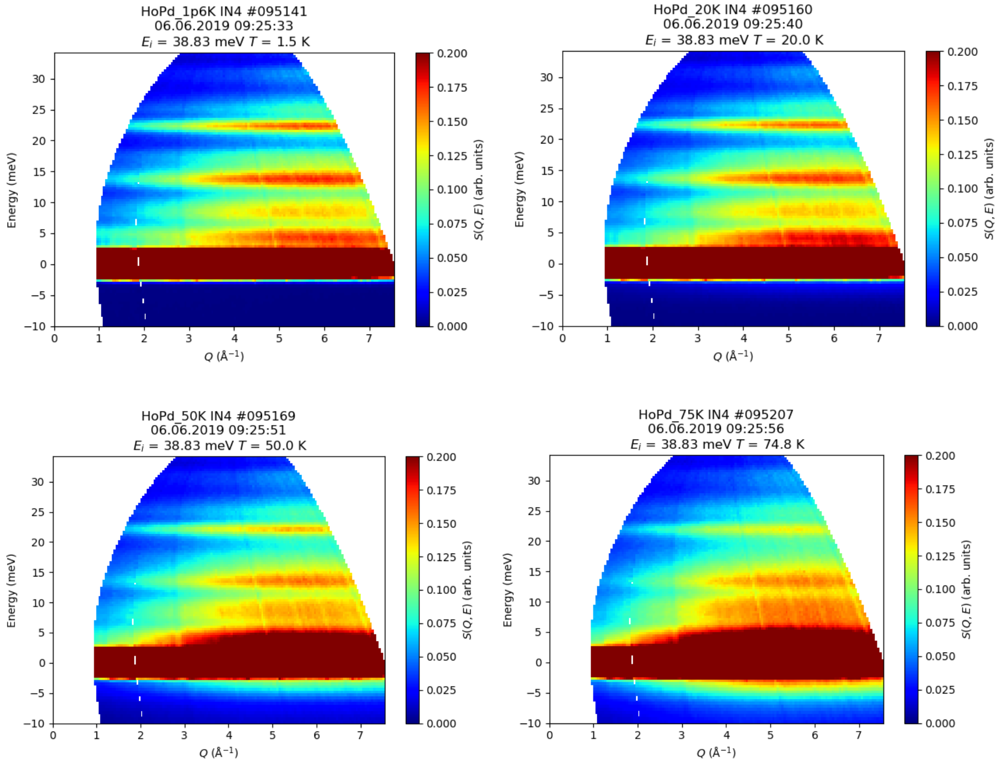

Figure S14. Stokes-regime $S(Q,\omega)$ of **HoPd** measured with incident neutron wavelength $\lambda_i =$ 1.45 Å at T = 1.5 (top left), 25 (top right), 50 (bottom left), and 75 K (bottom right). Energy conversion: 1 meV = 8.065 cm^{-1}.

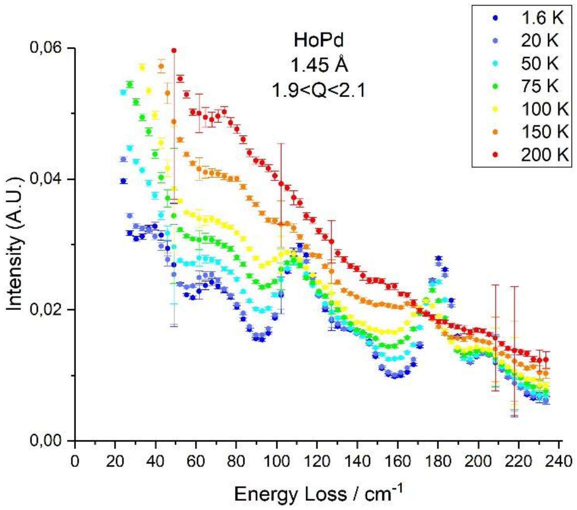

Figure S15. INS spectra of HoPd measured at incident neutron wavelength $\lambda_i = 1.45$ Å at T = 1.5, 25, 50, 75, 100, 150, and 200 K, integrated in the range $1.8 \leq Q \leq 2.2$ Å^{-1}.

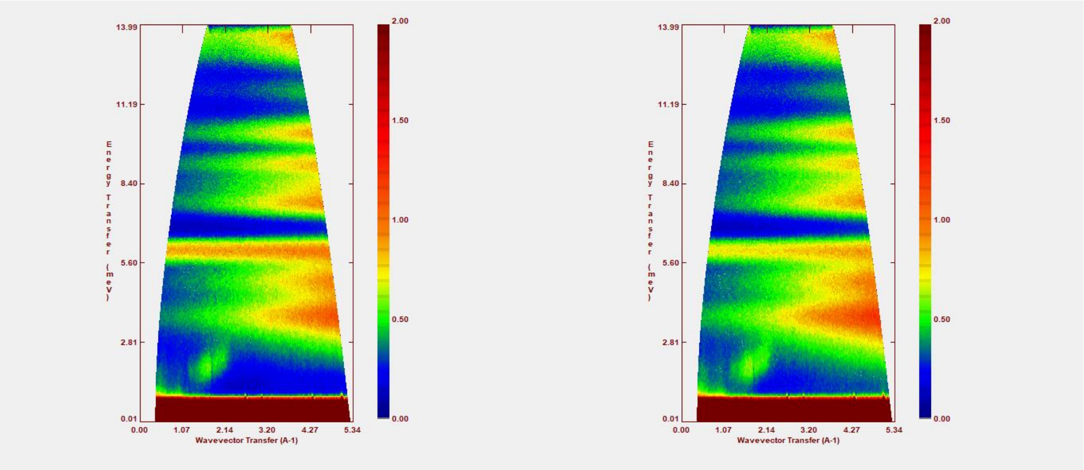

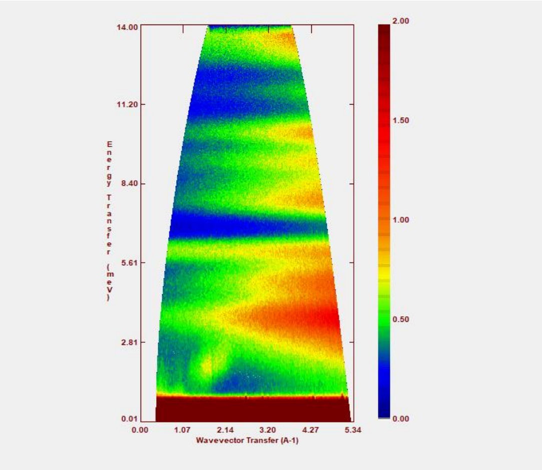

Figure S16. Stokes-regime $S(Q,\omega)$ of **ErPd** measured with incident neutron wavelength $\lambda_i = 2.2$ Å at T = 1.5 K (top left), 20 K (top right), and 35 K (bottom left).

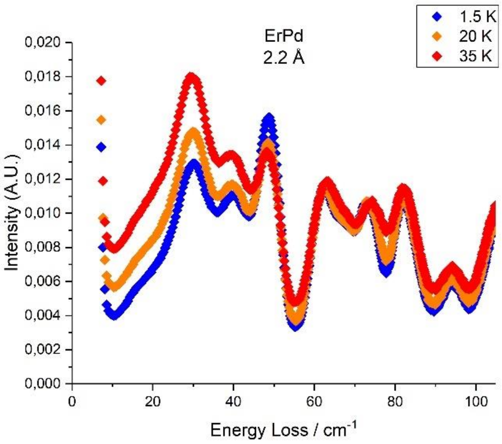

Figure S17. INS spectra of **ErPd** measured at incident neutron wavelength $\lambda_i = 2.2$ Å at T = 1.5, 20, and 35 K (uncertainty smaller than point size). Spectrum integrated over the entire available Q-range.

3. CF parameters, energy levels and errors

The adopted conversion between Wybourne ($B_k{}^q$) and Stevens ($b_k{}^q$) formalism was: $b_k^q = RnB_k^q$, where *R* is the appropriate reduced matrix element reported in Table 20 of Abragam and Bleaney[2] and *n* is a conversion factor reported in Table A.1 of Stewart.[3]

Table S2. Stevens parameters for **TbPd**, **DyPd, HoPd** and **ErPd**.

	TbPd	**DyPd**	**HoPd**	**ErPd**
b_2^0 / cm^{-1}	0.7778	0.2063	0.2133	-0.2057
b_4^0 / cm^{-1}	-14.8 10^{-3}	7.90 10^{-3}	4.10 10^{-3}	-4.50 10^{-3}
b_6^0 / cm^{-1}	-2.102 10^{-5}	1.863 10^{-5}	-2.709 10^{-5}	4.955 10^{-5}
b_4^4 / cm^{-1}	-12.0 10^{-3}	7.0 10^{-3}	4.00 10^{-3}	-5.33 10^{-3}

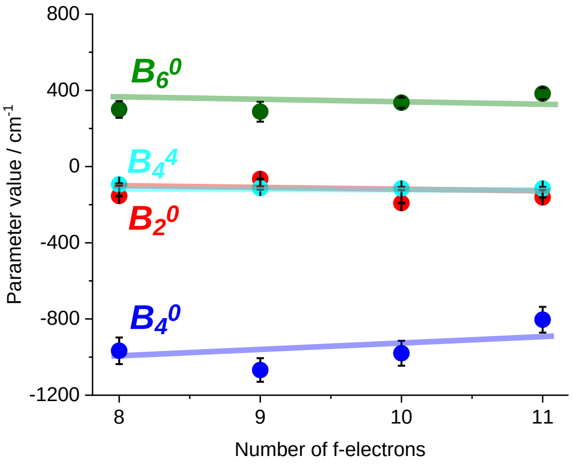

Figure S18. CF parameters' (Wybourne notation) variation along the series. The lines are guides to the eye.

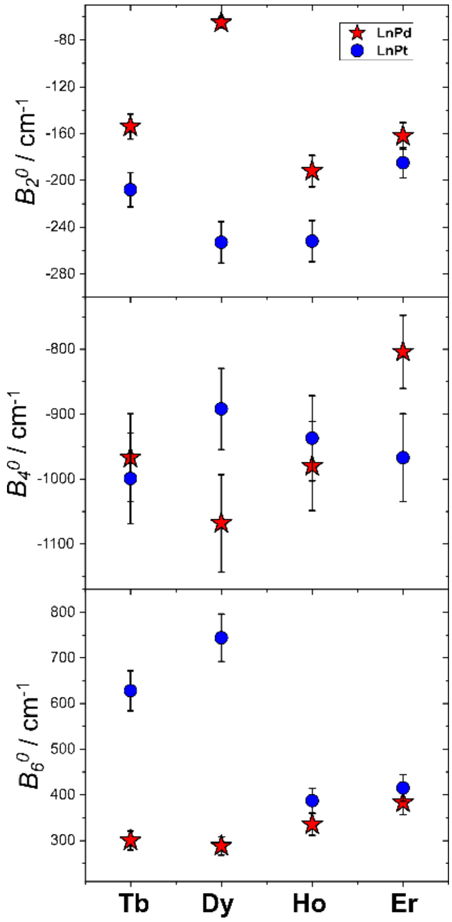

Figure S19. Crystal field parameters of **LnPd** (red stars) and **LnPt**[4, 5] (blue circles).

Table S3. CF strength calculated as: $S_k = \sqrt{\frac{1}{2k+1}\left(|B_k^0|^2 + 2\sum_{q\neq 0}|B_k^q|^2\right)}$ and $S_{tot} = \frac{S_2+S_4+S_6}{3}$ for **LnPd** (this work) and **LnPt**.[4, 5]

	TbPd	**DyPd**	**HoPd**	**ErPd**	**TbPt**	**DyPt**	**HoPt**	**ErPt**
S_2 / cm^{-1}	69	29	86	72	93	113	113	83
S_4 / cm^{-1}	325	360	331	273	336	302	317	327
S_6 / cm^{-1}	83	80	93	106	174	206	107	115
S_{tot} / cm^{-1}	159	156	170	151	201	207	179	175

Table S4. Composition of the eigenvectors for **TbPd**. The coefficients give the composition of the wavefunction, to get the percentage of each state the coefficients must be squared. Contributions < 0.5 % were omitted.

E [cm^{-1}]	E exp. [cm^{-1}]	Composition
0	-	$+0.998\|0\rangle$
16.6	15.40	$+0.083\|+3\rangle + 0.996\|-1\rangle$
16.6	15.40	$+0.996\|+1\rangle + 0.083\|-3\rangle$
53.6	55.7	$+0.266\|+6\rangle + 0.655\|+2\rangle + 0.655\|-2\rangle + 0.266\|-6\rangle$
60.8	61.6	$+0.690\|+6\rangle + 0.155\|+2\rangle - 0.155\|-2\rangle - 0.690\|-6\rangle$
62.8	61.6	$+0.655\|+6\rangle - 0.266\|+2\rangle - 0.266\|-2\rangle + 0.655\|-6\rangle$
75.7		$+0.155\|+6\rangle - 0.690\|+2\rangle + 0.690\|-2\rangle - 0.155\|-6\rangle$
131.7		$-0.083\|+1\rangle + 0.997\|-3\rangle$
131.7		$+0.997\|+3\rangle - 0.083\|-1\rangle$
190.1		$-0.707\|+4\rangle + 0.707\|-4\rangle$
190.8		$-0.706\|+4\rangle - 0.706\|-4\rangle$
194.7		$+1.000\|-5\rangle$
194.7		$+1.000\|+5\rangle$

Table S5. Composition of the eigenvectors for **DyPd**. The coefficients give the composition of the wavefunction, to get the percentage of each state the coefficients must be squared. Contributions < 0.5 % were omitted.

E [cm^{-1}]	E exp. [cm^{-1}]	Composition
0		$+0.998\left\|\mp\frac{11}{2}\right\rangle$

28.2	27.42	$+0.081\left\|\mp\frac{1}{2}\right\rangle - 0.997\left\|\mp\frac{9}{2}\right\rangle$
48.9	47.59	$-0.082\left\|\mp\frac{5}{2}\right\rangle + 0.997\left\|\mp\frac{13}{2}\right\rangle$
76.9		$-0.137\left\|\pm\frac{1}{2}\right\rangle + 0.990\left\|\mp\frac{7}{2}\right\rangle$
118.1		$+0.361\left\|\pm\frac{3}{2}\right\rangle - 0.929\left\|\mp\frac{5}{2}\right\rangle - 0.080\left\|\mp\frac{13}{2}\right\rangle$
158.4		$+0.362\left\|\pm\frac{5}{2}\right\rangle + 0.931\left\|\mp\frac{3}{2}\right\rangle$
169.5		$+0.139\left\|\pm\frac{7}{2}\right\rangle + 0.987\left\|\mp\frac{1}{2}\right\rangle + 0.078\left\|\mp\frac{9}{2}\right\rangle$
277.45		$+1.000\left\|\mp\frac{15}{2}\right\rangle$

Table S6. Composition of the eigenvectors for **HoPd**. The coefficients give the composition of the wavefunction, to get the percentage of each state the coefficients must be squared. Contributions < 0.5 % were omitted.

E [cm^{-1}]	**E exp. [cm^{-1}]**	**Composition**
0		$+0.706\|+4\rangle + 0.706\|-4\rangle$
0.85	0.82	$+0.707\|+4\rangle - 0.707\|-4\rangle$
4.1	4.19	$-0.999\|-5\rangle$
4.1	4.19	$+0.999\|+5\rangle$
44.7	44.36	$+0.080\|+1\rangle - 0.996\|-3\rangle$
44.7	44.36	$+0.996\|+3\rangle - 0.080\|+1\rangle$
64.2	65.5	$+0.698\|+6\rangle - 0.112\|+2\rangle + 0.112\|-2\rangle - 0.698\|-6\rangle$
64.5	65.5	$-0.703\|+6\rangle + 0.073\|+2\rangle + 0.073\|-2\rangle - 0.703\|-6\rangle$
101.9		$+0.112\|+6\rangle + 0.698\|+2\rangle - 0.698\|-2\rangle - 0.112\|-6\rangle$

121.7		$-0.073\|+6\rangle - 0.703\|+2\rangle - 0.703\|-2\rangle - 0.073\|-6\rangle$
152.5		$+0.999\|-7\rangle$
152.5		$+0.999\|+7\rangle$
167.0		$-0.081\|+3\rangle - 0.995\|-1\rangle$
167.0		$+0.995\|+1\rangle + 0.081\|-3\rangle$
171.4		$-0.707\|+8\rangle - 0.707\|-8\rangle$
171.4		$+0.707\|+8\rangle - 0.707\|-8\rangle$
187.8		$-0.998\|0\rangle$

Table S7. Composition of the eigenvectors for **ErPd**. The coefficients give the composition of the wavefunction, to get the percentage of each state the coefficients must be squared. Contributions < 0.5 % were omitted.

E [cm^{-1}]	**E exp. [cm^{-1}]**	**Composition**
0		$+0.998\left\|\mp\frac{1}{2}\right\rangle$
21.5		$+0.999\left\|\mp\frac{13}{2}\right\rangle$
39.7		$+1.000\left\|\mp\frac{15}{2}\right\rangle$
48.1	48.39	$+0.133\left\|\pm\frac{5}{2}\right\rangle + 0.987\left\|\mp\frac{3}{2}\right\rangle + 0.093\left\|\mp\frac{11}{2}\right\rangle$
118.2		$+0.125\left\|\pm\frac{5}{2}\right\rangle + 0.077\left\|\mp\frac{3}{2}\right\rangle - 0.989\left\|\mp\frac{11}{2}\right\rangle$
126.0		$+0.114\left\|\pm\frac{11}{2}\right\rangle - 0.144\left\|\pm\frac{3}{2}\right\rangle + 0.982\left\|\mp\frac{5}{2}\right\rangle$
183.4		$+0.160\left\|\pm\frac{9}{2}\right\rangle - 0.986\left\|\mp\frac{7}{2}\right\rangle$

186.2	$+0.157\left|\pm\frac{7}{2}\right\rangle + 0.986\left|\mp\frac{9}{2}\right\rangle$

Errors

The estimation of the errors on the extracted parameters is not trivial because the used program fitted at the same time spectroscopic and thermodynamic data, thus we used an empirical factor to define a ratio between the weight of one experimental energy and one CTM point. This factor (always >> 1) was progressively decreased over several iterations to obtain the best compromise between INS and CTM fit. If the factor is decreased to zero (the energies were not fitted at all), the accuracy on each parameter obtained with the MINUIT subroutine[6] is approximately 1% of the parameter value. This can be considered a lower limit for the estimation of the error. A more reliable estimation was instead obtained considering the impact of a slight variation of the parameters on the resultant energies. Following this method, we can estimate that the error on each parameter is approximately 5-7 % of its value.

4. NMR

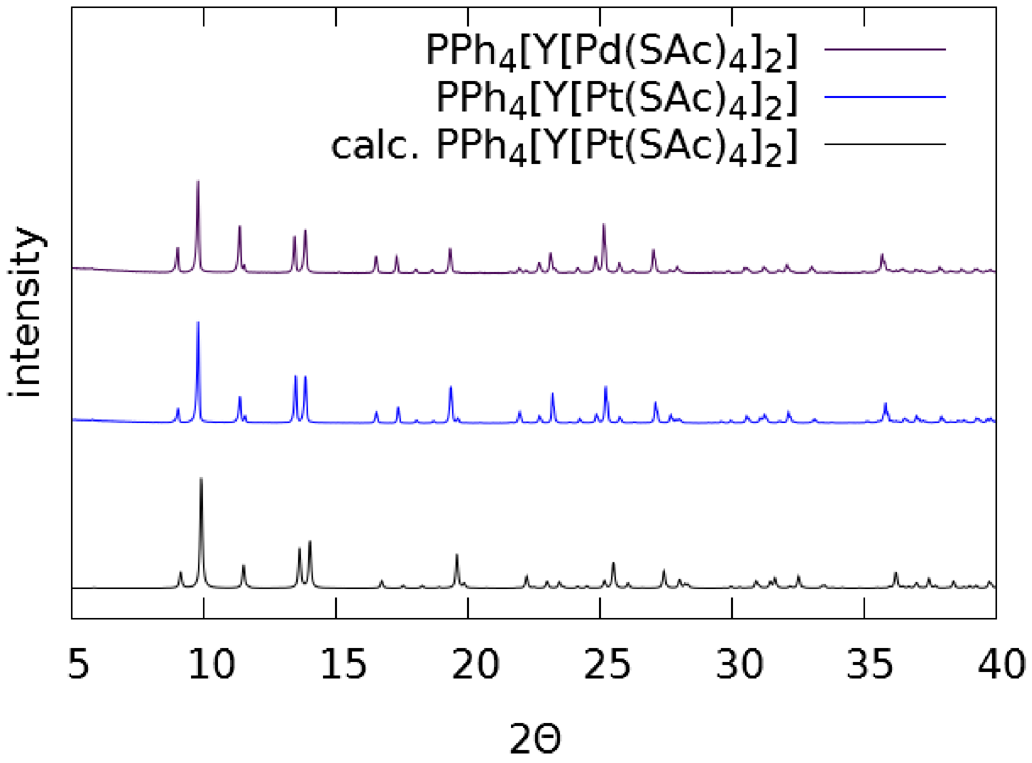

Figure S20. Powder X-ray diffractograms of **YPd** (purple) and **YPt** (blue). The black line is the corresponding powder diffractogram calculated for **YPt** (the calculated **YPd** diffractogram is superimposable).

Table S8. Coordinates for the optimized geometry of $[Y(H_2O)_8]^{3+}$ used for calculating reference shielding.

Y	0.041741	-0.36301	-0.01298
O	-2.19111	-0.80083	0.586008
H	-2.97541	-0.30363	0.328154
O	-1.08758	1.570021	-0.73529
H	-1.55572	1.69886	-1.5679
O	-0.28423	0.971262	1.897308
H	0.413261	1.399729	2.406098
O	1.362724	0.588577	-1.71081
H	2.078239	0.168771	-2.20144
O	2.170073	-0.00317	0.922278
H	2.521289	-0.37519	1.739158
O	1.292657	-2.19224	-0.80788
H	1.011659	-2.80153	-1.49981

O	0.104399	-1.93689	1.733909
H	0.475003	-2.82376	1.663188
O	-1.02728	-1.09548	-1.97407
H	-0.70631	-1.01372	-2.87934
H	-2.48801	-1.54458	1.122396
H	-0.09617	-1.78662	2.664609
H	2.885397	0.48748	0.502359
H	-1.11203	1.117933	2.368862
H	-1.24461	2.354193	-0.19734
H	1.2415	1.469664	-2.08219
H	2.184994	-2.44837	-0.54867
H	-1.90377	-1.49383	-2.01829

Table S9. Experimental and calculated chemical shifts and deviations. Chemical shift (in ppm) calculated from shielding as $\delta_A = \frac{\sigma_{ref}-\sigma_A}{1-\sigma_{ref}}$.

	YPt	**YPd**
Exp. $\delta(^{89}Y)$	-114.5	-100.5
PBE $\delta(^{89}Y)$	-116(1)	-96(4)
PBE with f_{XC} $\delta(^{89}Y)$	-114.6(1)	-95(5)
BP86 $\delta(^{89}Y)$	-118(3)	-98(3)
BP86 with f_{XC} $\delta(^{89}Y)$	-116(2)	-97(4)

5. DC Magnetometry

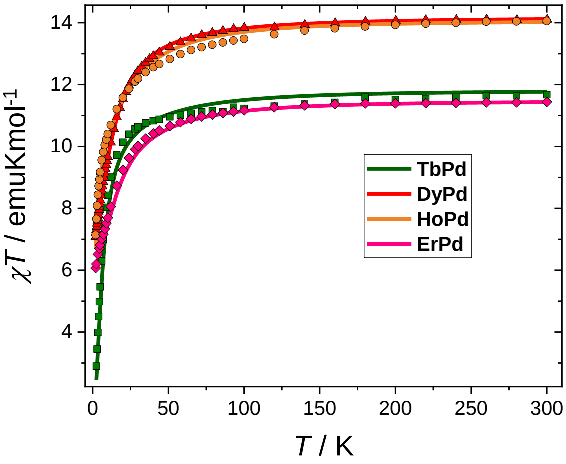

Figure S21. χT vs T curves recorded with a static field B = 0.1 T. The lines are the best fit (see main text).

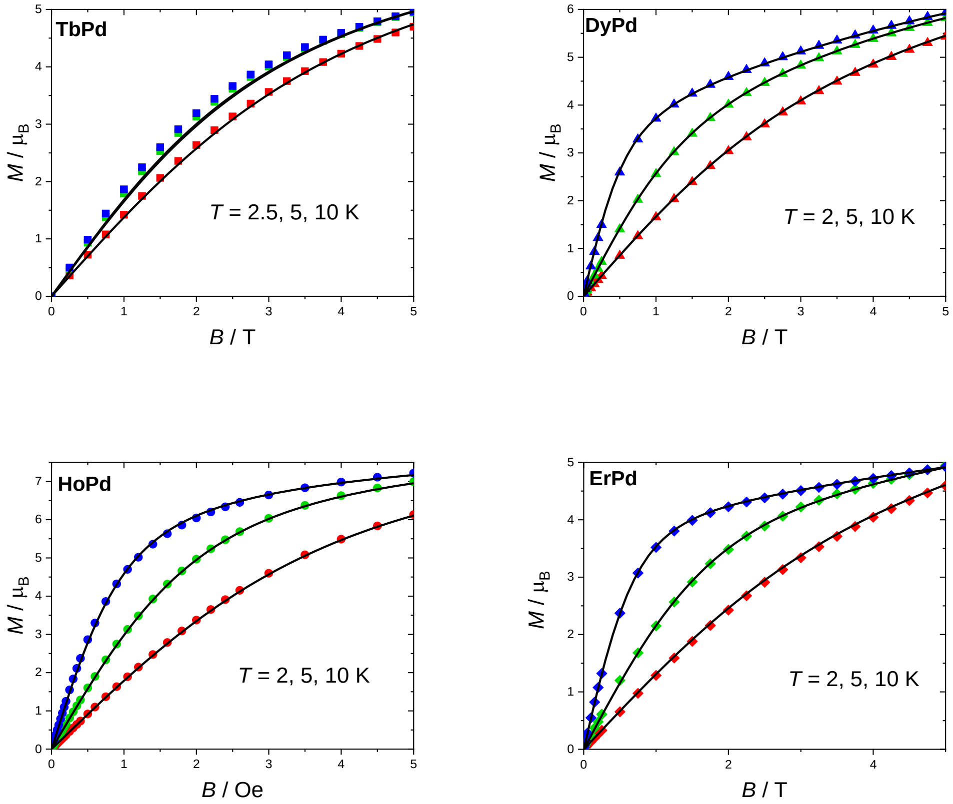

Figure S22. Magnetization curves at several temperatures recorded. The black lines are the best fit (see main text).

6. Magnetic anisotropy phase diagrams

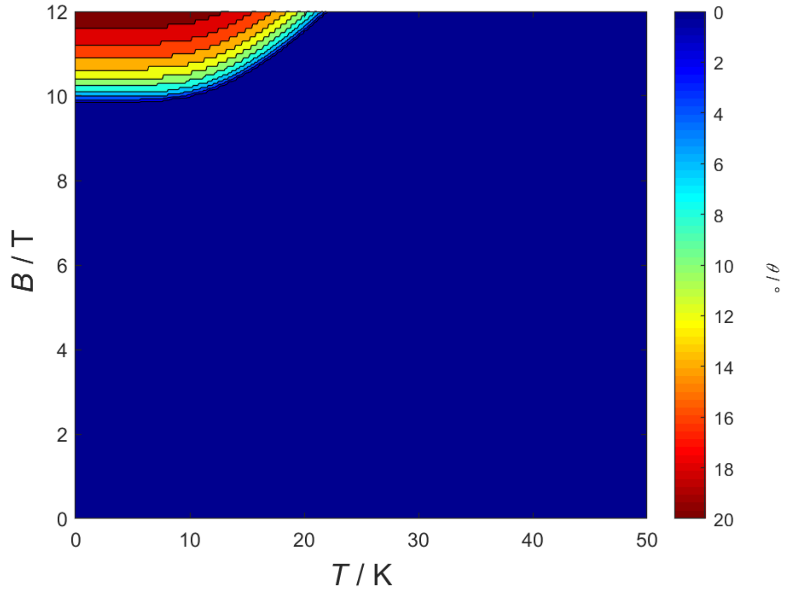

Figure S23: *B* vs *T* magnetic anisotropy phase diagram for **DyPd**. The color code corresponds to the angle between the *z* axis and the minimum of the free energy (0° and 90° correspond to easy axis and easy plane, respectively).

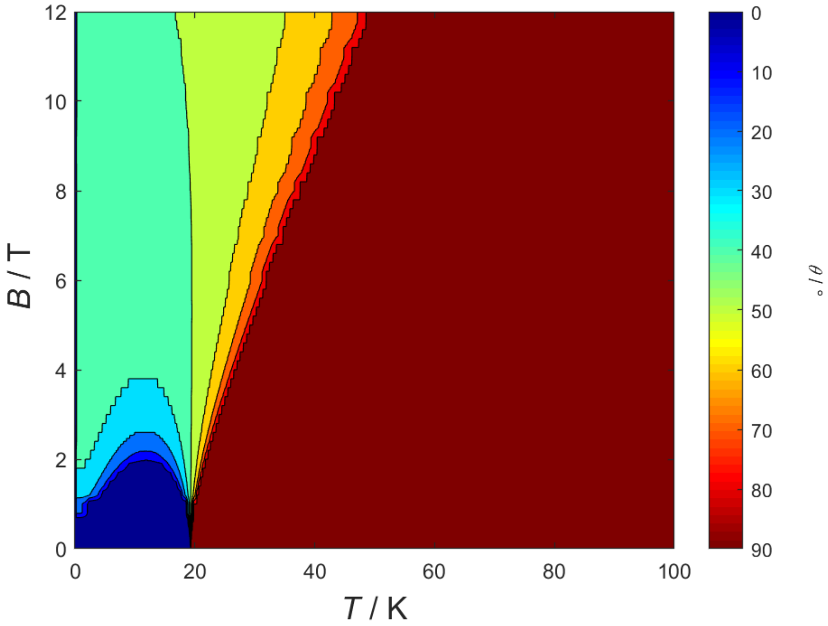

Figure S24: *B* vs *T* magnetic anisotropy phase diagram for **HoPd**. The color code corresponds to the angle between the *z* axis and the minimum of the free energy (0° and 90° correspond to easy axis and easy plane, respectively).

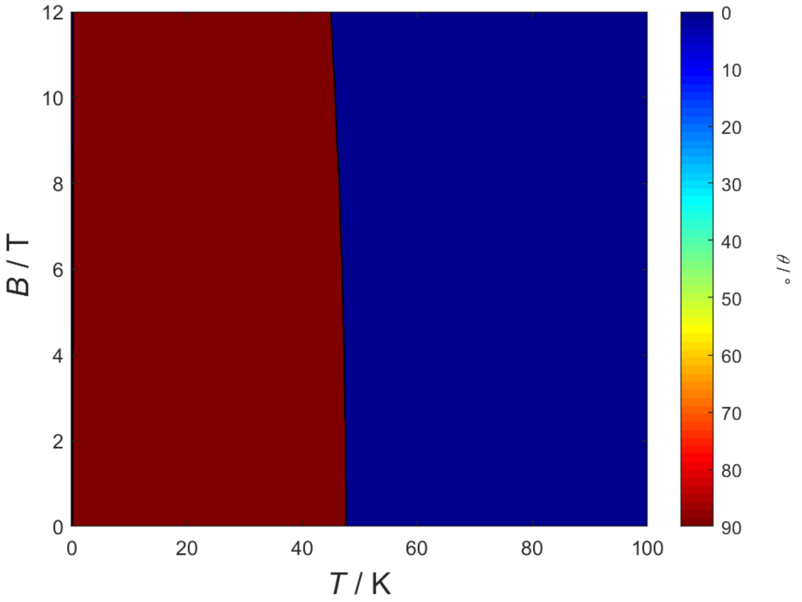

Figure S25: *B* vs *T* magnetic anisotropy phase diagram for **ErPd**. The color code corresponds to the angle between the *z* axis and the minimum of the free energy (0° and 90° correspond to easy axis and easy plane, respectively).

7. AC Magnetometry

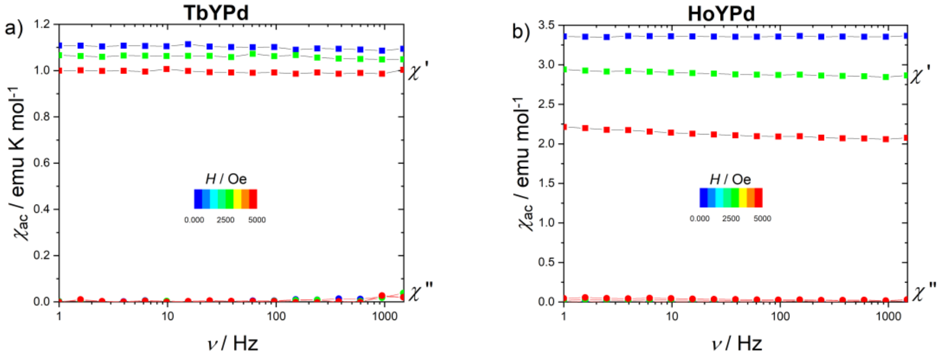

Figure S26. Field scan of the in phase (χ') and out-of-phase (χ'') components of the ac magnetic susceptibility of a) **TbYPd** and b) **HoYPd**. A constant value of χ' and a zero χ'' mean that no slow relaxation is occurring.

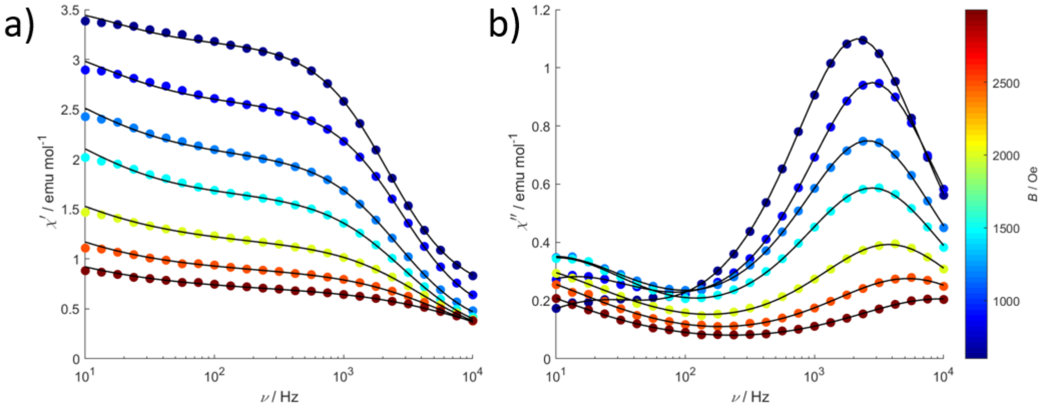

Figure S27. Field scan of the in phase (left) and out-of-phase (right) components of the ac magnetic susceptibility of **ErPd**. The black lines are the best fit (see text).

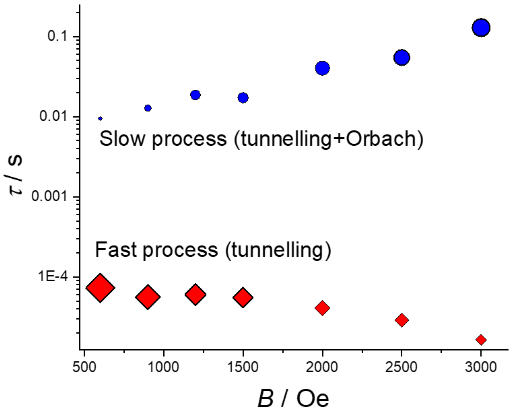

Figure S28. Slow (blue dots) and fast (red diamonds) relaxation times extracted from the field scan on **ErPd**. The dimension of the symbols is proportional to the fraction of the slow relaxing molecules following a certain pathway, calculated from the χ_T-χ_S difference.[6]

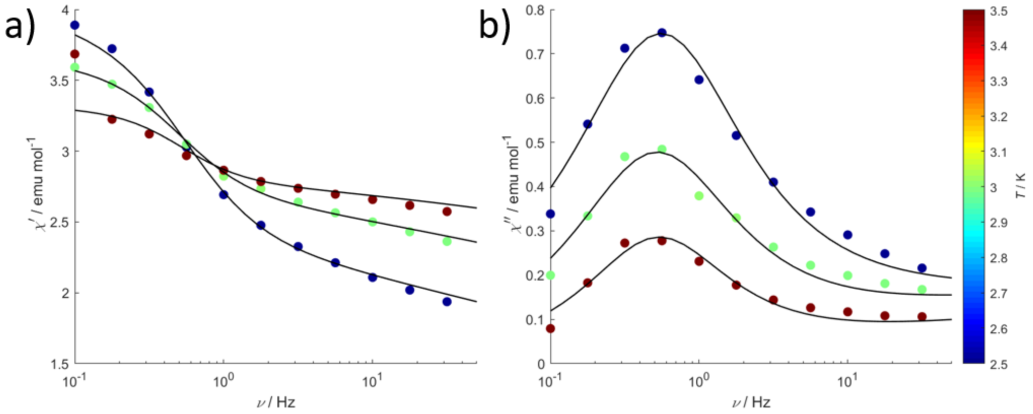

Figure S29. Temperature scan of the a) in-phase and b) out-of-phase component of the ac magnetic susceptibility of **ErPd** with an applied dc field B = 0.5 T. The black lines are the best fit (see text).

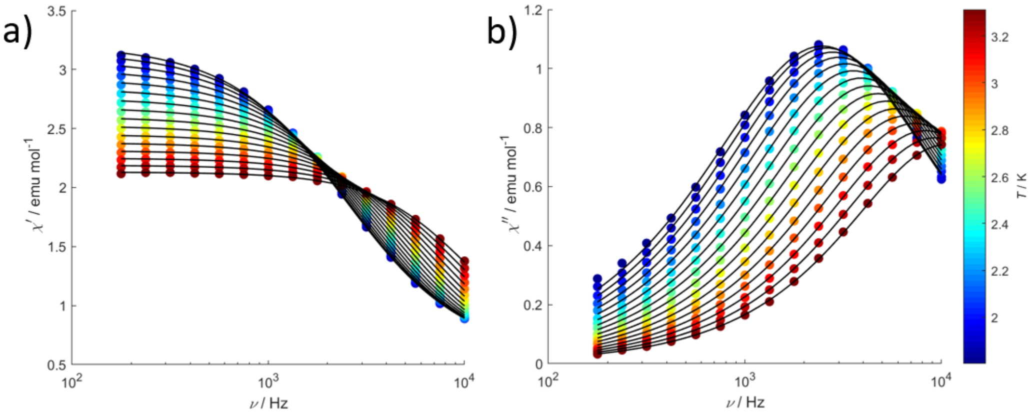

Figure S30. Temperature scan of the a) in-phase and b) out-of-phase component of the ac magnetic susceptibility of **ErPd** with an applied field H_{dc} = 0.06 T. The black lines are the best fit (see text).

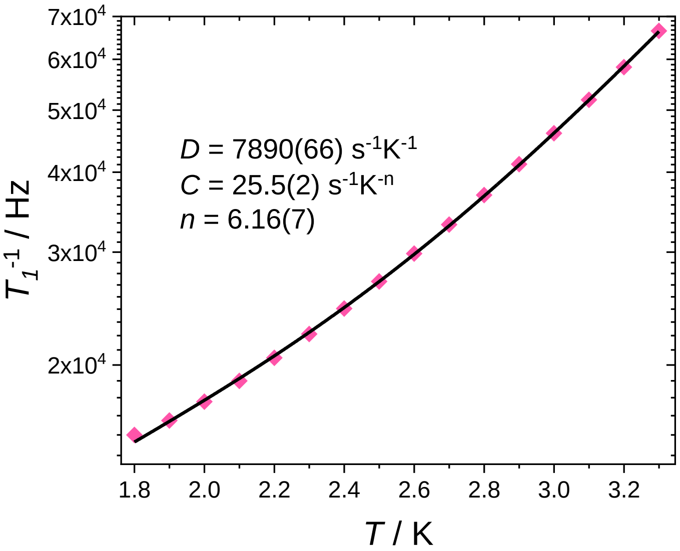

Figure S31. Longitudinal relaxation time extracted from the fit of the ac susceptibility of **ErPd** in H_{dc} = 0.06 T applied field (pink diamonds). The black line is the best fit obtained using a combination of Direct and Raman processes: $T_1^{-1} = DT + CT^n$.

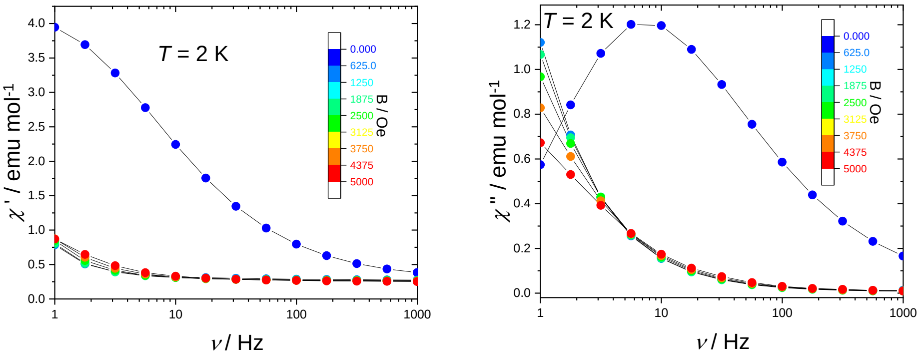

Figure S32. Field scan of the a) in-phase and b) out-of-phase component of the ac magnetic susceptibility of **DyPd** at T = 1.8 K. The black lines are a guide to the eye.

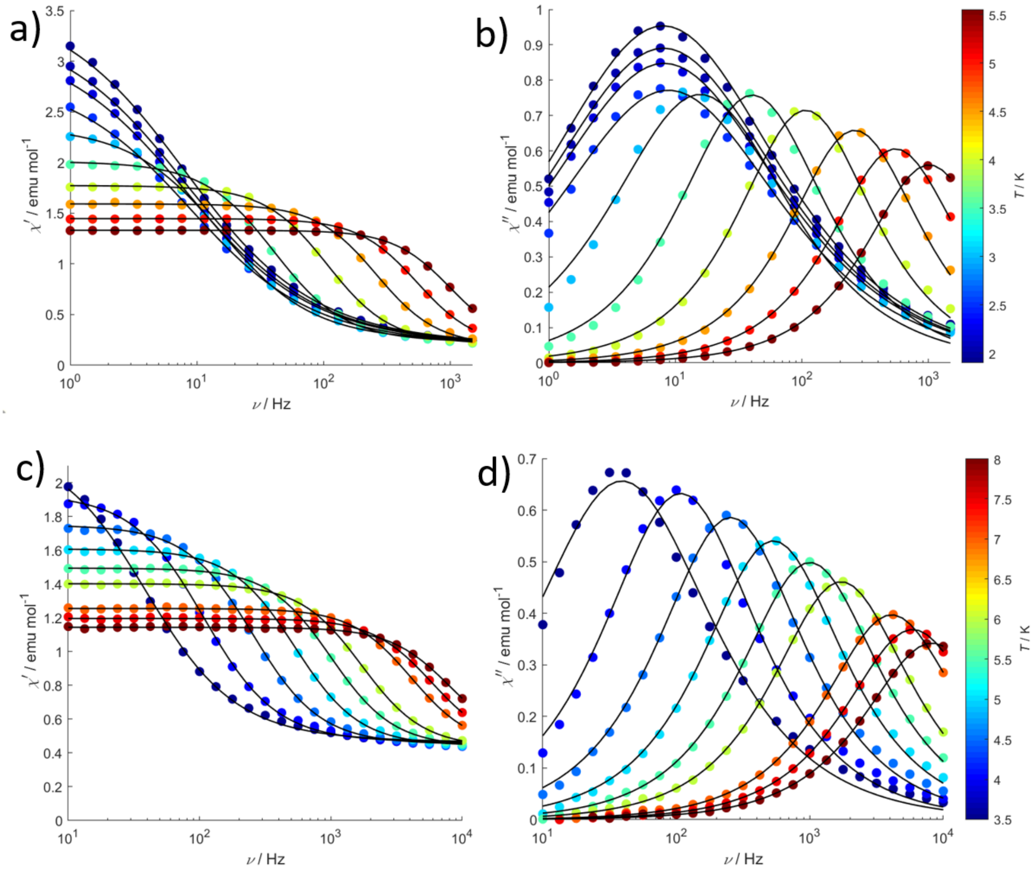

Figure S33. Temperature scan of the ac magnetic susceptibility of **DyPd** in zero applied dc magnetic field. a) Real component b) Imaginary component recorded in the frequency range 1-1100 Hz. c) Real component b) Imaginary component recorded in the frequency range 10-10000 Hz. The black lines are the best fit (see text).

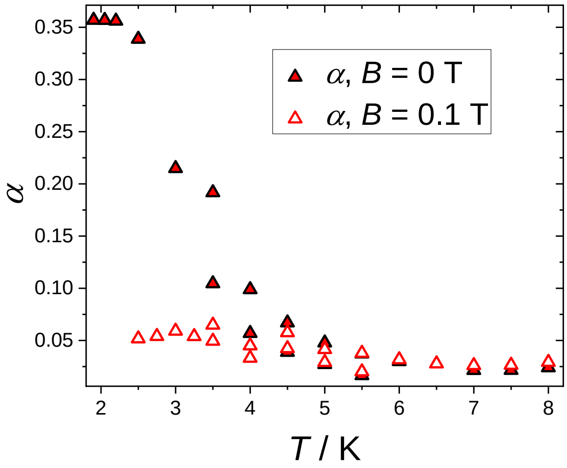

Figure S34. Thermal evolution of the distribution of the relaxation times in **DyPd** in zero applied field (full triangles) and in B = 0.1 T (empty triangles).

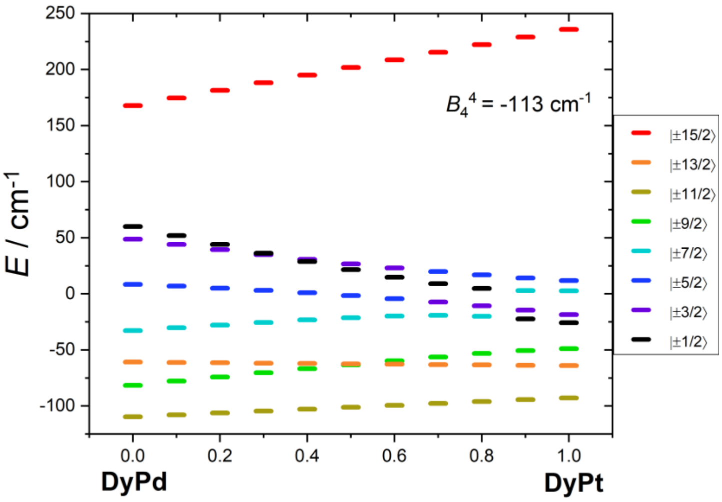

Figure S35. Changes in the energy level scheme from **DyPd** to **DyPt**. The three diagonal CF parameters were varied linearly from the **DyPd** (corresponding to x = 0) values to the **DyPt** values (corresponding to x = 1). The color scheme represents the *main* composition of the state (notice that close lying states are strongly admixed). The purity of the ground state is mainly determined by the energy difference between the |±11/2⟩ doublet (gold) and the |±3/2⟩ doublet (violet).

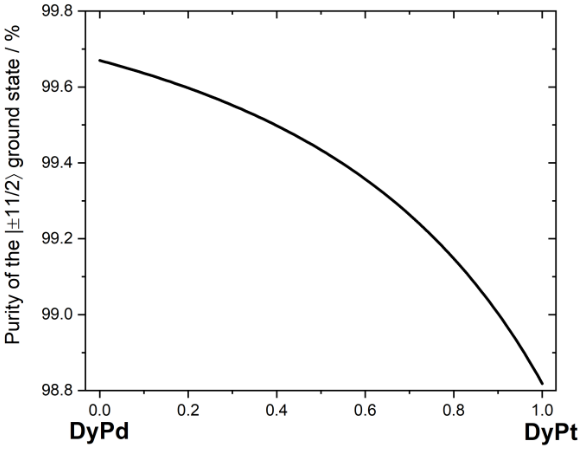

Figure S36. Purity of the ground state. The three diagonal CF parameters were varied linearly from the **DyPd** (corresponding to $x = 0$) values to the **DyPt** values (corresponding to $x = 1$).

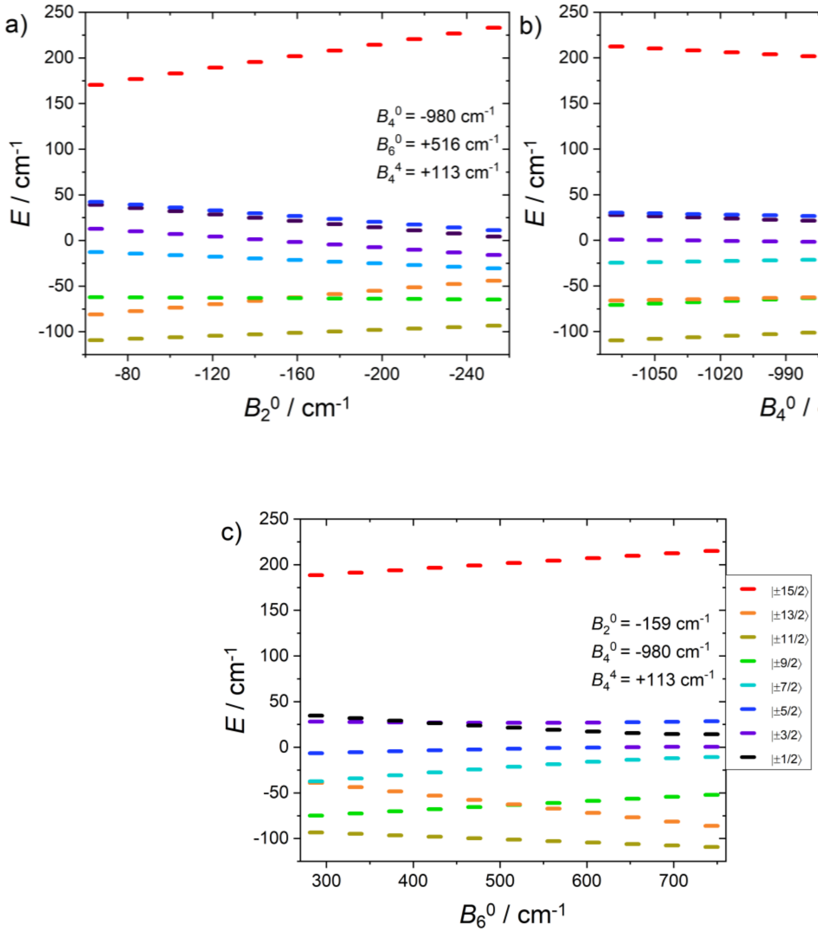

Figure S37. Changes in the energy level scheme for a Dy complex (J = 15/2, g_J = 4/3) with crystal field parameters (expressed in cm^{-1}): a) $-65 \geq B_2^0 \geq -253$, $B_4^0 = -980$, $B_6^0 = 516$, $B_4^4 = 113$; b) $B_2^0 = -159$, $-1068 \leq B_4^0 \leq -946$, $B_6^0 = 516$, $B_4^4 = 113$; c) $B_2^0 = -159$, $B_4^0 = -980$, $288 \leq B_6^0 \leq 744$, $B_4^4 = 113$. The color scheme represents the *main* composition of the state (notice that close lying states are strongly admixed). The purity of the ground state is, at the first order of approximation, inversely proportional to the energy difference between the |±11/2⟩ ground doublet (gold) and the |±3/2⟩ doublet (violet).

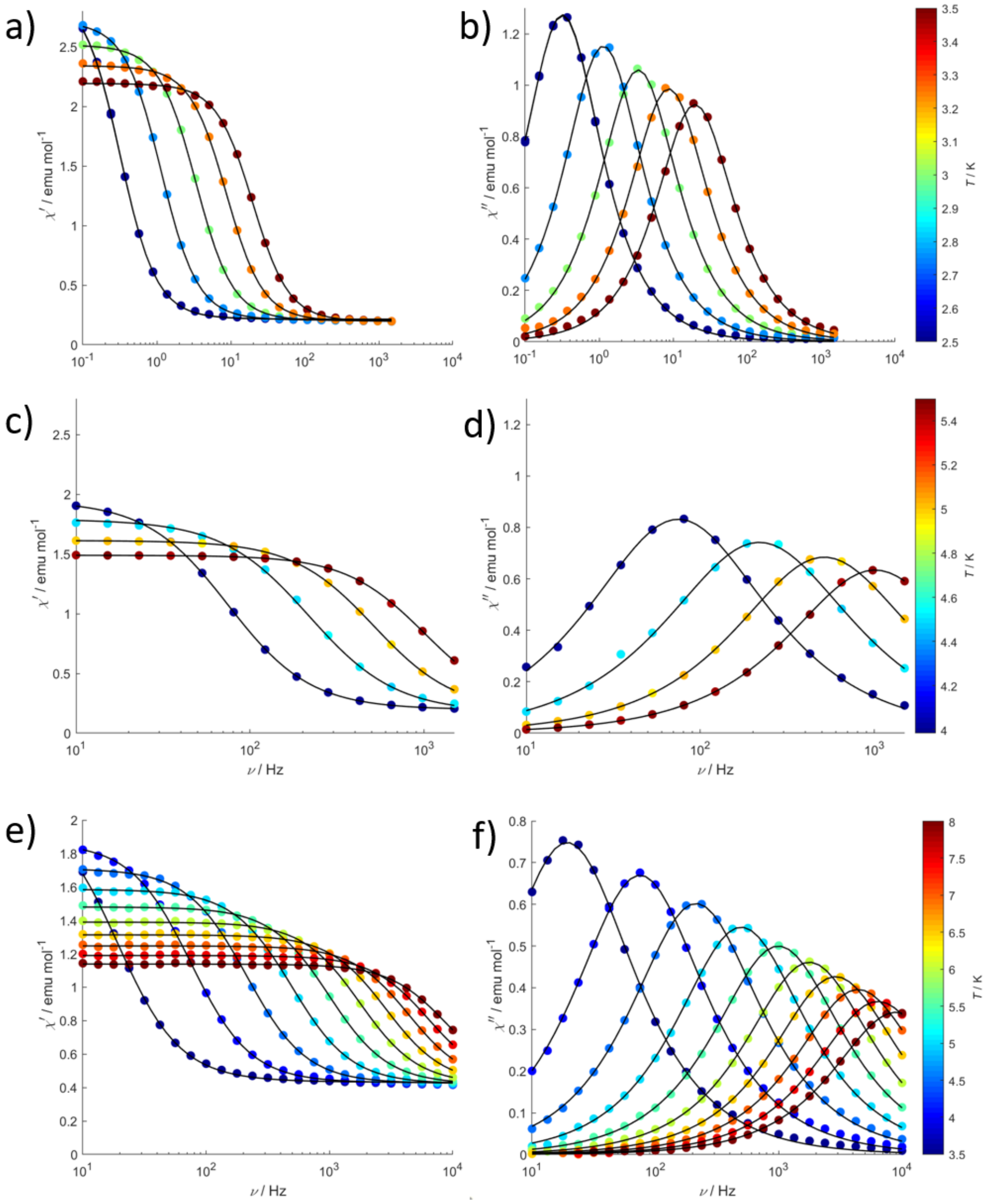

Figure S38. Temperature scan of the ac magnetic susceptibility of **DyPd** in B = 0.1 T applied dc magnetic field. a,c) Real component b,d) Imaginary component recorded in the frequency range 1-1100 Hz. e) Real component f) Imaginary component recorded in the frequency range 10-10000 Hz. The black lines are the best fit (see text).

References:

1. Perfetti, M., Cantilever torque magnetometry on coordination compounds: from theory to experiments. *Coord. Chem. Rev.* **2017,** *348*, 171-186.
2. Abragam, A.; Bleaney, B., *Electron Paramagnetic Resonance of Transition Ions*. Dover: New York, 1986.
3. Stewart, G., On the interpretation of nuclear quadrupole interaction data for rare-earth nuclei at low symmetry sites. *Hyperfine Interact.* **1985,** *23* (1), 1-16.
4. Perfetti, M.; Sørensen, M. A.; Hansen, U. B.; Bamberger, H.; Lenz, S.; Hallmen, P. P.; Fennell, T.; Simeoni, G. G.; Arauzo, A.; Bartolomé, J.; Bartolomé, E.; Lefmann, K.; Weihe, H.; van Slageren, J.; Bendix, J., Magnetic Anisotropy Switch: Easy Axis to Easy Plane Conversion and Vice Versa. *Adv. Funct. Mater.* **2018,** *32* (28), 1801846.
5. Sørensen, M. A.; Hansen, U. B.; Perfetti, M.; Pedersen, K. S.; Bartolomé, E.; Simeoni, G. G.; Mutka, H.; Rols, S.; Jeong, M.; Zivkovic, I.; Retuerto, M.; Arauzo, A.; Bartolomé, J.; Piligkos, S.; Weihe, H.; Doerrer, L. H.; van Slageren, J.; Rønnow, H. M.; Lefmann, K.; Bendix, J., Chemical tunnel-splitting-engineering in a dysprosium-based molecular nanomagnet. *Nat. Commun.* **2018,** *9* (1), 1292.
6. Car, P. E.; Perfetti, M.; Mannini, M.; Favre, A.; Caneschi, A.; Sessoli, R., Giant field dependence of the low temperature relaxation of the magnetization in a dysprosium(III)-DOTA complex. *Chem. Commun.* **2011,** *47* (13), 3751-3753.

NAB-2

Unequal sensitivities of energy levels in a high-symmetry Ho 3+ complex towards lattice distortions.

Bonde, N. A., Appel, M., Ollivier, J., Weihe, H., & Bendix, J.

Chemical Communications 2022.

https://doi.org/10.1039/D2CC02068H

ChemComm

ROYAL SOCIETY OF CHEMISTRY

COMMUNICATION

View Article Online
View Journal

Cite this: DOI: 10.1039/d2cc02068h

Received 11th April 2022,
Accepted 6th June 2022

DOI: 10.1039/d2cc02068h

rsc.li/chemcomm

Unequal sensitivities of energy levels in a high-symmetry Ho^{3+} complex towards lattice distortions†

Niels A. Bonde, *[ab] Markus Appel, [b] Jacques Ollivier, [b] Høgni Weihe [a] and Jesper Bendix *[a]

High-resolution inelastic neutron scattering has been used to study low-energy magnetic transitions in a Ho^{3+} complex. This complex crystallises in the high-symmetry space group *P*4/*m* and has near-perfect D_{4d} symmetry, which has allowed for the determination of all relevant spin-Hamiltonian parameters. Static and dynamic inhomogeneity in the crystal lattice manifests as a temperature-dependent broadening of the observed magnetic excitations. By implementing distributions in the spin-Hamiltonian parameters, it is possible to reproduce with great accuracy the observed magnetic transition spectrum. This reveals the range to which extraneous perturbations of the crystal field affect low-energy electronic states, such as those involved in quantum tunnelling of magnetisation, in atomic clock transitions, or in spintronics.

Within the field of molecular magnetism and spintronics, the quest for accurate determination of electronic states has no end.[1] For single-ion lanthanide systems, the determination of the electronic states, and their concomitant magnetic properties, is made complicated by the fact that the energy of the pertinent interactions span several orders of magnitude: Hyperfine $\approx 10^{-2}$–10^{-1} cm^{-1} $\leq$ Electronic Zeeman $\approx$ Magnetic Exchange $\approx 10^{-1}$–10^{0} cm^{-1} $\leq$ Crystal Field $\approx 10^{1}$–10^{3} cm^{-1}. With the Crystal Field (CF) being the operative component of the spin-Hamiltonian, most research has been aimed at the design of static CFs in an attempt to engineer their corresponding magnetic properties.[2] The difficulty lies in taking properly into account the static and dynamic properties of the crystal lattice acting on the CF of the lanthanide ion. First, a site-dependent variation in the CF is caused by static disorder, and secondly, due to phonons (quantized vibrations of the crystal lattice), each lanthanide is subject to a CF varying with time. The dynamic magnetic properties of single-ion lanthanide systems are dictated in large part by spin-lattice relaxation, in which a direct coupling between the lanthanide Single-Molecule Magnet (abbr. SMM) and the phonons is formed. Here, absorption and emission of phonons offer pathways by which the SMMs may lose their magnetization.[3,4] A common way of measuring this effect is by ac-SQUID magnetometry, from which magnetic relaxation rates may be extracted. This technique however reveals no information on the energy levels of the SMM or of the phonon modes. This information is necessary to understand the spin-lattice relaxation process. Consequently, spectroscopic techniques are required. The challenge is to investigate both magnetic and solid state dynamics across several orders of magnitude, and the only spectroscopic technique capable of doing so is Inelastic Neutron Scattering (abbr. INS), which is pre-eminent in offering information on Ln SMMs.[5] We present here a high-resolution INS experiment (see Fig. 1) on the compound $PPh_4[Ho\{Pd(SAc)_4\}_2]$ (SAc = thioacetate, abbr. **HoPd**, see Fig. 2), where it is possible to quantify the direct perturbation from phonons on the lowest energy states.

The square-planar complex $[Pt(SAc)_4]^{2-}$ was first employed as a tetradentate ligand towards first-row transition metals,[6] but has since then been used across the periodic table.[7] By utilising the structure-directing properties of this ligand or its Pd^{2+} analogue (see ESI,† Fig. S1), it is possible to engineer high-symmetry lanthanide complexes of the type $[Ln\{M(SAc)_4\}_2]^-$ (M = Pd^{2+}/Pt^{2+}, abbr. **LnM**) wherein a lanthanide ion is encapsulated with two of the tetradentate Pd^{2+}/Pt^{2+} metaloligands.[8] This series of complexes has been the focus of much research, because their static and dynamic magnetic properties can be fine-tuned by chemical design. The angle of rotation between the two metaloligands (illustrated in Fig. 2 as ϕ) can be controlled by changing the counter ion, and this angle was shown to be instrumental in defining the rate of quantum tunnelling of magnetisation.[9] It was also shown possible to switch the magnetic anisotropy of the lanthanide ion by simply changing temperature and magnetic field.[10] This result has led

---

[a] *University of Copenhagen, Department of Chemistry, Inorganic Section. Universitetsparken 5, 2100 Copenhagen, Denmark. E-mail: Nielsandreasbonde@gmail.com, Bendix@chem.ku.dk*
[b] *Institut Laue-Langevin, 71 Avenue des Martyrs, 38000 Grenoble, France*

† Electronic supplementary information (ESI) available. See DOI: https://doi.org/10.1039/d2cc02068h

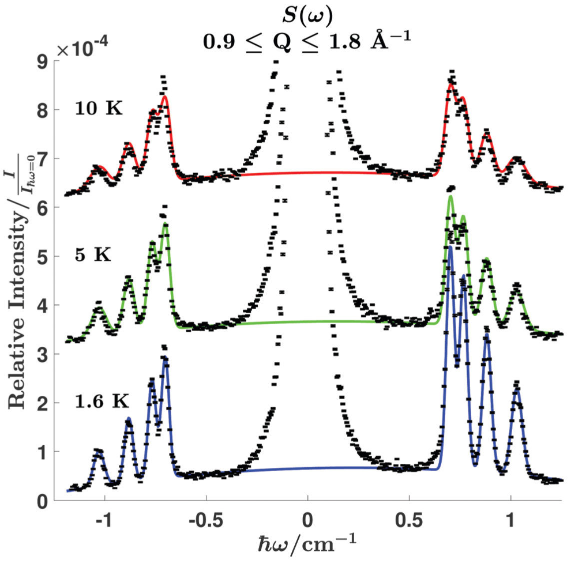

Fig. 1 INS spectra of **HoPd** as points with error bars. The abscissa is neutron energy loss and the ordinate is intensity relative to the elastic peak (truncated) at zero energy transfer. The spectra at 5 and 10 K have been offset from the spectrum at 1.6 K to highlight the temperature dependence. Calculated spectra are shown as solid lines.

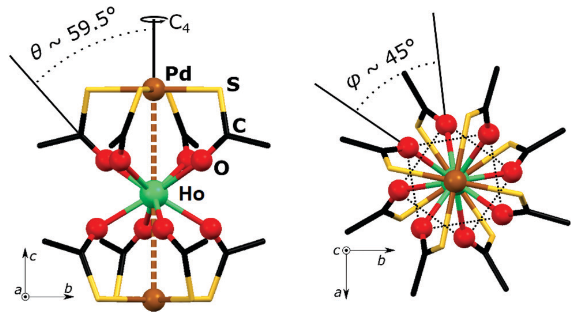

Fig. 2 Crystal Structure of **HoPd**. Space group *P*4/*m*. $\mathrm{PPh_4}^+$ counter ion and hydrogen omitted for clarity. θ is the angle between the $\mathrm{C_4}$ rotation axis (crystallographic *c* axis) and the Ho–O bond. ϕ is the angle of rotation between the two coplanar squares of oxygen.

to a new understanding of magnetic anisotropy, with phase diagrams being better descriptors.[11] By comparing the static and dynamic magnetic properties of two series of isostructural compounds **LnPd** and **LnPt** (Ln = Tb, Dy, Ho and Er), it was concluded that the apical $\mathrm{Pt^{2+}/Pd^{2+}}$ ions directly interact with the lanthanide ion.[12] This $\mathrm{Ln^{3+}{-}M^{2+}}$ ($\mathrm{M = Pt^{2+}, Pd^{2+}}$) interaction and its influence on the static and dynamic magnetic properties of the lanthanide ion has also been investigated in low-symmetry systems by other groups.[13,14]

Because of the high symmetry of the **LnM** series of complexes, it has been possible to derive a CF-parametrisation that is consistent across multiple lanthanides. Only because of the accuracy of that parametrisation, it is now possible to investigate subtle effects influencing the properties of the SMM, such as a perturbation of the CF by phonons. **HoPd** is a prime candidate for such investigations, as it has a rich energy-level spectrum in the range 0–1 cm^{-1}, from which it is possible to gain insight in the dynamic nature of the CF. $\mathrm{Ho^{3+}}$ is a $4f^{10}$ ion with a $^5I_8$ ground term, and for **HoPd**, the ground state pseudo-doublet $|m_J\rangle = |\pm 4\rangle$ is split due to a small contribution from the off-diagonal CF parameter B_4^4 (Stevens parametrisation[15]), which arises from minor deviations from ideal $D_{4\mathrm{d}}$ symmetry.[16] Furthermore, the only naturally occurring isotope of holmium is ^{165}Ho, which has a nuclear spin of $I = 7/2$, and a hyperfine interaction between this nucleus and the $J = 8$ manifold further splits the pseudo-doublet into states of total angular momentum $\vec{F} = \vec{J} + \vec{I}$. The resultant set of states yield multiple allowed INS transitions, which manifest as the four Stokes and anti-Stokes peaks in Fig. 1. The observed peaks have significantly different intensities and line widths, and, importantly, all of the line widths are broader than the instrumental resolution. The line width is also noted to increase with temperature (see ESI,† Fig. S2). This indicates an effective distribution of the energies of the electronic states, which depends on thermally activated processes. Since the energies of the INS transitions depend only on the two parameters B_4^4 and A (see eqn (1)), the broadening of the line widths result from distributions in these two parameters. A distribution in both B_4^4 and A is necessary to account for the different line widths of each transition. A Gaussian distribution is therefore implemented for each. The effective spin-Hamiltonian reads:

$$\hat{H}\left[G_{B_4^4}, G_\mathrm{A}\right] = \sum_{k=2,4,6} B_k^0 \hat{O}_k^0 + B_4^4 \hat{O}_4^4 + A\,\hat{I}\cdot\hat{J} \qquad (1)$$

The Hamiltonian is parametrically defined by a probability, given as the product of the two Gaussians, each defining the probability of finding the $\mathrm{Ho^{3+}}$ with that value of B_4^4 and A.

$$\begin{aligned} G_{B_4^4} &= \frac{1}{\sigma_{B_4^4}\sqrt{2\pi}} \exp\left(\frac{-\left(B_4^4 - \mu_{B_4^4}\right)^2}{2{\sigma_{B_4^4}}^2}\right) \\ G_\mathrm{A} &= \frac{1}{\sigma_\mathrm{A}\sqrt{2\pi}} \exp\left(\frac{-(A-\mu_A)^2}{2{\sigma_\mathrm{A}}^2}\right) \end{aligned} \qquad (2)$$

Here G_x, μ_x and σ_x (where x = A or B_4^4) are the Gaussian probabilities, expectation values and standard deviations, respectively, where each Gaussian may be discretised by n points. The spin-Hamiltonian must then be solved n^2 times, with a resulting INS spectrum to be calculated each time. The spectra are then weighted appropriately by the by the product of the Gaussian probabilities $G_{B_4^4}$ G_A and summed. The values of $\sigma_{B_4^4}$ and σ_A (see Table 1) were found by an iterative fitting routine, which simulated the full magnetic INS spectrum of **HoPd** (*vide infra*).

The experiment[17] was performed at Institut Laue–Langevin with the high-resolution backscattering spectrometer IN16 BATS (see ESI† for details).[18] The inelastic magnetic scattering

Table 1 Fitted parameters for the distribution of the Crystal Field. μ_A = 829.7 MHz and $\mu_{B_4^4} = 3.623 \times 10^{-3}$ cm^{-1} are the expectation values for the Gaussian distributions

Temperature (K)	σ_A (MHz)	σ_A/μ_A (%)	$\sigma_{B_4^4}$ (cm^{-1})	$\sigma_{B_4^4}/\mu_{B_4^4}$ (%)
1.6	31.49	3.80	3.762×10^{-5}	1.04
5	47.99	5.78	4.859×10^{-5}	1.34
10	59.34	7.15	5.949×10^{-5}	1.64

from lanthanide single-ion systems covering both the electronic and nuclear contributions is given by eqn (3).[19,20]

$$\frac{\mathrm{d}^2\sigma}{\mathrm{d}\Omega\mathrm{d}E_\mathrm{f}} = \frac{k_\mathrm{f}}{k_\mathrm{i}}\sum_{m_\mathrm{F}'}\sum_{m_\mathrm{F}} P_{m_\mathrm{F}} \cdot \left|\left\langle Fm_\mathrm{F}'\right| -\frac{1}{2}\gamma r_0 g_J F_{\mathrm{Ho}^{3+}}(Q)\left[\hat{J} \times \vec{Q}\right] \times\vec{Q} + \left(\frac{1}{2I+1}((I+1)b^+ + Ib^-) + \frac{1}{2I+1}(b^+ - b^-)\hat{I}\right)\left|Fm_\mathrm{F}\right\rangle\right|^2 \tag{3}$$

The scattering intensity as function of energy- and momentum-transfer, $\frac{\mathrm{d}^2\sigma}{\mathrm{d}\Omega\mathrm{d}E_\mathrm{f}}$ is calculated as contributions from transitions between all states of total angular momentum $\vec{F} = \vec{J} + \vec{I}$, each transition being weighted by the Boltzmann population factor for the originating state and to the ratio of the neutron momentum-transfer $\frac{k_\mathrm{f}}{k_\mathrm{i}}$. The first part of the operator governs the interaction of the neutron with the angular momentum associated with the electrons where $\gamma = -1.913\ \mu_\mathrm{N}$ is the neutron magnetic moment, $r_0 = 2.818 \times 10^{-15}$ m is the classical radius of the electron, g_J is the Landé g-factor, and $F_{\mathrm{Ho}^{3+}}$ is the form factor for Ho^{3+}. The second part governs the interaction of the neutron with the nuclear spin of Ho^{3+}, with b^+ and b^- being scattering lengths. Simulations were made using a locally written program that solves eqn (3) for various combinations of the distributed parameters B_4^4 and A, each combination being weighted appropriately with the corresponding Gaussian weights. The sum of spectra is scaled *ex post facto* and the measured background is added (see ESI† for details).

Although the observed transitions retain intensity from both the electronic and nuclear contributions, it is amenable to distinguish ESR-active and NMR-active transitions, depending on which contribution to the scattering is greater. In the present case, the intensities of the ESR-active transitions (highlighted in the middle panel of Fig. 3 as black arrows) are larger than the NMR-active transitions by two orders of magnitude. The NMR-active transitions are of course fully simulated by the above-mentioned approach, but their contribution to the total scattering is minuscule and not resolved.

Our findings conclude that $\sigma_{B_4^4}$ and σ_A increase with temperature, which is consistent with the initial observation that the width of the transition peaks increase with temperature. Any temperature-dependence of $\sigma_{B_4^4}$ and σ_A must be the result of dynamic distortions of the crystal lattice. There will also be a static CF-distribution, which can be understood as the limit of $\sigma_{B_4^4}$ and σ_A as temperature approaches 0 K, but as $\sigma_{B_4^4}$ and σ_A nearly double in value going from 1.6 K to 10 K, we may assume that static contributions are swamped at temperatures higher than a few kelvin.

The effect of the CF-distribution is to smear the energy levels; no longer are they defined by exact energies, but rather each has a distribution of its own. The extent to which this is true is, however, not equal for all states. In Fig. 3, the distribution in energies of the tunnelling-gap states are shown, and it is evident that the lowest quartet of Kramers doublets are significantly more perturbed by the CF distribution. This is caused by the different sensitivities of the quartets to the parameters A

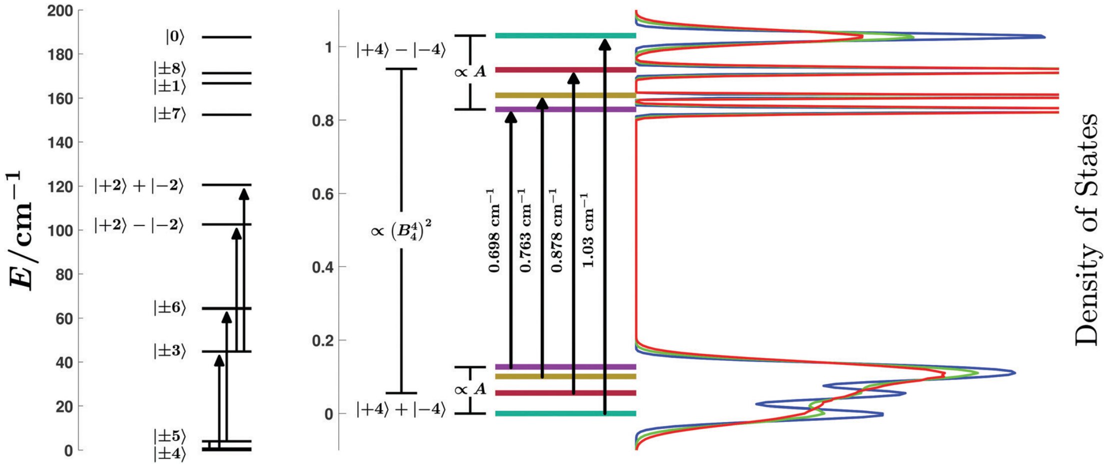

Fig. 3 Left panel: Energy level diagram with $|m_J\rangle$ designations of **HoPd**. Black arrows indicate INS transitions previously observed.[12] Middle panel: Expansion of the lowest energy $|\pm4\rangle$ electronic pseudo-doublet. Hyperfine levels are indicated with colors corresponding to the nuclear spin component of the state as $|m_I\rangle = |\pm7/2\rangle$ (jade), $|\pm5/2\rangle$ (ruby), $|\pm3/2\rangle$ (amber), and $|\pm1/2\rangle$ (amethyst). Black arrows indicate INS transitions observed in this work. Right panel: Density of states (truncated) as obtained from the theoretical modelling of the observed INS spectra. Blue, green, and red indicate 1.6 K, 5 K, and 10 K, respectively.

and B_4^4. The slope of the energy (see ESI,† Fig. S3) for the lowest quartet as function of B_4^4 is greater than that of the highest, resulting in a wider distribution of energy levels. This results from the slight admixture of the $|0\rangle$ state into the lowest quartet. The degree to which this mixing happens is dependent on the relative size of the axial CF parameters, which suggests that control over the energetic distribution of the lowest quartet is found in the design of the axial CF. In contrast, the slope as function of A is nearly identical for the upper and lower quartet.

Conceptualising distributions in the CF parameters (here B_4^4 but principally for all) is straightforward, as it is easy to intuit the influence of vibrating ligands on the electrostatic potential the Ho^{3+}-ion observes. This is less so the case for a distribution in the hyperfine coupling constant. They are, however, entirely equivalent; the hyperfine interaction acts on the spin-orbit angular momentum $\vec{J} = \vec{L} + \vec{S}$, and so does the CF. Any change in the CF by vibrations affects the entire J-multiplet. Thus, a distribution in the hyperfine coupling is equally well understood as a perturbation of the entire J-multiplet.

HoPd share many characteristics with another notable Ho^{3+} complex, and it is therefore possible to compare their physical properties. The polyoxometalate complex $Na_9[Ho(W_5O_{18})_2]\cdot nH_2O$ (abbr. **HoW_{10}**),[21] for which it was shown that stable atomic clock transitions can exist in molecular systems,[22,23] has a structure similar to **HoPd**. In both cases, the coordination environment is a distorted square anti-prism, in which the extra-diagonal element B_4^4 splits the ground state pseudo-doublet $|\pm 4\rangle$, and in both cases, a hyperfine interaction of 830 MHz further splits these states. Despite the very comparable values of $\mu_{B_4^4}$ in **HoPd** (3.623×10^3 cm^{-1}) and **HoW_{10}** (3.14×10^3 cm^{-1}), the observed standard deviations are significantly different; Given as a percentage of $\mu_{B_4^4}$, at 5 K $\sigma_{B_4^4}$ is 1.34% for **HoPd** and 0.67% for **HoW_{10}**.‡ It is quite possible that the lower standard deviation in **HoW_{10}** is a sign of higher resilience toward dynamic distortions, which seems plausible considering the significantly higher rigidity of the $[W_5O_{18}]^{6-}$ metaloligand compared to $[Pd(SAc)_4]^{2-}$. Whether it is for this reason that **HoW_{10}** shows dynamic magnetic properties on the time scale of SQUID magnetometry and **HoPd** does not, cannot be known at this point. Although, the computational process required to show the correlation between ligand rigidity, lattice dynamics, and dynamic magnetic properties have in recent years been laid out,[24,25] such demanding computations have unfortunately yet to be carried out for systems as complex as **HoPd** or **HoW_{10}**.

In conclusion, INS has been used to study the lowest-energy states of the Ho^{3+}-analogue of a series of archetypical Ln SMMs. Because of the precise determination of the CF across this series, and the unique CF- and HF-splittings of **HoPd**, it has been possible to deconvolute the energetic perturbation of the lowest-energy states by dynamic distortions of the crystal lattice. Having only studied the distributions in the two parameters B_4^4 and A, we found that the standard deviation of the energy of the each state is unique and increasing with temperature. For the ground state at 1.6 K, $\sigma_E = 1.7 \times 10^{-2}$ cm^{-1} $\approx$ 500 MHz which is in the high-energy range of radiofrequency radiation. Dynamic processes involving this state, like those involved in quantum tunnelling of magnetisation, in atomic clock transitions, or in spintronics, will be dependent on that distribution in energy. Notably, the low-energy states of **HoPd** have widely different sensitivities toward dynamic distortions, resulting from different admixtures of the $|0\rangle$ state. This provides a way of chemically controlling the dynamic properties, since the magnitude of the admixture is defined by the axial CF components.

The authors send their gratitude to M. A. Sørensen, M. Perfetti, and U. B. Hansen. N. A. Bonde sends his personal regards to E. M. H. Larsen and N. Kofod.

Conflicts of interest

There are no conflicts to declare.

Notes and references

‡ This is despite the fact, that the inhomogeneous broadening observed in the ESR spectra of **HoW_{10}** is calculated using only a distribution in B_4^4, whereas the inhomogeneous broadening observed in the INS spectra of **HoPd** is calculated using a distribution in both B_4^4 and A. In **HoW_{10}**, $\sigma_{B_4^4}$ is therefore forced to account for both distributions.

1 M. N. Leuenberger and D. Loss, *Nature*, 2001, **410**, 789–793.
2 J. D. Rinehart and J. R. Long, *Chem. Sci.*, 2011, **2**, 2078–2085.
3 L. Gu and R. Wu, *Phys. Rev. Lett.*, 2020, **125**, 117203.
4 A. Lunghi and S. Sanvito, *Sci. Adv.*, 2019, **5**, 1–8.
5 M. A. Dunstan, R. A. Mole and C. Boskovic, *Eur. J. Inorg. Chem.*, 2019, 1090–1105.
6 F. G. Baddour, S. R. Fiedler, M. P. Shores, J. A. Golen, A. L. Rheingold and L. H. Doerrer, *Inorg. Chem.*, 2013, **52**, 4926–4933.
7 S. A. Beach and L. H. Doerrer, *Acc. Chem. Res.*, 2018, **51**, 1063–1072.
8 M. A. Sørensen, H. Weihe, M. G. Vinum, J. S. Mortensen, L. H. Doerrer and J. Bendix, *Chem. Sci.*, 2017, **8**, 3566–3575.
9 M. A. Sørensen, U. B. Hansen, M. Perfetti, K. S. Pedersen, E. Bartolomé, G. G. Simeoni, H. Mutka, S. Rols, M. Jeong, I. Zivkovic, M. Retuerto, A. Arauzo, J. Bartolomé, S. Piligkos, H. Weihe, L. H. Doerrer, J. van Slageren, H. M. Rønnow, K. Lefmann and J. Bendix, *Nat. Commun.*, 2018, **9**, 1292.
10 M. Perfetti, M. A. Sørensen, U. B. Hansen, H. Bamberger, S. Lenz, P. P. Hallmen, T. Fennell, G. G. Simeoni, A. Arauzo, J. Bartolomé, E. Bartolomé, K. Lefmann, H. Weihe, J. van Slageren and J. Bendix, *Adv. Funct. Mater.*, 2018, **28**, 1–8.
11 M. Perfetti and J. Bendix, *Inorg. Chem.*, 2019, **58**, 11875–11882.
12 N. A. Bonde, J. B. Petersen, M. A. Sørensen, U. G. Nielsen, B. Fåk, S. Rols, J. Ollivier, H. Weihe, J. Bendix and M. Perfetti, *Inorg. Chem.*, 2020, **59**, 235–243.
13 D. C. Izuogu, T. Yoshida, H. Zhang, G. Cosquer, K. Katoh, S. Ogata, M. Hasegawa, H. Nojiri, M. Damjanović, W. Wernsdorfer, T. Uruga, T. Ina, B. K. Breedlove and M. Yamashita, *Chem. – Eur. J.*, 2018, **24**, 9285–9294.
14 T. Yoshida, D. C. Izuogu, H. T. Zhang, G. Cosquer, H. Abe, W. Wernsdorfer, B. K. Breedlove and M. Yamashita, *Dalton Trans.*, 2019, **48**, 7144–7149.
15 K. W. Stevens, *Proc. Phys. Soc., London, Sect. A*, 1952, **65**, 209–215.
16 J. J. Baldoví, S. Cardona-Serra, J. M. Clemente-Juan, E. Coronado, A. Gaita-Ariño and A. Palii, *Inorg. Chem.*, 2012, **51**, 12565–12574.
17 J. Ollivier, M. Appel, N. A. Bonde, H. Weihe and J. Bendix, *High Resolution on the Ho SMM, Institut Laue-Langevin (ILL), Grenoble*, 2018, DOI: **10.5291/ILL-DATA.TEST-2872**.
18 M. Appel, B. Frick and A. Magerl, *Sci. Rep.*, 2018, **8**, 1–8.
19 S.-H. Lee and I. A. Zaliznyak, *Magn. Neutron Scattering,* Brookhaven National Laboratory, 2004, pp. 11–31.
20 G. L. Squires, *Introd. Theory Therm. Neutron Scattering*, Cambridge University Press, 2012, pp. 129–195.
21 S. Ghosh, S. Datta, L. Friend, S. Cardona-Serra, A. Gaita-Ariño, E. Coronado and S. Hill, *Dalton Trans.*, 2012, **41**, 13697–13704.
22 M. Shiddiq, D. Komijani, Y. Duan, A. Gaita-Ariño, E. Coronado and S. Hill, *Nature*, 2016, **531**, 348–351.
23 S. Giménez-Santamarina, S. Cardona-Serra, J. M. Clemente-Juan, A. Gaita-Ariño and E. Coronado, *Chem. Sci.*, 2020, **11**, 10718–10728.
24 A. Lunghi and S. Sanvito, *J. Phys. Chem. Lett.*, 2020, **11**, 6273–6278.
25 M. Briganti, F. Santanni, L. Tesi, F. Totti, R. Sessoli and A. Lunghi, *J. Am. Chem. Soc.*, 2021, **143**, 13633–13645.

Electronic Supplementary Material (ESI) for ChemComm.

Supporting Information

Unequal Sensitivities of Energy Levels in a High-Symmetry Ho^{3+} Complex Towards Lattice Distortions

Niels A. Bonde,[a,b] Markus Appel,[b] Jacques Ollivier,[b] Høgni Weihe,[a] and Jesper Bendix*[a]

[a] *a. University of Copenhagen, Department of Chemistry, Inorganic Section. Universitetsparken 5, 2100 Copenhagen.* [b] *b. Institut Laue-Langevin, 71 Avenue des Martyrs, 38000 Grenoble, France.* * *Corresponding Author.*

Structure

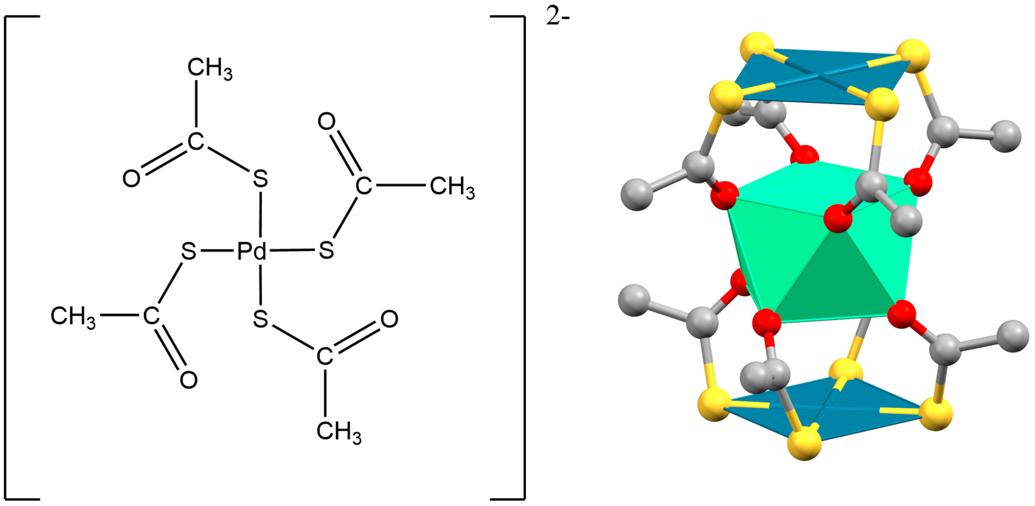

Figure 1: **Left:** Illustration of the $[Pd(SAc)_4]^{2-}$ metaloligand. **Right:** Crystal structure of **HoPd** with highlighted square anti-prismatic coordination around Ho^{3+}. Hydrogen and PPh_4^+ counter ion omitted for clarity.

Experimental

Inelastic Neutron Scattering:
HoPd was synthesised according to published procedure.[1] A sample of 2g was wrapped in aluminium foil and packed in a standard ILL aluminium sample container. Data acquisition was performed using the low repetition rate chopper setting with a 4° slit opening, which offered a energy window of 2.7 cm^{-1}. The sample was measured for 6 hours each at 1.6, 5, and 10 K, and data was normalized to a standard vanadium sample. Data reduction was performed in Mantid[2] and exported to Matlab for plotting. The resolution of the experiment is modelled as follows: A Gaussian approximation of the elastic peak gave a temperature-independent standard deviation of 0,01302 cm^{-1}. This is taken as the resolution at zero energy transfer. The energy transfer-dependence of the resolution has been given by Appel[3] and is linear with these instrument settings.

Simulation software was built on the Matlab package Easyspin[4], which was used to set up the spin system of **HoPd** and to generate all spin operators necessary to calculate INS transition probabilities. Due to the scale and complexity of the simulation, a full description can not be provided here, but code and detailed explanations can be shared upon request.

Zoom of INS Spectrum

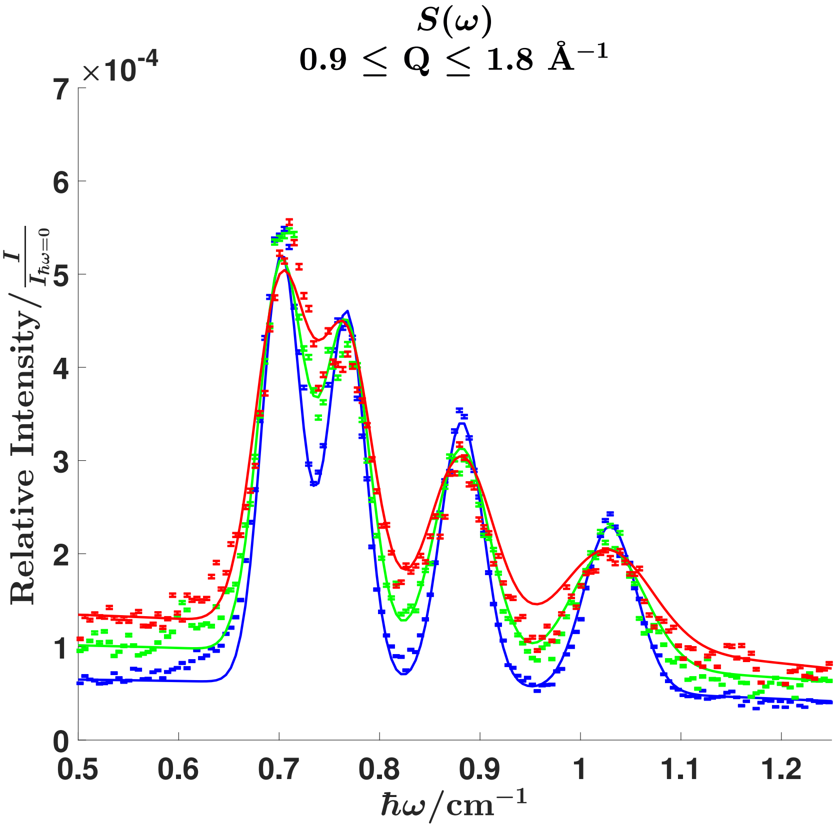

Figure 2: Zoom of the INS spectra shown in fig. 1. The spectra at 5 and 10 K are scaled to approximately the same intensity as 1.6 K to highlight the broadening of the peaks with increasing temperature.

Energy Level Surface Diagram

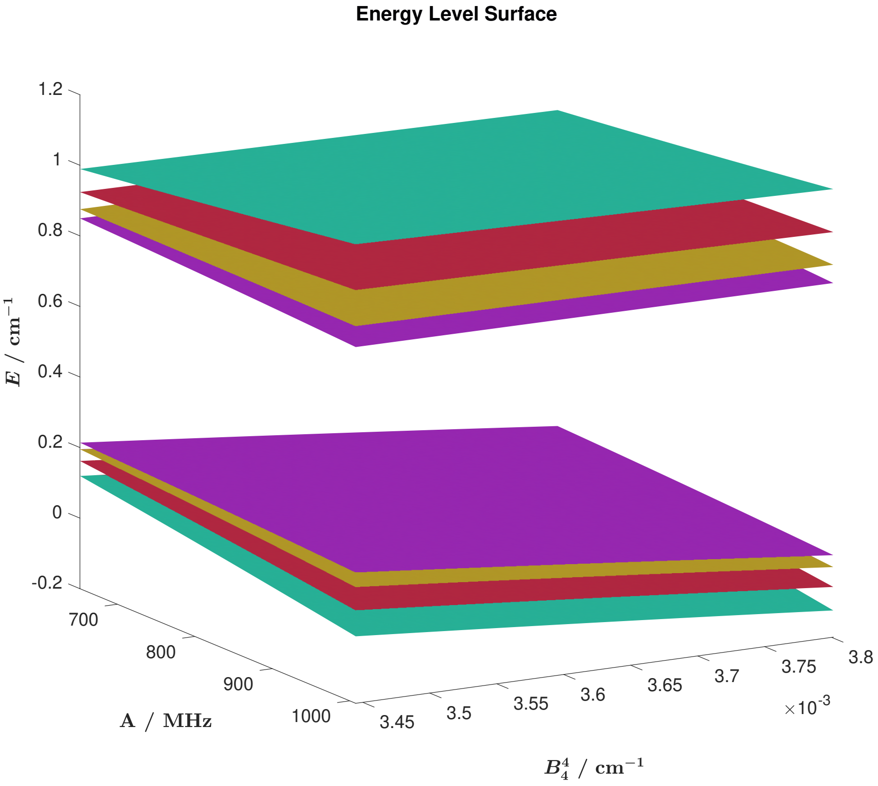

Figure 3: Energy level surface diagram of the HF-split pseudo-doublet calculated within 3σ of A and B_4^4. Surfaces are coloured corresponding to the nuclear spin component of the state as $|m_I> = |\pm 7/2>$ (jade), $|\pm 5/2>$ (ruby), $|\pm 3/2>$ (amber), and $|\pm 1/2>$ (amethyst).

References

[1] M. A. Sørensen, H. Weihe, M. G. Vinum, J. S. Mortensen, L. H. Doerrer and J. Bendix, *Chem. Sci.*, 2017, **8**, 3566–3575.

[2] O. Arnold, J. C. Bilheux, J. M. Borreguero, A. Buts, S. I. Campbell, L. Chapon, M. Doucet, N. Draper, R. Ferraz Leal, M. A. Gigg, V. E. Lynch, A. Markvardsen, D. J. Mikkelson, R. L. Mikkelson, R. Miller, K. Palmen, P. Parker, G. Passos, T. G. Perring, P. F. Peterson, S. Ren, M. A. Reuter, A. T. Savici, J. W. Taylor, R. J. Taylor, R. Tolchenov, W. Zhou and J. Zikovsky, *Nucl. Instrum. Methods Phys. Res., Sect. A*, 2014, **764**, 156–166.

[3] M. Appel, B. Frick and A. Magerl, *Sci. Rep.*, 2018, **8**, 1–8.

[4] S. Stoll and A. Schweiger, *J. Mag. Reson.*, 2006, **178**, 42–55.

NAB-3

Experimental Assignment of Long-Range Magnetic Communication Through Pd & Pt Metallophilic Contacts

Emil M. H. Larsen, Niels A. Bonde, Høgni Weihe, Jacques Ollivier, Tom Vosch, Thomas Lohmiller, Karsten Holldack, Alexander Schnegg, Mauro Perfetti, & Jesper Bendix

Submitted to Chemical Science on 16/09-2022

Journal Name

ARTICLE TYPE

Cite this: DOI: 00.0000/xxxxxxxxxx

Experimental Assignment of Long-Range Magnetic Communication Through Pd & Pt Metallophilic Contacts†

Emil M. H. Larsen,[‡a] Niels A. Bonde,[‡a,b] Høgni Weihe,[a] Jacques Ollivier,[b] Tom Vosch,[a] Thomas Lohmiller,[c,d] Karsten Holldack,[f] Alexander Schnegg,[d,e] Mauro Perfetti,[g] and Jesper Bendix*[a]

Received Date
Accepted Date

DOI: 00.0000/xxxxxxxxxx

Record-breaking magnetic exchange interactions have previously been reported for 3d-metal dimers of the form $[M(Pt(SAc)_4)(pyNO_2)]_2$ (M = Ni or Co) that are linked in the solid state via metallophilic Pt···Pt bridges. This contrasts the terminally capped monomers $[M(Pt(SAc)_4)(py)_2]$, for which neither metallophilic bridges nor magnetic exchange interactions are found. Computational modeling has shown that the magnetic exchange interaction is facilitated by the pseudo-closed shell $d^8 \cdots d^8$ metallophilic interaction between the filled Pt^{2+} $5d_{z^2}$ orbitals. We present here inelastic neutron scattering experiments on these complexes, wherein the dimers present an oscillatory momentum-transfer-dependence of the magnetic transitions. This allows for the unequivocal experimental assignment of the distance between the coupled ions, which matches exactly the coupling pathway via the metallophilic bridges. Furthermore, we have synthesized and magnetically characterized the isostructural palladium-analogues. The magnetic coupling across the Pd···Pd bridge is found through SQUID-magnetometry and FD-FT THz-EPR spectroscopy to be much weaker than via the Pt···Pt bridge. The weaker coupling is traced to the larger radial extent of the $5d_{z^2}$ orbitals compared to that of the $4d_{z^2}$ orbitals. The existence of a palladium metallophilic interaction is evaluated computationally from potential surface cuts along the metal stretching direction. Similar behavior is found for the Pd···Pd and Pt···Pt-systems with clear minima along this coordinate and provide estimates for the force constant for this distortion. The estimated M···M stretching frequencies are found to match experimental observed, polarized bands in single-crystal Raman spectra close to 45 cm^{-1}. This substantiates the existence of energetically relevant Pd···Pd metallophilic interactions. The unique properties of both Pt^{2+} and Pd^{2+} constitutes an orthogonal reactivity, which can be utilized for steering both the direction and strength of magnetic interactions.

1 Introduction

Structure-property relations are the cornerstone of the development of molecule-based magnetic systems. This is true for both

---

† Electronic supplementary information (ESI) available: Experimentals, crystallographic details(CCDC 2207828-2207833), Computational data, INS data, FD-FT THz-EPR data. For ESI and crystallographic data in CIF or other electronic format see DOI: 00.0000/00000000.

‡ These authors contributed equally to this work.

[a] *Department of Chemistry, University of Copenhagen, Universitetsparken 5, DK-2100 Copenhagen, Denmark.*

[b] *Institut Laue-Langevin, 71 avenue des Martyrs, CS 20156, 38042 Grenoble Cedex 9, France*

[c] *Humboldt-Universität zu Berlin, Institut für Chemie, Brook-Taylor-Str. 2, 12489 Berlin, Germany*

[d] *EPR4Energy Joint Lab, Department Spins in Energy Conversion and Quantum Information Science, Helmholtz Zentrum Berlin für Materialien und Energie GmbH, Albert-Einstein-Straße 15, 12489 Berlin, Germany*

[e] *Max Planck Institute for Chemical Energy Conversion, Stiftstrasse 34-36, D-45470 Mülheim an der Ruhr, Germany*

[f] *Department of Optics and Beamlines, Helmholtz Zentrum Berlin für Materialien und Energie GmbH, Albert-Einstein-Straße 15, 12489 Berlin, Germany*

[g] *Department of Chemistry "U. Schiff", University of Florence, Via della Lastruccia 3-13,*

fundamental science as well as for application-directed research towards quantum computing and spintronics.[1–5] However, controlling the molecular structure and the solid state packing of coordination compounds remains a difficult and yet unsolved challenge.[6–10] This can be considered a result of the much narrower range of orthogonal reaction pathways in coordination chemistry compared to the vast range of selective, orthogonal reactions in the toolbox of organic synthetic chemistry. The ideal ligand in molecular magnetism provides not only structural control but also opportunities for strong and tunable magnetic exchange coupling pathways and ideally a second coordination sphere amenable for modular buildup of polynuclear assemblies or for deposition on surfaces. A recently introduced class of metalloligands $[\mathrm{M'(SOCR)_4}]^{2-}$ (M' = $\mathrm{Pt^{2+}}$/ $\mathrm{Pd^{2+}}$, SOCR = thiocarboxylate) has been found to meet these criteria in a way no other ligand has. In these metalloligands, the soft sulfur of the thiocarboxylate group coordinates to the soft $\mathrm{Pt^{2+}}$/$\mathrm{Pd^{2+}}$ ion, leaving the hard oxygen open for coordination towards another ion. They have been shown to act as tetradentate chelating ligands toward a range of hard metal ions (see scheme in Fig. 1). For nearly a decade, the Doerrer group has been working on developing the science of heterobimetalic lantern complexes incorporating the Pt-metalloligands and a variable hard metal ion of group two and first-row transition metals.[11–19] In parallel, the coordination chemistry of both the Pt- and Pd-metalloligands with the lanthanide elements has been developed by us[20–24] and the group of Yamashita.[25–29]

In the transition metal chemistry of the Pt-ligands, the complexes are formed by the bridging action of the four thiocarboxylate linking the soft $\mathrm{Pt^{2+}}$ ion with the hard metal ion. An apical ligand may coordinate either metal termini, thereby completing the coordination environment(see scheme in Fig. 1). Monodentate apical ligands may be chosen such that they bind to either the $\mathrm{Pt^{2+}}$ ion, the hard metal ion, or both. In the cases where the apical ligand binds only to the hard metal ion, the complexes often form dimeric structures in the crystalline phase. The dimerisation is caused by a metallophilic interaction, where the $\mathrm{Pt^{2+}}$ ions of two lantern complexes interact with one another, forming a weak "bond". It was found by the Doerrer group for complexes of $\mathrm{Co^{2+}}$ and $\mathrm{Ni^{2+}}$ that pyridine (py) coordinates both the hard and soft metal ions, thereby forming monomeric $[\mathrm{M(Pt(SAc)_4)(py)_2}]$ structures, but 3-nitropyridine ($\mathrm{pyNO_2}$) coordinates only the hard metal ion, thereby forming dimeric $[\mathrm{M(Pt(SAc)_4)(pyNO_2)}]_2$ structures. The monomeric complexes of $\mathrm{Co^{2+}}$ and $\mathrm{Ni^{2+}}$ (abbr. {**CoPt**} and {**NiPt**}) and their dimeric congeners (abbr. $\{\mathbf{CoPt}\}_2$ and $\{\mathbf{NiPt}\}_2$) provide an unique opportunity to investigate the ability of the metallophilic bond to direct the formation of dinuclear assemblies and to mediate a magnetic exchange interaction between the paramagnetic ions. In order to probe the magnetic exchange via metallophilic bridges we synthesize and determine the properties of both monomeric and dimeric palladium analogues of the above-mentioned platinum systems.

For $\{\mathbf{CoPt}\}_2$ and $\{\mathbf{NiPt}\}_2$, a surprisingly strong magnetic exchange interaction has been reported to occur over distances of more than 8.5 Å. In the early days of molecular magnetism, Coffman and Buettner[30] proposed an upper limit function for an antiferromagnetic exchange interaction ($j > 0$, $\hat{\mathbf{H}}_{HDvV} = j\hat{\mathbf{S}}_1 \cdot \hat{\mathbf{S}}_2$ formalism), which would limit interactions over 8.5 Å to a maximum of 2.5 $\mathrm{cm^{-1}}$. $\{\mathbf{NiPt}\}_2$ breaks this limit by one order of magnitude. To verify the strength of the exchange interaction and that the coupling pathway is indeed via metallophilic Pt···Pt bridges, inelastic neutron scattering (INS) was employed. It is well-known that INS is capable of investigating both the strength and pathway of magnetic exchange interactions. This is most commonly used for extended systems, but it also holds for molecular magnetic materials. This was first illustrated by Furrer and Güdel for exchange-coupled dimers using powder-averaged INS. They observed that the magnetic transitions show a momentum-transfer-dependence that decays with the magnetic formfactors of the coupled ions, but does so in an oscillatory manner. The rate of oscillation was shown to be directly determined by the distance between the coupled ions. This has been coined an 'interference effect', because of its connection with the interference of scattered waves from e.g. a double slit. The momentum-transfer-dependence of magnetic transitions thus gives a fingerprint of the exchange pathway, which can be used to unravel complex molecular magnetic materials.[31,32] A similar oscillatory momentum-transfer-dependence is observed for $\{\mathbf{CoPt}\}_2$ and $\{\mathbf{NiPt}\}_2$, fully consistent with the distance between paramagnetic ions across the metallophilic bond and corroborated by our simulations of the INS. We analyze the strength of the magnetic coupling in Pd···Pd versus Pt···Pt dimerized systems by magnetometry and THz spectroscopy and demonstrate a drastic difference. Therefrom, we go on to establish that this difference does not imply that the Pd···Pd metallophilic interactions are correspondingly weaker than those in the platinum-bridged systems. Rather, they are energetically similar and addressable by vibrational spectroscopy.

2 Experimental

2.1 Synthesis

All chemicals were purchased commercially and were used without further purification. Elemental analysis was performed using a FlashEA 1112 instrument. For simplicity, the complexes will be abbreviated with the metals and denoted as either a monomeric or dimeric structure. So, $[\mathrm{Ni(Pt(SAc)_4(pyNO_2)}]_2$ will be $\{\mathbf{NiPt}\}_2$ and the corresponding monomer {**NiPt**}. The complexes $\{\mathbf{CoPt}\}_2$, {**CoPt**} and {**NiPt**} were synthesized with modified published procedures. Detailed synthetic work for the remaining complexes can be found in SI.

2.2 Magnetic Measurements

Magnetic measurements were performed on a Quantum Design MPMS-XL SQUID magnetometer equipped with a 5 T magnet. All samples were ground to a fine powder and congregated with hexadecane before loaded into a polycarbonate capsule. The dc susceptibility measurement was carried out with a field at 0.1 T and in the temperature range 2 to 300 K. The data work-up were done by a locally-written program based on the EasySpin[33] package

---

Sesto Fiorentino, 50019, Italy

input to the MATLAB software, and the experimental data were fitted incorporating a g-factor, an axial (D) and rhombic (E) zero-field splitting, a TIP parameter, and a coupling (j) expressed with the Hamiltonian: $\hat{\mathbf{H}}_{HDvV} = j\hat{\mathbf{S}}_1 \cdot \hat{\mathbf{S}}_2$. Diamagnetic corrections were done using tabulated data for Pascal's constants.[34] The dimeric platinum compounds were fitted incorporating a magnetic impurity which was assumed to be a the monomeric phase without an inter-molecular metallophilic interaction.

2.3 Single Crystal and Powder X-ray Diffraction

Single crystal X-ray diffraction data were collected on a Bruker D8 VENTURE diffractometer equipped with a Mo Kα X-ray ($\lambda = 0.71073$ Å), and a PHOTON 100 CMOS detector. For low temperature measurements at either 100 or 120 K the diffractometer is equipped with an Oxford Cryosystem. All crystals were mounted on capton loops with a small amount of silicone grease. The data reductions were performed in the APEX3 software, and the absorption correction was carried out with the multi-scan method SADABS. The structures were solved in the Olex2 (ver. 1.3) software with the ShelXT software package included. Powder X-ray diffraction data were collected on a Bruker D8 ADVANCE powder diffractometer equipped with a Cu Kα X-ray source ($\lambda = 1.5418$ Å).

2.4 Computational

DFT calculations were done on both {**NiPt**}$_2$ and {**NiPd**}$_2$. By varying the distance between the two either Pt or Pd metal centers, final stage energies were calculated for a geometry optimized structure in both cases. The calculations were done in ORCA with the PBE0 functional and the def2-TZVP basis set. A ZORA formalism was used for the Pt and Pd elements to invoke relativistic effects together with Grimmes dispersion correction to reasonably handle the soft character of the metallophilic interactions.

2.5 Inelastic Neutron Scattering

Inelastic Neutron Scattering (INS) was performed on the samples {**CoPt**}, {**CoPt**}$_2$, {**NiPt**}, and {**NiPt**}$_2$ at the time-of-flight cold neutron spectrometer IN5 at Institut Laue-Langevin, Grenoble, France. Samples of approximately 1 g were wrapped in aluminium foil and packed in aluminium canisters. Using a standard ILL Orange Cryostat, the samples were measured at select temperatures in the range of 1.5 to 100 K and with varying incident neutron wavelength in the range 2 to 3 Å. All measurements were normalized to a standard Vanadium sample. Data was reduced using the program Large Array Manipulation Program (LAMP)[35] and cuts in S(Q,ω) were exported for plotting. All observed magnetic scattering and the corresponding spin Hamiltonian parameters derived therefrom were corroborated by simulating the magnetic scattering. The magnetic scattering by localized spins is given by eq. 1.[36,37]

$$\frac{\delta^2\sigma}{\delta\Omega\delta Q} = \left(-\frac{1}{2}\gamma r_0\right)^2 \frac{1}{Q^2}\frac{k_f}{k_i}\sum_{\Psi_f}\sum_{\Psi_i}\sum_{n=1}^{N} P_{\Psi_i}\cdot \left|\left\langle \Psi_f \left| g_n F_n(Q) e^{i\vec{R}_n\cdot\vec{Q}} \left[\hat{S}_n \times \vec{Q}\right] \times \vec{Q} \right| \Psi_i \right\rangle\right|^2 \qquad (1)$$

Here, the scattering $\frac{\delta^2\sigma}{\delta\Omega\delta Q}$ is expressed as a sum of all possible magnetic transitions. For N = 1 it describes the scattering from paramagnetic monomers, ie. Ψ is the single-ion eigenfunction. Equally, N = 2 describes the scattering from the dimers, where Ψ is the coupled eigenfunction. Here, $\gamma = -1.913\,\mu_N$ is the neutron magnetic moment, $r_0 = 2.818 \cdot 10^{-15}$ m is the classical radius of the electron. $\vec{Q} = \vec{k}_i - \vec{k}_f$ is the neutron momentum transfer, with Q, k_i, and k_f being the length of the corresponding vectors. g_n, $F_n(Q)$, R_n, and $\hat{S}_n$ is the g-factor, magnetic form factor, position, and spin of the n'th ion, respectively. Simulation of magnetic INS spectra were performed with a locally written program, which solves eq. 1 for the given spin system. All simulations are powder-averaged and expressed as $S(Q,\omega)$. Constant-Q or constant-$\hbar\omega$ cuts are scaled ex post facto.

2.6 THz Spectroscopy

Frequency Domain-Fourier Transform THz-EPR (FD-FT THz-EPR) samples of the {**CoPd**}$_2$, {**NiPd**}$_2$, {**NiPd**}, {**NiPt**}$_2$ and {**NiPt**} were prepared by blending 83-103 mg of the respective polycrystalline sample with 50-62 mg polyethylene powder and pressing it into a pellet. FD-FT THz-EPR spectra were recorded in Voigt geometry using low-α mode coherent synchrotron radiation.[38,39] Spectra were recorded in Voigt geometry with its magnetic field component B_1 perpendicular to the static magnetic field B_0. The experimental resolution was 0.5 cm^{-1}. To remove the incident background transmission from the spectrum, referencing was done between spectra recorded at different fields. Magnetic-field division spectra (MDS) at two magnetic fields B_i and B_j are presented as relative transmittance T, experimentally obtained from the measured spectral intensities I as $T_{exp} = I_{B_i}/I_{B_j}$, and calculated from the simulated absorbance spectra A as $T_{sim} = 10^{A_{Bj}-A_{Bi}}$. A 1st-order polynomial baseline correction was applied to the experimental MDS. Simulations were performed using the EasySpin toolbox.[33]

2.7 Raman Spectroscopy

Raman measurements were performed using a micro-Raman setup in back-scattering geometry. The 632.8 nm line of a HeNe laser (Melles-Griot 25-LHR-991-230) was used (85 μW on top of the objective). The beam was focused in an inverted confocal microscope (Olympus IX71) by an Olympus 100X, 1.4-NA oil immersion objective into a diffraction-limited spot. A LL01-633 filter (Semrock) and a BP-633 filter (Optigrate) were used to clean and spectrally narrow the laser light in the excitation path. The polarization of the light was controlled using a polarizing beam splitter (Thorlabs). Raman spectra were recorded using a Princeton Instruments SPEC 10:100 B/LN-eXcelon CCD detector and a SP 2356 spectrometer with a 600 grooves per millimetre grating.

A 30:70 beam splitter (XF122 Omega Optical) was used instead of a dichroic mirror in the microscope. Three RFS-633-OD3-11M filters (Optigrate) were used to block the laser light in the detection path. X-axis calibration was performed with a Neon spectral calibration lamp (6032 Newport). No Y-axis corrections or background removal procedures were performed.

3 Results and Discussion

The fundamental design of the lantern complexes was developed in the Doerrer group[11], here, we expand the series of lantern complexes with the Pd analogs of the complexes $[Ni(Pt(SAc)_4)(pyNO_2)]_2$, $[Co(Pt(SAc)_4)(pyNO_2)]_2$, $[Co(Pt(SAc)_4)(py)_2]$ and $[Ni(Pt(SAc)_4)(py)_2]$. The synthesis of the Pd complexes proved more challenging compared to the Pt complexes. The combination of a more labile metal center and the insolubility of the binary sulfides restricts reaction conditions and care must be taken to obtain phase-pure products. Simultaneously, the Pd···Pd metallophilic interaction is weaker than the Pt···Pt interaction to the extent that formation of the dimerized products is contingent on exact reaction conditions and solvent purity. Thus, the Pd complexes with apical 3-nitropyridine ligands were observed to crystallize both in a monomeric phase without the metallophilic interaction as well as a dimeric phase with the desired metallophilic interaction. The two phases with identical stoichiometry and comparable stability resulted in a mixture of the two crystalline phases for bulk samples if the described synthetic procedures were not carefully followed. To overcome a monomeric impurity in bulk samples of $\{\mathbf{NiPd}\}_2$, it was found that evaporation to dryness from solvent mixtures yielded phase-pure products. While constituting a synthetic complicating factor, the existence of the compounds as monomers and dimers of identical stoichiometry provides for the most direct comparison between monomer and dimer systems. Conversely, a bulk sample with a pure monomeric crystalline phase of the platinum systems, $[M(Pt(SAc)_4)(pyNO_2)]$ was never obtained. However, small levels of monomeric impurities could be detected in powder diffractograms for bulk sample preparations of the dimer phases of $[M(Pt(SAc)_4)(pyNO_2)]_2$. To circumvent that higher propensity of platinum for metallophilic interactions, we have chosen to include monomeric systems with apical ligators on both metals, namely the $[M(Pt(SAc)_4)(py)_2]$ (M = Co, Ni). To make a direct comparison of Pt versus Pd complexes the *bis*-pyrdine Pd based monomers have been synthesized as well.

The structure of all new compounds were characterized crystallographically, and the data are summarized in Table S1 and S2 in the SI. The solid-state structure of $\{\mathbf{CoPd}\}_2$ and $\{\mathbf{NiPd}\}_2$ showed a metallophilic interaction between the two Pd metals linking two lantern complexes, similar to the interaction observed in the dimeric Pt complexes previously reported. In the dimerization of the two lantern units, the rotational barrier of the M'···M' bond (M' = Pd, Pt) is expected to be small and the ensuing conformational freedom to be governed by crystal packing interactions. The conformation is quantified with an averaged dihedral twist angle (τ) across the two MS_4 entities. Not all M···M'···M'···M cores of the dimeric complexes are observed to be linear. Accordingly, a parameter, the displacement angle ϕ: (M···M'···M'), expresses the divergence from the ideal linear metallophilic geometry (ϕ = 180 deg). The four dimeric complexes $\{\mathbf{CoPd}\}_2$, $\{\mathbf{NiPd}\}_2$, $\{\mathbf{CoPt}\}_2$ and $\{\mathbf{NiPt}\}_2$ presented in this work are all in an eclipsed conformation. Compared to the previously reported $[Ni(Pt(SAc)_4)(pyNO_2)]_2$ complex in the staggered conformer the series of four complexes in the same conformer makes for a better direct comparison. Hence, without the conformal change the $\{\mathbf{NiPt}\}_2$ in the eclipsed conformer exhibits a longer metallophilic interaction (3.421 vs. 3.058 Å)[13] and a smaller displacement angle (158.8 vs. 177.8 deg) making the structural parameters significantly more comparable to the remaining three dimers. The dimerization of the two lantern units and the eclipsed conformer for $\{\mathbf{CoPd}\}_2$ is seen in Figure 1

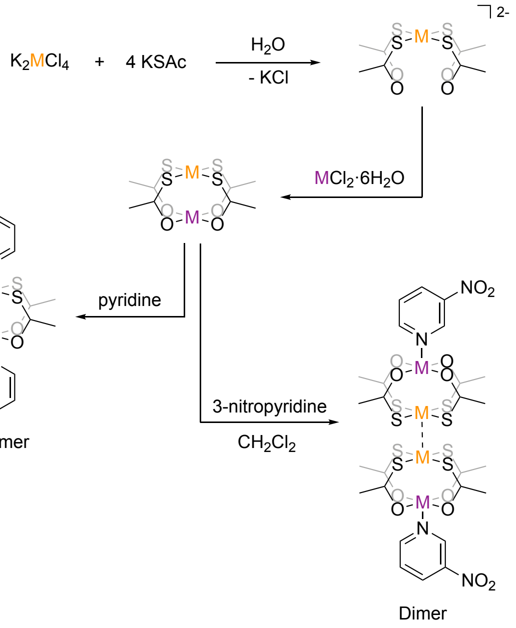

Fig. 1 Schematization of the synthetic pathways to the monomeric and dimeric structures. Orange metal = Pd or Pt and purple metal = Co or Ni.

The four dimeric complexes are iso-structural. However, the $\{\mathbf{NiPd}\}_2$ stands out from the remaining with a slightly longer metallophilic interaction. Some key structural parameters are summarized in Table 1.

In these structures the Pd^{2+} centers are arguably 6-coordinated, which, of course, is a rare situation for Pd(II) and mostly observed in the higher oxidation III and IV. An experimental argument for considering the 3d metals as ligands towards the 4d and 5d centers is the trans-influence weakening of the Pd···Pd interaction going from d^7 (Co^{2+}) to d^8 (Ni^{2+}). The length of the metallophilic interaction in the dimeric Pd complexes is similar to the one in the Pt complexes. Examples of complexes which exhibit non-ligand-supported Pd···Pd metallophilic interactions are quite sparse, but the complex *catena*$-[Pd_2(\text{dithiopropionato})_4]$[40] has an intermolecular metallophilic interaction at 3.439 Å, similar to

Table 1 Selected structural parameters, M = Co or Ni, M’ = Pd or Pt.

Compound	M···M’···M’···M Distance / Å	M···M’···M’···M Distance / Å	M···M’···M’···M Distance / Å	Average displacement angle ϕ / deg	Average dihedral angle τ / deg
$\{\mathbf{CoPd}\}_2$	2.640	3.498	8.778	155.8	0.870
$\{\mathbf{CoPt}\}_2$	2.627	3.437	8.691	160.5	0.630
$\{\mathbf{NiPd}\}_2$	2.595	3.500	8.690	152.9	0.600
$\{\mathbf{NiPt}\}_2$	2.587	3.421	8.595	158.8	0.495
$\{\mathbf{CoPd}\}$	2.612	-	-	-	-
$\{\mathbf{CoPt}\}$	2.582	-	-	-	-
$\{\mathbf{NiPd}\}$	2.574	-	-	-	-
$\{\mathbf{NiPt}\}$	2.551	-	-	-	-

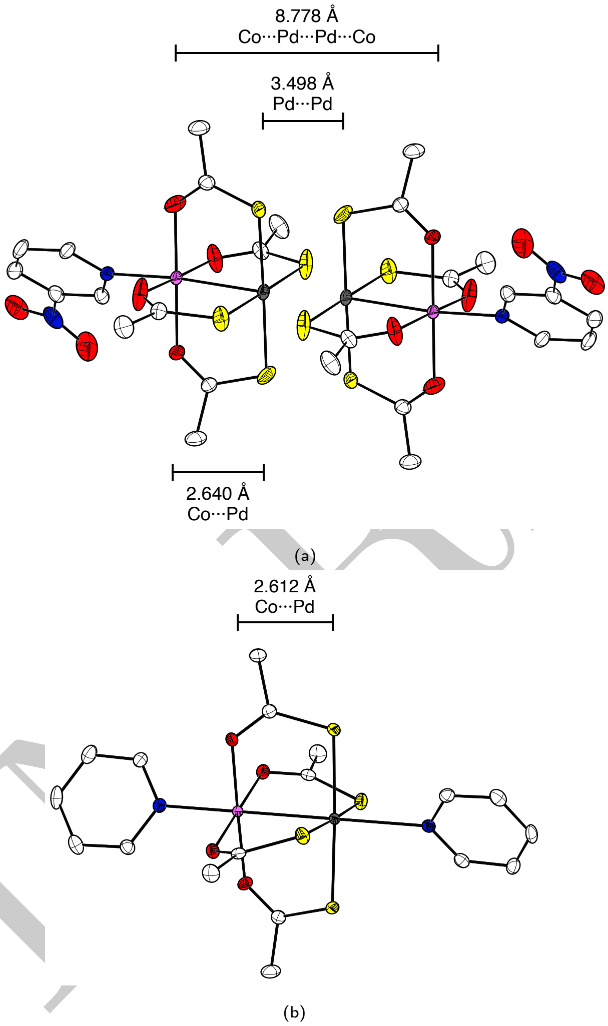

Fig. 2 ORTEP with 50 % probability ellipsoids representation of the Crystal structure of (a) {CoPd}$_2$ and (b) {CoPd}. Hydrogen atoms are omitted for clarity. Color code: white: carbon, red: oxygen, blue: nitrogen, yellow: sulphur, grey: palladium and light purple: cobalt.

the distances observed for the complexes $\{\mathbf{CoPd}\}_2$ and $\{\mathbf{NiPd}\}_2$, at 3.438 Å and 3.500 Å, respectively.

INS was performed on the Pt-analogues of both the monomer and dimer compounds. Fig. 3 illustrates the observed INS spectra (see Fig. S8 for $S(Q,\omega)$ plots) and simulations of the magnetic scattering. From the spectra of the monomers, the zero-field splitting of the Co^{2+} $S = 3/2$ and the Ni^{2+} $S = 1$ is given by the observed magnetic transitions.

$\{\mathbf{CoPt}\}$ (Fig. 3 (a)) showed one magnetic transition at $\hbar\omega = 65$ cm^{-1} corresponding to the $|{+3/2}\rangle \leftarrow |{+1/2}\rangle$ transition. The large positive axial zero-field splitting is corroborated by SQUID (cf. the global fitting in Table 2).

$\{\mathbf{NiPt}\}$ (Fig. 3 (d)) showed one magnetic transition at $\hbar\omega = 12$ cm^{-1} which shifts slightly to lower energy with increasing temperature. This is explained by a negative axial zero-field ($D = -12$ cm^{-1}) and a small rhombic term ($E = 0.6$ cm^{-1}).

For the dimers, the spectra contain more information, as the energy of the magnetic transitions is defined by the zero-field splitting and the exchange-interaction. Furthermore, the Q-dependence of the transitions is dependent on the distance between the coupled ions (vide infra).

$\{\mathbf{CoPt}\}_2$ (Fig. 3 (b)) showed three magnetic transitions in the range 10-40 cm^{-1}. Assuming an identical zero-field splitting as in $\{\mathbf{CoPt}\}$, SQUID magnetometry indicates an anti-ferromagnetic exchange interaction. This identifies these transitions as stemming from the $S = 0$ (coupled basis) to an $S = 1$ first exited state. Reproducing the energy, relative intensity, and momentum-transfer-dependence (vide infra) of these three transitions is only possible by implementing an anisotropic exchange interaction $j = [10, 7, 13]$ cm^{-1}, which splits the $S = 1$ multiplet. This is the first experimental evidence of anisotropic exchange in these dimeric compounds, which shows that the mechanism of magnetic exchange across the metallophillic Pt···Pt bond is far more complicated than hitherto assumed. The assignment of the anisotropic exchange parameters is corroborated by SQUID-magnetometry, as they perfectly reproduce the observed susceptibility.

$\{\mathbf{NiPt}\}_2$ (Fig. 3 (e)) shows two magnetic transitions. Interestingly, there is no evidence of anisotropy in the exchange-interaction. However, the value $j = 24.5$ cm^{-1} is much higher than is to be expected of ions coupled across more than 8 Å.[30] The axial zero-field splitting ($D = -8$ cm^{-1}) is significantly reduced relative to $\{\mathbf{NiPt}\}$ ($D = -12$ cm^{-1}). The difference in coordination strength of pyNO$_2$ (dimer axial ligand) and py (monomer axial ligand) is not great enough to cause such a drastic decrease in D. It is therefore believed that the decrease partially results from the delocalization of electrons from the filled Pt^{2+} d_{z^2} orbital into bonding (metallophillic) molecular orbitals[41], thereby reducing its coordination strength towards Ni^{2+}.

For $\{\mathbf{CoPt}\}_2$ and $\{\mathbf{NiPt}\}_2$, the momentum-transfer (Q) dependence of the magnetic transitions show an interference effect, that results from the geometry of the coupled ions. This interference effect manifests as an oscillation in the Q-dependence superimposed on the magnetic form factor. The rate of oscillation is a direct result of the distance between the coupled ions and can therefore serve as an indicator for the nature of the coupling.

For $\{\mathbf{CoPt}\}_2$ (Fig. 3 (c)) and $\{\mathbf{NiPt}\}_2$ (Fig. 3 (f)), the Q-dependence of the two highest-intensity magnetic transitions is shown. Superimposed on the measured Q-dependence (errorbars) is a simulation of the magnetic excitatations. It is noted that the transitions do not decay with increasing Q, following the magnetic form factors. This is due to a monotonically increasing incoherent phonon background, which is approximated in the simulations as an added term of Q^2. The simulations accurately reproduce the energy and relative intensity of these transitions, giving merit to the spin-Hamiltonian parametrization. The simulation of the Q-dependence has been done based on the full anisotropic spin-Hamiltonian description contrary to earlier approaches, which for dimers have only dealt with coupled isotropic paramagnetic centers. The rate of oscillation is consistent with two ions separated by 8.5 Å, which is the distance between the two paramagnetic ions across the Pt···Pt bridge. This proves that the exchange-interaction is mediated by a metallophilic Pt···Pt bond, and not a through-space coupling to the nearest neighbor, which is only 7 Å away (see Fig. S5 in the SI). A Q-dependence corresponding to 7 Å cannot reproduce the experimental result.

To support the INS data and modeling SQUID magnetometry was performed on all eight compounds. The solid-state molar magnetic susceptibility data for all eight species and their modeling are shown in Figure 4.

At 300 K the $\chi_M T$ product for $\{\mathbf{CoPd}\}_2$, $\{\mathbf{CoPt}\}_2$, $\{\mathbf{NiPd}\}_2$ and $\{\mathbf{NiPt}\}_2$ are 5.55, 6.06, 2.35 and 2.38 emu·K·mol^{-1} respectively. The experimental values are higher than expected for two uncoupled $S = 3/2$ for Co and $S = 1$ for Ni, consistent with a coupling of the two spins and an unquenched orbital contribution to the total angular momentum. The monomeric complexes were synthesized and magnetic characterized in respect to correlate the parameters between the monomeric and dimeric complexes and provide an consistent model for magnetometry and INS data. The $\chi_M T$ curve for all four dimeric complexes shows a drastic drop at low temperature concurring with an anti-ferromagnetic coupling of two paramagnetic metals. The coupling was fitted to an isotropic exchange model for all dimeric complexes, except the $\{\mathbf{CoPt}\}_2$ for which, the INS data mandates modeling with an anisotropic coupling. The modeling of the low temperature regime of the $\{\mathbf{CoPd}\}$ data is not perfect. It could be improved by including weak (0.5 cm^{-1} $> j$) anti-ferromagnetic couplings within a tetrameric unit of Co centers. However, for ad hoc improvent has not been included as we consider it beyond the scope of unfolding the present story. From the parameters extracted from the model of the magnetic susceptibility and INS data two primary trends emerge. First, the coupling constant in the $\{\mathbf{CoPd}\}_2$ and $\{\mathbf{NiPd}\}_2$ complexes are significantly smaller than their respective Pt complexes. The Pd and Pt complexes are iso-structural with a minimal derivation in the molecular distances and angles in the solid-state structure. Therefore, the influence on the magnetic coupling must be found in the change from Pd to Pt and the communication between the two lantern units. The metallophilic interaction originates from an orbital overlap of the orbitals of either Pt or Pd. In the Pt complexes the metallophilic interaction is a consequence of an overlap of two $5d_{z^2}$ orbitals where in the Pd complexes it is two $4d_{z^2}$ orbitals. With an increase in the principal quantum number for the orbital going from Pd to Pt the radial extension increases as well. A larger orbital extension makes way for a better orbital overlap. This argument is valid if the inter- and intra-molecular distances between the metals are similar as is true for the complexes presented here. Second, for $\{\mathbf{NiPd}\}_2$ to $\{\mathbf{NiPt}\}_2$ the relative increase in the coupling is remarkably larger than the change going from $\{\mathbf{CoPd}\}_2$ to $\{\mathbf{CoPt}\}_2$. The $\{\mathbf{NiPd}\}_2$ stood out from the remaining dimeric complexes with a slightly longer metallophilic interaction. This elongation of the metallophilic bond contributes to the more drastic change, and hence a larger span of the coupling constants.

To obtain further insight into the spin coupling parameters and correlate them to the metallophilic interaction of either Pt···Pt or Pd···Pd, the Ni dimers ($\{\mathbf{NiPt}\}_2$, $\{\mathbf{NiPd}\}_2$) and monomers ($\{\mathbf{NiPt}\}$, $\{\mathbf{NiPd}\}$) were investigated by FD-FT THz-EPR at liquid He temperatures at the BESSY II storage ring. All of them showed field-dependent signals from magnetic transitions in the magnetic-field division spectra (MDS), which were simulated using the same spin-Hamiltonian as for the magnetometry data.

Resulting magnetic-field division spectra are shown for $\{\mathbf{NiPt}\}$ and $\{\mathbf{NiPt}\}_2$ in Fig. 5 A detailed discussion on the analysis of the THz data as well as the spectra of $\{\mathbf{NiPd}\}$ and $\{\mathbf{NiPd}\}_2$ can be found in SI:6.

$\{\mathbf{NiPt}\}$ exhibits a doublet signal centered at 12.3 cm^{-1}, the zero-field peaks of which appear at 12.0 and 12.6 cm^{-1} in the MDS (Fig. 5a). This readily determines the ZFS parameters to be $D = -12.3$ cm^{-1} and $|E| = 0.6$ cm^{-1}, exactly the optimized parameters from the simulations. For $\{\mathbf{NiPt}\}_2$, no transitions are discernible at the lowest temperature of 5 K, while starting from 9 K, a transition with a zero-field transition energy of 8.0 cm^{-1} gains intensity, reaching its maximum at 23 K (see Figs. 5b and S10). This is assigned as an internal transition within the excited triplet state, consistent with the difference between the observed INS transitions at 20 and 28 cm^{-1} and also corroborating the strong antiferromagnetic coupling in the platinum bridged dimer.

For the $\{\mathbf{NiPd}\}_2$ (see Fig. S9b)on the contrary signals are observed already at $T = 5$ K which are not present in the $\{\mathbf{NiPd}\}$ spectrum (see Fig. S9a). Thus, the coupling in the $\{\mathbf{NiPd}\}_2$ must be significantly smaller than for $\{\mathbf{NiPt}\}_2$ and the significant population of the excited triplet state at $T = 5$ K is consistent with the coupling strength of $j = 1.65$ cm^{-1} determined from magnetometry. The dramatically lower magnetic coupling via the Pd···Pd bridge as compared to that occurring via the Pt···Pt bridge may spur suspicion concerning the existence of an actual Pd···Pd metallophilic interaction. This hesitation may be further fueled by the

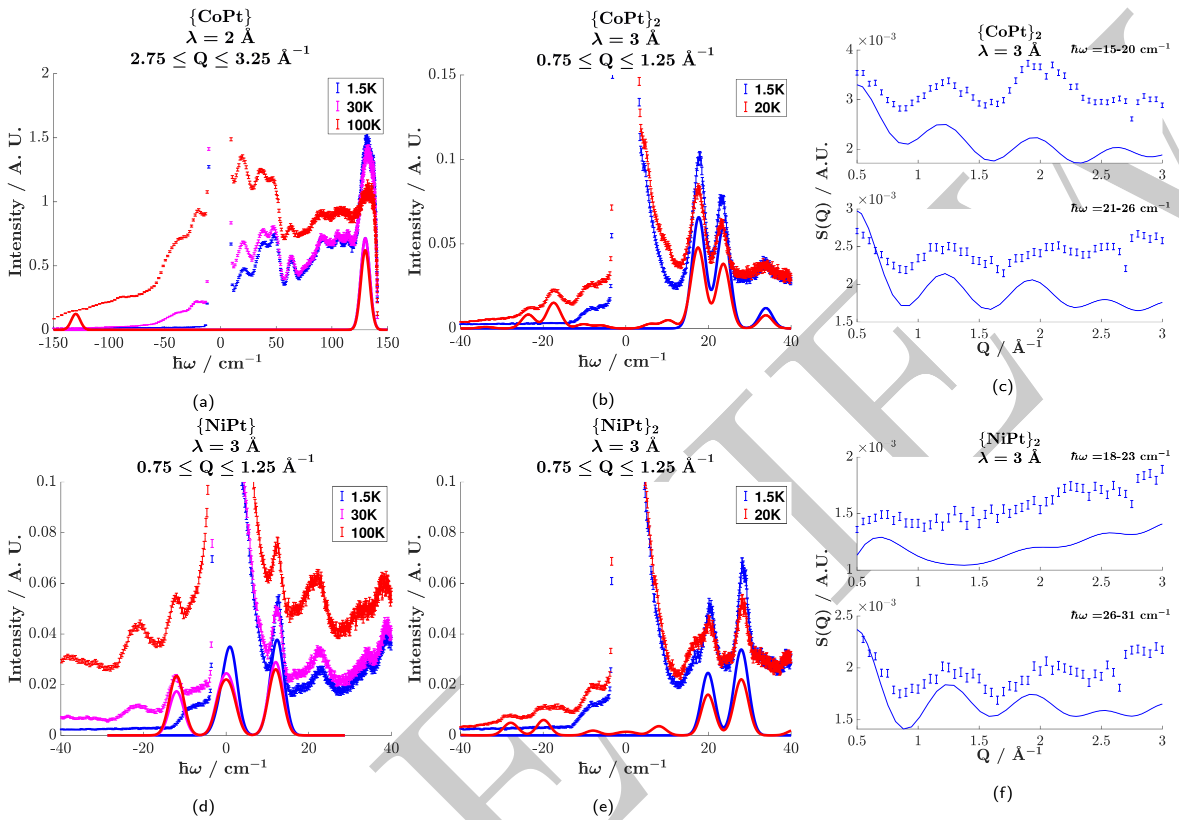

(a) (b) (c)

(d) (e) (f)

Fig. 3 Inelastic Neutron Scattering. Observed constant-Q spectra of {CoPt} (a), {CoPt}$_2$ (b), {NiPt} (d), and {NiPt}$_2$ (e) expressed as error bars with corresponding simulations of the magnetic scattering as solid lines. The Q-dependence of the two main transitions of {CoPt}$_2$ (c) and {NiPt}$_2$ (f) show the interference effect resulting from the coupling of two ions.

Table 2 Spin-Hamiltonian parameters. ZFS parameters D and E are determined spectroscopic. g-factors and TIP found by fitting of magnetometry. The magnitude of the exchange coupling is found spectroscopically to be in great accordance with SQUID magnetometry.

	{CoPt}	**{CoPt}$_2$**	**{NiPt}**	**{NiPt}$_2$**	**{CoPd}**	**{CoPd}$_2$**	**{NiPd}**	**{NiPd}$_2$**
D / cm^{-1}	65	65	-12	-8	70	65	-12	-12
E / cm^{-1}	-	-	0.6	0.6	-	-	0.6	0.6
g	2.53	2.65	2.21	2.29	2.59	2.48	2.17	2.17
j / cm^{-1}	-	[10, 7, 13]	-	24.5	-	1.3	-	1.65
TIP / emu·mol^{-1}	-	$5.9 \cdot 10^{-3}$	-	$5 \cdot 10^{-4}$	$5 \cdot 10^{-4}$	-	$1 \cdot 10^{-3}$	-

preparative challenges associated with obtaining the monomeric platinum systems and the dimeric palladium systems, respectively. In order to address this question we decided to computationally investigate the potential surface along the M’···M’ stretching coordinate for both the platinum and palladium dimers. We chose similar level of theory and methodology as that employed in a recent study of the exchange coupling in related dinuclear platinum systems.[41] DFT calculations were performed for both **{NiPt}**$_2$ and **{NiPd}**$_2$. Geometry scans of the Pt···Pt and Pd···Pd distances were done on geometry optimized rigid structures for the remaining internal coordinates using the ORCA software and including dispersion correction to account for the soft M’···M’ interaction.

The energy curves in Fig. 6 are referenced to the practically dissociated system with a separation of 6 Å. The variation of the total energy of the system along the M’···M’ stretching coordinate shows a clear energy minimum valley validating the presence of an actual interaction between the Pd centers as well as between the Pt centers. The calculated minima lie at shorter distances than the experimental structures, which has been observed, previously, and which is not unexpected for computational modeling of a low-energy interaction disregarding crystal packing effects. Notably, though, the minima occur at very similar distances for the two metals as observed in the experimental crystal structures. 3.421 Å for **{NiPt}**$_2$ and 3.500 Å for **{NiPd}**$_2$, with the computed minimum for the Pd···Pd interaction occurring at similar M’···M’ separation as for the platinum system. Most significantly is the very similar energy stabilization of ca. 0.5 eV for both metals

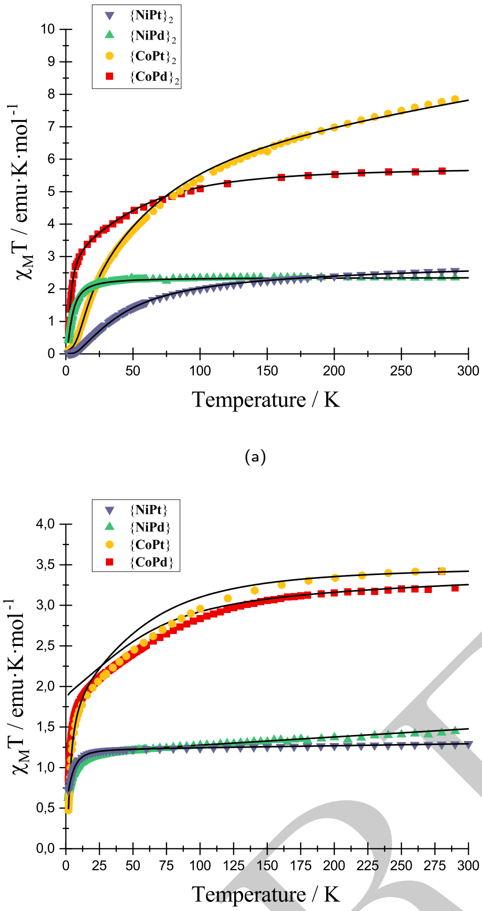

Fig. 4 Magnetic susceptibility measured at 0.1 T and plotted versus temperature for (a) all four dimerazied structures ({CoPd}$_2$, {CoPt}$_2$, {NiPd}$_2$ and {NiPt}$_2$) and (b) monomeric structures ({CoPd}, {CoPt}, {NiPd} and {NiPt}) experimental data represented with scatters and best fitted model with solid black lines.

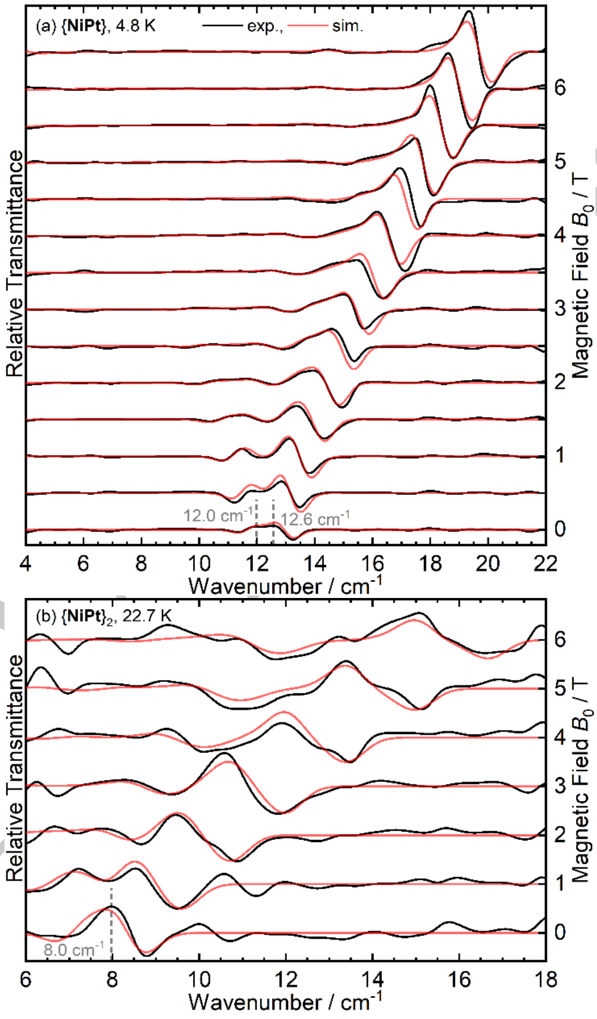

Fig. 5 Experimental (black) and simulated (red) FD-FT THz-EPR magnetic-field division spectra of (a) {NiPt} at $T = 4.8$ K and of (b) {NiPt}$_2$ at $T = 22.7$ K. Spectra were calculated by division of a transmission spectrum at (a) B0 + 0.5 T or (b) B0 + 1 T by a corresponding one at B0. Thus, maxima correspond to stronger absorption at B0, minima to increased absorption at the higher field

upon formation of the dimers, and almost identical curvature of the potential surfaces near the energy minimum. This points to similar strength and force constants for both "bonds". The computed potential energy surfaces demonstrating reasonable stabilization and concomitant curvature around the minima raises the question of whether the M'···M' stretching may actually be experimentally observable. Although the question is far from trivial with several potential soft local and phononic modes conceivable, the simultaneous existence of isostructural Pd···Pd and Pt···Pt dimers facilitates the task. Furthermore, although the dimers do not crystallize with high crystallographic local symmetry, the packing is fortunate enough to align the individual dimers relatively well as illustrated in the top panel of Fig. 7 The dimers crystallize in nice single crystals with dimensions easily reaching 4-500 μm.

Collecting Raman spectra on such a crystallographically indexed single crystal with the electric field component polarized approximately parallel and perpendicular to the M'···M' directions in the crystal lattice reveals strongly polarized transitions at 46 cm^{-1} for {**NiPd**}$_2$ and 44 cm^{-1} for {**NiPt**}$_2$.

Considering as a reference system for these vibrations the dimeric Hg(I) cation, Hg_2^{2+}, computation was performed with the identical level of theory as the Pd and Pt dimers. The curvatures of the potential surfaces were fitted to a harmonic potential near the minimum distance and the relative curvatures were determined to be {**NiPd**}$_2$: 0.036(4); {**NiPt**}$_2$: 0.046(5); Hg···Hg: 0.128(17), which translates into relative vibrational frequencies of 0.53:0.58:1.00 assuming identical reduced masses. With the low range of [Hg···Hg]$^{2+}$ stretching frequencies reported around

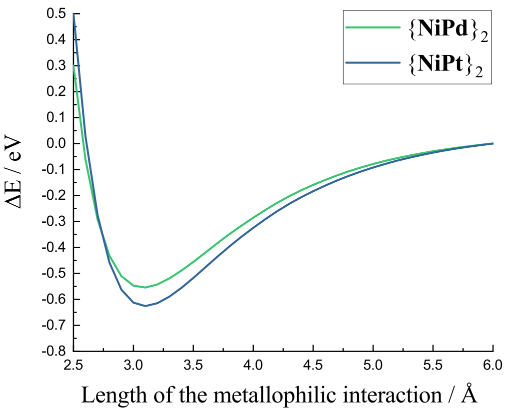

Fig. 6 Final stage energy calculations obtained while making a geometrical scan of the Pt···Pt distance in {NiPt}$_2$ and the Pd···Pd distance in {NiPd}$_2$.

110 cm^{-1},[42] the assignment of the M'···M' stretch to the distinctly polarized bands just below 50 cm^{-1} appears consistent and suggests that the metallophilic interactions might indeed be prone to direct spectroscopic observation.

4 Conclusions

We have further developed the metallophilic interactions as an orthogonal reactivity allowing control of molecular structure and solid-state packing for molecule-based magnetic systems. This was done by augmenting the interesting group of mono- and dimeric systems featuring Pt···Pt bridging[12,13] with their palladium counterparts. Synthetically, it was found to be significantly more challenging to obtain the dimerized palladium systems. In total four of these complexes, $[M(M'(SAc)_4)(pyNO_2)]_2$, (M = Co, Ni; M' = Pt, Pd) dimerize in the solid-state through a metallophilic interaction which facilitates an exchange coupling that was demonstrated to be both anisotropic (for Co) and large (for Ni). An inelastic neutron scattering study on the platinum systems yielded detailed spectroscopic information on both the zero-field splitting and the exchange interaction parameters. For the dimers, INS showed a distinct oscillation in the *Q*-dependence, which complies perfectly with two coupled paramagnetic ions being separated by a distance of 8.5 Å. This matches the crystallographically determined intra dimer separation of the paramagnetic centers and hence proves the intramolecular pathway for strong exchange. To give a consistent parametrization of the series of anti-ferromagnetically coupled dimers the INS was supported by magnetometry on all systems and THz spectroscopy on the Ni members of the series. While the palladium-bridged systems had very comparable ZFS compared to the platinum systems, the magnetic interaction via the Pd···Pd metallophilic interaction was found to be much reduced compared to the platinum-bridged dimers which correlates with longer M'···M' distances in the solid state for the smaller Pd(II) and most notably with significantly smaller radial extent of the $4d_{z^2}$ orbitals of Pd(II) as compared to the $5d_{z^2}$ ordital on Pt(II). A similar difference in the interaction of Pd(II) and Pt(II) with trivalent lanthanides was previously reported.[23] Concerns regarding the actual existence of an energetically relevant Pd···Pd interaction were addressed computationally and found that the energetic stabilization is quite similar and no more than ca. 10 % reduced for the Pd···Pd linked dimer. A single crystal Raman investigation comparing {**NiPd**}$_2$ and {**NiPt**}$_2$ demonstrated polarized vibrational bands at frequencies consistent with estimates from the potential energy curves and provides support for similar interaction strengths in the metallophilic interactions. This makes Pd(II) a credible structure-directing motif for assembly of polynuclear, molecular magnetic systems and allows for significantly different magnetic interaction strength compared to the established Pt-Pt metallophilic interactions.

Author Contributions

E.M.H.L. and N.A.B contributed equally to this work.

Conflicts of interest

There are no conflicts to declare

Acknowledgements

We thank Helmholtz-Zentrum Berlin for the allocation of synchrotron radiation beamtime at BESSY II (201-09107, 202-09859). We are grateful to Dirk Ponwitz for assistance with the FD-FT THz-EPR experiments. TL is indepted to the Deutsche Forschungsgemeinschaft (DFG, Project No. LO 2898/1-1). We also also thank Institut Laue-Langevin for providing the facilities for the INS experiments and analysis thereof. JB acknowledges support from Independent Research Fund Denmark in grant 8021-00410B. This project has received funding from the European Research Council (ERC) under the European Union's Horizon 2020 research and innovation programme (Project ELECTRA, Grant agreement No. 101039890).

Notes and references

1 M. M. Hänninen, A. J. Mota, R. Sillanpää, S. Dey, G. Velmurugan, G. Rajaraman and E. Colacio, *Inorganic Chemistry*, 2018, **57**, 3683–3698.
2 M. A. AlDamen, J. M. Clemente-Juan, E. Coronado, C. Martí-Gastaldo and A. Gaita-Ariño, *Journal of the American Chemical Society*, 2008, **130**, 8874–8875.
3 J. P. S. Walsh, S. Sproules, N. F. Chilton, A.-L. Barra, G. A. Timco, D. Collison, E. J. L. McInnes and R. E. P. Winpenny, *Inorganic Chemistry*, 2014, **53**, 8464–8472.
4 S. Giménez-Santamarina, S. Cardona-Serra, J. M. Clemente-Juan, A. Gaita-Ariño and E. Coronado, *Chem. Sci.*, 2020, **11**, 10718–10728.
5 M. Shiddiq, D. Komijani, Y. Duan, A. Gaita-Ariño, E. Coronado and S. Hill, *Nature*, 2016, **531**, 348–351.
6 C. Rovira and J. Veciana, *CrystEngComm*, 2009, **11**, 2031–2031.
7 M.-X. Xu, Z. Liu, B.-W. Dong, H.-H. Cui, Y.-X. Wang, J. Su,

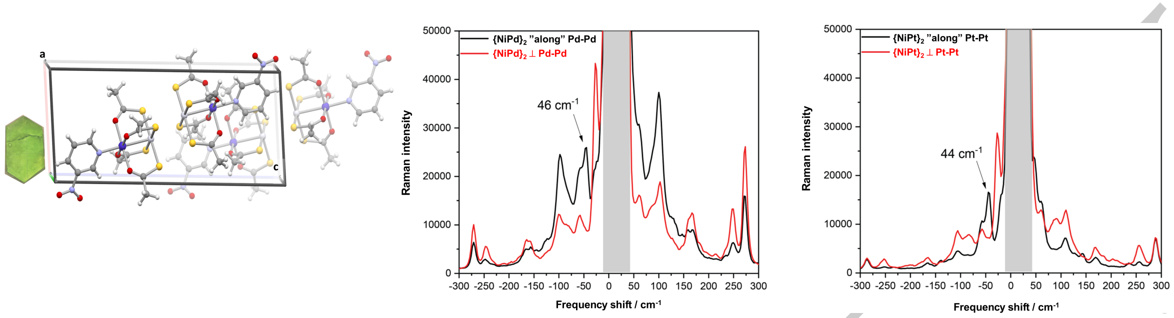

(a) (b) (c)

Fig. 7 (a) Single crystal of {NiPt}$_2$ in spacegroup ($P2_1/c$) resting on the (010) surface and an excerpt of the crystal packing in the pertinent orientation. Raman spectra recorded on oriented crystals of {NiPd}$_2$ (b) and {NiPt}$_2$ (c) with the electrical field component of the excitation polarized approximately along and perpendicular to the M'···M' directions in the crystal.

Z. Wang, Y. Song, X.-T. Chen, S.-D. Jiang and S. Gao, *Inorganic Chemistry*, 2019, **58**, 2330–2335.

8 E. Garlatti, L. Tesi, A. Lunghi, M. Atzori, D. J. Voneshen, P. Santini, S. Sanvito, T. Guidi, R. Sessoli and S. Carretta, *Nature Communications*, 2020, **11**, 1751.

9 A. Lunghi and S. Sanvito, *Science Advances*, 2019, **5**, eaax7163.

10 D. Reta, J. G. C. Kragskow and N. F. Chilton, *Journal of the American Chemical Society*, 2021, **143**, 5943–5950.

11 E. W. Dahl, F. G. Baddour, S. R. Fiedler, W. A. Hoffert, M. P. Shores, G. T. Yee, J. P. Djukic, J. W. Bacon, A. L. Rheingold and L. H. Doerrer, *Chemical Science*, 2012, **3**, 602–609.

12 F. G. Baddour, S. R. Fiedler, M. P. Shores, J. W. Bacon, J. A. Golen, A. L. Rheingold and L. H. Doerrer, *Inorganic Chemistry*, 2013, **52**, 13562–13575.

13 F. G. Baddour, S. R. Fiedler, M. P. Shores, J. A. Golen, A. L. Rheingold and L. H. Doerrer, *Inorganic Chemistry*, 2013, **52**, 4926–4933.

14 J. L. Guillet, I. Bhowmick, M. P. Shores, C. J. Daley, M. Gembicky, J. A. Golen, A. L. Rheingold and L. H. Doerrer, *Inorganic Chemistry*, 2016, **55**, 8099–8109.

15 A. Nimthong-Roldán, J. L. Guillet, J. McNeely, T. J. Ozumerzifon, M. P. Shores, J. A. Golen, A. L. Rheingold and L. H. Doerrer, *Dalton Transactions*, 2017, **46**, 5546–5557.

16 F. G. Baddour, A. S. Hyre, J. L. Guillet, D. Pascual, J. M. Lopez-De-Luzuriaga, T. M. Alam, J. W. Bacon and L. H. Doerrer, *Inorganic Chemistry*, 2017, **56**, 452–469.

17 S. A. Beach and L. H. Doerrer, *Accounts of Chemical Research*, 2018, **51**, 1063–1072.

18 H. Skipper, C. May, A. Rheingold, L. Doerrer and M. Kamenetska, *J. Am. Chem. Soc*, 2021, **143**, 16439–16447.

19 S. A. Beach, A. L. Rheingold and L. H. Doerrer, *Polyhedron*, 2021, **208**, 115403.

20 M. A. Sørensen, H. Weihe, M. G. Vinum, J. S. Mortensen, L. H. Doerrer and J. Bendix, *Chemical Science*, 2017, **8**, 3566–3575.

21 M. A. Sørensen, U. B. Hansen, M. Perfetti, K. S. Pedersen, E. Bartolomé, G. G. Simeoni, H. Mutka, S. Rols, M. Jeong, I. Zivkovic, M. Retuerto, A. Arauzo, J. Bartolomé, S. Piligkos, H. Weihe, L. H. Doerrer, J. Van Slageren, H. M. Rønnow, K. Lefmann and J. Bendix, *Nature Communications*, 2018, **9**, 1–9.

22 M. Perfetti, M. A. Sørensen, U. B. Hansen, H. Bamberger, S. Lenz, P. P. Hallmen, T. Fennell, G. G. Simeoni, A. Arauzo, J. Bartolomé, E. Bartolomé, K. Lefmann, H. Weihe, J. van Slageren and J. Bendix, *Advanced Functional Materials*, 2018, **28**, 1–8.

23 N. A. Bonde, J. B. Petersen, M. A. Sørensen, U. G. Nielsen, B. Fåk, S. Rols, J. Ollivier, H. Weihe, J. Bendix and M. Perfetti, *Inorganic Chemistry*, 2020, **59**, 235–243.

24 N. A. Bonde, M. Appel, J. Ollivier, H. Weihe and J. Bendix, *Chemical Communications*, 2022.

25 T. Yoshida, D. C. Izougu, D. Iwasawa, S. Ogata, M. Hasegawa, B. K. Breedlove, G. Cosquer, W. Wernsdorfer and M. Yamashita, *Chemistry - A European Journal*, 2017, **23**, 10527–10531.

26 T. Yoshida, G. Cosquer, D. C. Izuogu, H. Ohtsu, M. Kawano, Y. Lan, W. Wernsdorfer, H. Nojiri, B. K. Breedlove and M. Yamashita, *Chemistry - A European Journal*, 2017, **23**, 4551–4556.

27 D. C. Izuogu, T. Yoshida, H. Zhang, G. Cosquer, K. Katoh, S. Ogata, M. Hasegawa, H. Nojiri, M. Damjanović, W. Wernsdorfer, T. Uruga, T. Ina, B. K. Breedlove and M. Yamashita, *Chemistry - A European Journal*, 2018, **24**, 9285–9294.

28 T. Yoshida, D. C. Izuogu, H. T. Zhang, G. Cosquer, H. Abe, W. Wernsdorfer, B. K. Breedlove and M. Yamashita, *Dalton Transactions*, 2019, **48**, 7144–7149.

29 D. C. Izuogu, T. Yoshida, G. Cosquer, J. N. Asegbeloyin, H. Zhang, A. J. Thom and M. Yamashita, *Chemistry - A European Journal*, 2020, **26**, 6036–6049.

30 R. E. Coffman and G. R. Buettner, *The Journal of Physical Chemistry*, 1979, **83**, 2387–2392.

31 M. L. Baker, T. Guidi, S. Carretta, J. Ollivier, H. Mutka, H. U. Güdel, G. A. Timco, E. J. Mcinnes, G. Amoretti, R. E. Winpenny and P. Santini, *Nature Physics*, 2012, **8**, 906–911.

32 A. Chiesa, F. Tacchino, M. Grossi, P. Santini, I. Tavernelli, D. Gerace and S. Carretta, *Nature Physics*, 2019, **15**, year.

33 *EasySpin*, `http://www.easyspin.org`.

34 G. A. Bain and J. F. Berry, *Journal of Chemical Education*, 2008, **85**, 532–536.

35 D. Richard, M. Ferrand and G. J. Kearley, *Journal of Neutron Research*, 1996, **4**, 33–39.

36 M. A. Dunstan, R. A. Mole and C. Boskovic, *European Journal of Inorganic Chemistry*, 2019, **2019**, 1090–1105.

37 S.-H. Lee and I. A. Zaliznyak, *Magnetic Neutron Scattering*, 2004.

38 J. Nehrkorn, K. Holldack, R. Bittl and A. Schnegg, *Journal of Magnetic Resonance*, 2017, **280**, 10–19.

39 A. Schnegg, J. Behrends, K. Lips, R. Bittl and K. Holldack, *Phys. Chem. Chem. Phys.*, 2009, **11**, 6820–6825.

40 A. Kobayashi, T. Kojima, R. Ikeda and H. Kitagawa, *Inorganic Chemistry*, 2006, **45**, 322–327.

41 Z. Sandoval-Olivares, E. Solis-Céspedes and D. Páez-Hernández, *Inorganic Chemistry*, 2022, **61**, 1401–1417.

42 P. A. W. Dean and D. G. Ibbott, *Canadian Journal of Chemistry*, 1976, **54**, 177–187.

Supporting Information

Experimental Assignment of Long-Range Magnetic Communication Through Pd & Pt Metallophilic Contacts

Emil M. H. Larsen,[‡a] Niels A. Bonde,[‡a,b] Høgni Weihe,[a] Jacques Ollivier,[b] Tom Vosch,[a] Thomas Lohmiller,[c,d] Karsten Holldack,[f] Alexander Schnegg,[d,e] Mauro Perfetti,[f] and Jesper Bendix*[a]

* *Corresponding Author.*

Contents

[0†] Electronic supplementary information (ESI) available: Experimentals, crystallographic details(CCDC 2207828-2207833), Computational data, INS data, FD-FT THz-EPR data. For ESI and crystallographic data in CIF or other electronic format see DOI: 00.0000/00000000.

[0‡] These authors contributed equally to this work.

[0a] *Department of Chemistry, University of Copenhagen, Universitetsparken 5, DK-2100 Copenhagen, Denmark.*

[0b] *Institut Laue-Langevin, 71 avenue des Martyrs, CS 20156, 38042 Grenoble Cedex 9, France*

[0c] *Humboldt-Universität zu Berlin, Institut für Chemie, Brook-Taylor-Str. 2, 12489 Berlin, Germany*

[0d] *EPR4Energy Joint Lab, Department Spins in Energy Conversion and Quantum Information Science, Helmholtz Zentrum Berlin für Materialien und Energie GmbH, Albert-Einstein-Straße 15, 12489 Berlin, Germany*

[0e] *Max Planck Institute for Chemical Energy Conversion, Stiftstrasse 34-36, D-45470 Mülheim an der Ruhr, Germany*

[0f] *Department of Optics and Beamlines, Helmholtz Zentrum Berlin für Materialien und Energie GmbH, Albert-Einstein-Straße 15, 12489 Berlin, Germany*

[0g] *Department of Chemistry "U. Schiff", University of Florence, Via della Lastruccia 3-13, Sesto Fiorentino, 50019, Italy*

1 Experimentals

[Co(Pd(SAc)$_4$)(OH$_2$)] 172 mg (151 mmol) KSAc was dissolved in 2 ml water. To this a solution of 100 mg (0.340 mmol) $Na_2[PdCl_4]$ in 2 ml water was added dropwise at a rate so that no permanent brown precipitate was observed, and was then left stirring for 30 min. A solution 80.8 mg (0.340 mmol) $CoCl_2 \cdot 6\,H_2O$ was added in a minimal amount of water and a green powder immediately precipitated. The green powder was isolated and dried briefly on a sintered glass funnel. Yield: 43 % based on Pd. Elemental analysis calculated for $PdCoC_8H_{14}O_5S_4$: C; 19.9 %, H; 2.92 %, N; 0.00 %. Found: C; 19.6 %, H; 3.15 %, N; 0.00 %.

[Ni(Pd(Sac)$_4$)(OH$_2$)] was obtained in a similar fashion to **[Co(Pd(SAc)$_4$)(OH$_2$)]**: $CoCl_2 \cdot 6\,H_2O$ was replaced with $NiCl_2 \cdot 6\,H_2O$ and the precipitate was of a yellow color. Yield: 65 % based on Pd. Elemental analysis calculated for $PdNiC_8H_{14}O_5S_4$: C; 19.9 %, H; 2.92 %, N; 0.00 %. Found: C; 19.5 %, H; 3.20 %, N; 0.00 %.

[Co(Pt(SAc)$_4$)(OH$_2$)] was obtained with a modification of the synthetic procedure reported[1] 100 mg (0.963 mmol) KSAc was dissolved in 30 ml water and to this a solution of 100 mg (0.241 mmol), $K_2[PtCl_4]$ in 3 ml water was added dropwise. The solution was stirred for 1.5 hour. To the resulting yellow solution 57.3 mg (0.241 mmol), $CoCl_2 \cdot 6\,H_2O$ dissolved in 3 ml water was added, and a gray powder immediately precipitated. The suspension was left at 5 °C overnight, where the particle size increased significantly. The powder was isolated and dried on a sintered glass funnel. Yield: 35 % based on Pt.

[Ni(Pt(SAc)$_4$)(OH$_2$)] was obtained in a similar fashion to [Co(Pt(SAc)$_4$)(OH$_2$)] where $CoCl_2 \cdot 6\,H_2O$ was replaced with $NiCl_2 \cdot 6\,H_2O$. The resulting precipitate was yellow in color and was isolated via centrifugation rather than filtration and dried under a stream of N_2. Yield: 80 % based on Pt.

[Co(Pd(SAc)$_4$)(pyNO$_2$)], 33.0 mg (0.0682 mmol) [Co(Pd(SAc)$_4$)(OH$_2$)] was dissolved in 5 ml CH_2Cl_2 and diluted with 10 ml of ethanol. With rapid stirring a solution of 8.47 mg (0.0682 mmol) 3-nitropyridine in a minimal amount of CH_2Cl_2, was added dropwise. The solution was stirred for 24 hours at RT resulting in a color change from green to dark yellow. After 24 hours the solution was left for evaporation at room temperature where brown crystals suitable for X-ray diffraction experiments were grown. Yield: 54 % based on Pd. Elemental analysis calculated for $PdCoC_{13}H_{16}N_2O_6S_4$: C; 26.5 %, H; 2.73 %, N; 4.75 %. Found: C; 26.8 %, H; 2.69 %, N; 4.80 %.

[Co(Pd(SAc)$_4$)(pyNO$_2$)]$_2$, {CoPd}$_2$, 92.1 mg (0.146 mmol) [CoPd(SAc)4(OH2)] was suspended in 4 ml CH_2Cl_2, and dropwised added a solution of 18.1 mg (0.146 mmol) 3-nitropyridine in a minimal amount of CH_2Cl_2. Upon addition of the 3-nitropyridine the remaining precipitate was dissolved, and while stirring for 24 hours the solution changed color from green to dark yellow. Crystals suitable for X-ray diffraction experiments were grown by slow evaporation of the resulting solution at room temperature. Yield: 56 % based on Pd. Elemental analysis calculated for $Pd_2Co_2C_{26}H_{32}N_4O_{12}S_8$: C; 26.5 %, H; 2.73 %, N; 4.75 %. Found: C; 26.5 %, H; 2.71 %, N; 4.81 %.

[Ni(Pd(SAc)$_4$)(pyNO$_2$)], 33 mg (0.0682 mmol) of [Ni(Pd(SAc)$_4$)(OH$_2$)] was dissolved in 1 ml CH_2Cl_2 and dropwised adding, a solution of 8.47 mg (0.0682 mmol) 3-nitropyridine in a minimal amount of CH_2Cl_2. The solution was then stirred for 1 hour with a resulting change of color from yellow to bright green. The solution was then filtered and left for evaporation at room temperature. Bright green plank-shaped crystals were grown over the course of 24 hours and were suitable for X-ray diffraction experiments. Yield: 40 % based on Pd. Elemental analysis calculated for $PdNiC_{13}H_{16}N_2O_6S_4$: C; 26.5 %, H; 2.74 %, N; 4.75 %. Found: C; 26.9 %, H; 2.70 %, N; 4.95 %.

[Ni(Pd(SAc)$_4$)(pyNO$_2$)]$_2$, {NiPd}$_2$, 33.0 mg (0.0682 mmol) of [Ni(Pd(SAc)$_4$)(OH$_2$)] was dissovled in 1 ml CH_2Cl_2, followed by dropwise addition of a solution of 8.47 mg (0.0682 mmol) 3-nitropyridine in a minimal amount of CH_2Cl_2. The solution was stirred for 1 hour during which the solution changed color from yellow to green. The solution was then filtered and 166 μl (1/6 volume) of dichloroethane was added. The solution was left for slow evaporation for 24 hours and then left at 5 °C for several days, where bright green irregularly shaped crystals suitable for X-ray diffraction were obtained. To obtain a crystalline phase-pure bulk sample of NiPd2 a filtered solution with a concentration of 0.0682 mM of [Ni(Pd(SAc)$_4$)(pyNO$_2$)] was gently heated to dryness over open flame. Yield: 32 % based on Pd. Elemental analysis calculated for $Pd_2Ni_2C_{26}H_{32}N_4O_{12}S_8$: C; 26.5 %, H; 2.74 %, N; 4.75 %. Found: C; 26.7 %, H; 2.85 %, N; 4.79 %.

[Co(Pt(SAc)$_4$)(pyNO$_2$)]$_2$, {CoPt}$_2$, 30 mg (0.0524 mmol) of [Co(Pt(SAc)$_4$)(OH$_2$)] was suspended in a mixture of 1 ml acetone and 10 ml CH_2Cl_2. To the suspension, a solution of 65 mg (0.524 mmol) 3-nitropyridine in a minimal amount of CH_2Cl_2 was added dropwise. The suspension was then stirred for 6 hours where the color of the filtrate changed from grayish to brown while the precipitate remained gray. The brown filtrate was isolated and carefully heated until dryness over open flame yielding brown block-shaped crystals suitable for X-ray diffraction experiments. Yield: 43 % based on Pt. Elemental analysis calculated for $Pt_2Co_2C_{26}H_{32}N_4O_{12}S_8$: C; 23.0 %, H; 2.38 %, N; 4.13 %. Found: C; 23.1 %, H; 2.40 %, N; 4.17 %.

[Ni(Pt(SAc)$_4$)(pyNO$_2$)]$_2$, {NiPt}$_2$, 30 mg (0.0524 mmol) of [Ni(Pt(SAc)$_4$)(OH$_2$)] was dissolved in 1 ml CH_2Cl_2 and dropwise adding a solution of 6.51 mg (0.0524 mmol) 3-nitropyridine in a minimal amount of CH_2Cl_2. The solution was then stirred for 1 hour. The remaining green solution was filtered and gently heated over open flame until a minimal amount of solvent remained. At this point the glassware was left at a cold surface were bright green block-shaped crystals were grown within an hour. Yield: 71 % based on Pt. Elemental analysis calculated for $Pt_2Ni_2C_{26}H_{32}N_4O_{12}S_8$: C; 23.0 %, H; 2.38 %, N; 4.13 %. Found: C; 23.1 %, H; 2.45 %, N; 4.20 %.

The complexes [Co(Pt(SAc)$_4$)(py)$_2$]$_2$ and [Ni(Pt(SAc)$_4$)(py)$_2$]$_2$ (**{CoPt}** and **{NiPt}**) were synthesized following previously reported procedures[2] and verified by powder X-ray diffraction.

[Co(Pd(SAc)$_4$)(py)$_2$]$_2$, {CoPd}, 50 mg, 0.103 mmol [Co(Pd(SAc)$_4$)(OH$_2$)] was dissolved in 15 ml of pyridine. The solution was then gently heated over open flame and left on a cold surface and within the hour plank shaped brown crystal were grown in close to quantitative yield. Crystals suitable for X-ray diffraction experiments were grown by diluting the solution and prolonging crystallization time.

[Ni(Pd(SAc)$_4$)(py)$_2$]$_2$, {NiPd}, was obtained in a similar fashion to the **{CoPd}** were the precursor was replaced with [Ni(Pd(SAc)$_4$)(OH$_2$)].
For both the synthesis of **{CoPd}** and **{NiPd}** the starting material could be replaced with dimerized complexes showing the greater affinity for the pyridine ligand.

2 Single Crystal X-ray diffraction

Single crystal X-ray diffraction data were collected on a Bruker D8 VENTURE diffractometer equipped with a Mo Kα X-ray ($\lambda = 0.71073$ Å), and a PHOTON 100 CMOS detector. For low temperature measurements the diffractometer is equipped with an Oxford Cryosystem. All crystals were mounted on capton loops with a small amount of silicone grease. The data reductions were performed in the APEX3 software, and the absorption correction was carried out with the multi-scan method SADABS. The data collections were done at either 120 K or 100 K. The structures were solved in the Olex2 (ver. 1.3) software with the ShelXT software package included.
New structures presented in this work are found Figure S1-S4 and the crystallographic parameters can be found in Tables S1 and S2.

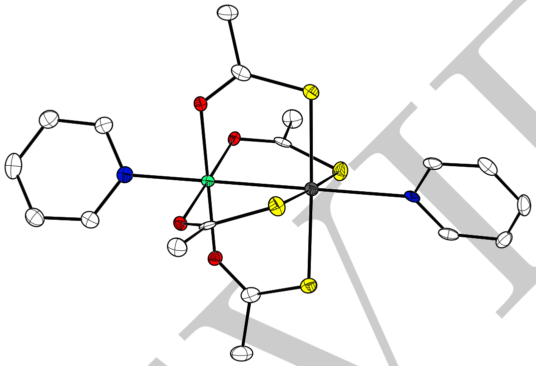

Figure S1: ORTEP representation of the crystal structure of **{NiPd}**, with 50 % probability ellipsoid. Hydrogen atoms are omitted for clarity. Color code: White: Carbon, red: Oxygen, blue: Nitrogen, yellow: Sulphur, grey: Palladium and aquamarine: Nickel.

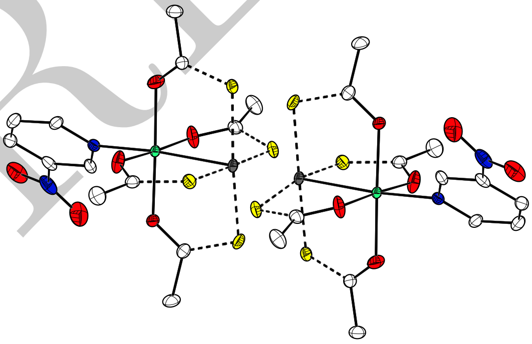

Figure S2: ORTEP representation of the crystal structure of **$\{NiPd\}_2$**, with 50 % probability ellipsoid. Hydrogen atoms as well as disordered sulphur atoms are omitted for clarity. Color code: White: Carbon, red: Oxygen, blue: Nitrogen, yellow: Sulphur, grey: Palladium and aquamarine: Nickel.

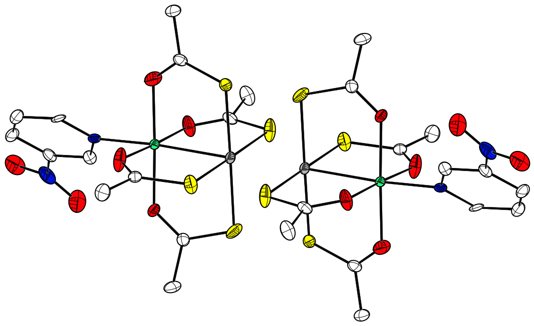

Figure S3: ORTEP representation of the crystal structure of $\mathbf{\{NiPt\}_2}$, with 50 % probability ellipsoid. Hydrogen atoms are omitted for clarity. Color code: White: Carbon, red: Oxygen, blue: Nitrogen, yellow: Sulphur, light grey: Platinum and aquamarine: Nickel.

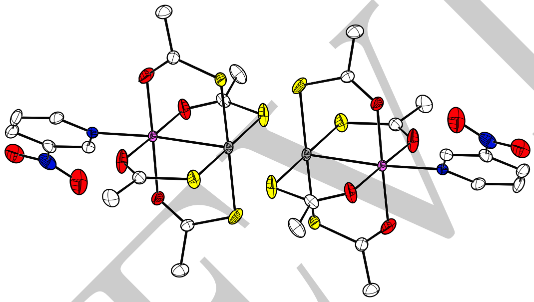

Figure S4: ORTEP representation of the crystal structure of $\mathbf{\{CoPt\}_2}$, with 50 % probability ellipsoid. Hydrogen atoms are omitted for clarity. Color code: White: Carbon, red: Oxygen, blue: Nitrogen, yellow: Sulphur, light grey: Platinum and lightpurple: Cobalt.

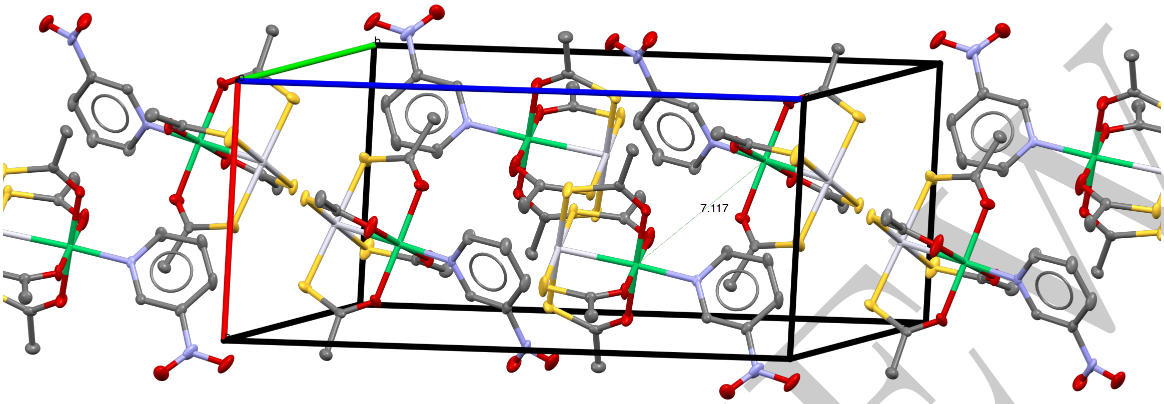

Figure S5: ORTEP representation of the crystal structure of $\mathbf{\{NiPt\}_2}$ showing the crystal packing with nearest neighbor at 7.1 Å. With 50 % probability ellipsoid and hydrogen atoms are omitted for clarity. Color code: White: Carbon, red: Oxygen, blue: Nitrogen, yellow: Sulphur, light grey: Platinum and aquamarine: Nickel.

Table S1: Crystallographic parameters

Compound	**{CoPd}**	**$\{CoPd\}_2$**	**{NiPd}**
Formula	$C_{18}H_{22}N_2CoO_4PdS_4$	$C_{13}H_{16}CoN_2O_6PdS_4$	$C_{18}H_{22}N_2NiO_4PdS_4$
Formula weight [g/mol]	623.94	589.8	623.72
Crystal system	Monoclinic	Monoclinic	Monoclinic
Space group	C 2/c	P 2_1/c	C 2/c
a / Å	9.7593(7)	8.4837	9.7142(7)
b / Å	18.2739(12)	12.3085(7)	18.2617(16)
c / Å	13.1854(8)	19.8273(11)	13.1518(12)
α / deg	90	90	90
β / deg	97.317(2)	93.171(2)	97.378
γ / deg	90	90	90
V / Å^3	2332.3(3)	2062.36(19)	2313.8
Z	4	4	4
ρ / g cm^{-3}	1.777	1.900	1.791
μ / mm^{-1}	1.867	2.112	1.979
Temperature / K	100	120	100
Radiation	Mo Kα (λ = 0.71073 Å)		
Crystal size / mm	0.251 x 0.186 x 0.126	0.488 x 0.223 x 0.156	0.282 x 0.055 x 0.049
2θ range / deg	4.458 to 61.012	5.282 to 67.608	2.46 to 50.048
Reflection collected	23760	88501	15895
Unique reflections	3562	8243	2050
R_{int}/R_{σ}	0.0496/0.0351	0.0372/0.0206	0.0972/0.0502
Parameters/restraints	141/0	248/0	141/0
Goodness of fit	1.029	1.069	1.021
R_1/wR_2 (I$\geq 2\sigma$(I))	0.0287/0.0514	0.0325/0.0693	0.0321/0.0546
R_1/wR_2 (all data)	0.0431/0.0555	0.0430/0.0747	0.0546/0.0598
$\Delta\rho_{max}/\Delta\rho_{min}$ / e Å^{-3}	0.70/-0.66	1.59/-1.65	0.44/-0.52

Table S2: Crystallographic parameters continued, *identical to previously published

Compound	**$\{NiPd\}_2$**	**$\{CoPt\}_2$** *	**$\{NiPt\}_2$**
Formula	$C_{13}H_{16}NiN_2O_6PdS_{4.03}$	$C_{13}H_{16}CoN_2O_6PtS_4$	$C_{13}H_{16}NiN_2O_6PtS_4$
Formula weight [g/mol]	590.5	678.5	678.3
Crystal system	Monoclinic	Monoclinic	Monoclinic
Space group	P 2_1/c	P 2_1/c	P 2_1/c
a / Å	8.4953(6)	8.4704(10)	8.4782(4)
b / Å	12.3011(9)	12.2809(13)	12.2733(5)
c / Å	19.6004(14)	19.820(2)	19.6523(8)
α / deg	90	90	90
β / deg	92.680	93.914	93.668(2)
γ / deg	90	90	90
V / Å^3	2046.0(3)	2057.0(4)	2040.74(15)
Z	4	4	4
ρ / g cm^{-3}	1.917	2.191	2.208
μ / mm^{-1}	2.242	8.037	8.211
Temperature / K	100	100	100
Radiation	Mo Kα (λ = 0.71073 Å)		
Crystal size / mm	0.262 x 0.153 x 0.101	0.182 x 0.132 x 0.121	0.310 x 0.205 x 0.145
2θ range / deg	3.91 to 51.354	4.82 to 55.754	3.914 to 52.044
Reflection collected	30344	43264	26515
Unique reflections	3882	4899	3998
R_{int}/R_{σ}	0.0890/0.0442	0.0678/0.0341	0.0919/0.0559
Parameters/restraints	268/0	248/0	248/0
Goodness of fit	1.011	1.037	1.016
R_1/wR_2 (I$\geq 2\sigma$(I))	0.0192/0.0410	0.0226/0.0391	0.0318/0.0637
R_1/wR_2 (all data)	0.0454/0.0639	0.0330/0.0417	0.0465/0.0686
$\Delta\rho_{max}/\Delta\rho_{min}$ / e Å^{-3}	0.73/-0.99	0.60/-0.81	0.98/-1.70

3 Powder X-ray diffraction

The Powder X-ray diffraction data were collected on a Bruker D8 ADVANCE powder diffractometer equipped with a Cu Kα X-ray source ($\lambda = 1.5418$ Å).

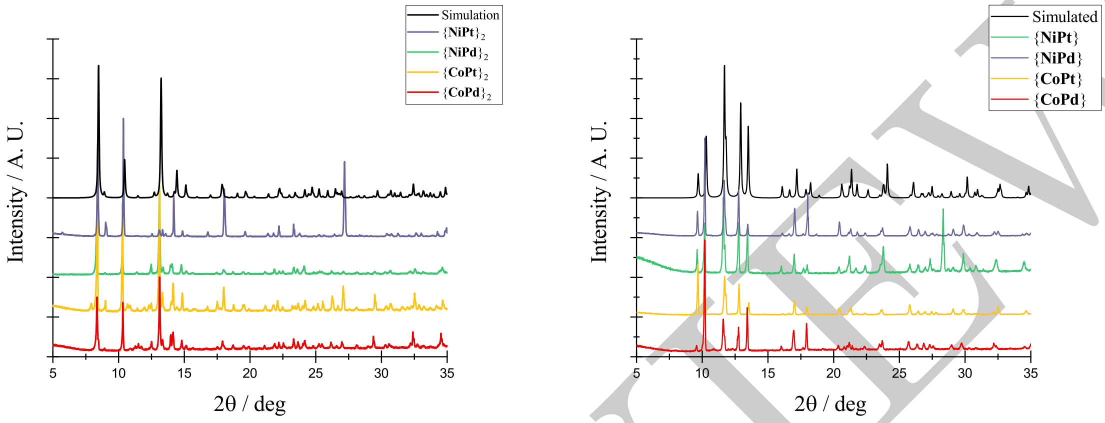

(a)

(b)

Figure S6: Powder X-ray diffraction of (a) dimerized structures compared to a simulated structure and (b) monomeric structures compared to a simulated structure.

4 Calculated Energy Levels

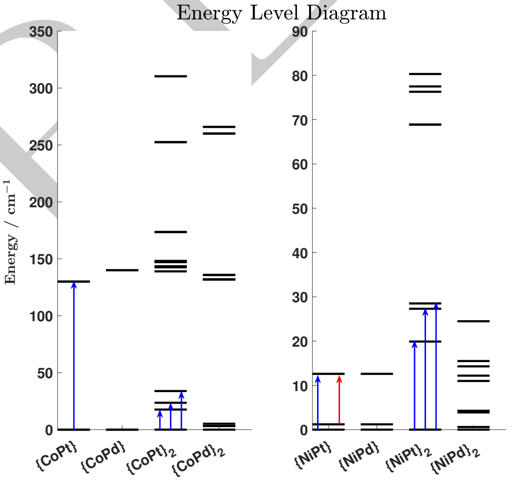

Figure S7: Calculated energy level diagram simulated from fitted parameters. Arrows indicate observed INS transitions, with blue representing transitions from the ground state and red from the first excited state.

5 Inelastic Neutron Scattering

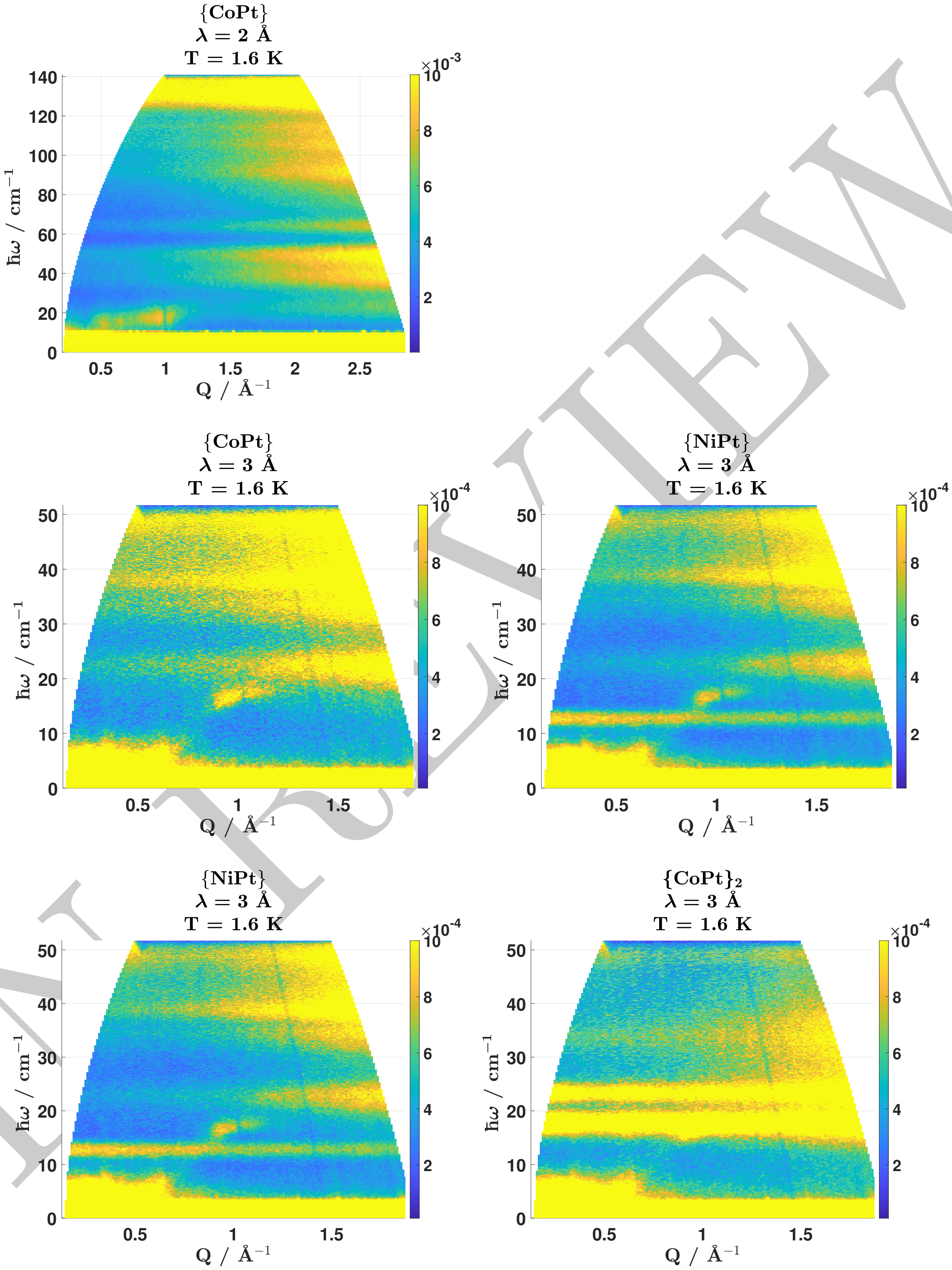

Figure S8: S(Q,ω) plots (neutron energy loss/) at 1.6 K. **{CoPt}** was measured at $\lambda = 2$ and 3 Å, whereas **{CoPt}$_2$**, **{NiPt}**, and **{NiPt}$_2$** were only measured at $\lambda = 3$ Å. A spurion is present at $Q = 1$ Å^{-1} and $\hbar\omega = 18$ cm^{-1}.

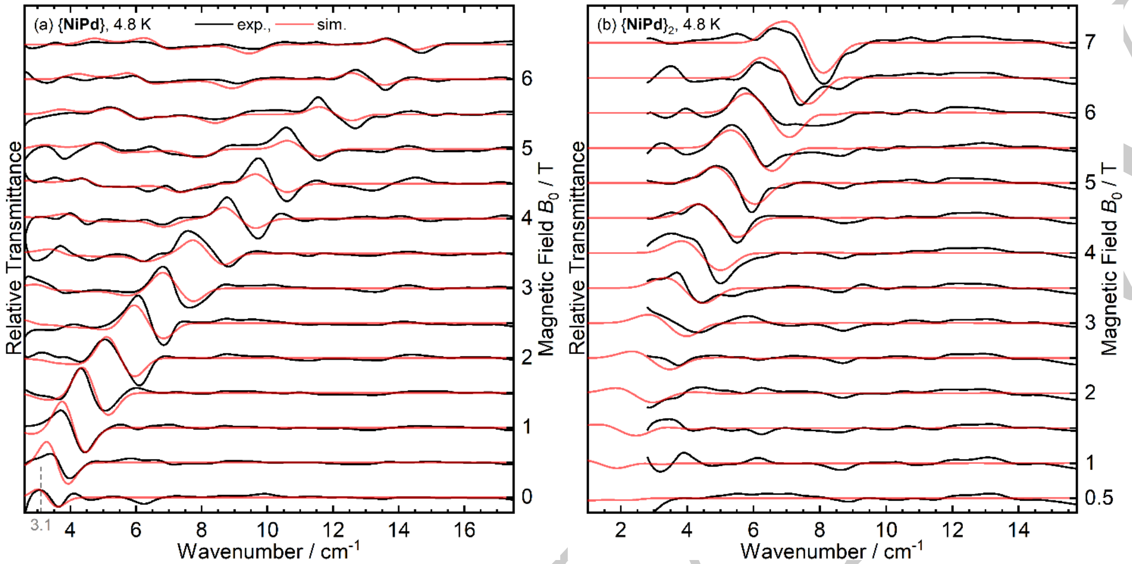

Figure S9: Experimental (black) and simulated (red) FD-FT THz-EPR magnetic-field division spectra of (a) **{NiPd}** and of (b) **$\{\mathbf{NiPd}\}_2$** recorded at $T = 4.8\,\mathrm{K}$. Spectra were calculated by division of a transmission spectrum at B0 + 0.5 T by a corresponding one at B0. Thus, maxima correspond to stronger absorption at B0, minima to increased absorption at the higher field.

FD-FT THz-EPR alone is capable of giving a parametrization of **{NiPt}**, **$\{\mathbf{NiPt}\}_2$**, **{NiPd}**, and **$\{\mathbf{NiPd}\}_2$** which is found to be in great accordance with the values found by SQUID magnetometry and INS. The following is a discussion on the extraction of parameters exclusively from THz.

Spectral simulations afford on-site Ni^{2+} parameters $D = -7.7\ \mathrm{cm}^{-1}$ and $|E| = 0.4\ \mathrm{cm}^{-1}$ and with a fixed $j = 24.5\ \mathrm{cm}^{-1}$ reproduce the temperature-dependent signal intensities very precisely. (Simulations with variable j provide a fitted value of 21.8 cm^{-1}, which is in very good agreement with INS considering the S/N of the THz-EPR spectra.) For the Pd^{2+}-containing compounds **{NiPd}** and **{NiPd}**, two major differences are found compared to the Pt^{2+}-containing ones. (i) The signals are found at substantially lower transition energies. For **{NiPd}**, the zero-field peak is at 3.1 cm^{-1}, the lower edge of the experimentally accessible range, and appears unsplit. For **$\{\mathbf{NiPd}\}_2$**, the zero-field transitions are even located below the accessible energies, yet simulations of the field-dependency still allow to extract the Ni^{2+} ZFS parameters. With $D = -2.6\ \mathrm{cm}^{-1}$ and $|E| = 0.6\ \mathrm{cm}^{-1}$ for **{NiPd}** and $D = -0.9\ \mathrm{cm}^{-1}$ and $|E| = 0.17\ \mathrm{cm}^{-1}$ for **$\{\mathbf{NiPd}\}_2$**, it is apparent that D is substantially lower than in the corresponding Pt^{2+}-containing complexes, while the rhombicity is systematically larger. Furthermore, it is seen that the ZFS is smaller in both monomers as compared to the dimers. (ii) The second major difference is that in contrast to **$\{\mathbf{NiPt}\}_2$**, **$\{\mathbf{NiPd}\}_2$** signals are readily detectable at temperatures as low as 4.8 K already, consistent with a significantly smaller exchange interaction on the order of the thermal energy and confirmed by the simulations with a fixed $j = 5.0\ \mathrm{cm}^{-1}$.

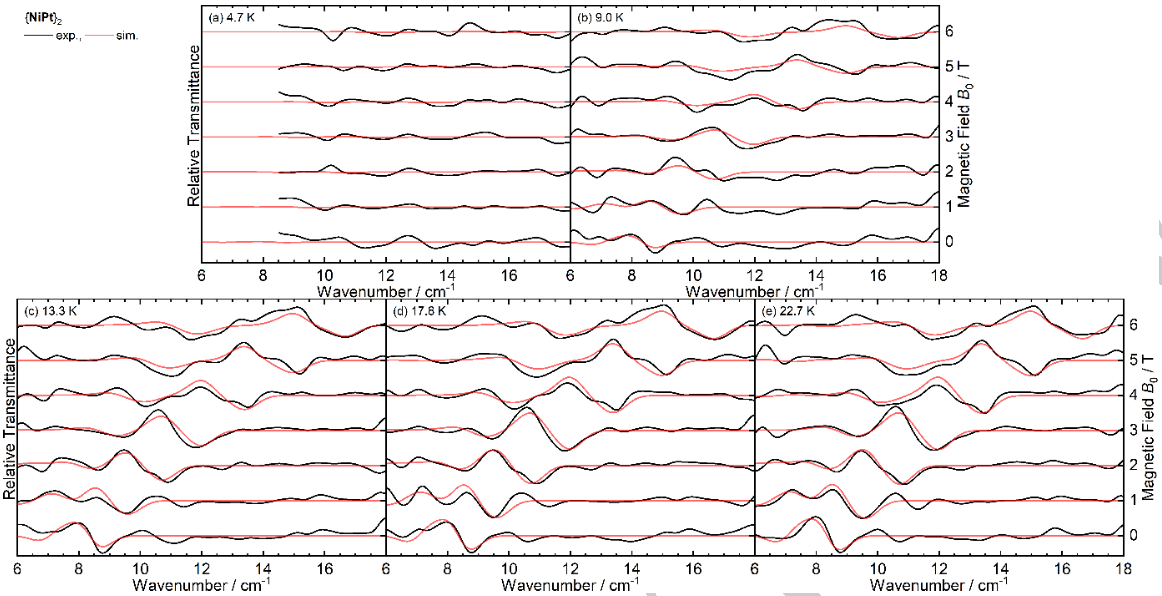

Figure S10: Experimental (black) and simulated (red) FD-FT THz-EPR magnetic-field division spectra of **{NiPt}$_2$** recorded at T = (a) 4.7, (b) 9.0, (c) 13.3, (d) 17.8 , and (e) 22.7 K. Spectra were calculated by division of a transmission spectrum at B0 + 1 T by a corresponding one at B0. Thus, maxima correspond to stronger absorption at B0, minima to increased absorption at the higher field. In (a), overly noisy data in the region ¡ 8.5 cm^{-1} due to the use of a different beam splitter (23 μm instead of 125 μm) are not shown.

References

[1] F. G. Baddour, A. S. Hyre, J. L. Guillet, D. Pascual, J. M. Lopez-De-Luzuriaga, T. M. Alam, J. W. Bacon and L. H. Doerrer, *Inorganic Chemistry*, 2017, **56**, 452–469.

[2] F. G. Baddour, S. R. Fiedler, M. P. Shores, J. W. Bacon, J. A. Golen, A. L. Rheingold and L. H. Doerrer, *Inorganic Chemistry*, 2013, **52**, 13562–13575.